PhD-FSTM-2022-134
The Faculty of Science, Technology and Medicine

DISSERTATION

Defence held on 07/10/2022 in Luxembourg

to obtain the degree of

DOCTEUR DE L'UNIVERSITÉ DU LUXEMBOURG

EN SCIENCES DE L'INGENIEUR

by

Marie-Alix DALLE
Born on 7 June 1990 in Grenoble, (France)

EXPERIMENTAL AND THEORETICAL INVESTIGATIONS FOR THE IMPROVEMENT OF AGMD ENERGY EFFICIENCY

Dissertation defence committee

Dr Leyer Stephan, dissertation supervisor
Professor, Université du Luxembourg

Dr Hansen Joachim
Professor, Université du Luxembourg

Dr Maas Stefan, Chairman
Professor, Université du Luxembourg

Dr Bandelier Philippe
Professor, CEA

Dr Koschikowski Joachim
Professor, Fraunhofer Institute

Experimental and Theoretical Investigations for the improvement of AGMD Energy Efficiency

Marie-Alix Dalle

December 25, 2022

Contents

List of Figures

Marie-Alix Dalle

List of Tables

Nomenclature

Acronyms

$AGMD$ Air-Gap Membrane Distillation

CFD Computational Fluid Dynamics

CKT Classical Kinetic Theory

CoV Coefficient of Variation

$DCMD$ Direct Contact Membrane Distillation

GOR Gain Output Ratio

LCA Life-Cycle Assessment

MD Membrane Distillation

MED Multi-Effect Distillation

MSF Multi-stage flash

OPL Optical path length m

RO Reverse Osmosis

RR Recovery Ratio   %

$SGMD$ Sweeping Gas Membrane Distillation

SM Static Mixing

SRT Statistical Rate Theory

VMD Vacuum Membrane Distillation

Greek Symbols

α deflection angle rad

β thermal expansion coefficient K^{-1}

δ^m membrane thickness m

δ^s thickness of the spacer mesh m

ϵ membrane porosity

ϵ^s voidage of the spacer

η dynamic viscosity $Pa.s$

γ frequency of the light oscillation Hz

γ_L liquid surface tension $N.m^{-1}$

ι dielectric constant

κ	thermal diffusivity	$m^2.s^{-1}$
λ	light wavelength	m
μ	permeability	m^2
ν	kinematic viscosity	$m^2.s^{-1}$
ω	angle between the fibers of the spacer net	rad
Ω	angular frequency	Hz
Φ	light phase	rad
ρ	density of water	$kg.m^{-3}$
σ	Stefan' constant	$W.m^{-2}.K^{-4}$
σ_{cond}	fraction of molecules striking the interface and condensating	
σ_{evap}	fraction of molecules striking the interface and evaporating	
τ	temperature polarization coefficient	
θ	liquid solid contact angle	rad
Ξ	angle between the flow direction and the spacer net-grid	rad
ξ	pore tortuosity	

Roman Symbols

Δa	displacement of the light beam in vertical direction z above the knife-edge	m
ΔH_v	molar latent heat of vaporization	$J.mol^{-1}$
C	concentration	$kg.m^{-3}$
c	light velocity in vacuum	$m.s^{-1}$
c_0	light velocity in the considered medium	$m.s^{-1}$
D	diffusion coefficient	$m^2.s^{-1}$
d^{po}	membrane pore size	m
d_e	collision diameter of molecules	m
D_k	Knudsen diffusion coefficient	$m^2.s^{-1}$
d_{min}	minimum observable distance from the membrane	m
e	air-gap thickness	m
$f1$	mirror's focal length	m
$f2$	imaging lens' focal length	m
h^a	air heat transfer coefficient	$W.m^{-1}.K^{-1}$
h^h	hot feed heat transfer coefficient	$W.m^{-1}.K^{-1}$
$h^{m,s}$	membrane's polymer thermal conductivity	$W.m^{-1}.K^{-1}$
h^{mg}	gas thermal conductivity in the membrane	$W.m^{-1}.K^{-1}$
h^m	effective membrane thermal conductivity	$W.m^{-1}.K^{-1}$
h^p	permeate thermal conductivity	$W.m^{-1}.K^{-1}$
j^L	equilibrium collision rate of the water molecules with a flat liquid vapor surface	$kg.m^{-2}.s^{-1}$

j^V	equilibrium collision rate of the vapor molecules with a flat liquid vapor surface	$kg.m^{-2}.s^{-1}$
j^{LV}	resulting evaporation rate	$kg.m^{-2}.s^{-1}$
k	wave number	m^{-1}
k_B	Boltzmann constant	$m^2.kg.s^{-1}.K^{-1}$
k_m	mass transfer coefficient	$m.s^{-1}$
K_n	Knudsen number $= \frac{l}{d^{po}}$	
L	length of the module	m
l	mean free path of transported molecules	m
l_s	length of the spacer mesh	m
n	refraction index	
n^{po}	pore density	
N_d	molecular diffusion mass flux	$kg.m^{-2}.s^{-1}$
N_k	Knudsen mass flux	$kg.m^{-2}.s^{-1}$
N_p	Poiseuille mass flux	$kg.m^{-2}.s^{-1}$
Pv	vapor pressure	Pa
q^{LV}	net evaporative heat flux	$W.m^{-2}$
q^{po}	single pore flow	$m^3.s^{-1}$
Re	Reynolds number	
Sh	Sherwood number	
T	temperature	K
u	wave disturbance	
Vp	mean velocity perpendicular to the membrane (along z axis) in a plane (x, y) located 0.1mm from the membrane	$m.s^{-1}$
Y_{ln}	log mean partial pressure of air present within the pores	

Superscripts

a	air-gap
c	cold channel
h	hot water feed
L	liquid
m	membrane
p	permeate
po	pore
V	vapor

Subscripts

b	in bulk flow
CKT	according to Classical Kinetic Theory

eq   at equilibrium

iam   at the interface between the air-gap and the membrane

ic   at the condensation interface

ie   at the evaporation interface

int   at the interface

s   spacer

SRT   according to Statistical Rate Theory

Other Symbols

ray   the minimum element of a light beam

Conventions

In the whole thesis, the following conventions will be used (Figure 1):
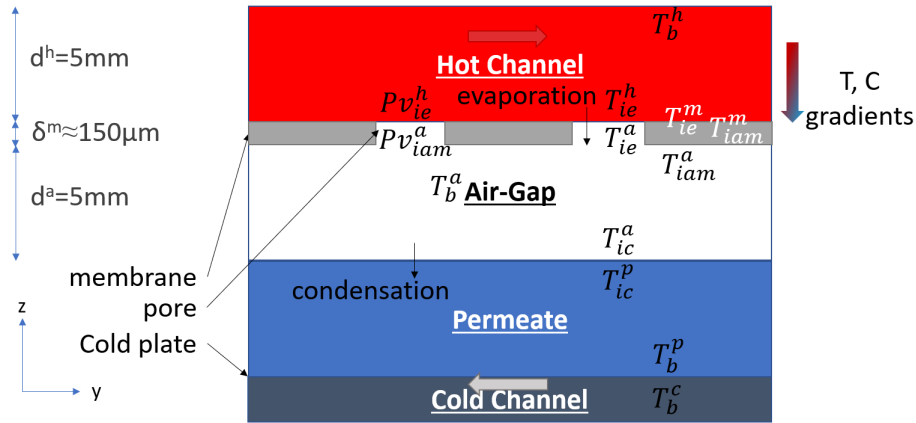
Figure 1: Conventions for temperature and pressure variables in the AGMD module

T and Pv stand for the temperature and the vapor pressure. The superscripts define the phase to which belongs the variable (h for the hot water feed, m for the membrane, a for the air-gap, p for the permeate, c for the cold channel); while the subscripts indicate the localization at which the variable is taken (b in the bulk flow, ie at the evaporation interface, ic at the condensation interface, iam at the interface between the air-gap and the membrane).

The coordinate system in figure 1 is consistent all throughout the thesis.

Abstract

Water and power related resources (energy sources and required material) are both critical and crucial resources that have become even more and more strategic as a result of climate change and geopolitics. By making a large store of salty water available, desalination appears to be a viable solution to the water crisis already affecting 40% of the population today. However, because existing desalination procedures are power intensive and rely on non-renewable energy resources, their power use at large scale is unsustainable. Alternative techniques exist that are promising in terms of environmental impact, but not yet competitive in terms of fresh water outflow and energy efficiency.

The focus of this work is on one of these alternatives, Air-Gap Membrane Distillation (AGMD), which was chosen because it relies on low-grade heat that is easy to collect from solar radiations or from industrial waste heat. This technique mimics the water cycle, thanks to the use of a membrane, allowing to bring the hot and cold water streams closer together. As a result, the temperature difference that drives evaporation is strengthened and the process accelerated. However, the development of a boundary layer at the membrane interface reduces this temperature difference and thus decreases the overall performance of the process. Thus this technique still requires some improvements to become industrially attractive, in terms of fresh water outflow per kWh and energy use. The goal of this thesis work is to contribute to AGMD energy efficiency and output flow enhancement by leveraging both experimental and theoretical considerations.

A test facility characterizing the boundary layer based on a Schlieren method as well as an adapted AGMD module were designed and built. By interacting with the boundary layer, the laser allows the observation of the continuous temperature profile in the hot water channel of a flat sheet AGMD module. The measurement can be performed in close proximity to the membrane and under a variety of operational conditions (inlet hot and cold temperatures, inlet velocities). In parallel, the fresh water outflow corresponding to these experimental conditions can be measured. Moreover, the experimental layout opens the way for further observations of the AGMD process from a different angle - such as concentration profiles or experimentation in the air-gap - with very little addition.

The overall experimental set-up has eventually been used to produce a first set of data over a range of temperature (60-75°C), which is then interpreted thanks to a custom algorithm deriving the temperature profiles and boundary layer thicknesses. A three dimensional heat and mass transfer model for AGMD (3DH&MT) - previously developed in the research team - has been used to numerically reproduce the experimental conditions and compare the results. The comparison showed promising results as the temperature gradients at the membrane interface and fresh water outflows present similar orders of magnitude and trends. The accuracy of the experiment can be further increased through several adaptations in the set-up. This 3DH&MT model could be used to simulate more complex AGMD module designs, such as spiral modules in order to optimize the operating conditions and the overall shape of the AGMD module to enhance its performances.

Finally, in the aim of improving the energy efficiency and fresh water outflow of the AGMD process, spacers are usually added in the individual channels to boost mixing and thus reduce the boundary layer thickness, which improves evaporation flux. Two novel spacer geometries inspired by current industrial mixing state of the art and nature have been proposed and investigated, yielding interesting results for two distinct applications. One is particularly well-suited to maximizing mixing regardless of the energy used, hence improving the energy efficiency of the process. The second is optimal for minimizing energy consumption while maintaining a decent mixing result, thus enhancing the fresh water outflow of the process. A couple of indicators have also been proposed to assess the mixing performance of more complex 3D geometries.

Overall this work broadens the current AGMD research by providing an experimental test-bench enabling the continuous temperature profile measurement, and the validation of a 3D heat and mass transfer model. Moreover, interesting tracks for improving the design of spacers are proposed in order to minimize the AGMD process's energy efficiency resistance.

AGMD is an extremely promising water treatment technique since it is applicable to a broader range of waters than just seawater. The test equipment described in this work is sufficiently adaptable to investigate this potential as well as variants of AGMD processes that might boost its attractiveness. As it is based on readily available materials and technologies, it may be used anywhere and its reliance on a naturally available energy flow (solar radiation) makes it attractive in isolated regions.

Acknowledgment

This work, although quite solitary, could not have been completed without the assistance and support of a variety of people, whether they were directly involved in the work, or simply made my life easier and full of pili-pili to keep my spirits up.

First and foremost, I'd like to express my gratitude to the entire technical team at the University of Luxembourg's Campus Kirchberg, particularly Grace, Marc and Gilbert, for their efficient and relevant everyday support; and Claude Wolf for his design assistance, 3D printed modules and laser cuts. Thank you also to Grace, who provided me with much more than technical assistance, especially through all of the shokies we shared at the canteen.

Thank you also to my research group's colleagues, especially Michel, for sharing the water lab and a slew of very insightful ideas. A special thank you also to Filip for your patience and kindness during our lengthy chats, as well as your well-illustrated explanations! And of course, thank you for bringing in Agnieszka, who arrived just in time to help me getting up and moving forward when I was stuck.

Tobias and Veronika, I have not enough words to describe how grateful I am to have met you, and how much our friendship has helped me get through this challenge, thanks to our highly inspiring lunches, and side-work activities, whether rock-climbing or game nights. Of course I am not forgetting Kerstin, Suzanna, Hanka, Shilton, Andrii, Tamineh and the rest of you who brightened my days at Uni with your friendship and joyful lunches.

Above all, I want to express my gratitude to Pr. Leyer for creating an atmosphere of autonomy, liberty and respect, in which I was able to do my research, thanks to his open mind and encouragement.

I'd like to thank Silvia for sharing her membrane knowledge, Alexander Kroiss and his team for providing optical guidance and welcoming me for a few days at TUM, and Bojan Niceno for supporting me with T-Flows.

In addition, I am extremely grateful to Pr. Joachim Hansen and Pr. Stefan Mass for being part of my CET over the past four years, and to Pr. Philippe Bandelier and Dr. Joachim Koschikowski for agreeing to be part of my jury.

The DESCOM, the Scienteens lab and the MNHN made this journey extremely enjoyable, especially Nicole, Conrad David and Una, and Sandrine, who gave me with the opportunity to share my enthusiasm for science through many interactive means.

My stay in Luxembourg would have had a very different flavor if I did not meet the Transition community: thank you Daniel, Anne-Marie, Sandra, Camille, for these sunny (and less sunny) week-end afternoon where I learned a lot at the Garden; thank you Riccardo, Elodie, Delphine, Delphine and Marine, for this fantastic Altercoop adventure. Thank you also to Shifters and Fresqueurs, Fred, Mark, Thomas, Elorri, for our fruitful and enriching debates on how to make the world a better place.

Audrey, Caro I am so happy I met you, thank you for all of our adventures, physical or cultural.

To Irène, I know I will always find in you an understanding ear to my metaphysical questions, and with Val, a pair of coaches adding sportive challenges to my life, while supporting my crazy adventures with sloths. Thank you for everything.

Thank you very much to my parents for their education and support, without which I would not be here today and would not have become who I am.

Last but not least, I would like to extend a heartfelt thank you to Jeremy, without whom this journey would never have existed, and who played an important role in the completion of this thesis. Thank you for your everyday patience, listening and support during these past four years. And above all thank you for choosing to share your projects with me and to accept my crazy ideas, making this episode one small part of our bigger adventure.

Preface

General introduction

According to the World Health Organization's most recent paper, "in 2015, 844 million people [1 person out of 10] still lacked even a basic drinking water service [160] that is, an improved source within 30 minutes' round trip to collect water". Moreover, four out of ten people are already affected by water scarcity every day [159]. In line with this observation, the 6th sustainable development goal strives to ensure the supply of clean water for current and future generations [66].

The latest IPCC report [90] confirms that the greenhouse gases emissions due to human activities, paired with intense deforestation caused by escalating urbanization and intensive agriculture, increase this water stress by intensifying droughts and floods.

In this light, finding a water treatment process that is both low-fossil fuel energy using and highly efficient looks to be critical.

This work explores the current situation of the world's water and energy resources, as well as existing fresh water procurement alternatives, with the goal of proposing the best sustainable fresh water procurement strategy.

Overview of the content of the thesis

This thesis is divided into three main chapters, each starting with keypoints. References to other sections or figures are interactive.

The first section provides relevant introductory material as well as information about the rationale for selecting this work's subject of study, and the motivations for the research's direction. The global context of water and energy supplies and consumption is examined, highlighting desalination as a pertinent solution to this challenge. Then, a review of the different desalination solutions available, both natural and man-made, is shown. The energy forms and sources required for these various technologies are compared and contrasted, in order to find the most environmentally friendly and passive process, which leads to the selection of Air-Gap Membrane Distillation (AGMD) as the subject of this study. Literature on this technology is reviewed and state of the art in modeling and optimization of this process is analyzed. This results in the formulation of the following research questions: providing an experimental and numerical study framework to support the design and identification of optimized AGMD configurations; and formulating a concrete and argued improvement path for the module design.

All the necessary preliminary information to answer these research questions is covered in the second section. The different physical phenomena involved in the selected process are discussed, and the main limitation is identified. Then an experimental and numerical framework for study of this limitation is proposed. A general test facility is described, and after review of different temperature and concentration observation methods, the Schlieren method is selected. A three dimensional heat and mass transfer model for AGMD (3DH&MT) is presented to complete this study framework, that the experimental facility intends to validate. Finally, in order to alleviate the identified limitation, various static mixing procedures are discussed from which inspiration for a spacer computational fluid dynamic (CFD) analysis is drawn.

The results of these works are presented and discussed in the third section of this thesis. The designed test facility is described, as well as the associated AGMD module and the computational tool developed to forecast the expected observations. The experimental findings obtained with this test facility are

presented and compared to the numerical results obtained using the 3DH&MT model. Finally, CFD simulations are used to analyze the effect of two novel spacer geometries on the AGMD performances.

The appendix compiles supplementary aspects related to the context.

One chapter explores the evaporation models in order to understand better the mass transfer resistance mechanisms inside AGMD, and concludes that diffusion might be the main limitant factor, in agreement with the assumption made in literature.

The second chapter explores solutions from nature and low-tech to improve even more AGMD energy efficiency and proposes an adapted AGMD module taking into account these propositions.

Marie-Alix Dalle

Part I

Background and state of the art

Highlights from Part I

Fresh water and power related resources (energy sources and raw material) are scarce resources to save.

⇒ A low fossil fuel consuming water desalination solution appears as a consistent solution.

Among all existing desalination solutions, Air-Gap Membrane Distillation appears as a relevant alternative, relying on a naturally available energy flow.

⇒ Its energy efficiency and output flow still has to be improved to become industrially scalable.

The current state of the art of AGMD research lacks knowledge about the actual boundary layers building up inside the hot water channel and the air-gap, and modeling strategies allowing for convection to occur in the air-gap.

⇒ A test facility allowing such observation will be set up, and used to validate a three-dimensional heat and mass transfer model of AGMD. A CFD analysis will be performed on novel spacer geometries to reduce these boundary layers.

Chapter 1

Global water and energy context

Water and energy resources are closely linked, as the first requires the second to be treated, while the use of the second impacts the availability of the first.

1.1 Water resources

Although it is covered with water and its oceans are deeper than the highest peaks on the planet, the Earth has only 0.023% of its total mass in water resources. 97% of this water is held in seas and oceans (thus salted), 2% is stuck under ice form, and only 1% is liquid fresh water, with surface fresh waters (rivers, lakes...) accounting for only 0.01% of the total water resources on Earth [32].

According to WHO, between 50 and 100 liters of water per person per day are required to meet the majority of basic needs while posing few health concerns. However, fresh water is required for more than just drinking. It is primarily utilized in agriculture, and also in industry to some level. And, according to the Water Resources Group 2030, global water use is anticipated to rise in the near future.

A fresh water footprint is estimated as the total amount of fresh water needed to generate the goods and services consumed, which is roughly $1240m^3/year/person$ on average globally, with significant variation among regions.

This uneven distribution of resources and uses leads to very different water stress levels across the Globe (fig. 1.1):
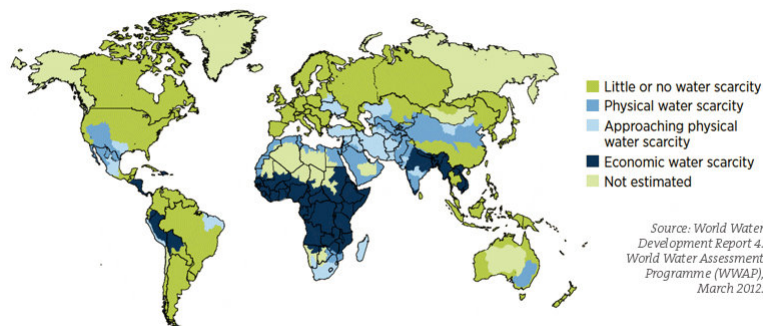
Figure 1.1: Water Stress across the World [110]

In particular, the countries most affected by water stress are almost always located along the shore, with direct access to seas and oceans, and surrounding the tropics, which have the best insulation.

Desalination appears to be a viable solution to the fresh water issues faced in this period, given the ubiquity of sea water on Earth and its accessibility to most countries experiencing water stress, as well as the declining quantity of fresh water.

1.2 Energy resources

To transform salty water into fresh water, an energy flow is required. Most of the energy flows used globally come from energy storages [6] that are renewed more slowly than they are used [46], generate pollution and disrupt water cycle and ecosystems [90]. The necessary power can nevertheless be also extracted from naturally available energy flows. In particular, solar radiation is the main energy flow reaching Earth, responsible for most of the other energy flows that humanity uses (section G.1).

To convert these energy sources into the final useful energy flow form (electricity, heat, work, food), a converter is required with a given efficiency below 100%, and requiring material to be built. The more conversions, the greater the energy losses; and the less dense the energy storage or energy flow source, the more raw material is required [97].

Moreover, not all energy forms are equivalent. For instance, electricity can be used to produce pressure, heat, or electrical current with an efficiency of almost 100%: its exergy (see section G.1.2) content is thus about 100%. On the other hand, heat is the most degraded form of energy. To produce something else than heat from heat, a thermal machine is required, whose yield (and thus exergy) is maximum 60% (Carnot). For low grade heat the real efficiency is even lower, up to 20%.

Relying on the most abundant energy flow and the closest energy form from the original, and making the process the most energy efficient is thus a good way to save resources. Additionally, making use of low grade heat for desalination is a good way to preserve exergy.

1.3 Energy for water treatment

Nowadays, approximately $0.5kWh.m^{-3}$ is required to treat fresh water, $1kWh.m^{-3}$ to treat waste water and $2kWh.m^{-3}$ to treat salty water [47], and this value is nearly at its theoretical minimum.

Indeed, theoretical reasoning can provide an estimate of the minimum amount of energy required for the desalination process. In an ideal system, with no irreversibility, no loss and a 100% yield, the minimum energy to introduce into the system is that required to overcome the osmotic pressure in Reverse Osmosis (RO), and that required to overcome the ebullioscopic deviation (the difference between the boiling temperatures of salt water and fresh water at a given pressure) in evaporation-based processes.

For Reverse Osmosis, this minimum energy requirement, corresponds to the work needed to transfer 1kg of water to a pressure deviation equal to osmotic pressure. The osmotic pressure of sea water is approximately $29.10^5 Pa$, or 30 times the atmospheric pressure, but in order to achieve a significant flux and compensate for the increasing osmotic pressure as the water is extracted, the work pressure should be between 60 and 70.10^5 Pa: $W_{RO} = VP_{\text{osmotic, salty water}} = \frac{m}{\rho_{\text{pure water}}} P_{\text{osmotic, salty water}} = 0.81kWh.m^{-3}$.

For distillation, when pure water and salty water are both kept at temperature of 25°C, the partial water vapor pressure above salty water ($P_{v,\text{salty water}} = 3105Pa$) will be slightly lower than that above pure water ($P_{v,\text{pure water}} = 3170Pa$). This means that in order to reach the same pressure, the salty water should be slightly warmer than the pure water (or that salty water boils at a higher temperature than fresh water). The minimum desalination energy required is the amount of work required to raise the pressure of 1kg of vapor from the pressure above salty water ($P_{v,\text{salty water}}$) to the pressure above pure water ($P_{v,\text{pure water}}$). According to the law of reversible isothermal compression, the work to provide for distillation is: $W_{distillation} = \frac{m}{M}RTln(\frac{P_{\text{pure water}}}{P_{\text{salty water}}}) = 0.79kWh.m^{-3}$.

According to the first principle of thermodynamics, and taking into account the processes' identical initial (salty water) and final (fresh water) states and total reversibility, it is normal to find $W_{RO} \approx W_{distillation}$ [23].

However, as mentioned in section 1.2, the quality of energy required in both processes differ: in the case of Reverse Osmosis, the electricity needed contains a high amount of exergy whereas for Membrane Distillation, the necessary low grade heat represents a low quantity of exergy.

The average annual water consumption is approximately $4.10^{12}m^3$ [1], and the energy required to treat, retreat and distribute it is of the order of $120MToe$ (fig. 1.2), which represents about 1.5% of total World energy consumption [17].
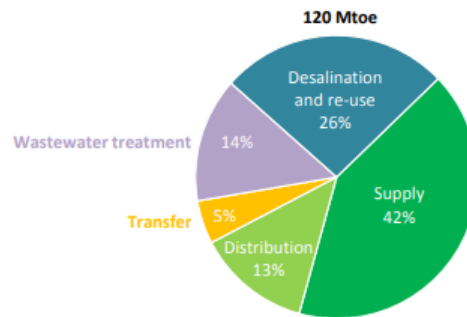
Figure 1.2: Energy uses in Water sector (World Energy Outlook 2018 [6])

According to fig. 1.3, the countries relying the most on desalination are Saudi Arabia, United Arab Emirates and Spain:

Figure 1.3: Countries relying the most on desalination [1]
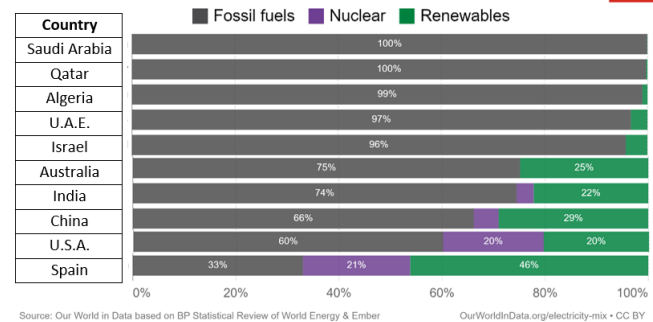
Figure 1.4: Electricity mix of the countries relying the most on desalination [117]

As can be seen in fig. 1.4, the electricity mix on which relies the desalination plants of most of these countries is highly carbonated.

Only a few of these plants rely solely on renewable energies as reported in Abdelkareema et al. [3] (table 1.1).

---

[1] https://ourworldindata.org/water-use-stress

Country	Total Mm^3/d	Geothermal (m^3/d)	Wind (m^3/h)	Solar (m^3/d)
Saudi Arabia	5.2	0	0	0
UAE	4.1	0	0	0
Spain	3.3	0	3.1	0.2
USA	2.9	98.4	0	0
China	2.4	0	0	0
Algeria	2.2	0	0	0
Australia	1.7	0	5.4	9.3
Israel	1.4	0	0	0
India	1.1	0	0	3.8
Quatar	1.0	0	0	0

Table 1.1: Comparison of the total volume of desalinated water with the volume produced by desalination plant relying on renewable energies in the top 10 countries regarding installed desalination capacity [3]

Thus most of the energy forms used for water desalination in the World rely on fossil sources of energy.

Energy appears as being both part of the solution, as it is needed for fresh water production, and part of the problem, as 80% of current energy consumption rely on fossil fuels which contributes to climate change exacerbating fresh water scarcity.

As a result, the water desalination technology selected should take this into account and aim to minimize its energy footprint.

1.4 Conclusion on global water and energy context

Examination of Earth' water and energy resources highlighted solar-powered desalination as a relevant solution to the fresh water issues faced in this period.

Chapter 2

Water desalination

Desalination occurs naturally in several occasions, and has been also exploited industrially under various processes. Several of these desalination solutions and technologies are examined and compared in terms of their energy requirement and environmental impact.

2.1 Preliminary definitions

In this work, a system is said passive if it relies only on a naturally available energy flow (gravity, wind, solar radiation...).

A system is said to be sustainable if it does not rely on depletable resources, does not cause lasting damage to a resource or minimizes its use, and minimizes the pollution and other environmental footprint (land use).

A low-tech system relies on simple and cheap technologies for which the required knowledge is freely available, can be handled by a small group of person and does not necessitate specializations.

The ideal desalination process would fulfill all of these criteria, to reach the smallest environmental footprint, whether in terms of resources (fossil fuels, rocks, rare earth, raw material etc...) and pollution, and be accessible to the majority of countries.

2.2 Natural desalination processes

Numerous natural processes already provide methods for desalinating or purifying water, and several technologies are inspired by them.

These processes can be classified as phase change processes or filtration processes.

2.2.1 Phase change based solutions

Phase change solutions rely on the difference in phase change temperatures to separate water from its pollutants.

2.2.1.1 Water cycle

The most common natural method of water desalination is through the water cycle. Based on evaporation and condensation, this process is quite simple as it mostly requires a heat source (the sun) and a heat sink (high atmosphere), but is characterized by large spatio-temporal scales.

At the core of this process is the evaporation of molecules mainly from the ocean heated by the sun, then rising in the air as vapor, where they encounter cooler areas and nucleation sites causing them to condensate, before falling down as fresh water.

Its motor, the sun, is the main source of power reaching Earth, thus naturally accessible. By identifying ways to make it more compact and faster, this process is easy to replicate.

2.2.1.2 Freezing

At the planet's poles, under the influence of cooler temperature, the salty liquid water freezes under the form of icebergs composed of fresh water, as a result of crystal formation. Due to the fact that the

enthalpy of water solidification ($335 kJ.kg^{-1}$) is significantly lower than the enthalpy of water vaporization ($2260 kJ.kg^{-1}$), freezing appears to be a promising technology.

However, its source of power, the cold, is not naturally accessible everywhere.

2.2.2 Filtration based solutions

Another way to separate water from pollutants is to pass it through a filter medium.

2.2.2.1 Kidneys

Kidneys are a natural filtration system based on a double barrier of charge and size selectivity, as they are composed of negatively charged cells, and holes covered capillaries (60-100nm diameter) [118].

The main energy source for this process is the living organism's body, which generates pressure that causes some of the fluid to pass through the glomerulus membrane pores, and the charged proteins.

2.2.2.2 Chloride cells in gills

Fish survive in salty water thanks to the enzyme Na+,K+,ATPase reestablishing the concentration balance between the fish's blood and sea water, by allowing chloride ions to enter the organism through the chloride cells of the teguments in response to the ambient salt concentration.

Apart from this system, fishes adapt their behavior as well: in salty water, they consume a large amount of water to compensate for the natural osmosis effect between their body and the salty water, which draws fresh water out of their bodies. They also reject a very scarce and extremely concentrated urine to conserve as much fresh water as possible inside their bodies.

This process mainly depends on pressure, which is used to draw water through the teguments, and the enzyme, both produced by the fish (while swimming, or chemically).

2.2.2.3 Mangroves and halophilic plants

Mangroves are a type of vegetation growing in salt water, where no other plant can grow, thanks to unique strategies depending on the specie. The first specie growing the closest to the shore in deep water stops the salt up to nearly 90% thanks to their roots, impregnated with suberin making them impermeable. The species living on higher grounds are only submerged during high tides, when the pneumatophores (tubes erected towards the sky) provide oxygen to the plant. The salty water coming in their roots is filtered via a simple non metabolic ultrafiltration process, combined with ion transport [127], to produce a salt free sap.

The entire water collection and filtering system is driven by transpiration, powered by solar radiation, and resulting in capillary pumping into the root. The water thus drawn in is then filtered through a membrane [150].

Several projects such as the FreshWater Factory (2013), or a Central Paris project, have attempted to implement the use of mangroves to desalinate water, but without concrete realization.

2.2.2.4 Aquaporin

A class of membrane protein called Aquaporin and present in the cells of most living beings (animal and humans) enables the selective passage of water into and out of cell membranes [27].

The main energy required in this process is the production of this selective molecule.

The company Aquaporin is developing a water treatment process based on this molecule.

2.2.3 Conclusion on natural desalination processes

The water cycle and the mangrove desalination processes, relying on solar radiation as the energy flow, can be classified as passive processes, which can serve as basis for inspiration for a sustainable desalination process.

2.3 Man-made desalination processes

Desalination was discovered a long time ago: Aristotle wrote in Meteorologica "I proved experimentally that the evaporating salt water becomes fresh and that the condensing vapor does not form salt water again". Over the years, Man developed various desalination technologies.

2.3.1 Main industrial processes

Between 1880 and 1960, the dominant technology was the Multi-Effect Distillation (MED) (section 2.3.1.2.2), which was subsequently supplanted in the 1960's by Multi-stage Flash Evaporation (MSF) (section 2.3.1.2.1). Both of these technologies rely on heat and low pressures, which are typically generated by fossil fuel power plants. In the 1970', the development of new membranes facilitated the dominance of Reverse Osmosis (RO) (section 2.3.1.1), a high pressure-based process.

Today, these three technologies continue to be the most widely used, accounting for 94% of total desalinated water production: Reverse Osmosis accounts for 84% of total number of operational desalination plants and 69% of total global desalinated water production [66].

The current installed capacity for desalinated water production reaches 95.37 million m^3/day [60], or about 0.8% of the fresh water consumption[1].

2.3.1.1 Reverse Osmosis

Reverse Osmosis relies on chemical interactions between the salts. Naturally, the less concentrated water flows toward the most concentrated one in order to homogenize the concentrations. Reverse Osmosis is the inverse of this natural phenomenon. A high pressure is applied to the more concentrated solution, in order to compensate for the difference in osmotic pressure between it and the less concentrated solution separated by a membrane. Consequently, the water molecules from the more concentrated compartment migrates toward the less concentrated compartment, leaving the salts on the other side of the membrane.

The theoretical minimum required pressure, expressed by the Van't Hoff equation, is about $29.10^5 Pa$. The RO processes actually reach pressures ranging around $60 - 70.10^5 Pa$, as seen in section 1.3. The membranes must then withstand very large pressure differences.

2.3.1.2 Distillation

Distillation is the simplest process: when water is heated, the salts are deposited as the water molecules evaporate, before condensing.

One disadvantage of simple distillation is the high energetic cost to boil the salty water.

The second disadvantage is the presence of reverse solubility salts, becoming less and less solubles as the temperature rises (carbonates, calcium sulfate, magnesium, present at about 4.5g/l). Working at lower temperatures (below 60 °C) is one way to avoid the formation of such precipitates. However, achieving distillation conditions requires working at a reduced pressure (approximately 200hPa) [23].

2.3.1.2.1 Multi-Stage Flash

Multi-Stage Flash is a desalination process consisting of heating sea water then injecting it in a series of cells where pressure is lower than the saturation pressure. Overheated water will spontaneously boil, quite violently (hence "flash"), in order to return to thermodynamic equilibrium. The vapor produced is condensed using sea water which is thus pre-heated, saving part of the required energy [23].

2.3.1.2.2 Multi-Effect Distillation

The Multi-Effect Distillation was developed specifically to save thermal energy. The name "effect" refers to the different evaporators placed one after the other. The thermal power supplied to the first evaporator is used to evaporate sea water. The generated vapor is condensed in the subsequent effect. The condensation enthalpy is then used to evaporate sea water again, and so on until the final condensator is reached.

---

[1]https://ourworldindata.org/water-use-stress

2.3.1.3 Pervaporation

Pervaporation is the partial vaporization of a liquid through a dense membrane. It consists in an adsorption, a diffusion and a desorption step. It is the contraction of "permeation" through the membrane, and "evaporation" into the vapor phase.

2.3.1.4 Electrodialysis

Electrodialysis is powered by electricity and works by causing ions to move through a stack of anionic and cationic ion exchange membrane layers.

2.3.2 Emerging desalination processes

In parallel of these main industrial technologies, other desalination processes emerge. The two processes presented in this section were selected according to the guidelines presented in section 2.1. Indeed, both processes rely on natural energy gradients for their core desalination process, even though another energy source might be required for the fluid circulation for instance. Their set up and maintenance is quite easy, and the required material are mostly widespread, except for the membrane which requires more complex processes for its production.

2.3.2.1 Nanoseen

Nanoseen [93] created special nanofiltration membranes based on different nanomaterials, to capture salt and other impurities in their pores, using gravitation as a natural energy flow source and thus not necessitating any other energy source (fig. 2.1).
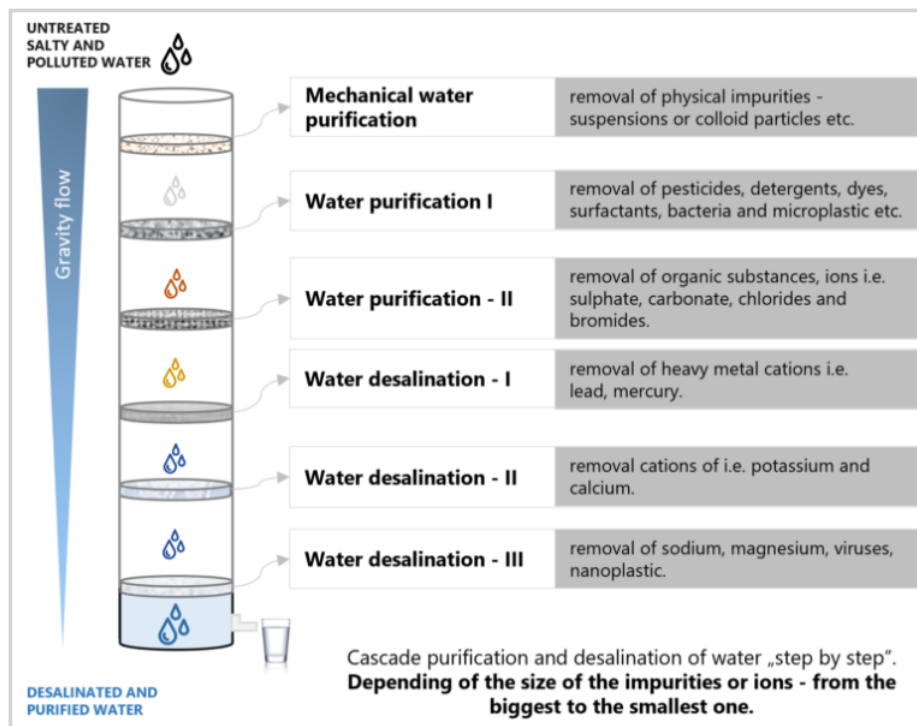
Figure 2.1: Concept of Nanoseen [93]

2.3.2.2 Membrane Distillation

Membrane Distillation (MD) is a hybrid process, both membrane-based and thermal-driven.

Rather than being driven by a difference in mechanical pressure, the process is driven by a difference in vapor pressure between the two sides of the membrane, caused by a temperature difference, which causes the vapor to migrate through the membrane and condense on the cold point.

This technology has a better selectivity than reverse osmosis, is very compact, operates at low temperature and is less prone to fouling. However it has never reached industrial scale due to the membrane's low fresh water outflow.

2.3.2.2.1 Membrane configurations

The difference in vapor pressure across the membrane driving the MD process can be imposed in a variety of ways, depending on the MD design [80] (fig. 2.2):

- DCMD: Direct Contact Membrane Distillation: a temperature difference across the membrane caused by the direct contact of a cooling fluid with the membrane
- AGMD: Air-Gap Membrane Distillation: a temperature difference across the membrane and an air-gap separating the membrane from the condensing surface maintained at a low temperature thanks to a coolant fluid
- SGMD: Sweeping Gas Membrane Distillation: a gas sweeping off the surface of the membrane
- VMD: Vacuum Membrane Distillation
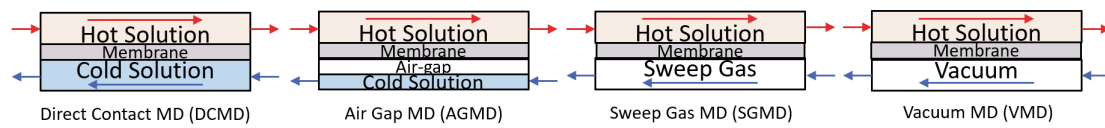
Figure 2.2: Sketch of the different membrane distillation processes

The table below summarizes the advantages and drawbacks of these various designs (table 2.1):

	DCMD	AGMD	SGMD	VMD
Advantages	- high desalinated water flux (competing RO) - simplest configuration : requires less equipment and easy to operate	- heat loss by conduction reduced - most versatile MD configuration - high energy efficiency - capability for latent heat recovery	- heat loss by conduction reduced - mass transfer coefficient enhanced because not stationary	- heat loss by conduction negligible thus greater driving force - high desalinated water flux
Drawbacks	- heat loss by conduction - high temperature polarization - low energy efficiency	- low desalinated water flux due to resistance to mass transfer caused by stagnant air	- small volume of desalinated water transported in a large sweep gas volume - external condenser needed (increase in investment, energy use and running costs)	- external condenser needed (increase in investment, energy use and running costs) - high probability of pore wetting
Applications	desalination processes concentration of aqueous solutions acid manufacturing	any applications	remove volatile compounds from aqueous solutions	separate aqueous volatile solutions

Table 2.1: Comparison of the different membrane distillation processes

Energy efficiency and permeate flow vary in the opposite way. Because of the project emphasis on energy efficiency, the AGMD design is selected.

2.3.2.2.2 AGMD at industrial level

According to Winter et al. [161], the majority of industrial MD modules today are spiral modules. Exemples of AGMD producers at an industrial scale are AQUASTILL (Netherlands), Fraunhofer Institute, Memstill.

Solar powered membrane distillation systems are listed in Saffarini et al. [122].

The applications of AGMD can be diverse, including water desalination, water recycling, brines pretreatment [67], Oxygen-18 stable isotopes enrichment, and heavy metal removal [18]. As the dependency of the permeate flow to high salt concentration is very small, AGMD can be used to treat highly salinated brines [69]. Additionally, it can be used to separate VOCs, volatile organic compounds.

2.3.2.2.3 AGMD pretreatment

In order to reduce membrane fouling and scaling, drastically reducing the lifetime of the MD device, pre-treatment of the feed water must be applied, to remove big particles as well as microplastics in particular in the case of ocean water used as feed.

2.3.3 Low-tech desalination processes

At the margin of the technologies presented until now, several initiatives aim at providing simple to implement and use desalination devices in order to ensure fresh water access to everyone. Some of these projects are presented in this section. As they rely on a natural energy gradient, and their set up and every day use is the simplest, they are classified as low-tech and passive processes.

2.3.3.1 Eliodomestico

Eliodomestico (fig. 2.3) is an open-source low-tech water desalination project, designed by Gabriele Diamenti (2013). The sun heats the water contained beneath the black lid. Water evaporates and condensates again on the clay plate at the bottom of the device. It is constructed of soil, steel and ceramic, and can provide up to 5l/day of drinking water, depending on the amount of sunlight.

Figure 2.3: Eliodomestico [39]

2.3.3.2 Watercone

The water cone (fig. 2.4) is a very similar solution to Eliodomestico, made of plastic.

Function

1. Pour salty / brackish Water into pan. Then float the Watercone® on top. The black pan absorbs the sunlight and heats up the water to support evaporation..

2. The evaporated Water condensates in the form of droplets on the inner wall of the cone. These droplets trickle down the inner wall into a circular trough at the inner base of the cone.

3. By unscrewing the cap at the tip of the cone and turning the cone upside down, one can empty the potable Water gathered in the trough directly into a drinking device.

Figure 2.4: Watercone [19]

2.3.3.3 Dew Bank

The dew bank (fig. 2.5) is another very similar solution, made of stainless steel.

Figure 2.5: Dew Bank [99]

2.3.3.4 Desert Cloud

The Desert Cloud (fig. 2.6) is a work of art as well as a water generating machine based on evaporation. Created by Graham Stevens, it is a structure that self-inflates as a result of rising hot air, and on which the water vapor contained in air condenses.

Figure 2.6: Desert Cloud by Graham Stevens [59]

2.3.3.5 Aquaba

Aquaba (fig. 2.7) is an NGO which developed a low-tech solar water desalination device. Inspired by air-gap membrane distillation, this device makes the most of solar radiation by capturing them in a black soaked fabric to heat the hot water. The water evaporates and condensates on the glass located just above.

Figure 2.7: Aquaba (https://aquaba.eu/)
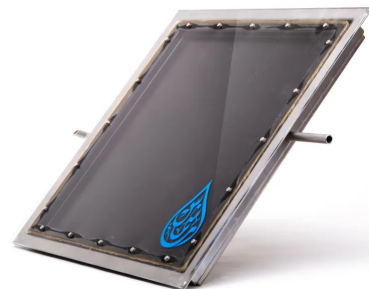
2.4 Evaluation Parameters of the different processes

Several indicators are used to compare these technologies.

2.4.1 Permeate flow

The average permeate flow rate (or fresh water outflow) of an AGMD is approximately $10kg/m^2/h$ for an input temperature of 70° [137]. For RO, it is between 20 and $40kg/m^2/h$ [50]. However the permeate flow highly varies with the membrane characteristics.

In the case of the low tech processes the permeate flow is on the order of magnitude of <5l/day.

2.4.2 Gain Output Ratio (GOR)

The Gain Output Ratio is used to quantify the distillation processes' performance. Without unit, it is generally calculated as the ratio of the amount of thermal energy required to vaporize the mass of water produced to the total thermal energy input to the system $GOR = \frac{m_d * h_{fg}}{Q_{in}}$ with $Q_{in} = m_f * C_p * (T_{fin} - T_{heater,in})$ [122]. A higher GOR is synonym of higher energy efficiency.

For MSF, GOR ranges between 7 and 12, whereas for MED it is between 80% and 90% of the number of effects (due to irreversibilities) [23] (between 10 and 16 according to [50], 12 according to [137]); and between 4 and 6 for MD, or even 1 to 2 according to [85]. According to Swaminathan et al. [139], VMD can achieve a maximum GOR of 1, the GOR value for SGMD is limited to 4, and DCMD and AGMD can achieve higher GOR values, below 8 [10], with an advantage for AGMD [34]. CGMD even outperforms AMGD in terms of GOR [139]. [137] compared the effect of various parameters (length, inlet temperature, top temperature...) on GOR for different MD configurations.

MD GORs' can be improved to become as attractive as MED and MSF.

2.4.3 Energy consumption

As seen previously (see section 1.3), the energy required to perform the transformation from salty water into fresh water is equal for all processes. However, depending on the real technical solution chosen, the amount of exergy required differ. In particular, for pressure-based solutions (RO, MSF, MED), the energy required is electricity composed essentially of exergy, whereas the low grade heat required in Membrane Distillation contains mainly anergy.

The energy consumption of the different desalination processes depends on the operating parameters, and of the GOR for instance.

The electrical energy consumption of Reverse Osmosis on sea water is comprised between 4 and $6kWh_e/m^3$ [50], while it is between 40 to $65kWh_t/m^3$ thermal energy for MED (equivalent to 18 to $30kWh_e/m^3$)[50] and between 1.5 and $2kWh.m^{-3}$ for brines. According to Wangnick et al. [154], the energy consumption of MED ranges from $230 - 390kJ/kg$ of thermal energy, corresponding to an equivalent electrical energy of $5 - 8.5kWh_e/m^3$, for a total energy consumption of $6.5 - 11kWh_e/m^3$ when pumping energy is added ($1.5 - 2.5kWh_e/m^3$). Similarly, MSF energy consumption ranges from $190 - 390kJ/kg$, corresponding to an electrical energy consumption (calculated with the assumption of a 30% efficiency of power plants) of $9.5 - 19.5kWh_e/m^3$, for a total of $13.5 - 25.5kWh_e/m^3$ when the electrical consumption for pumping ($4 - 6kWh_e/m^3$) [154].

Duong et al. [41] calculated an energy consumption for a stable AGMD process of $90kWh_t/m^3$ and $0.15kWh_e/m^3$ (which would convert into about $40kWh_e$ if the same ratio between h_e and h_t than in Guillen-Burrieza et al. [50] is used).

According to Sosa et al. [134], the energy required for electrodialysis varies from 70 to $140Wh/m^3$ depending on the configurations.

Woldemariam et al. [162] mention that the material of the condensation plate is critical for the AGMD process's exergy efficiency: stainless steel or high density polyethylene should be privileged because of their high thermal conductivity. This same study also states that the exergy efficiency of AGMD processes increases as the temperature difference between the hot and cold channels grows. This conclusion highlights the necessity to optimize the heat transfers in the AGMD module in order to increase the energy efficiency of the overall process.

2.4.4 Recovery Ratio (RR)

The Recovery Ratio (RR) is defined as the volumetric processing efficiency of the purification process: it indicates the proportion of intake water that is converted into high quality (low salinity) water for sectoral use. The remaining water (calculated as $(1 - RR)$) is the proportion of intake water that is converted into a waste (brine) stream, which requires management [66].

According to Saffarini et al. [122], the RR of RO can be as high as 40% to 60% for seawater and up to 60–85% for brackish water, while it is only of 15 to 50% for multi-stage flash (MSF) or multiple effect distillation (MED) with seawater. For AGMD, the different systems presented in this article showed a RR of a few percent, between 1 and 6%.

2.4.5 Life-cycle assessment

A life-cycle assessment (LCA) takes into account the environmental footprint of a process encompassing its construction, operation and discard. Several LCA methodologies exist: to be able to compare the LCA of the different technologies between themselves, they should be performed using the same methodology.

Raluy et al. [112] evaluated the LCA of MSF, MED and RO using the Eco-Indicator 99 method. MSF totalizes $1.614 Mpoints/hm^3$, MED, $1.277 Mpoints/hm^3$ and RO $0.084 Mpoints/hm^3$.

Jijakli et al. [63] compare a solar still (MD) and RO under different configuration: material used for the solar still (steel, PVC, scrap), and energy source (photovoltaics, gas, nuclear) and delivery mode (decentralized RO or truck delivery) using the Eco-Indicator 99. The solar still made of scrap present similar results as the RO powered by solar panels, about $1200 points/m^3$, or about $0.1200 Mpoints/hm^3$, which is on the same order of magnitude as the previous study.

2.4.6 Energy efficiency

Another interesting indicator could be the generalization of the GOR indicator by taking into account the overall energy consumption of the process. This indicator would be defined as the total fresh water outflow over the total power consumed for heating and pumping. A similar indicator could take into account the overall fresh water production expected over the overall energy required for the building, use and disposal (LCA approach) of the process.

2.5 Water desalination impacts

Desalination may have a negative impact on five domains: land use, groundwater, the marine environment, noise pollution, and finally increased energy consumption [42].

The brines rejected can increase salinity and temperature locally, threatening certain species (like the Posidonie herbs, where fishes reproduce)[61].

Reverse-Osmosis pre-treatment is also a source of pollutants in the environment [61].

Brines pose a serious threat to the environment. The majority of existing desalination projects discharge the brines into the ocean, where they cause salt stratification and decreased circulation, which can even result in anoxia. Additionally, the salt creates turbid water, which reduces the amount of incoming light [66].

Another effect of the rejected brine is its heat, which can affect the water's temperature and disrupt the biodiversity balance [42].

The thesis will not reflect on this issue.

2.6 Conclusion on the existing desalination processes

As fresh water needs will increase in the future, and energy resources will require reasonable use, the need for a low-cost, environmentally friendly and low exergy consuming technology for water desalination becomes apparent.

Desalination technology can be thought of as a black box, into which salty water enters and fresh water exits, via a specific process that requires a specific form of energy, and generates some wastes. The objective is to maximize the fresh water flow while minimizing the energy consumption and the environmental impact.

The existing natural and man-made processes discussed in this part (fig. 2.2) can be compared according to the definitions specified in section 2.1. In particular, it is noticeable that low-tech processes provide a much lower fresh water output than the industrial technologies. Emerging processes, as hybrids between the two, appear as an interesting compromise, providing a better resilience and accessibility than industrial technologies, whereas their fresh water production is higher than the low-tech ones.

AGMD is selected as an almost passive process as it relies on an existing energy flow (solar radiation or wasted heat) for most of its required energy (except for pumping energy which only represents an infinitesimal fraction of the overall required energy). This process can almost be considered low-tech, apart from the hydrophobic membranes production. Compared to Nanoseen, the membranes are less prone to fouling in AGMD and thus need less frequent replacement, making this process more durable. Its permeate flow is the highest of the low-tech processes. However, if its exergy consumption is low, its energy efficiency can be improved and its permeate flow can be increased, to make it more competitive compared to existing industrial desalination technologies.

	Process	Mechanism	Energy Form	Energy source	Converter	Exergy[2]	Permeate flow	RR	GOR	Energy consumption	Passive	LCA - EI99 ($Mpoints/hm^3$)
natural	Water Cycle	Phase change	heat	sun	environment	low ($\approx 20\%$)	(very variable)	-	-	(not known)	x	(not known)
	Freezing	Phase change	cold	space	environment	low	(very variable)	-	-	(not known)	x	(not known)
	Kidneys	Filtration	chemical	food	body	low	$\approx 2l/day$	-	-	(not known)		(not known)
	Chloride Cells in gills	Filtration	chemical	food	body	low	(very variable)	-	-	(not known)		(not known)
	Mangroves	Filtration	chemical & heat	food & sun	plant	low	(very variable)	-	-	(not known)	x	(not known)
	Aquaporin	Filtration	chemical	food	body	low	(very variable)	-	-	(not known)		(not known)
industrial	Reverse Osmosis	Filtration	high pressure	fossil fuels	high-tech device	high ($\approx 60\%$)	$40\ kg/m^2/h$	40-60%	-	$4\text{-}6kWh_e/m^3$		0.084
	Multi Stage Flash	Phase change	heat and low pressure	fossil fuels	high-tech device	average	(very variable)	15-50%	7-12	$13.5\text{-}25.5\ kWh_e/m^3$		1.614
	Multi Effect Distillation	Phase change	heat and low pressure	fossil fuels	high-tech device	average	(very variable)	15-50%	10-16	$6.5\text{-}11\ kWh_e/m^3$		1.277
	Pervaporation	Phase change	heat	fossil fuels	high-tech device	low	(very variable)	-	-	-		(not known)
	Electrodialysis	Filtration	electricity	fossil fuels	High-tech device	high ($\approx 60\%$)	(very variable)	-	-	$70 - 140Wh/m^3$		(not known)
em	Nanoseen	Filtration	gravity	gravity	almost low-tech	average	up to 1000l/d	-	-		x	(not known)
	Membrane Distillation	**Phase change**	**low grade heat**	**sun and wasted heat**	**almost low-tech**	**low**	**$10\ kg/m^2/h$**	**1-6%**	**<8**	**$40kWh_e/m^3$**	**x**	**0.1200**
low-tech	Eliodomestico	Phase change	heat	sun	low-tech device	low	$5l/day$	-	-	0	x	(not known)
	Water Cone	Phase change	heat	sun	low-tech device	low	1.7 l/day	-	-	0	x	(not known)
	Desert Cloud	Phase change	heat	sun	low-tech device	low	(not known)	-	-	0	x	(not known)
	Aquaba	Phase change	heat	sun	low-tech device	low	(not known)	-	-	0	x	(not known)
	Dew Bank	Phase change	heat	sun	low-tech device	low	(not known)	-	-	0	x	(not known)

Table 2.2: Comparison of desalination processes (em.=emerging)

[2]This value is provided as an indication only. Low amounts of exergy are consumed by processes requiring heat. The exergy of processes requiring electricity or pressure is high. If this electricity is generated from heat (fossil fuel thermal power plant), the exergy is approximately 60% (Carnot efficiency), whereas it is almost 100% if it is generated by renewable energy. For processes requiring chemical energy, if the converter is the body, the exergy should be low due to the body's other use of food for metabolism.

Chapter 3

Air-Gap Membrane Distillation literature review

While the majority of publications on membrane distillation deal with DCMD [122], AGMD has been investigated experimentally and theoretically in the literature.

3.1 Module designs and geometries

Although the flat sheet membrane is the most common AGMD module geometry, membrane distillation can also be performed via hollow fibers, tubular membranes or spiral wound membranes [9][53] [121].

The configurations are distinguished from each other by the compactness of the modules (packing density), the easiness to clean and replace the different elements (cleaning and replace), the operating costs and energy consumption of the whole process, and the temperature polarization generated inside the module (directly impacting its energy efficiency).

In particular, Alkhudhiri et al. [9] shows that the spiral membrane modules appear as a good compromise presenting the highest compactness with a reasonable easiness to maintain and acceptable energy consumption.

Two distinct spiral wound membrane geometries were identified: one developed by the Fraunhofer Institute (fig. 3.1a), purely spirally, with spacers in each layer (hot/airgap/cold channels); and one developed by Aquastill (fig. 3.1b), for which a patent was deposited [95], slightly more complex than a spiral as the membranes foils are firstly folded in zig-zag like pattern prior to be rolled in spiral.

(a) a)

(b) b) (source [95])
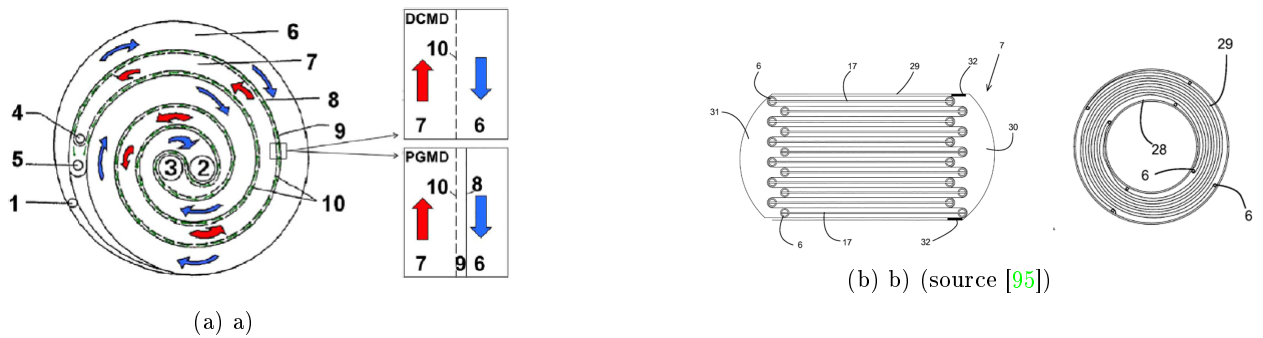
Figure 3.1: Spiral AGMD modules from a) Fraunhofer and b) Aquastill

A helical prototype has also been designed (fig. 3.2, [129]): an internal cylinder with fins and filled with cold water serves as the condenser plate, with the fins also acting as support for the membrane rolled around the cylinder. The membrane's external side is fed with hot water.
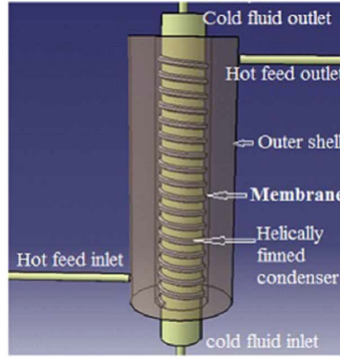
Figure 3.2: Helical Air-Gap membrane Distillation module [129]

These more compact and hence more industrially attractive AGMD geometries require three-dimensional numerical models to be simulated, in order to highlight possible three-dimensional phenomena.

3.2 Air-Gap Membrane Distillation enhancements

As seen in the table 2.2, AGMD can be improved in terms of fresh water outflow, and energy efficiency. Several strategies for that matter are presented in literature.

Indeed, in an AGMD module, the temperature difference between the hot and cold water channels decreases due to the apparition of a temperature gradient in the hot water channel and air-gap, along the flow away from the input and with time until reaching a steady state. The driving force of evaporation is thus reduced, and the fresh water outflow decreased. Both energy efficiency and fresh water outflow are closely intertwined.

3.2.1 Fresh water outflow enhancement

Warsinger et al. [157] proposes a superhydrophobic coating for the cold plate of the air-gap. By forcing the water out of the air-gap faster, the hydrophobic coating avoids the filling of the air-gap thus maintaining the heat transfer resistance high. Moreover, it enhances the condensation and hence the permeate flow.

3.2.2 Energy efficiency enhancement

Many strategies exist to reduce the temperature variations occurring during operations in the hot channel in MD. Some techniques, like spacers or corrugated membrane surfaces, are passive, while others, such as surface vibration, flow vibration, or ultrasonic field, are active [83]. Some are concerned with membrane fabrication (nanostructured membranes, nanoheated membranes, metallic membranes) or with their heating (solar, joule, or induction), while others are concerned with flow promoters (feed spacers, corrugated feed channels, and flashed feed channels) [13].

Lawal [79] proposes a multi(2)-stage AGMD process (Multi Effect Membrane Distillation, MEMD) to recollect heat from one stage to the other and reduce the energy losses.

Some research groups imposed a small air-gap (<1mm) and allowed it to fill with permeate (Permeate Gap Membrane Distillation, PGMD) [122]), or filled the air-gap with different medium (sand, water, liquid etc...) (Material Gap Membrane Distillation, MGMD) [4]. As a conclusion, the water-gap membrane distillation provides a better efficiency, notably reducing specific thermal energy consumption (55.63%) and substantially increasing the fresh water outflow (76.26%).

A DCMD-VMD coupling is also considered, driving the distillate stream flow by a negative pressure created by placing a front pressure valve before the entrance to the membrane and changing the position of the distillate pump (vacuum enhanced direct contact membrane distillation: VEDCMD, [122]).

Wang et al. [152] directed heat to the membrane interface via conducting shims and membrane supports, thereby avoiding heat losses due to the temperature variations and along the membrane surface.

In Ho et al. [58], a helical wire is added to the smooth surface of a cylindrical AGMD module, acting like a spacer, in order to generate turbulences and hence reduce the temperature variations.

Of all these techniques, passive techniques are preferred from an overall energy consumption aspect, and particularly spacers, for their ease of use and interchangeability. Moreover, spacers holds more than the energy efficiency improvement role and are most of the time indispensable in a MD module. Indeed, they have three functions: supporting the membrane; increasing mixing thus enhancing heat and mass exchanges[52]; and reducing fouling [72].

However, as kinetic energy losses and drag grow, pressure drops across the channel occur, needing additional pumping energy [35]. This requires balancing the benefits of improved mixing with the risks of wetting the membrane and pumping energy raise [52].

3.3 AGMD modeling

In order to forecast the fresh water outflow of an AGMD configuration, optimize the different operating parameters, or the overall geometry of the module or spacers, numerous novel approaches to AGMD modeling are described in literature.

Artificial neural networks have been used to forecast permeate flux [5]. Despite the fact that this approach is specific to a given experimentation and cannot be generalized to other boundary conditions, it allows to overcomes all of usual simulation's shortcomings, such as the need of fitting parameters or specific assumptions.

Genetic programs (evolving programs of artificial intelligence) have also been tested on AGMD processes [15], demonstrating that feed temperature, feed concentration, and feed and coolant flow rate all interact. Indeed, the optimal solution is not higher feed temperature lower feed concentration higher feed and coolant rates, as one might expect.

A 3D AGMD CFD model was also developed by Rabie et al. [111] using FLUENT. By coupling the mass transfer through the membrane with the one through the air-gap, and the condensation flux altogether, this approach prevents convection to occur in the air-gap.

Hitsov et al. [57] propose a full scale CFD model experimentally validated for an AGMD process that is parameter-free and simulates the flooding of the air-gap to palliate the deficiency of the current models regarding the permeate thickness modeling. However, only mass diffusion is modeled in the air-gap again.

This literature review highlights the interest for a 3D conceptual heat and mass transfer model of an AGMD module, allowing convection to occur in the air-gap, applicable to a wide range of configurations and validated against experimental datas.

3.4 Experimentation

Several articles ([22], [68],[84], [76], [89], [24], [100]) propose AGMD experiments, conducted to assess the impact of different parameters on the fresh water outflow and energy efficiency of the process. The following table 3.3 summarizes the main conclusions:

AGMD	Molar Flux (N)	Limit heat losses	Limit wetting	Conclusion	Values in publications
Membrane Porosity (ε)	↗	↗		The more porous membrane	60-86%
Membrane Thickness (δ)	↘	↗		Membrane thickness bounded	60-200μm
Pore size (d_p)	↗		↘	Ideal d_p depend on Pressure Gradient	0.1-1μm
Pore Tortuosity (ξ)	↘			The more cylindrical pores	
Air-Gap Thickness (l)	↘			The thinner air-gap	1.2-7mm
Feed Flow (Q_h)	insig. effect				
Coolant Flow (Q_c)	insig. effect				
Feed Temperature (T_h)	↗				20-80°C
Coolant Temperature (T_c)	insig. effect				15-30°C
Pressure (P)	↗ (↗permeability)	↘ (↗thermal conductivity)			
Salt concentration	↘			Impact of high [NaCl] lower than in RO	

Figure 3.3: Influences of different parameters on AGMD efficiency [22], [68],[84], [76], [89], [24], [100]

The rising arrows indicate a positive correlation (increase in the AGMD boundary parameter increases the phenomenon listed in the column head) whereas a decreasing arrow indicates a negative correlation.

In particular, the parameters improving the fresh water outflow can be structural, linked to membrane properties (increased porosity and pore size, and decreased thickness and pore tortuosity) or air-gap thickness (smallest); or operational, mainly linked to the feed temperature. Indeed, increasing the hot channel water increases the production of water vapor. However, lowering the cold channel's water temperature increases the relative air concentration adjacent to the cooling plate, thus diminishing the exchange coefficient, which counterbalances the increase in driving force caused by this temperature decrease.

Choosing a membrane with the highest membrane porosity and the biggest thickness improves the energy efficiency, while to optimize the molar flux, the membrane thickness should be minimal.

Most of publications experimentally studying AGMD only monitor the feed and coolant inlet and outlet temperatures and pressures ([84], [76], [21], [165]).

Several research groups investigated the measurement of the temperature inside the module, either by evenly spacing thermocouples on the outer surface and membrane surface of both the hot and cold channels [62], or by using thermochromic liquids to determine the temperature distribution at the membrane surface [140].

The permeate regime was also investigated thanks to a visualization experiment [158].

No continuous temperature and concentration profiles investigation were conducted, neither across the hot channel nor across the air-gap. However, such profiles could provide useful information regarding the heat losses occurring at the membrane interface and hence the polarization, affecting the AGMD performances.

3.5 Conclusion on air-gap membrane distillation literature review

Following a review of existing literature on AGMD, several areas of improvement are identified.

On the modeling part, none of the existing models validated experimentally allow convection to occur in the air-gap: this heat and mass transfer phenomenon could improve the performance of the device.

No internal continuous measurement of the hot fluid thermal and concentration variations nor of the air-gap phenomena perpendicular to the membrane in an AGMD module has been conducted yet. Deepening the understanding of the influence of the different parameters on the AGMD driving force and thus on the fresh water outflow and energy efficiency could help for scaling up the process, which is lacking at the moment.

Regarding energy efficiency, spacers appear to be a viable technique whose performance could be enhanced through research.

Conclusion of part I: research questions

Based on this background information, air-gap membrane distillation appears to be a viable solution to the water crisis, as it provides a good balance between technology complexity, freshwater output, and sustainability.

To increase the appeal of this process, its performances (fresh water output and energy efficiency) can be enhanced. According to the current state-of-the-art air-gap membrane distillation research, one major challenge is identified as the obstacles to energy transfers in the AGMD device, which hinders its energy efficiency. Following this, three major research motivations are identified, regarding energy efficiency.

The two first questions tackle the heat transfer efficiency quantification inside the module:

- *what does the temperature gradient inside the AGMD' hot channel look like?*
- *how accurate are the existing models to describe this temperature gradient?*

The answer to the first question aims at providing an experimental input for the second question in order to compare models to experiments.

The third question focuses on the heat transfer optimization via the geometry:

- *how can spacer geometries influence AGMD performances?*

Part II

Theory and methodology

Highlights from Part II

💡 The physical phenomena at stake in AGMD are extensively explained and the three-dimensional heat and mass transfer model to be validated is described.

⇒ The major resistance to heat and mass transfers is the building of boundary layers in the hot water channel.

💡 An experimental set-up enabling the measurement of the permeate flow and the observation of these heat transfers is designed. Different experimental methods to measure temperature and concentration profiles are explored.

⇒ Schlieren Method is selected as the simulateneous temperature and concentration continuous profile observation method.

💡 Several mixing strategies are analyzed.

⇒ Two novel spacer geometries are proposed, along with two new indicators to assess their performance.

Chapter 4

AGMD operation principle

An AGMD module is composed of a hot feed water channel where hot salty (or contaminated) water enters. This channel is separated from the air-gap by a hydrophobic membrane, that the fresh water vapor crosses, before condensing on a cold plate in the other side of the air-gap. This plate is cooled down by the cold water channel.

Several phenomena are involved in an AGMD system: heat transfers, mass transfers, and evaporation and condensation (fig. 4.1).

The hot and cold water fluxes create a temperature (and partial vapor pressure) difference between the two sides of the membrane, which drives the heat and mass diffusion across it. There is:

- diffusion and advection of heat and mass in the hot water channel, and evaporation at its surface;
- heat conduction and heat and mass diffusion through the membrane
- heat and mass diffusion and advection, if a sufficient macroscopic air mass flux in the air-gap is generated artificially or geometrically (via a Venturi effect for instance), through the air-gap.
- condensation on the cold plate.
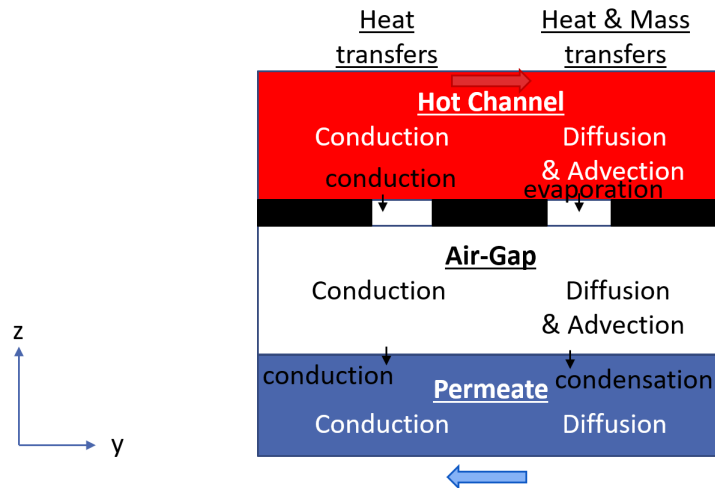
Figure 4.1: Heat and mass transfers in an AGMD module

The air-gap increases the overall system's energy efficiency by increasing the insulation between the hot and cold channels, thus decreasing the temperature variation inside the hot water channel along the flow direction. However, it also slows down mass transfer by providing an additional resistance (fig. 4.5). Understanding the relative importance of these two influences is required to determine which configuration of air-gap has a beneficial effect on the overall AGMD process' efficiency.

In the rest of the thesis, the following conventions will be used (Figure 4.2):
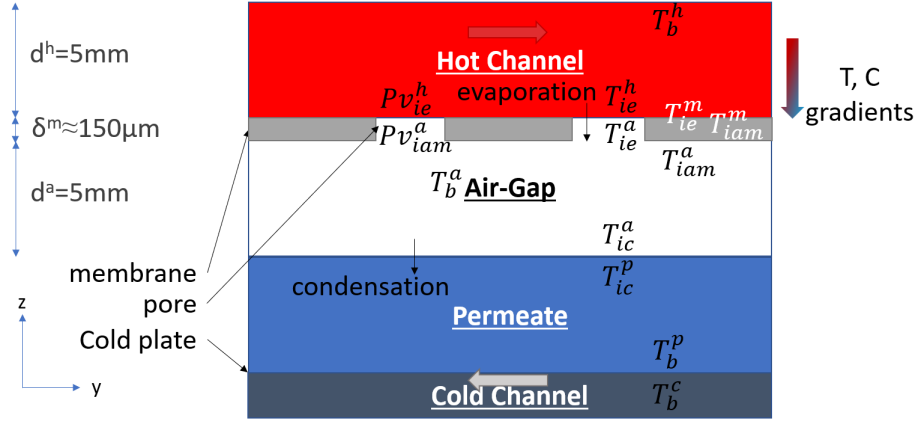
Figure 4.2: Conventions for temperature and pressure variables in the AGMD module

T and Pv stand for the temperature and the vapor pressure. The superscripts define the phase to which belongs the variable (h for the hot water feed, m for the membrane, a for the air-gap, p for the permeate, c for the cold channel); while the subscripts indicate the localization at which the variable is taken (b in the bulk flow, ie at the evaporation interface, ic at the condensation interface, iam at the interface between the air-gap and the membrane).

4.1 Physical phenomena in AGMD

Evaporation at the membrane interface leads to heat and mass transfers across the AGMD device, that manifest themselves through different mechanisms depending on the module's layer.

4.1.1 Heat transfers

Heat transfers in a MD module occur through different mechanisms :
- **convection** heat transfer in the hot water feed boundary layer: $Q^h = h^h(T_b^h - T_{ie}^h)$ with h^h the hot feed water heat transfer coefficient
- **latent** (lat) heat transfer at the evaporation interface between the membrane surface and the hot water channel (energy required for the transition between the liquid and the vapor states): $Q_{ie,lat}^m = N \Delta H_v$
- **conduction** (ccond) heat transfer in the membrane material: $Q_{m,cond}^m = \frac{h^m}{\delta^m}(T_{ie}^h - T_{iam}^a)$ and in the air-gap $Q_c^a = \frac{h^a}{\delta^m}(T_{iam}^a - T_{ic}^a)$, with h^m the effective thermal conductivity of the membrane calculated from the proportions of gas and solid membrane $h^m = \epsilon h^{m,g} + (1-\epsilon)h^{m,s}$, h_{mg} the gas thermal conductivity and $h^{m,s}$ the membrane's polymer thermal conductivity
- **convection** heat transfer in the air-gap: $Q^a = h^a(T_{ic}^a - T_{ie}^a)$ with h^a the air heat transfer coefficient
- **convection** heat transfer in the permeate boundary layer: $Q^p = h^p(T_b^p - T_{ic}^p)$ with h^p the permeate thermal conductivity

Due to the fact that conduction heat transfer is not linked to a mass transport of water vapor particles, it is regarded as an energy loss as it does not contribute to the fresh water outflow. Thus, conduction heat transfer must be minimized in order to optimize the process. Given the preceding expression for h^m above, and the fact that $h^{m,g}$ is typically smaller than $h^{m,s}$, minimizing conduction heat transfer is equivalent to maximizing membrane porosity ϵ.

This thesis work aims at observing and optimizing the heat convection phenomenon occurring in the hot water channel and the air-gap, to characterize T_b^h, T_{ie}^h, T_{ic}^a and T_{ie}^a.

4.1.2 Mass transfers

Mass is conveyed across the module via different mechanisms.

4.1.2.1 Mass transfers through the membrane

Mass transfer in the membrane can occur through different mechanisms depending on the scale and temperature range the process is operated at [126]:

- **Knudsen diffusion**: describes a flux (N_k) where the collisions between the molecules and the inside walls of the membrane are dominant over the collisions between the molecules

$$N_k = \frac{D_k \epsilon}{\xi} \frac{(c_{iam}^a - c_{ie}^h)}{\delta^m} \tag{4.1}$$

with $\frac{D_k \epsilon}{\xi}$ Knudsen diffusion coefficient ($D_k = \frac{d^{po}}{3}(\frac{8RT}{\pi M})^{0.5}$) corrected for membrane porosity ϵ and pore tortuosity ξ , and $\frac{(c_1 - c_0)}{\delta^m}$ the concentration driving force, with $c_i = \frac{P_i M}{RT}$ and δ^m the membrane thickness (thus $N_k \propto \frac{d^{po} \epsilon}{\xi \delta^m}$)

- **Molecular diffusion**: describes a mass flux (N_d) where molecules move corresponding to each other under the influence of a concentration gradient. The collision between the molecules represent then the dominating diffusion resistance.

$$N_d = \frac{1}{Y_{ln}} \frac{D \epsilon}{\xi \delta^m} \frac{M}{RT} (Pv_{iam}^a - Pv_{ie}^h) \tag{4.2}$$

with D the diffusion coefficient and Y_{ln} the log mean partial pressure of air present within the pores (thus this model is not adequate at low partial pressures of air).

- **Poiseuille advection**: describes a viscous flow (N_P) through a capillary, where the gas molecules act as a continuous fluid, driven by a total pressure gradient

$$N_P = \frac{q^{po} n^{po} M P^m}{RT} \tag{4.3}$$

with P^m the mean pressure in the membrane, q^{po} the single pore flow given by $\frac{\pi r^4 \Delta P}{8 \eta \delta^m \xi}$, and n^{po} the pore density given by $\frac{\epsilon}{\pi \left(\frac{d^{po}}{2}\right)^2}$ (thus $N_p \propto \frac{d^{po 2} \epsilon}{\xi \delta^m}$)

This flow is mainly noticeable in VMD or de-aerated DCMD, because then there is no more stationary film of air through which the vapor has to diffuse. It is neglected in AGMD as the total pressure difference across the membrane is negligible.

Knudsen diffusion occurs when the scale length of a system is comparable to or smaller than the mean free path of the particles involved. The Knudsen number defined as K_n, the ratio of the mean free path of transported molecules (l) to the membrane pore size (d^{po}) [9], delimits the preponderance domains of Knudsen diffusion and molecular diffusion (fig. 4.3):

- if $K_n > 1$ or $d^{po} < l$: Knudsen region: molecule-pore wall collisions are dominant over inter-molecule collisions
- if $K_n < 0.01$ or $d^{po} > 1000l$: Continuum region: ordinary molecular diffusion model represents the diffusion of the vapor flux through stationary air film
- if $0.01 < K_n < 1$ or $l < d^{po} < 1000l$: Transition region: the water vapor molecules collide with each other and also diffuse through the air film
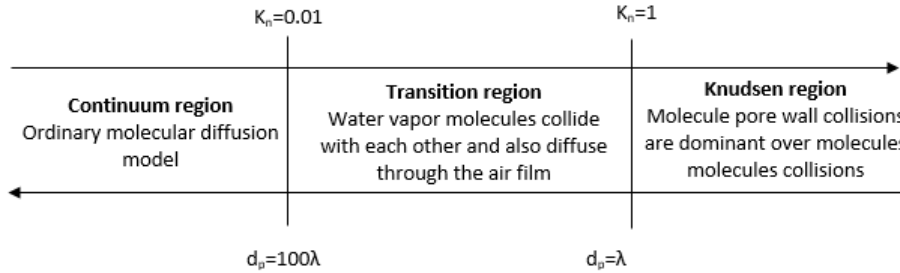
Figure 4.3: Representation of the different diffusion regions

The mean free path of molecules can be written $l = \frac{k_B T}{\sqrt{2}\pi P d_e^2}$, with k_B the Boltzmann constant, T the absolute temperature in the membrane, P the average pressure in the membrane, and d_e the collision diameter of the molecules. For instance, collision diameter for water vapor and air are about $2.64.10^{-10}m$ and $3.66.10^{-10}m$ respectively [9].

Whatever the diffusion mass transfer mechanism, the relationship describing the flux is proportional to the partial pressure gradient: $N = C(Pv_{iam}^a - Pv_{ie}^h)$ where C is dependent on temperature and on the average mole fraction of air present in the pores. In the case of advection, the flux is proportional to the total pressure gradient, and C depends on the mean membrane pore geometry.

In most of the papers dealing with AGMD theory and modeling ([80], [9], [68], [37], [84]), the liquid-vapor equilibrium at the temperature and pressure within the pores is assumed, ie $T_{ie}^h = T_{ie}^a$. Hence the partial pressure difference ΔP in these formulas, which is difficult to measure, is transformed into a temperature difference ΔT, easier to measure, thanks to:

- the approximation that the dilute solutions have values of $\Delta T < 10°C$, which allows to write [126]:
$\frac{Pv_{iam}^a - Pv_{ie}^h}{T_{iam}^a - T_{ie}^h} = \frac{dP}{dT} \mid_{T_m}$ hence $N = C\frac{dP}{dT} \mid_{T_m} (T_{iam}^a - T_{ie}^h)$
- the Clausius-Clapeyron equation, used to simplify the vapor-pressure temperature relationship [80]:
$\frac{dP}{dT} \mid_{T_m} = \frac{P\Delta H_v}{RT^2} \mid_{T_m}$, with ΔH_v the molar latent heat of vaporization and P the saturation pressure
- Antoine equation [68], which estimates the saturation pressure of a substance at a given temperature T, taking into consideration that for pure liquids or low concentrated liquids, partial vapor pressure is equivalent to the component's saturation pressure $P = e^{A - \frac{B}{C+T}}$, with A, B and C Antoine's coefficients. This is only valid for low concentration solutions, for which it is assumed that the vapor pressure is a function of temperature only (and not pressure).

4.1.2.2 Mass transfers across the air-gap

Mass transfer across the air-gap is modeled by Navier Stokes equations.

Rayleigh number, comparing Archimede' buoyancy to dissipation, can be used to determine whether the transport of the gas across the air-gap can occur solely by diffusion or if convection has to be taken into account: $Ra = \frac{\rho g \beta \Delta T e^3}{\kappa \eta}$, with ρ the volume mass, β the thermal expansion coefficient, e the layer thickness, κ the thermal diffusivity and η the dynamic viscosity.

For Ra<1708 [120] (or 103 according to Khayet et al. [69]), convection is negligible due to the fact that buoyancy forces are less than viscosity and thus no macroscopic flux may appear, and conduction only can be considered. The geometric ratio between the vertical and horizontal dimensions of the enclosure influences the relative predominance of both phenomenon. Indeed, as the ratio approaches one, the convective heat transfer effect becomes maximal; while as the ratio tends toward 0 or $+\infty$, this convective transfer vanishes [22].

According to Khayet et al. [69], the typical Rayleigh number in an air-gap process is 85, making reasonable the assumption that almost no convection caused by the temperature difference between the hot fluid and the condensation plate, only diffusion, occurs in the air-gap. This is even more true when the hot water channel is on the top of the AGMD module and no natural convection can occur (see section 4.2.4.

The comparison between the air-gap and the membrane fluxes can be expressed as follows:

$$\frac{N^m}{N^a} = \frac{\frac{-\epsilon}{\xi \delta^m} \frac{1}{\frac{1}{D_k} + \frac{1}{D_{v,air}}}}{\frac{D_{v,air}}{\delta^a}} = \frac{-\epsilon}{\xi} \frac{\delta^a}{\delta^m} \frac{D_k}{D_{v,air} + D_k} \tag{4.4}$$

Since the air-gap is 10 to 100 times thicker than the membrane, $\frac{\delta^a}{\delta^m} \approx 10$. Moreover, as $D_k = 3.914.10^{-5}m^2.s^{-1}$ and $D_{v,air,20°C,1bar} = 2.42.10^{-5}m^2.s^{-1}$, $\frac{D_k}{D_{air}+D_k} \approx 2$. Typical values for membrane porosity and tortuosity are 0.8 and 1.5 respectively. As a conclusion, the effect of the air in the membrane can be neglected [9], leaving the air-gap as the main mass transfer resistance ($N^m \approx \frac{\delta^a}{\delta^m}N^a$). As a result, a thinner air-gap should be preferred.

4.1.3 Evaporation

Evaporation is a thermal phenomenon causing and caused by heat and mass fluxes: some molecules change phase and become vapor molecules.

4.1.3.1 Heat fluxes for evaporation

Since water molecules are transported between phases, in non-equilibrium conditions, a convective heat flux is carried across the interface.

Evaporation is also the result of heat fluxes towards the interface water molecules. Indeed, evaporation is the process by which surface water molecules break free from the hydrogen bonds that connect them to other water molecules of the surface. To overcome this bonds energy barrier known as latent heat of vaporization, the surface water molecules receive energy by collisions from molecules in the gaseous state, or by an external heat flux agitating their neighboring water molecules and transferred to them by conduction. The more energy the water molecules receive the hotter and more vibrating they become, until they can break their bonds and become vapor molecules.

During this process, the liquid phase of the interface loses highly energetic molecules while the vapor phase gains them. This phenomenon, called evaporative cooling [2], may account for the temperature discontinuity observed at the evaporation interface in various studies [104]. This observed discontinuity, which is not modeled in current MD numerical models, calls into question the way evaporation is modeled as well as the liquid-vapor equilibrium assumption in these algorithms. This is discussed in section A.1.

4.1.3.2 Mass fluxes for evaporation

Evaporation results in a convective mass flux across the interface in non-equilibrium situations.

Evaporation can also be at the origin of convective mass fluxes (evaporative convection) within the water body when the evaporation occurs at the top surface. Indeed, as a result of evaporative cooling (see section 4.1.3.1), the water surface cools down and becomes heavier than the hotter water below: instabilities develop and buoyancy-driven convection cells (Bénard convection cells) can be observed. This evaporative cooling also accounts for local variations in surface tension, which decreases with temperature, resulting in thermocapillary convection, or Marangoni effect.

The importance of these phenomena and cells patterns are dependent on the temperature difference between air and water, the depth of the water channel, the presence of contamination at the water surface, the fluid's viscosity, and the fluid's surface tension [26].

In an AGMD configuration where the evaporation happens at the top of the hot water channel (see section 4.2.4), these phenomena can occur and generate natural mixing, reducing the boundary layer thickness.

4.1.3.3 Saturation pressure

Evaporation continues until there are as many water molecules escaping the liquid water as vapor molecules integrating it. Indeed, at equilibrium (when the vapor and liquid phases are at the same temperature), the number of vapor molecules is such that, in mean, the energy exchanged by collisions from the vapor molecules on the water molecules equals the energy exchanged by collisions from the water molecules on the vapor molecules. This is possible even if the vapor molecules are less dense than the water molecules, as the vapor molecules are more agitated due to their lack of covalent bond. The pressure corresponding to this equilibrium situation is referred to as the vapor saturation pressure, and it is dependent on on the liquid temperature.

If the system is not at equilibrium, the vapor saturation pressure is still the pressure balancing the evaporative flux and dependent only on the liquid temperature.

Hence, evaporation is driven by the difference between the actual partial vapor pressure of water vapor just above the water surface, dependent on the number of water vapor molecules and their temperature, and the saturated partial vapor pressure, dependent on the liquid temperature.

The previously stated assumption of liquid-vapor equilibrium appears to violate this concept: indeed, when liquid and vapor are in equilibrium, the partial pressure equals the saturation vapor pressure, and evaporation loses its driving power. This adds to the interest of questioning this assumption (see section A.1).

4.1.3.4 Resistance to evaporation

Two phenomenon limiting evaporation must be overcome in order to optimize the evaporation rate and increase the permeate flux of the membrane distillation module:

- **the H bonds connecting the water molecules**: the water molecules must gain at least as much energy to overcome this barrier and break free from their neighboring water molecules. This barrier has a fixed value, however it is possible to assist water molecules from the surface in overcoming this barrier faster, by providing a sufficient heat transfer at the surface, and compensating for evaporative cooling: either by heating directly at the evaporation interface, or by accelerating the energy supply to the interface via mass convection, if the evaporation surface is on top of the hot water channel for instance (section 4.2.4).

- **the saturation pressure**: once reached the saturation pressure, no additional water molecules can evaporate (some can but are instantly replaced by condensating molecules). Reaching this saturation can be avoided by removing the evaporated particles as quickly as possible, for instance by adding a convective flux in the air-gap if the diffusion is not fast enough. However, this implies that the water vapor would remain in the vapor-state in the air flux, requiring a separate set-up to condensate it later (by cooling it for instance), requiring additional energy. Another technique to avoid saturation in the air-gap is to increase the condensation flow at the opposite interface, for example, by directing the vapor onto a fast-condensing surface via a convective flux induced by the Venturi effect or a specialized geometric arrangement (eg. slope).

4.1.4 Temperature and concentration polarization

Evaporation at the membrane surface results in the formation of a boundary layer at the membrane, where concentration and temperature fluctuate along a profile. These boundary layers indicate the thermal and concentration barrier to energy transport toward the membrane, whereas the evaporation enthalpy represents the resistance to energy transport at the interface, both of which have an effect on mass flux.

The temperature polarization coefficient is defined as $\tau = \frac{T_{ie}^h - T_{iam}^a}{T_b^h - T_b^c}$ [89], where T_{ie}^h and T_{iam}^a are the temperatures on both sides of the membrane, and T_b^h and T_b^c the temperature in the hot water and cold water channel bulk phases (fig. 4.4). When the temperature polarization coefficient of an MD design is close to 1, the heat transfer resistance is minimized. The temperature gradient across the membrane equates the temperature differential between the hot and cold channels, implying that no heat is lost [9] and that the design is energy efficient.
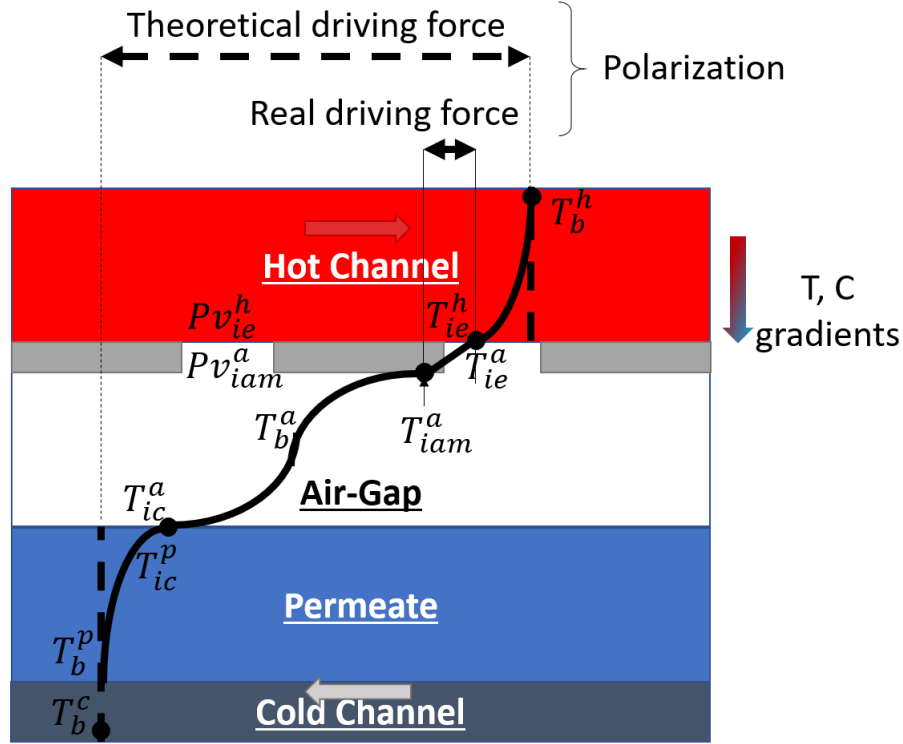
Figure 4.4: Representation of the polarization inside an AGMD device

Temperature polarization occurs due to heat exchanges in the module. In particular, when evaporating, a liquid water molecule extracts energy from the liquid (ΔH_v). Thus at the membrane interface, when evaporation occurs the temperature of the feed flow decreases ($T_{ie}^h < T_b^h$). On the other side of the membrane, when the vapor condensates on the cold plate, energy is released and the temperature rises ($T_{ic}^p < T_b^p$).

The risk of thermal polarization is that the temperatures on both sides of the membrane become equal and the vapor flux stops.

Concentration polarization can influence fluid dynamics through various parameters among which heat capacity, thermal conductivity, viscosity, boiling temperature, flow velocity, geometry and vapor pressure.

As the evaporation process takes place, the salt concentration increases, thus the water fraction decreases and the partial pressure decreases. Moreover, an increase of salt in the solution may result in a decrease in the flux through the membrane due to a decrease in the driving force [8].

Solutions to mitigate the impact of polarizations are suggested in 3.2.

4.1.5 Surface tension and capillarity

Capillary length of a fluid delimits the scale below which the capillary forces (or surface tension) overcome gravity forces. Water has a capillary length of about 2.7mm, similar to the air-gap thickness and output dimensions. Thus, when the AGMD module is used horizontally, the water can stay stuck in the air-gap until it is full and the pressure overcomes the capillary forces. But then the air-gap is flooded. To get around this issue, Alsaadi et al. [12] use the module with channels oriented vertically: this way, gravitation counteracts the film building.

4.2 Role of the different part of an AGMD module

As seen previously, an AGMD device is composed of a hot and a cold channel separated by a membrane. Each of these elements plays a specific role in the performance of AGMD.

4.2.1 Membrane

The membrane selection is important as pore diameter (d^{po}) and pore density (porosity, n^{po}) determine the vapor flux and the dominant mass transfer model. In particular, according to section 3.4, the best membrane for AGMD should have the highest porosity n^{po} and pore size d^{po}, with the lowest thickness δ^m and pore tortuosity ξ. Moreover, as pore diameter also determines the propensity of the membrane to get wet (see section 4.2.1.3), its values are bounded. In particular, the average pore size allowed for MD is substantially bigger than the one for RO (respectively 100nm to 1microm and 0.1nm to $\sim$3nm) [78], as the pressure at which the process is operated is much lower. The wetting also depends on the hydrophobicity (liquid/solid angle with a salty solution) of the membrane. The thermal conductivity of the membrane and its chemical stability are also interesting parameters to take into account.

4.2.1.1 Molar flux

As seen in section 4.1.2, the molar flux through a pore can be written: $N \propto \frac{\langle (\frac{d^{po}}{2})^n \rangle \epsilon}{\xi \delta^m}$, where, depending on the predominant mass transfer mechanism in the process, $n = 1$ for Knudsen diffusion or $n = 2$ for viscous flux; ϵ is the membrane porosity; ξ is the membrane tortuosity and δ^m is the membrane thickness.

Thus, the molar flux is maximum for high values of d^{po} and ϵ, and the smallest transport path length through the membrane ($\xi \delta^m$)[80].

4.2.1.2 Heat losses

In section 4.1.1, it has be seen that a maximum value for ϵ is equivalent to a minimum of heat lost by conduction. A maximum value for δ^m would also reduce the heat losses.

4.2.1.3 Membrane wetting

Wetting is the phenomenon in which water enters the pore and causes the membrane to lose its hydrophobicity. The pressure at which this penetration occurs is given by the Laplace (Cantor) equation: $\Delta P_{entry} = \frac{-2B\gamma_L cos(\theta)}{\frac{d^{po}_{max}}{2}}$. Thus, the maximum size pore to avoid membrane wetting must satisfy the condition for which the partial vapor pressure difference between both sides of the membrane is smaller than this penetration pressure:

$$P_{liquid} - P_{vapor} = \Delta P_{interface} < \Delta P_{entry} = \frac{-2B\gamma_L cos(\theta)}{\frac{d^{po}_{max}}{2}} \quad (4.5)$$

with γ_L the liquid surface tension , θ the liquid solid contact angle , $\frac{d^{po}_{max}}{2}$ the largest pore radius and B a geometric pore factor determined by the pore structure (B=1 for a cylindrical pore) [80].

4.2.2 Role of the air-gap

As at 20°C and 1 bar the thermal conductivity of air is $\lambda_{air,20°C,1bar} = 0.0262 W.m^{-1}.K^{-1}$ while that of water is $\lambda_{eau,20°C,1bar} = 0.6 W.m^{-1}.K^{-1}$, air is a better insulator than water. Compared to the DCMD where two water channels are directly in contact, the air-gap of AGMD acts as an insulating layer. Indeed, it reduces the heat losses between the hot and cold channels, and improves the energy efficiency of the system by keeping the hot and cold temperatures different (fig. 4.5, left).

At the same time, since at 20°C and 1 bar, the diffusion coefficient of water vapor in a large excess of air is $D_{watervapor->air,20°C,1bar} = 2.42.10^{-5} m^2.s^{-1}$, the air-gap also slows down the mass transfer by providing a resistance to it (fig. 4.5, right).

Comparing the relative influence of these two phenomenons would be interesting to understand under which configuration the air-gap has a positive impact.
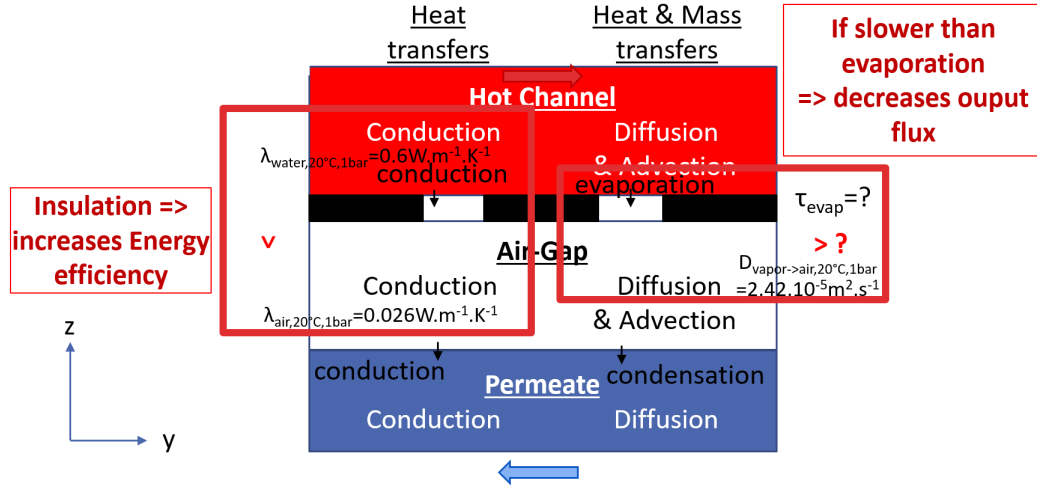
Figure 4.5: Role of the Air-Gap in an AGMD module

4.2.3 Role of the membrane

As the thermal conductivity of PTFE (the material of the membranes), $\lambda_{PTFE,25°C,1bar} = 0.25W.m^{-1}.K^{-1}$, is much higher than the thermal conductivity of air, and a bit lower than the conductivity of water, the membrane does not act as an insulating layer.

As the porosity of the membrane is about 80%, it reduces the evaporation surface (reducing the permeate flux) and the conduction surface (reducing the heat losses hence increasing the energy efficiency).

The mean free path of water vapor molecule in an air-water vapor mixture at $P = 1bar$ and $T = 0°C$ is about $\bar{l} = 6.8.10^{-8}m$, while the membrane pore size is of the order of magnitude of $d^{po} = 0.2\mu m$. Thus the Knudsen number is $0.01 < Kn = \frac{\bar{l}}{d^{po}} < 1$: this corresponds to the transition region where the water vapor molecules collide with the walls of the membrane pores (Knudsen diffusion) and also diffuse through the air in the membrane by molecular collisions (molecular diffusion). Since the Knudsen diffusion coefficient, $D_k = \frac{d^{po}}{3}(\frac{8RT}{\pi M})^{0.5} = 3.914.10^{-5}m^2.s^{-1}$, is slightly higher than the diffusion of the vapor in an excess of air, Knudsen diffusion accelerates a bit the diffusion process in the air-gap (fig. 4.6).

The membrane appears to play mainly a structural role in the process, maintaining the hot water channel apart from the air-gap ([91], [4]).
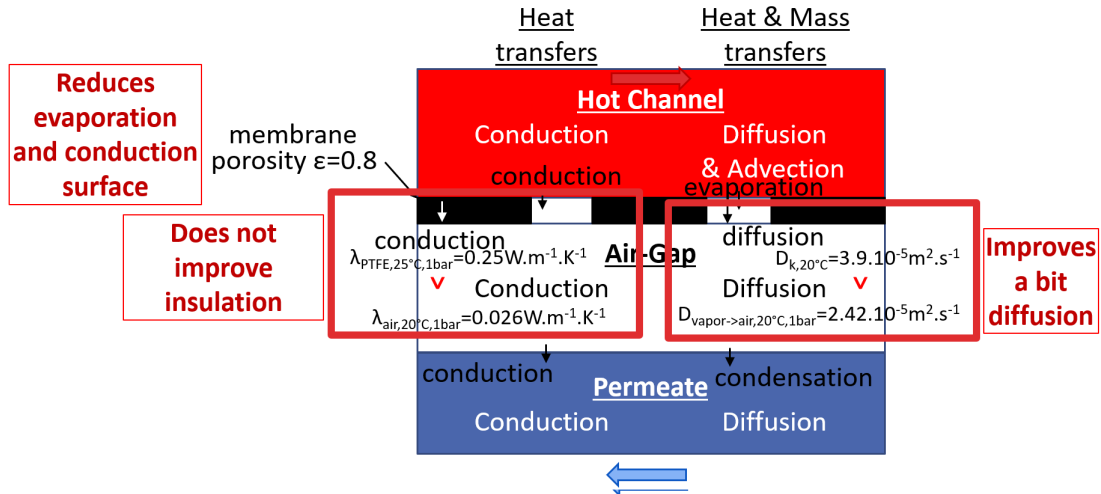
Figure 4.6: Role of the membrane in an AGMD module

Marie-Alix Dalle

4.2.4 Reversed air-gap membrane distillation configuration

A reversed configuration has been considered, with the hot flux at the bottom of the module, topped by the air-gap, on top of which lays the membrane, over which lays a thin film of condensed water, cooled by the cold flux at the top of the module (fig. 4.7).

This configuration was inspired by Wagensonner [151] which highlights that in a reversed configuration, temperature polarization, due to heat transfer by conduction and latent heat transfer, may be less than in the "normal" configuration (hot water at the top), thanks to natural convection causing natural mixing in the hot channel. Indeed, the cooler and more concentrated water created at the membrane interface due to evaporation sinks at the bottom of the hot water channel while the hot and less concentrated water replaces the cold water at the membrane surface. This configuration favors natural mixing. Moreover, Wagensonner suggests that this configuration with hot water at the bottom may help reduce membrane scaling and fouling issues if the water level does not touch the membrane.

To further enhance the appeal of this configuration, Cramer et al. [33] found that convection occurs in the air-gap for an 8mm high air-gap in this reversed configuration, increasing the removal of water molecules from the membrane interface and thus increasing the evaporation flux.
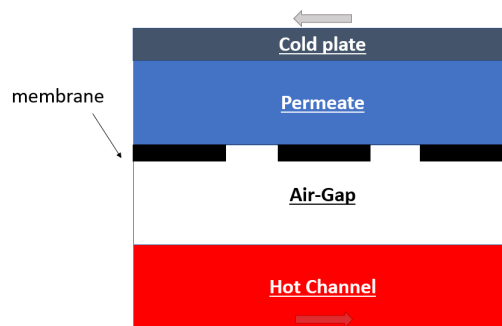
Figure 4.7: Reversed AGMD module

However this configuration requires a horizontal utilization and precise control of the hot channel's inlet and outlet, as it is no longer a loaded flow but an open surface one.

4.3 Conclusion on the physical phenomena in AGMD

After a review of the different physical phenomena at stake in AGMD, the polarization occurring in the hot water channel and air-gap is identified as the main source of AGMD performances' limitations.

Chapter 5

AGMD performances study framework

In order to overcome AGMD performances' main limitation and optimize its fresh water output and energy efficiency, both an experimental and a numerical study framework are proposed.

A test facility should allow the measurement of the fresh water production in different contexts, as well as the observation of the heat transfers in the hot water channel and air-gap at the origin of the polarization.

Aside, a 3D code was previously developed in order to forecast AGMD performances in a wider range of configurations than those possible experimentally.

Both experimental and numerical approaches complete each other, as the experimental approach also provides a mean to validate the numerical approach.

5.1 Test facility specifications

In order to select the most relevant observation method, the specifications of the test facility have to be defined.

The experimental set-up should be flexible enough to offer the opportunity to adjust operating parameters like hot and cold water temperatures, feed flow, and evaluate their influence on the process.

The facility should contain a desalination module, a pump to circulate the fluids, devices to heat and cool the water, and an observation method to characterize the polarization phenomenon. Temperatures and flows should be monitored.

5.2 Selection of the temperature and concentration profiles observation method

In order characterize the polarization phenomenon, an observation method allowing for the observation of temperature and concentration profiles both in the hot water channel and the air-gap is looked for.

The ideal measurement method would allow to simultaneously observe continuous temperature and concentration profiles inside both the air-gap and the hot water channel, without disrupting the process. Moreover, the ideal observation method should allow an observation very close to the membrane.

This chapter presents in detail the underlying theory and practical application of various temperature and concentration profiles measurement methods, either direct or indirect; intrusive or external.

5.2.1 Benchmark of the existing temperature and concentration measurement methods

Several temperature and concentration measurement method were considered and compared to select the best option.

5.2.1.1 Punctual temperature measurements

Some temperature sensors only provide punctual and discrete temperature values.

A bi-metal **thermostat** is a bonded strip of two metals with different expansion coefficients. The temperature differential causes the strip to flex when heated.

To detect bending, these sensors require a minimum length of the sensing material, limiting their spatial resolution.

Resistance Temperature Detector (**RTD**) are constructed of platinium, which has a fairly linear temperature-to-electrical resistance ratio.

Thermistors are less priced RTDs with a smaller temperature range. Thermistors come in two varieties: positive temperature coefficient (whose resistivity increases as temperature rises) and negative temperature coefficient (whose resistivity lowers as temperature rises).

Infra-Red **Pyrometers** detect and convert infrared radiation released by objects.

The **bandgap temperature sensor** works by measuring the forward voltage of a silicon diode, which is the base-emitter junction of a bipolar junction transistor. A voltage-temperature relationship is found by comparing two junctions with the same temperature but different currents.

Thermocouples work on the Seebeck effect: a potential difference arises at the junction of two metals when heated. They come in a variety of sizes and materials (metal couples) with varying properties (temperature range, resistance, etc.).

5.2.1.2   Concentration profiles measurement

Prasser et al. [108] created a **wire-mesh** device for measuring 2D conductivity of water between two emitter points. It is made up of two wire grids positioned 15mm apart in the flow. The plan composed of several electrodes has one emitter and one receiver. The wires are 0.12mm thick.

This approach detects bubbles in a flow [109] and may be calibrated to detect conductivity variations caused by contaminants.

Lokare et al. used **spectrophotometry**, or the absorption of light by metal transition salts ($CoCL_2$, $CuCl_2$ and $NiCl_2$) as a measure of the concentration variations.

5.2.1.3   Temperature profiles measurement

Ranaweera et al. [114] developed a **thermocouple wire-mesh sensor** that measures the temperature at N^2 points using only $2N$ thermoelements. The spatial resolution is also design-dependent, and can be increased by adding wires.

A **thermocamera** detects an object's infrared emission, also known as black body radiation. But it can only detect temperature variations on the module's sides. The camera characteristics determine the spatial resolution and temperature precision of the method.

Magnetic resonance thermometry [153] uses proton magnetic resonance frequency (7T) [119] to measure temperature.

Light excites dye molecules, which then emit light to return to their initial state. When a **temperature dependent fluorescent dye** absorbs the photon of a given energy, its energy state transitions from ground state towards higher electronic states. Part of this energy is then dissipated until the molecule reaches the lowest level of the first excited singlet state. From this singlet state, the molecule can come back to its ground state in different ways, one of it being fluorescence: a radioactive decay process wherein no further energy is dissipated by collision but just emitted. Due to the initial energy loss by dissipation, the emitted energy has a longer wavelength than the received energy. This wavelength shift, known as the Stokes shift [123], depends on the fluid's temperature [119]. Using a second dye, with a different temperature sensitivity [94], a comparable absorption spectra and a non-overlapping emission spectra helps compensate for incident light intensity fluctuations[123]. Indeed, the ratio of the two dyes' emissions no more depends on the incident light flux intensity, and if both dyes are similarly submitted to changes in concentration, the ratio merely depends on temperature.

This method used in microfluidic [119] can deliver a 3D image of the phenomenon thanks to lenses pointing the laser at a specific coordinate in the test module [123].

Liquid crystals' configuration changes with temperature, hence the wavelength they reflect changes: the molecules are organized in layers, whose spacing depends on the temperature, and the reflected wavelength is the one with the greatest constructive interference with Bragg diffraction.

Red cabbage's color varies with pH, which fluctuates with temperature. The water molecules vibrate more as the temperature rises, making ionization easier (producing H+ and OH- ions is endothermic, absorbing heat). According to Le Chapelier's Principle, if the system is heated, the equilibrium moves to absorb the heat and produce more ions. This reduces pH but does not increase acidity because both ions are created in equal amounts.
Experiments were inconclusive.

5.2.1.4 Simultaneous temperature and concentration profiles measurements

Light interacts with transparent medium via the refractive index n [101]:

$$n = \frac{c}{c_0} \tag{5.1}$$

with c the velocity of light in vacuum and c_0 the light velocity in the considered medium.

In an isotropic and transparent medium, this refractive index n is a unique function of the material density (ρ), which itself depends on the temperature (T) and concentration (C) of the medium. A general expression of the refractive index can be written:

$$\frac{n^2 - 1}{\rho(n^2 + 2)} = a_0 + a_1\rho + a_2T + a_3C \tag{5.2}$$

which can be simplified according to the Lorentz–Lorentz formula as:

$$\frac{n^2 - 1}{\rho(n^2 + 2)} = constant \tag{5.3}$$

For small temperature variations (up to 10 °C in air), density ρ and temperature T are linearly related as $\rho = \rho_0(1 - \beta(T - T_0))$, where $\beta > 0$.

Cauchy formula gives the refractive index's dependence on wavelength (λ):

$$n(\lambda) = A + \frac{B}{\lambda^2} + \frac{C}{\lambda^4} + ... \tag{5.4}$$

Thus all these equations establish a relationship between a material refractive index and its temperature and concentration, at various wavelengths. Hence, interacting light with a material can provide information regarding the material's temperature and concentration.

The three primary methods for interacting light with a media are:
- **Interferometry**: assuming straight line light travel, and based on phase change measurements (ie on the wave properties of light), it determines the refractive index
- **Schlieren**: based on ray deflection but not displacement (ie only on particles properties of light), it provides the first derivative of the refractive index, is less sensible to vibrations than interferometry, and more straightforward than Shadowgraph
- **Shadowgraph**: based on both ray deflection and displacement (ie only on particles properties of light), it provides the second derivative of the refractive index, but requires tedious quantitative analysis of the images.

The result of these three methods is a C or T field that has been ray-averaged over the module's length L. In liquids, the derivative $\frac{dn}{dT}$ or $\frac{dn}{dC}$ is approximately three orders of magnitude larger than in gases [75]. Hence, in comparison to air, only a small perturbation is required to observe refraction in liquids.

By using two wavelengths simultaneously, the influence of two parameters on the refractive index variations [101], temperature and contaminant concentration in this case, can be determined at the same time.

These optical methods are non-intrusive, inertia free, and can image cross-sections of the experimental apparatus.

5.2.1.5 Conclusion on the existing temperature and concentration profile measurements

The different temperature and concentration profiles measurement solutions examined previously are summarized in table 5.1.

For their non intrusiveness, the continuous profile they can provide, and their ability to resolve two variables simultaneously (temperature and concentration), the refractive index methods are retained.
The two-wavelength Schlieren method is selected as a good compromise between easiness to set-up and accuracy of the results compared to the other refractive-index based methods.
Ideally this set-up would be coupled with an Interferometry set-up to criss-cross the results and strengthen the conclusions.
Coupling both of these methods to the fluorescent dye technique was also an option considered, and taken into account in the choice of the material, however first experiments proved that the refractive index method and the dye one are incompatible as one requires the laser to go through the water while the other relies on the light being absorbed by the dye.

The next sections of this thesis focus on the methodology of the two-wavelength Schlieren method.

	Name	Spatial resolution	Temperature accuracy	Sensitivity	Advantages	Drawbacks
punctual T	Bi-metal Thermostat	NK	NK	NK	always working	intrusive
	RTD	$\approx 6mm$	$\pm 0.15 + 0.002|T|$[1]	0.38-$3.8\Omega/°C$[2]	easy to implement	intrusive
	Thermistor	$\approx 2mm$[3]	$\pm 1°C$[4]	$0.1°C$ [5]	easy to implement	intrusive
	IR pyrometer	pixsize	2-5K [105]	NK	easy to implement	only surfaces
	Bandgap T sensors	$0.0625°C$[6]	± 2 °C[7]	NK	easy to implement	intrusive
	Thermocouples	$10\mu m$[103]	$\pm 2.2°C$ or $\pm 0.75\%$[8]	17-$58\mu V/°C$[9]	easy to implement	intrusive
C grad	C wire mesh sensor	$\approx 2mm$[108]	NK	NK	easy to implement	intrusive
	Spectrophotometry	$4.5\mu m$ [86]	NK	NK	NK	intrusive
T grad	T wire mesh sensor	$\approx 2mm$	$\approx 0.5°C$	NK	easy to implement	intrusive
	Thermocamera	$0.01mm$[105]	$2K$[105]	NK	easy to implement	only surface
	Magnetic resonance	$1mm$ [119]	$1°C$[119]	NK	non-intrusive	requires heavy infrastructures
	Fluorescent dye	$1\mu m$[119]	0.03-$3.5°C$[119]	NK	easy to implement	intrusive
	Liquid crystals	pixsize	$\pm 1.5°C$ for a 40 K range $0.1K$ for a 0.7K range [123]	depends on compounds ($\approx 2\%/K^{-1}$) or $0.1°C$ [10]	easy to implement	intrusive
T and C grad	2 Wavelengths Interferometry	pixsize	depends on optics	depends on optics	provides T	lot of optics 2 test chambers discrete values
	Holography	pixsize	depends on optics	depends on optics	less optics	complex interpretation
	2 Wavelengths Schlieren	pixsize	depends on optics	depends on optics	simple set-up	provides $\frac{dT}{dx}$
	Shadowgraphy	pixsize	depends on optics	depends on optics	easiest set-up	provides $\frac{d^2T}{dx^2}$

Table 5.1: Measurement methods (NK indicates values not known)

5.2.2 Schlieren method

Image formation in a Schlieren system is due to deflection of the light ray in a variable refractive index field (in German, "schliere") toward regions of higher refractive index.

This optical process has already been used to determine the concentration and temperature variations inside a reverse osmosis process by Kroiss et al. ([45], [73], [148], [74]).

Indeed, the temperature and concentration variations occurring in the desalination module induce a density variation creating a refraction index variation.

5.2.2.1 General Method

Schlieren measurement quantifies the deflection of the light ray due to the refraction index variations by interacting with the ray and altering its intensity in response to its deflection. Thus the intensity variation observed on the screen can be related to the integral of the refraction index along the light ray's path.

A Schlieren set-up consists of a first part generating a beam of parallel light rays that illuminates the test section. Following this test section, a focusing element focuses the beam at its focal plane where its intensity is tampered via a knife or filter. The beam finally enters the imaging part of the set-up (fig. 5.1).
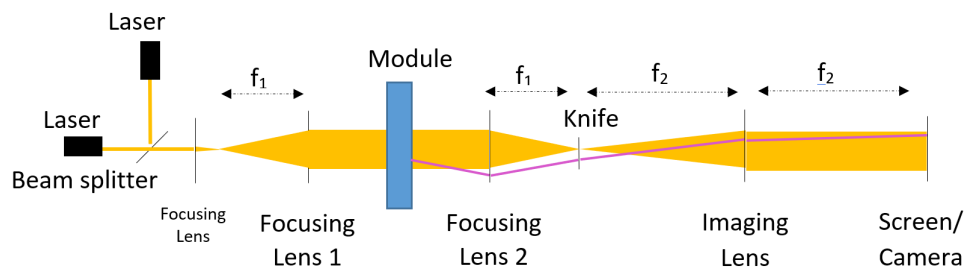
Figure 5.1: Schema of a Schlieren dispositive

Optics are positioned in such a way that the planes containing the light source and the knife or filter are conjugated, which means that what appears in one plane also appears in the other. The same occurs for the plane containing the test section, and the screen plane.

$$\tan(\beta) = \frac{x_0}{f_1} = \frac{x_f}{f_2}$$
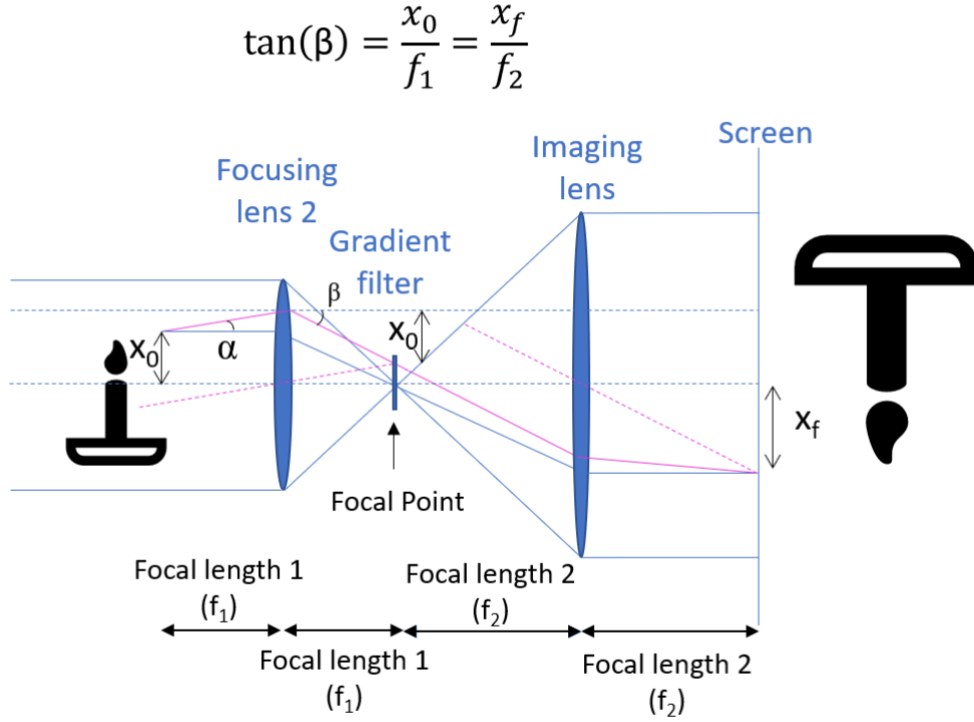
Figure 5.2: Ray path in a Schlieren set-up with a homogeneous temperature (blue) and with a temperature profile (purple)

This figure 5.2 shows that when the object to be observed is exactly at the focal plane of the second focusing optical element (mirror or lens), and the screen is precisely at the focal plane of the imaging lens, the final position of the ray on the screen $x_f = \frac{f_2}{f_1}x_0$ is determined solely by the initial position x_0, and not by the deflection α. Thus, regardless of the deflection angle α, the ray will end up in the correct location on the screen, and the image displayed on the viewing device in the absence of a filter or knife, is identical to that of the test section except for the magnification factor.

Placing a filter gradient at the focal point of this focusing element exploits this deflection angle by altering the intensity of this ray without changing its position. The rays' deflections are thus made visible on the imaging screen as variations in intensity of the object image.

The distance Δx traveled by the deflected ray subject to refraction index variations during the time interval $\Delta\tau$ is (fig. 5.3):

$$\Delta x = \Delta\tau \frac{c_0}{n} \tag{5.5}$$
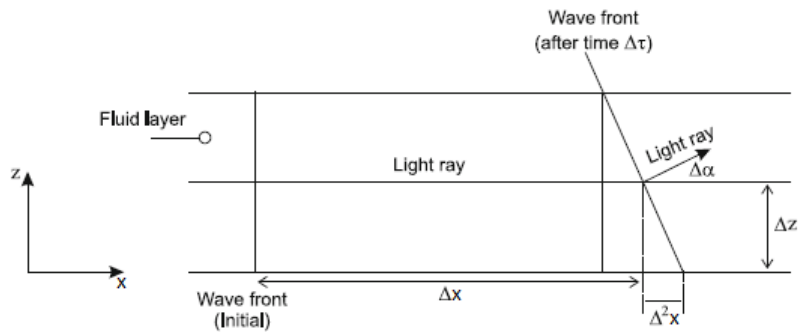
Figure 5.3: Path of a bent ray subject to refraction index variations [101]

If the deflection $\Delta\alpha$ is small, then it can be assumed that:

$$\Delta\alpha \approx \tan(\alpha) = \frac{\Delta^2 x}{\Delta z} \tag{5.6}$$

$\Delta^2 x$ can be rewritten $\Delta^2 x = \Delta x_z - \Delta x_{z+\Delta z} = \Delta x_z - \Delta x_z - \frac{\Delta}{\Delta z}(\Delta x)\Delta z = -\frac{\Delta}{\Delta z}(\Delta\tau\frac{c_0}{n})\Delta z$. Thus, $\Delta^2 x = -\frac{\Delta\frac{1}{n}}{\Delta z}c_0\Delta\tau\Delta z$, and in 5.6:

$$\Delta\alpha = -\frac{\Delta(\frac{1}{n})}{\Delta z}c_0\Delta\tau = -\frac{\Delta(\frac{1}{n})}{\Delta z}n\Delta x = -(-\frac{1}{n^2}\frac{\Delta n}{\Delta z})n\Delta x = \frac{1}{n}\frac{\Delta n}{\Delta z}\Delta x \tag{5.7}$$

Thus, at the limit, $d\alpha = \frac{\partial(ln(n))}{\partial z}dx$ so:

$$\alpha = \int_0^L \frac{\partial(ln(n))}{\partial z}dx \tag{5.8}$$

According to Snell law, $n_a \sin(\alpha'') = n\sin(\alpha)$, with n_a the refractive index of ambient air and α'' the angle of the light ray emerging from the test cell of refractive index n. Thus for small values of α'' and α, $\alpha'' \approx \frac{n}{n_a}\alpha$, and in 5.8:

$$\alpha'' = \frac{n}{n_a}\int_0^L \frac{1}{n}\frac{\partial n}{\partial z}dx \tag{5.9}$$

If $\frac{1}{n}$ does not change much through the test section and since $n_a \approx 1$, the previous equation becomes: $\alpha'' = \int_0^L \frac{\partial n}{\partial z}dx$, and if a constant refractive index gradient over the path L (=module length) of the light ray is assumed:

$$\frac{\partial n}{\partial z} \approx \frac{\alpha''}{L} \tag{5.10}$$

In the case where a knife is located at the focal point of the second focusing optical element (mirror or lens) (fig. 5.4), let:
- a_0 be the original diameter of the light source beam falling on the knife edge
- I_0 be the illumination at the screen when no knife edge is present
- a_k be the amount of the light beam cut off by the knife edge
- I_k be the illumination at the screen when the knife edge is present: $I_k = \frac{a_k}{a_0}I_0$ (I_k is uniform because since the light source is at the center of the mirror, every ray in its exact image at the center carries all the information from the initial light source: halving this exact image just dims the image on the screen).
- Δa be the displacement of the light beam in vertical direction z above the knife-edge corresponding to the angular deflection α'': $\Delta a = \pm f_1\alpha''$ with f_1 the focal length of the converging element placed after the module (focusing lens or concave mirror)
- I_f be the final illumination on the screen: $I_f = I_k\frac{a_k+\Delta a}{a_k}$
- ΔI be the change in light intensity: $\Delta I = I_f - I_k$
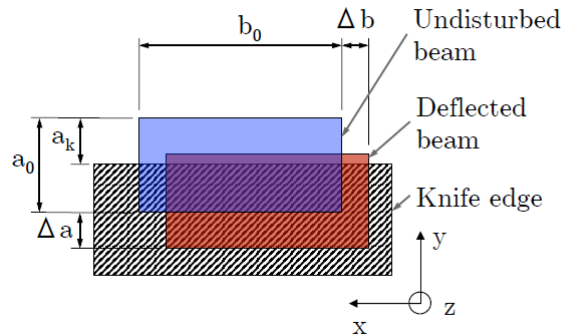
Figure 5.4: Undisturbed and deflected cross-section beam at the knife-edge [45]

Thus, the resulting contrast on the screen can be expressed as:

$$C = \frac{\Delta I}{I_k} = \frac{I_f - I_k}{I_k} = \frac{\Delta a}{a_k} = \frac{\alpha'' f_1}{a_k} = \frac{f_1}{a_k} \frac{n}{n_a} \int_0^L \frac{1}{n} \frac{\partial n}{\partial z} dx \approx \frac{f_1}{a_k} \int_0^L \frac{\partial n}{\partial z} dx \qquad (5.11)$$

Contrast is a function of the focal length f_1 of the converging element placed after the module (focusing lens or concave mirror): the longer the focal length the greater the sensitivity. It also depends on the unblocked portion of the light beam at the knife edge a_k. Moreover, as contrast is based on intensity ratios, absolute intensities are not required. Hence the camera must be linear (convert I into V linearily) and non-saturating.

The drawbacks of this general method are that:
- if the beam is completely deflected below the knife edge, information is lost
- if the light source is a perfect point source (eg. laser), it focuses as a perfect point at the focal point: $a_0 = 0$, and $a_k = 0$, the previous equation is no longer valid
- diffraction can occur at the knife edge
- saturation of the camera sensor can occur
- only one direction of a beam's bending can be observed at a time (depending on the position of the knife edge)

To resolve all these issues, except for the unidirectionality, a filter with a transmission gradient function t can be substituted for the knife, and equation 5.11 becomes:

$$C = \frac{\Delta I}{I_k} = \alpha'' f_1 \frac{1}{t_0} \frac{dt}{dp} cos(\varphi) \qquad (5.12)$$

with $\frac{dt}{dp}$ the gradient of transmission t of the filter as a function of the position p at the focal point, t_0 the transmission when no deflection occurs; and φ the angle between the direction of the deflection and the gradient of transmission t (in this case, $\varphi = 0$ as the filter will be used in the same direction as the deflection angle).

5.2.2.2   Sensitivity, range measurement and resolution

The Schlieren method's **measuring range** is defined as the maximum deflection angle α_{max} at the exit of the test section that the Schlieren set-up is capable of measuring: $\alpha_{max} = \arctan(\frac{a_0 + a_f}{f_1})$. Hence, the measuring range depends on the position of the Schlieren cut-off, the size of the source slit image a_0, the length of the gradient region of a gray graduation filter a_f ($a_f = 0$ for knife edge) and the focal length f_1 of the converging element placed after the module (focusing lens or concave mirror). For the maximum range in both directions (positive and negative deflections) the filter should be positioned in the middle of the source slit image. Then the measuring range is the interval $[-\frac{\alpha_{air,max}}{2}; \frac{\alpha_{air,max}}{2}]$ [45].

Sensitivity is defined as the change in contrast with respect to a change in refractive index gradient. This value is often called contrast sensitivity S. According to equation (5.11): $S = \frac{doutput}{dinput} = \frac{dC}{d(\frac{dn}{dz})} \approx \frac{L}{n_{air}} \frac{f_1}{a_k}$ [45] or $S = \frac{L}{n_{air}} \frac{f_1}{t_0} \frac{dt}{dp}$ in the case where a gradient filter is used instead of the knife. Thus sensitivity can be increased by either lengthening the test section L, increasing the focal length of the second focusing optical element (mirror or lens) f_1, or by reducing the unblocked length of the undisturbed beam a_k by translating the Schlieren cut-off [45]. In the case of a filter, sensitivity depends on the gradient of transmission of the filter.
Sensitivity and measuring range vary in opposite proportions.

Resolution is the minimal measurable refractive index gradient. It is a function of the minimum resolvable contrast in a Schlieren image, which is a property of the image capturing device as it depends on the minimum contrast the camera device can observe. Using a digital camera sensor which records an 8 bit image capable of resolving 256 intensity values, the theoretical minimum contrast is

$$C_{min} = \frac{\Delta I}{I} = \frac{1}{256} = 0.4\% \qquad (5.13)$$

Using S, the minimum measurable refractive index gradient can be estimated by [45]

$$(\frac{dn}{dz})_{min} = \frac{n_{air}}{L}\frac{a_k}{f_1}C_{min} = \frac{n_{air}}{L}\frac{t_0}{f_1}\frac{1}{\frac{dt}{dp}}C_{min} \tag{5.14}$$

the first expression being valid for a knife cutting a_k of the beam; the second for a filter with a transmission function t with a gradient over the filter $\frac{dt}{dp}$.

Sensitivity and resolution evolve on opposite directions.

5.2.2.3 Light source

In the case of a two-wavelengths Schlieren method, a spatial and time stable source of light for these two wavelengths of similar intensity is needed. Kroiss et al. used an arc light source with a xenon vapor lamp with 300W from LOT-QuantumDesign, and lasers are a less expensive option to this requirement.

As a point source (eg. a laser) is not indicated for a knife Schlieren set-up, as the value of a_k in eq. 5.11 is almost zero, a filter can be used instead of the knife, enlarging the measurement range.

5.2.2.4 Relation between water density, temperature and concentration, wavelength, pressure and the refractive index

The dependency of seawater density on salinity, temperature and pressure is described by the International Thermodynamic Equation of Seawater, defined by the Intergovernmental Oceanographic Commission. It is available in a MATLAB program [102], valid for water with a temperature up to 80 °C, and a salinity up to $70 g.kg^{-1}$.

The relationship between water temperature, density and pressure and its refractive index is described in Schiebener et al. [124]. Based on the Lorentz Lorentz equation, this new formulation is valid for wavelengths 0.2 to 2.5 pm, temperatures -10 to +500 °C and densities 0 to 1045 $kg.m^{-3}$.

5.2.2.5 Advantages and limitations

As Schlieren is based on the first and second order derivative of the refraction index, errors can propagate while integrating. Moreover, it requires high quality lenses.

The alignment and calibration is shorter than for the interferometry set-up but has to be done before each experimentation [45].

The main advantage of Schlieren is that it provides a continuous profile (discretized by the image capturing device, like camera chip pixel size), and the temperature at the membrane surface can be derived from the measured data without extrapolation [45].

Moreover, its sensibility can be adjusted through different ways (focal length of the convergent element placed after the module, length of the module, choice of the Schlieren cut-off or filter) [45].

5.3 3DH&MT AGMD model

Preceding this thesis work, a three dimensional heat and mass transfer model for AGMD (3DH&MT model) has been developed at University of Luxembourg by Cramer et al. [33], as an extension of T-Flows, an open source CFD software created by Niceno et al. [96]. This thesis work intends to validate this 3DH&MT model, in order to later on use it to simulate more complex module and spacer geometries and optimize the AGMD process.

5.3.1 Equations and models applied in the 3DH&MT AGMD model

The 3DH&MT model relies on the equations described in sections 4.1.1 and 4.1.2 to numerically solve for heat and mass transfers from the hot water channel to the condensation plate via the membrane and air-gap (fig. 5.5):

- in the hot channel: Navier-Stokes and energy conservation equations are solved in 3D
- at the evaporation interface: energy conservation equation is solved (all the heat contained in the water is either transferred to the membrane by conduction, or to the gas by evaporation)
- in the membrane: the flux through the membrane is solved using the Dusty Gas Model

- on the condensation plate: the reversed Antoine equation is used: since the water has evaporated into a warmer air and elevates in a colder air, the air becomes saturated (and maybe supersaturated) and hence condensates
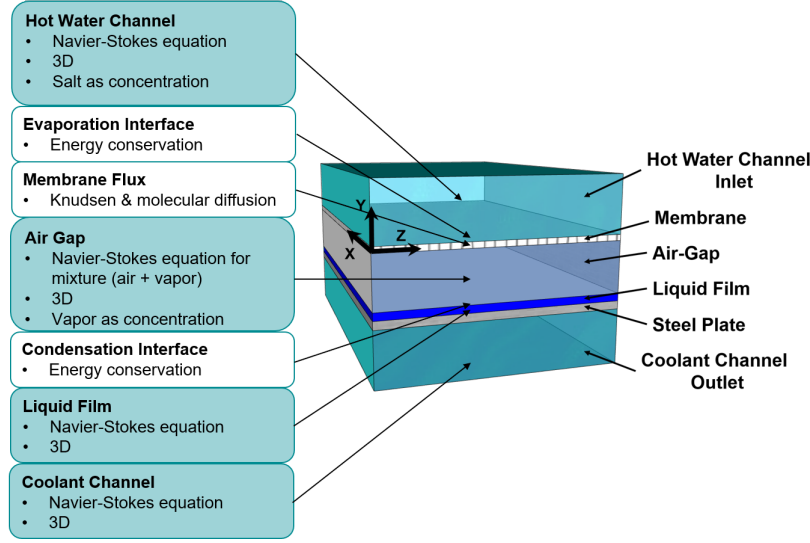
Figure 5.5: Macroscopic model used in the 3DH&MT model [33]

The evaporative mass flux $\dot{m}_{evap}$ is derived from energy conservation at the interface:

$$\dot{m}_{evap}.h_d = \epsilon h^h \frac{T_b^h - T_{ie}}{d^h} - \epsilon h^a \frac{T_{ie} - T_{iam}^a}{\delta^m} \tag{5.15}$$

and the diffusion mass flux $\dot{m}_D$ is written:

$$\dot{m}_D = C_D \frac{p_{v,sat}(T_{ie}) - p_{v,air-gap}}{\delta^m} \tag{5.16}$$

where $p_{v,sat}(T_{ie})$ is solved thanks to Antoine equation.

To satisfy mass conservation, $\dot{m}_{evap} = \dot{m}_D$: the system is closed as there is one equation for one unknown, T_{int}.

Thermal equilibrium is assumed at the evaporative interface, and thus the temperatures on both the liquid and vapor sides of the interface, T_{ie}^h and T_{ie}^a, are set to be equal to T_{ie}. From this thermal equilibrium assumption also results the saturation assumption at the hot water interface.

The liquid film is assumed to be 0.5mm thick.

5.3.2 Highlights of the model

Contrary to the majority of AGMD simulation models, this model is three-dimensional, allowing for the investigation of three-dimensional geometries such as the spiral geometries described in section 3.1.

In addition, the enabling of convection fluxes in the air-gap allows the simulation of a broader range of operating conditions, and hopefully, the identification of configurations in which the diffusion does not restrict evaporation.

5.3.3 Limitations of the model

As convection appears to occur in the air-gap in a reversed configuration (section 4.2.4) and a sufficiently high air-gap height ($\approx 8mm$), the assumption of saturation at the hot water interface is questioned: are the convection and diffusion rates in the air-gap always sufficiently low in comparison to the evaporation rate such that thermodynamic equilibrium is reached between the liquid surface and the air above before diffusion and convection remove all the vapor molecules from the membrane surface?

The assumption of thermal equilibrium at the evaporative interface ($T_{ie}^h = T_{ie}^a$) also differs from what is observed experimentally [104] and is discussed in section A.1.

Water surface tension should be integrated in the code in order to obtain a more realistic permeate film thickness. Indeed, the currently assumed thickness of 0.5mm is not consistent with reality (see section 7.2.4). This water property could also have an impact the shear stress at the membrane which is not accounted for at the moment.

Other current limitations of this code are its impossibility to handle non structured meshes, indispensable to simulate complex geometries like spirals. Moreover, its very refined membrane code renders it unable to handle huge module geometries such as the spiral modules of Aquastill or Fraunhofer, despite these geometries being 3D and thus a perfect fit to assess the interest of this 3DH&MT model.

5.4 Conclusion on the AGMD performances study framework

Combining an experimental facility with a numerical model enables to gain a better understanding of AGMD polarization phenomenon, and optimize its fresh water output and energy efficiency.

Chapter 6

Spacers study settings

One of the AGMD process enhancement to which the previously described combination of experimental set-up and numerical model could contribute to is spacers design.

Indeed, spacers are structural elements necessary in most MD geometries to maintain the height of the different channels. Moreover, they have been identified as a relevant solution to the polarization phenomenon: their impact on the hot water mixing prevents the occurrence of the polarization phenomenon at the membrane interface, which slows down the heat transfer to the water molecule and hence the permeate flow.
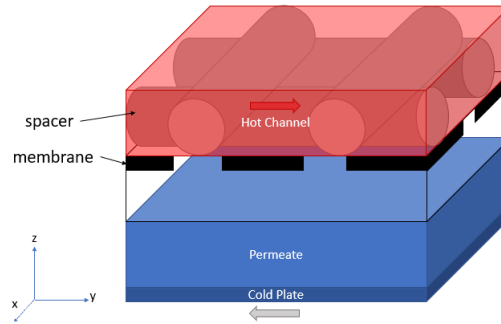
Figure 6.1: Example of spacer localisation in the hot water channel of an air-gap membrane distillation device

The coordinate system in fig. 6.1 is consistent all throughout the thesis and in particular with fig. 4.2.

The fastest heat transfer phenomenon is convection, over diffusion. In a laminar flow, heat is transferred from the bulk water phase to the surface molecules by heat diffusion, whereas turbulences and macroscopic liquid movement perpendicular to the flow direction contribute to heat exchange by convection. If a turbulent flow strikes as an obvious mixing strategy to ensure that the hot water stream delivers the greatest energy to the surface water molecules, it also loses kinetic energy by friction, increasing pressure losses in the MD module and thus reducing energy performance.

Finding spacer geometries increasing the mixing at a lower pumping energy demand is thus important research topic for MD.

6.1 Performance indicators

Important parameters to judge the efficiency of a spacer geometry are the mass mixing and the generated frictions and pressure losses.

To measure the mixing efficiency, several indicators can be used.

In spacer research for membrane distillation, the main indicator used to assess the mixing performance of a device is the Sherwood number, ratio of convective mass transfer over diffusion, $Sh = \frac{k_m L}{D}$ with k_m

the mass transfer coefficient, L a characteristic distance and D the mass diffusivity. However, various empirical correlations are proposed to calculate this number: for a rectangular slit of height H, Leveque [88] proposes $Sh = 1.467 \left(Re \frac{\nu}{D} \frac{H}{L} \right)^{1/3}$ with Re the Reynolds number, ν the kinematic viscosity, and L length of the channel ; or with $k = \frac{1}{A} \int_A \frac{1}{C_{bulk} - C_{wall}} \left(-D \frac{\partial C}{\partial y} \right)_{wall}$ [81], A being the spacer surface. Shrivstava et al. [131] extended the application of Lévêque equation [88] to other 2D spacer geometries than a rectangular slit by assuming that whenever the fluid encounters a new spacer barrier its concentration is instantly well mixed and behaves like an homogeneous solution entering a new tube. The spacer is thus discretized as a series of rectangular blocks. Their correlations show good agreement for simple spacer geometries, and they note that predictions for more complex geometries such as herringbones or helical spacers are more speculative due to the complexity of the resulting flows.

In industrial mixing, the coefficient of variation (CoV) measures the well-mixing of a mixture, and is defined as the variation of concentration of a tracer between several samples taken in the same cross-section, and calculated as:

$$CoV = \sqrt{\frac{\Sigma_{i=1}^{N} (Y_i - Y_{mean})^2}{N-1}} \frac{1}{Y_{mean}} \tag{6.1}$$

with Y the tracer's concentration in sample i, N the number of samples and Y_{mean} the mean tracer's concentration over the cross section [51]. If a normal distribution is assumed, approximately 95% of the sample values will lie within $\pm 2*CoV\%$ of the mean concentration. Therefore, a low CoV indicates a well-mixed mixture.

To assess the relevance of CoV as a mixing indicator, it was compared to Sherwood number in a case where the Leveque equation was easily adaptable according to Shrivstava et al. [131] methodology: the net-type spacer with cylindrical cross sections fibers (fig. 6.3).
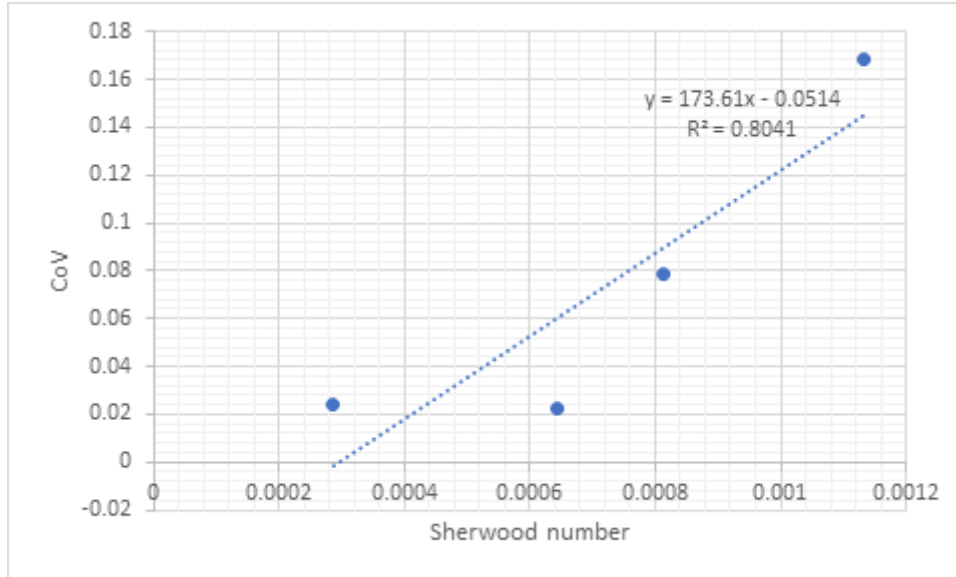
Figure 6.2: Relation of CoV against Sherwood number for cylindrical cross-section fibers position at 90°to each other

The observed correlation between the Sherwood number and CoV is strong (fig. 6.2). This suggests that CoV can be used as a measure for mixing performance for complex 3D geometries where an adaptation of Leveque equation and hence straightforward calculation of Sherwood number is not possible.

The friction can be evaluated through measurement of the pressure drop, $\Delta P = 4f \left(\frac{L}{D_e} \right) \rho \frac{u^2}{2}$ with ρ the fluid density, D_e the equivalent hydraulic diameter of the channel, $f = \frac{A}{Re^n}$ the friction factor and $Re = \frac{\rho u H}{\mu}$ the Reynolds number, L the channel length, u the flow velocity. Other ways to represent the pressure drop is through the ratio of friction factors between an empty channel and a mixer filled channel: $Z = \frac{f_{mixer}}{f_{empty}} = \frac{\Delta P_{mixer}}{\Delta P_{empty}}$ or via the power constant $P_n = f(Re, f)$ which can be different in different

publications ($P_n = 2fRe$ in Thakur et al. [147], $P_n = fRe^3$ in Liu et al. [65], and $P_n = \frac{\Delta Pu}{L}\frac{\rho^2 H^4}{\mu^3}$ in Li et al. [81], with μ the dynamic viscosity).

6.2   State of the art of mixing strategies

Mixing is a procedure well studied in different domains beyond MD. And even for MD, different strategies are explored.

6.2.1   Spacers in MD

Several articles study the impact of spacers geometries and orientation on flow and temperature and concentration polarization.

The most widely spread spacer geometry is the net-type (fig. 6.3). Relevant geometric parameters to take into account while assessing the impact of spacers on the flow and performances are: the angle Ξ between the flow direction and the net grid; the voidage of the spacers $\epsilon^s = \frac{V_{tot} - V_{spacer}}{V_{tot}}$ [35]; the angle ω between the fibers of the net; the length l_s of the spacer mesh (for commercial spacers, the mesh is a square, but for customized ones the mesh can have two length parameters l_1 and l_2 [82]); and the thickness of the spacer mesh δ^s.
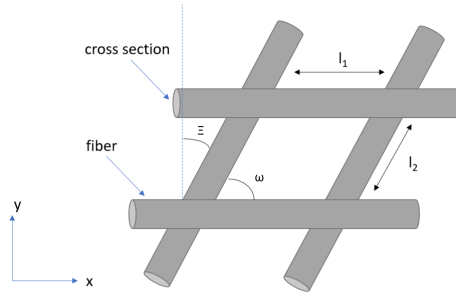
Figure 6.3: Main geometrical parameters of net spacers [83]

According to Chernyshov [30], the best results (high mixing and low pressure drop) are found for circular cross section fibers with an angle with the flow of 45°and an angle between the fibers of 90°; or fibers in the shape of twisted tapes with an angle to the flow of 30°and an angle between the filaments of 120°.

Al-Sharif et al. [7] built a 3D code on OPENFOAM to observe the impact of three different spacers configurations with varying distance relative to membrane surface on the pressure drop and temperature polarization (fig. 6.4). Shakaib et al. [130] also studied the effect of the position of spacers in the channel on the temperature polarization.
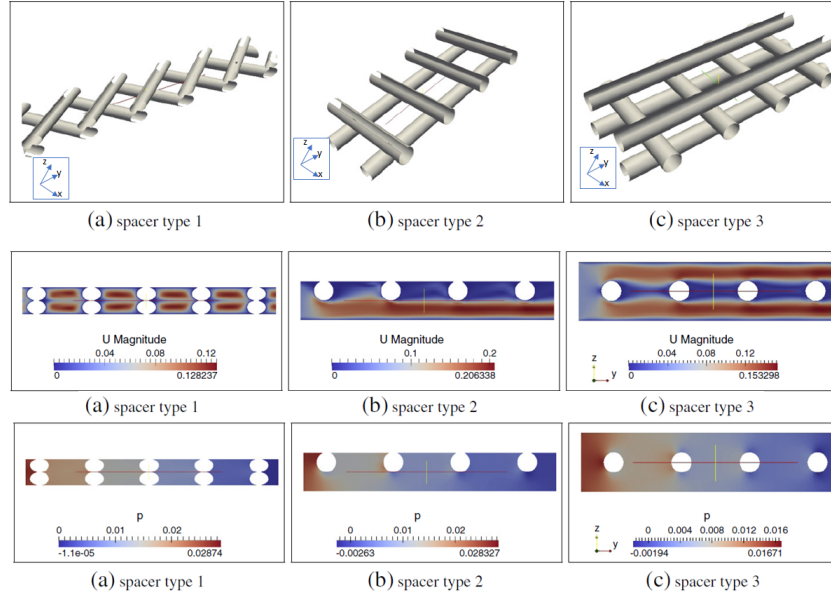
Figure 6.4: Velocity (U Magnitude, m/s) and pressure drop (P, Pa) fields for different spacers configurations. The water flows along the x axis, and the membrane is localized on top of the spacers, perpendicular to the z axis [7]

As can be seen in figure 6.4 representing the velocity (U Magnitude, m/s) and pressure drop (P, Pa) fields for different spacers configurations, the conclusions of these studies are that when the wires in contact with the membrane are perpendicular to the flow (b), a stagnant water layer is created at the membrane interface, thus increasing the temperature polarization and reducing the shear stress at the membrane. This figure also shows that configurations (a) and (c) present higher velocities at the membrane interface for similar pressure drops.

Dendukuri et al. [38] studied numerically different fibers cross-sections for net-type spacers (fig. 6.5).
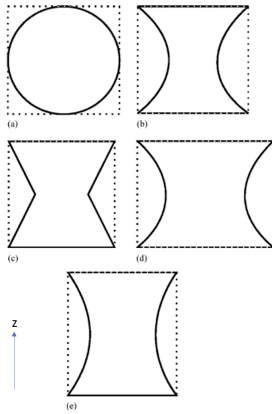
Figure 6.5: New fibers cross-sections for net-type spacer studied in Dendukuri et al. [38]. a) original, b) concave, c) rectangular (vertical), d) rectangular width/height=4/3, e) rectangular width/height=3/4. The membrane lies in the (xy) plane perpendicular to this plane.
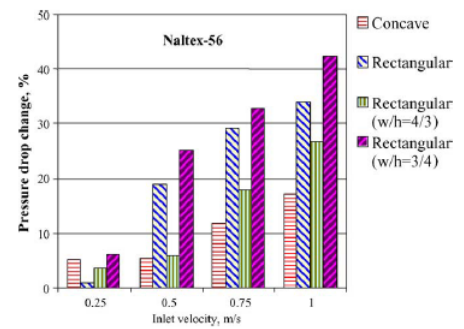
Figure 6.6: Pressure drop changes of the new spacers geometries studied in Dendukuri et al. [38] compared to a channel filled with the original spacer (a)

These new fibers' cross-sections increased the pressure drop across the channels containing spacers (fig. 6.6) compared to original spacer. Indeed, for all the inlet velocities simulated, the spacers with new

fibers cross-sections (6.5) presented up to 45% higher pressure drop than the original cylindrical fibers spacer.

Li et al. [83] also proposed new geometries for net-type spacers: a circular cross-section fiber with an added tab running in spiral all around the fiber (MLNF) with different geometry parameters ($\phi = 30°$, $\gamma = 120°$ for MLNF1 and $\phi = 45°$, $\gamma = 90°$ for MLNF2); a twister tape fiber (MLTT); and different configurations, with several layers. These new spacers are compared to a conventional net-type spacer with circular cross-section fibers (optimal non-woven spacer).

Figure 6.8: Geometry and configuration of MLTT [83]
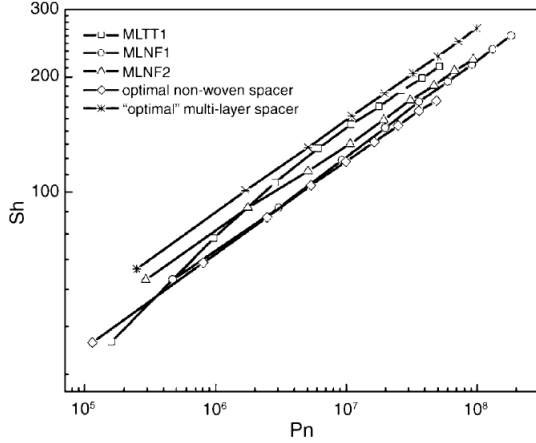
Figure 6.7: Performance of the novel spacer developed in Li et al. [83]

The MLNF spacer from Li et al. [83] does not perform much better than the conventional spacer, however the MLTT in a multi-layer configuration (fig. 6.8) provides promising performances with a Sherwood number (mixing indicator, see section 6.1) 30% higher than that of the conventional spacer at the same pressure drop, and the pressure drop is only 40% higher at the same average Sherwood number (fig. 6.7).

Apart from the net-type geometry, Liu et al. [65] developed a new spacer geometry for spiral wound membrane distillation module (fig. 6.9).
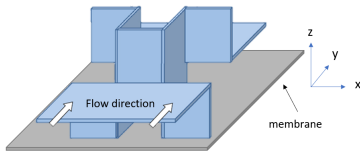
Figure 6.9: Geometry of the novel spacer developed in Liu et al. [65]
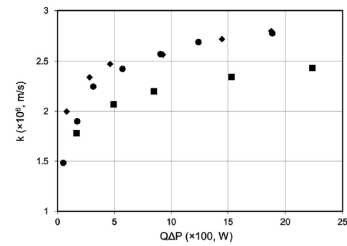
Figure 6.10: Performance of the new spacer developed in Liu et al. [65] circle: conventional spacer; diamond: 13 equally spaced spacer 1 element; square: 1 equally spaced spacer 2 elements

As can be seen in fig. 6.10 presenting the mass transfer coefficient (mixing indicator, see section 6.1) as a function of pressure drop for different spacer geometries, the new spacer geometry provides slightly better mass transfer coefficient k ($< 10\%$) than conventional spacers at a given pressure drop (fig. 6.10) only for low pressure drops.

Thanks to the new possibilities offered by 3D printing or fused deposition modeling [131], Thomas et al. ([149], [28]) presented innovative spacer designs based on triply periodic minimal surfaces, which are

mathematical surfaces known for their ability to minimize dead zone and provide the smoothest possible flow.

Chernyshov et al. [30] proposed a spacer analysis in an AGMD prototype, calculating both the mass flux through the membrane (F) and the pressure drop ($\Delta P/L$, with ΔP the pressure variation over a module length L), and defining a spacer efficiency as the ratio between both: $E = \frac{F}{\Delta P/L}$. Two geometries of the net-type are studied, one with cylindrical fibers and one with woven fibers, in different configurations (fig. 6.11, bottom).

Most of the spacers studied in Chernyshov et al. [30] do increase the transmembrane flux, as well as the pressure drop (fig. 6.11).

Spacer	Flow/fibers angle, χ	Fibers angle, ω	Spacer type	Fiber type	Thickness mm	Distance between fibers l_1 mm
1	120	30	Non-woven	circular	4	14
2	90	45	Non-woven	twisted-tape	4	14
3	90	45	Non-woven	circular	4	14
4	90	45	Woven	circular	4	14
5	120	30	Non-woven	twisted tape	4	14
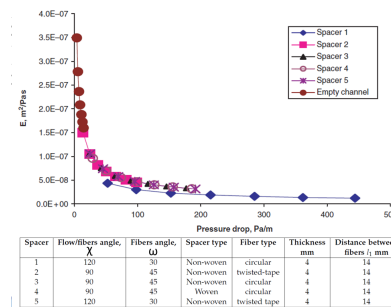
Figure 6.11: Spacer efficiency of different spacer configurations [30]

As a result, a channel without spacer is always the most energy efficient, despite the fact that it also provides the least permeate flux (fig. 6.11).

The underlying question appears to be whether a larger membrane surface without spacers or a smaller membrane surface with spacers and increased pumping consumption is more efficient and sustainable at similar permeate flux. The answer to this question depends on the price and sustainability of a membrane distillation module production, and on the prices and types of the energy sources. For instance, depending on the costs of producing desalination cells in comparison to the cost of consumed energy, a smaller module with a higher flux and a spacer may be more suitable.

To resolve this challenges, new spacers geometries can be numerically studied to reduce the pressure drop produced by spacers.

6.2.2 Industrial mixing strategies

Two main technical solutions are employed in industry for substance mixing: dynamic mixing and static mixing.

Dynamic mixing requires the use of energy, and is based in most cases on revolving blades. Static Mixing (SM) relies solely on static elements in the water channel to separate, twist, and recombine streams [135].

A turbulent flow would ordinarily be sufficient to induce adequate mixing, but the induced swirls lose energy through friction, which is measured as pressure drop. In a laminar flow, SM can boost mixing and reduce energy loss in turbulent mixing.

Flows can be described as either shear flow, where adjacent layers of fluid move parallel to each other with different speeds, or extensional flow, in which the volume of a fluid element stays constant [43]. A shear flow would spend more energy than an extensional flow with comparable mixing results [49].

As a result, SM devices aim to provide the most extensional flow feasible in order to reduce energy usage. Several shapes have already been investigated to enhance mixing with less power consumption in cylindrical pipes (fig. 6.12). The flow is thus parallel to the longest dimension of these elements.
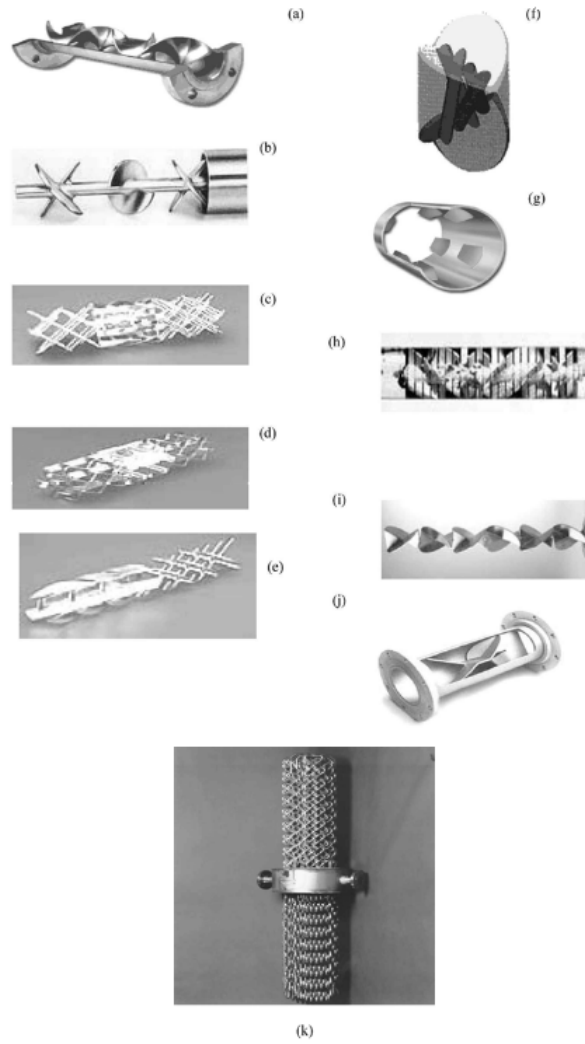
Figure 6.12: Main industrial mixers geometries [147] a) Kenics (Chemincer Inc.); b) low pressure drop LPD (Ross Engineering Inc.); c) SMV (Koch-Glitsch Inc.); d) SMX (Koch-Glitsch Inc.); e) SMLX (Koch-Glitsch Inc.); f)Interfacial Surface Generator ISG (Ross Engineering Inc.); g) HEV (Chemincer Inc.); h) Inliner series 50 (Lightnin Inc.); i) Inliner series 45 (Lightnin Inc.); j) Custody transfer mixer (Komax system Inc.); k) SMR (Koch-Glitsch Inc.)

The performances of some of these spacers are compiled in table 6.1 [147]:

Name of geometry	Z	P_n vendor	P_n literature	P_n CFD
Kenics (fig. 6.12 a)	-	170	195	255
LPD (fig. 6.12 b)	6	195	220	225
SMV (fig. 6.12 c)	60-300	-	-	-
ISG (fig. 6.12 f)	250-300	7210	8140	8460
Inliner (fig. 6.12 h,i)	9	240	270	300

Table 6.1: Comparison of pressure drop of different static mixers [147]

Mixers Kenics and LPD appear as the best performers, producing the smallest pressure drops.

Armbruster et al. [14] experimented a Kenics mixer geometry (from industry) along with 8 other twisted tape geometries, applied to MD in order to reduce fouling.

6.2.3 Conclusion on state of the art of mixing

Based on the performance of all the spacers and mixers shapes proposed (table 6.1), the geometry of the twisted tab and of the Kenics (fig. 6.12 a) and LPD mixers (fig. 6.12 b) (fig. 6.13) are used in this research work as an inspiration to design new spacers geometry for membrane distillation.
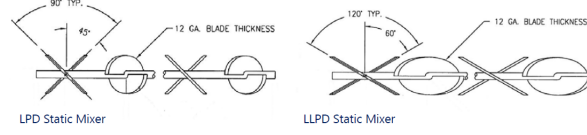
Figure 6.13: Low pressure drop (LPD) industrial static mixer (Ross and Son Company)

6.3 Proposed new spacer geometries

The first proposed geometry for numerical study in this work is a spiral (*spiral*, fig. 6.14 d) of voidage $\epsilon_{m,spiral} = 0.948$ inspired from the twisted tab and the Kenics mixer (as well as from nature tornado and whirlpool shapes), making the best energy use to increase water mixing. It can also be seen as an evolution of the best spacer performer identified in the spacer literature review (the twisted-tape), or of the Kenics mixer providing one the best pressure drop performances according to the mixer literature review.

The second geometry is based on industrial SM LPD design (Ross and Son Company) that was identified as producing the least pressure drops in the industrial sector static mixer review: a mixer (*mixer*) of voidage $\epsilon_{m,mixer} = 0.939$.
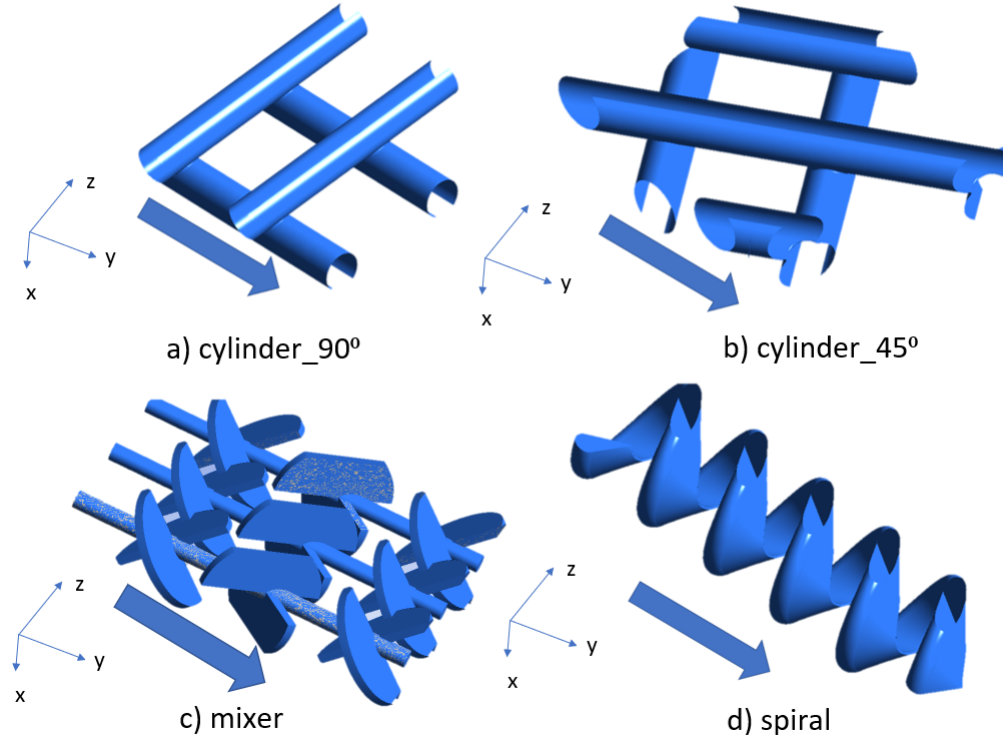
Figure 6.14: Geometry of the simulated spacers

To benchmark the performance of new spacer designs, a conventional standard spacer is defined as a net made of cylindrical fibers. Two configurations are tested based on the literature [38]: one where the fibers are parallel and perpendicular to the flow, $\Xi = 90°$ (*cylinder 90°*, fig. 6.14 a)), and one where

they are 45 °from the flow $\Xi = 45°$ (*cylinder 45°*, fig. 6.14 b)) and 90°between the fibers. The voidage of these two net-type spacers is $\epsilon_{m,cylinder} = 0.730$.

The thicknesses δ^s of all these spacers are equal, $\delta^s = 5mm$ such that it fills the hot water channel simulated. This is the normal layout for AGMD modules that use spacers for support.

A reference case is also simulated for comparison, with an empty channel.

The specifics of a spacer design's execution have an impact on its performance. A spiral geometry was chosen to examine this effect, and several variations of it were created (see table 6.2).

Spacer name	l_1 (mm)	l_2 (mm)	Number of turn
spiral	1.5	1.5	5
spiralb	1.5	1.5	3
spiralc	1.5	1.5	4
spirald	2	1.5	5
spirale	2.5	1.5	5

Table 6.2: spiral geometry parameters
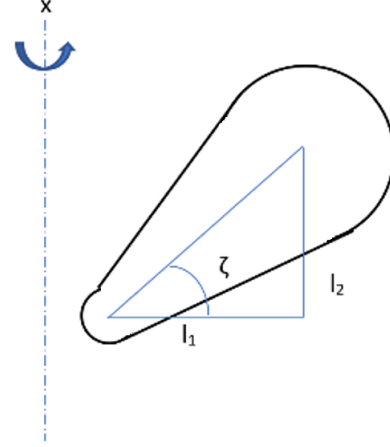
Figure 6.15: Cross section of the spiral geometry

Geometries *spiralb* and *spiralc* were produced to investigate the impact of the pitch of the spiral by varying the number of turns over the domain length. Geometries *spirald* and *spirale* were produced to evaluate the impact of spiral walls steepness by cross-section modification (as the ratio of l_2/l_1 grows, the spiral wall becomes steeper in an attempt to smooth the flow) (fig. 6.15).

6.4 Spacers simulations parameters

All the spacer geometries presented above (*cylinder 90°*, *cylinder 45°*, *mixer*, *spiral* and *empty* as well as the spiral variations *spiralb*, *spiralc*, *spirald* and *spirale*) are numerically simulated using a set of identical boundary conditions ($V_{in} = 0.01, 0.05, 0.1, 0.25m.s^{-1}$) in a 0.02*0.02*0.005m water channel until convergence is achieved. The height of this channel is chosen to reproduce standard hot water channels in MD. The volume length and width are chosen to be able to simulate at least 2 fibers in each direction for both of the conventional spacers, and 3 elements in each direction for the mixer spacer, assumed as minimum representative characteristic elements of each geometry. The observed Reynolds number did not exceed 125, confirming the laminar flow regime in the calculation domain.

Due to the 3DH&MT model's limitations presented in section 5.3.3, and in particular its non ability to handle non structured meshes indispensable for the two novel spacer geometries proposed, Ansys Fluent version 2022 R1 is used for the CFD simulations.

In particular, the spacers' meshes were produced using Fluent Meshing package, and a mesh independence study was conducted (table 6.3) for all used geometries to ensure that sufficient mesh resolution was used.

Geometry	Cell number	Pressure drop (Pa)
Cylinder 90°	478622	16.35
Cylinder 90°	868620	11.71
Cylinder 90°	1980593	10.90
Cylinder 45°	125241	5.06
Cylinder 45°	252066	4.37
Cylinder 45°	1153507	5.27
Mixer	204450	12.79
Mixer	984239	12.27
Mixer	445063	12.29
Spiral	793270	2.82
Spiral	848822	2.61
Spiral	1512296	2.60

Table 6.3: Results of the mesh independence analysis

Due to the current reserve on the ongoing evaporation theoretical models (section 3.3), evaporation was not simulated (energy equation was disabled).

As the temperature polarization at the membrane is most relevant in the context of MD, the thermal boundary layer thickness is an important indicator. As the conducted simulations are adiabatic it was not possible to observe it directly. Therefore, the formation of velocity boundary layer is observed as a proxy. To assess this, the mean velocity (Vp) perpendicular to the membrane (along z axis) in a plane (x, y) located 0.1mm from the membrane has also been used in this work. Indeed, if the flow presents a high Vp, it indicates that the surface water is renewed by hotter water from the bulk phase, decreasing the temperature gradient.

To assess the mixing performance of the novel spacer geometries, the CoV was preferred over the Sherwood number. Indeed, in the case of the novel spacers geometries analyzed in this work, the discretization in a series of rectangular block as proposed by Shrivstava to adapt Lévêque equation for Sherwood number calculation seems quite hazardous, as the induced velocity fields are three-dimensional. Therefore, in this work, the CoV will be used as a mixing quality indicator, simple to calculate from numerically obtained results. In order to reproduce the temperature layering occurring in the hot water channel due to heat losses, the inlet surface of the simulation domain has been divided into two equal parts in the horizontal direction (fig. 6.16). A species transport model with volume-weighted mixing law is then setup in order to enable the introduction of two liquids in each of these inlets. The liquids introduced are parametered to have identical physical properties as water, and same inlet velocity. One is named water and the other dye, which is used as a mixing tracer enabling the calculation of CoV.

In this setup, the CoV previously presented in equation 6.1 could produce misleadingly low values even if the dye would not reach the sampled plane. In this scenario each sampled concentration value would be equal to the plane mean concentration, incorrectly indicating good mixing performance. Rather than calculating the difference between the sample dye concentration and the actual plane mean, a value of 0.5 is used in place of the mean, which would indicate perfect mixing as follows:

$$CoV = \sqrt{\frac{\sum_{i=1}^{N}(Y_i - 0.5)^2}{N-1}} \frac{1}{0.5} \qquad (6.2)$$

The friction generation indicator selected for this work is the pressure drop between two planes of the simulated volume.

At the outlet a pressure outlet boundary condition is set (gauge pressure=0), and the remaining surfaces were defined as wall boundary condition (no slip).
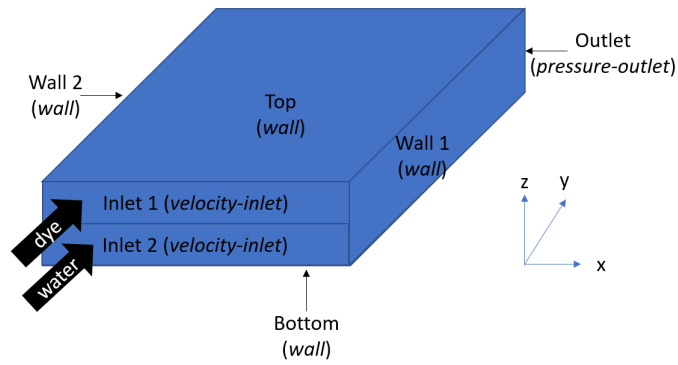
Figure 6.16: View of the simulated volume with the two inlets (dye ad water) for CoV calculation

Since calculation is adiabatic and both liquids introduced into the domain had the same density, gravity was not considered in the calculation.

6.5   Conclusion on the spacer study settings

After review of the mixing literature in different domains, two novel spacer geometries are proposed for study, and the numerical framework is described.

Conclusion of part II: selected working materials

As hinted in the first part, the way to improve both energy efficiency and permeate flow of AGMD modules is to reduce the energy transfer resistances through the boundary layers building up in the hot water channel, and the mass transfer resistance through the air-gap.

To understand better these resistances and find ways to optimize the AGMD performances, a test facility enabling the measurement of the permeate output as well as the continuous temperature and concentration profile at the membrane interface thanks to a two-wavelength Schlieren method (to be coupled with an Interferometry set-up in a second step) for different operating parameters is designed.

To act against these resistances, state-of-the-art spacers and industrial mixing strategies gave inspiration for novel spacer geometries to investigate.

Part III

Results and discussion

Highlights from Part III

A test facility allowing for the measurement of continuous temperature profiles and boundary layer thickness while varying the hot and cold inlet temperatures and the inlet flow is set up, and an AGMD module allowing for the use of this test facility is built.
Various operational and geometrical configurations can be tested using this boundary layer measurement test bench.

First temperature profiles, boundary layers thicknesses and permeate flows measurements are conducted, and compared to the 3DH&MT model with promising results.

Two novel spacer geometries and new mixing performance indicators for 3D geometries are proposed to enhance the mixing in the hot water channel and improve the energy efficiency and permeate outflow of AGMD.

Chapter 7

Test facility description

As specified in section 5, the test facility is an important tool to increase the understanding of AGMD limitations, and contribute to its performances improvement. The implementation of the three main parts of the set-up is detailed in this section: the general set-up allowing for the water treatment; the distillation module and the polarization observation method (fig. 7.1).
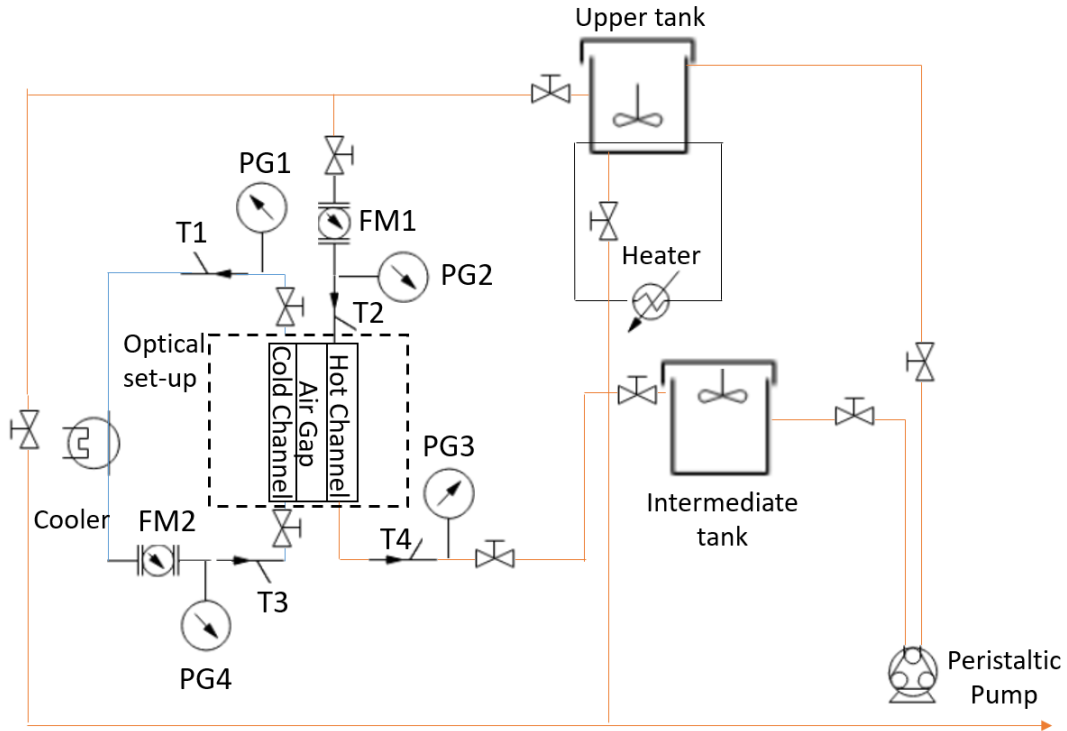
Figure 7.1: Representation of the Process and Instrumentation Diagram: temperature sensors (T), pressure gauges (PG), and flow direction (arrows)

The temperature sensors measurements are used to determine the heat losses. The pressure gauges are here to make sure the liquid entry pressure is not exceeded in the circuit.

7.1 Distillation process

The distillation process relies on the interaction between a hot water stream and a cold source.

7.1.1   Circuit

7.1.1.1   Fluid circulation

To circulate the fluid, a pump is used.

The centrifugal pumps available at the University of Luxembourg are creating vibrations imperceptible at first, but clearly visible on the Schlieren pictures.

One of the ideas evoked to dampen the vibrations is to use an intermediate closed tank. In theory, due to mass conservation and non compressibility of both air and water, the closed tank inlet water flow is the outlet water flow, and the small compressibility of the air dampens the pump vibrations. However, as hot water circulates, the heated air increases the pressure inside the tank (and thus the output flux), making it difficult to regulate the flux. Moreover, the closed tank in metal loses a lot of heat.

An alternative to remove the impact of vibrations is to add a tank at a higher position, alimented by the pump, feeding the rest of the circuit by gravity.

The height needed to feed the circuit by gravity is calculated from the pressure drop created in the circuit by the linear and singular pressure losses in the circuit, and the diameter of the output of the tank. The result of the calculation gives that a tank filled with 20cm high of water and a 1cm inner diameter output should be placed several meters (2-4m) above the main circuit for the required flows (0.5-2l/min). However the centrifugal pumps are not powerful enough to lift the intermediate tank to such height.

An alternative is to use a peristaltic pump: a flexible tubing is compressed between rolls in the pump head, forming packets of fluid sent to the circuit. The flow rate of the fluid is thus determined by the volume of the fluid packets and the frequency at which they are sent to the circuit. This pump can be set to send fluxes from $0.001l.min^{-1}$ to $18l.min^{-1}$ depending on the pump head and tubing options.

The advantage of such a pump is that there is no contact between the inside of the pump and the fluid: only the tubing is filled with the fluid. Thus, there is no contamination of the fluid and no risk of corroding of the pump, and more important, no risk of cavitation.

As this pump also creates vibration waves interacting with the sensors and invalidating the data, it is used in combination with a tank placed in heights.

Figure 7.2: Photo of the Peristaltic Pump

The fluid flow in the circuit can be controlled by the height of the tank (which could be adjusted with a motor), the water height inside the tank and a 1/4 valve adjusting the outflow of the tank. The pump flow must be adjusted very carefully so that the water level in the tank placed in heights, and hence the output flow, remains stable.

An alternative to this strenuous regulation is to put the heater tank on the top, and make sure that the intermediate tank, located at the module's height, stays always almost empty by imposing on the pump a higher flow than the module's output flow. As the pump is peristaltic, it does not risk to pump in a vacuum. This way, the water level of the tank placed in heights stays constant (apart from the

evaporated water), hence the feed flow of the module is constant. Moreover the heat losses are reduced as the overall pipe length between the heater tank and the module is halved.

Additionally, in order to reduce the vibrations, the inlet tube must not touch the tank placed in heights.

During the course of experiments, the water flow in the circuit was observed to be diminishing, because of the accumulation of air in the pipes, trapped in two main locations (at elbows, in local maxima). Valves were added in these local maxima, in order to be able to remove air bubbles regularly when the flow is stopped (if the flow is running, the bubbles remain stuck). Thus long measurement (over 15-30min) are not an option. This phenomenon is due to the fact that the solubility of air in water increases as the temperature of the water decreases. Thus, it happens regularly because at some point in the circuit the water gets colder thus imprisoning more air, before being reheated. So maybe a better heat insulation would reduce the apparition of the bubbles.

7.1.1.2 Heating and cooling

To maintain the temperature in the hot channel, a heater from Julabo (SL) is used. The heater heats a specific liquid (H20S) circulating in a coil at the bottom of the heater tank.

A Julabo cooler (F32) maintains the temperature in the cold channel by directly cooling the water.

7.1.2 Heat losses

To reduce heat losses through the different elements of the circuit, at the origin of a varying temperature of the inlet hot feed flow during the measurements, of a huge offset between the order given to the heater and the actual hot feed temperature, and a slowing inlet flow during measurement (section 7.2.5), all the pipes, the heater tank and the module are encased in insulating foam, which seems to be somehow efficient (fig. 7.3) as the tubes with foam (in gray in the left picture) appear slightly darker on the IR picture than the bare pipes (in pink in the left picture).
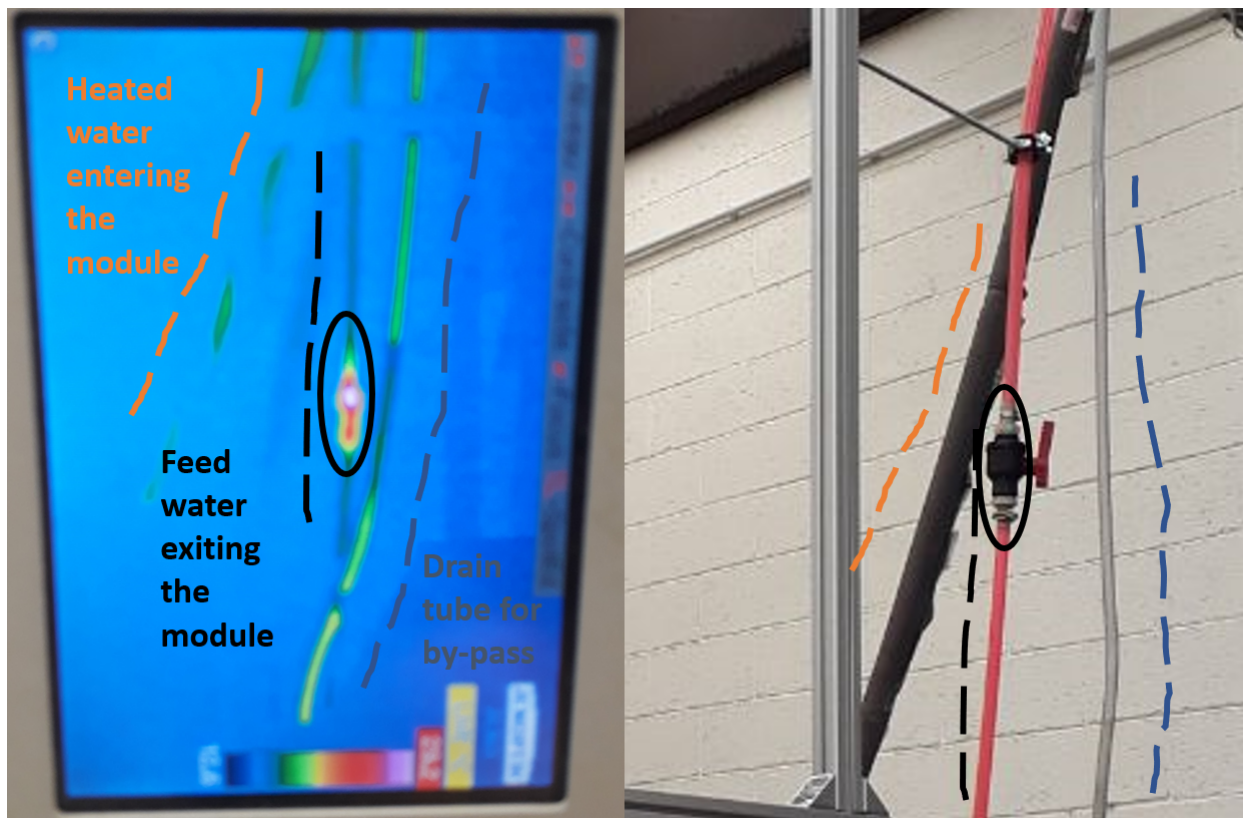
Figure 7.3: Infra-Red picture of the tubing

Additionally, the circuit's length is reduced to a minimum to lower these heat losses.

Heat losses are also increased as the inlet flow decreases (as the residential time in the pipes increases), so the temperature range of the experiments is limited by this constraint.

Fig. 7.4 is an infra red picture of the module during measurements.
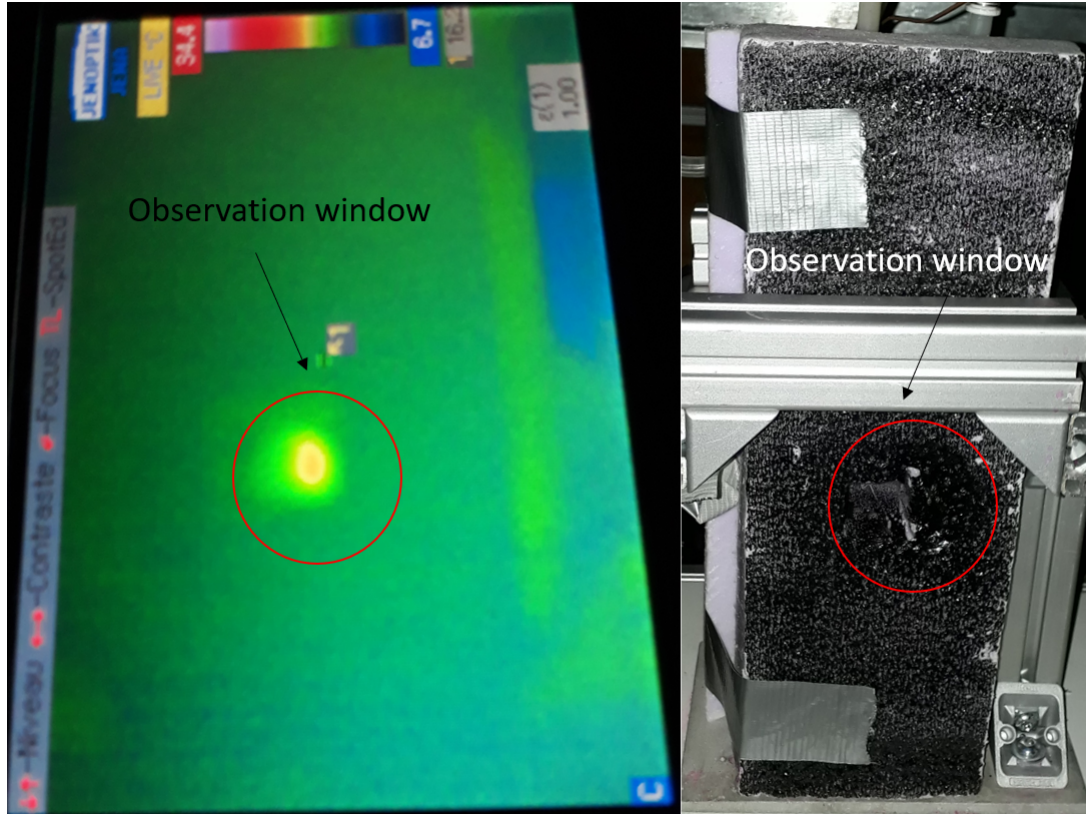
Figure 7.4: Infrared picture of the module

The bright point on fig. 7.4 is the window of the module: apart from this location, the heat losses seam reasonable around the module.

A comparison of the heat losses from the hot water to the heat gains of the cold water for different experimental conditions was attempted. However, the flow of the coolant is not known: the cooler user manual provides the flow at 0 bar (11-16l/min) and the maximal pressure without flow (0.22-0.45 bar). A rough estimation evaluates the cooling circuit's pressure drops (linear and singular) to between 0.27 to 0.5 bars, which makes it impossible to have a precise enough value for the coolant flow. However, the coolant flow necessary to absorb the heat losses of the hot water (cold flow*) is not unlikely (see table 7.1). It is possible that all the heat losses of the hot water are transferred to the cold water.

Horodate	T_{in}^h (°C)	T_{out}^h (°C)	T_{in}^c (°C)	T_{out}^c (°C)	Hot flow (kg/s)	Cold flow* (kg/s)
17/12/2021 16:59	73.08	66.58	15.45	15.86	$3.05.10^{-6}$	$4.8.10^{-5}$
21/12/2021 19:53	74.66	70.81	17.11	15.8	$5.73.10^{-6}$	$1.68.10^{-5}$
21/12/2021 20:52	75.32	72.09	17.11	15.88	$6.85.10^{-6}$	$1.8.10^{-5}$
21/12/2021 21:14	75.9	73.03	17.11	15.88	$8.1.10^{-6}$	$1.89.10^{-5}$
22/12/2021 17:24	73.14	70.09	17.12	15.91	$7.9.10^{-6}$	2.10^{-5}
22/12/2021 18:22	73.19	69.87	17.17	15.93	$7.71.10^{-6}$	$2.06.10^{-5}$
22/12/2021 19:50	72.3	69.42	17.15	15.85	$6.79.10^{-6}$	$1.5.10^{-5}$
23/12/2021 18:45	59.42	56.56	16.65	15.63	$6.71.10^{-6}$	$1.88.10^{-5}$
23/12/2021 19:37	59.65	57.22	16.66	15.57	$7.42.10^{-6}$	$1.65.10^{-5}$

Table 7.1: Comparison of heat losses and gains

7.1.3 Monitoring

Apart from the Schlieren observation method, the circuit is monitored for bulk inlet and outlet coolant and feed temperature as well as flow and pressure in the circuit needed for a good monitoring of the circuit (see fig. 7.1).

After a first idea implying an Arduino, following the technical team advices, a NI system of data collection is preferred: the pressure sensors are PXM309-002G10V from Omega, and the temperature sensors are T-G1/4-1-T-3 from Omega. They are read with NI cards NI 9219.

7.2 Air-Gap Membrane-Distillation module

To be able to operate the selected Schlieren set-up, the AGMD module must allow light to pass through the hot water channel and the air-gap. Moreover, because the temperature gradient at the membrane interface is critical for model validation, the module should allow for close monitoring of the membrane. Typically, a 1mm thick membrane support is not an option, which complicates the design and manufacturing of the AGMD module.

7.2.1 General characteristics

An initial AGMD module available from previous research work was first used and allowed to determine the required general characteristics.

This initial module (fig. 7.5) is a round and flat-panel air-gap module where the temperature of the inlet and outlet flow can be monitored, as well as the flow rate and the salinity. However there is no direct neither indirect access to the inside of this module, and the air-gap size can not be adjusted.
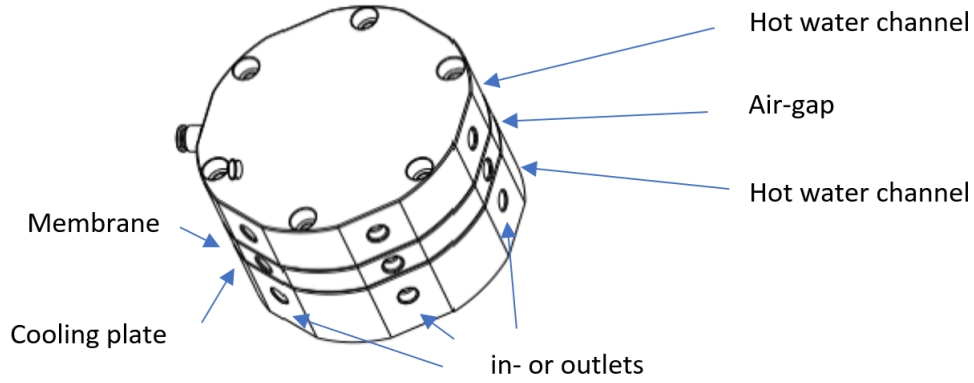
Figure 7.5: Sketch of the initial AGMD module

Based on the first experiments carried with this initial module, on experiences reported in the literature, and on the requirements for the Schlieren experiment, a list of features required in a new version of the module is made:

- **Insulation**: in order to limit the external temperature losses, and have a better estimation of the heat efficiency of the process
- **Uniform flow**: a good repartition of the inlet and outlet flows is important to have the most uniform flow inside the membrane and thus the less boundary phenomenon (section 7.2.1.2)
- **Orientation**: to be able to observe the behavior of the process with horizontal or vertical layers, or even upside-down.
- **Slope**: adding a slope to the feed flow could be considered in order to improve the efficiency [62]
- **Spacers**: assessing the effect of different spacer designs on the flow and performance of the module could reduce the temperature polarization and hence improve the efficiency of the process [29]
- **Transparency**: indispensable for boundary layer visualization, and also to have a sense of the flow regime of the condensing fluid on the coolant plate (droplets, flowing flux, air-gap filled with water...), and also for boundary layer visualization
- **Adjustable Air-gap thickness**: see section 7.2.1.1
- **Low T-deformation**: no deformation with temperature would be appreciated

7.2.1.1 Air-gap thickness

The wider the air-gap the higher the mass resistance hence the lower the permeate flux [22].

Moreover, depending on the geometry, convection can appear or not, which can impact the overall energy efficiency of the process. Thus an adjustable air-gap height is appreciable.

7.2.1.2 Dimensions

According to the MATLAB ray-tracing simulation, simulating the path of light rays across the module (section 7.4), to allow the ray observable by the camera closest to the membrane to exit the module, it should not be wider than 0.01m.

The module length should be such that the fully developed thermal and hydraulic conditions are reached in the module, so that the experimentation are consistent with industrial steady state operating conditions.

In order to be able to conduct experiments in laminar conditions, for this module width ($W = 0.01m$), at the velocities implemented in the 3DH&MT model ($0.1m.s^{-1}$, $0.5m.s^{-1}$, $0.025m.s^{-1}$), the thermal and hydrodynamic inlet lengths required to reach a laminar regime is consequent ($0.817m$ for $0.1m.s^{-1}$ to have $Re = 2000$) [120].

These criteria also allow to determine the maximum height of the hot channel required to stay in the laminar regime: it increases as the velocity decreases hence the height is fixed to 5mm, the minimum of these maximum heights (obtained for an inlet velocity of $0.1m.s^{-1}$).

By numerically solving Navier-Stokes equations for this $0.01m*0.005m$ channel, the steady state profile of the flow can be found (fig. 7.6), and an entry device designed, in order to help reach this steady state profile faster (hence reducing the entry length).
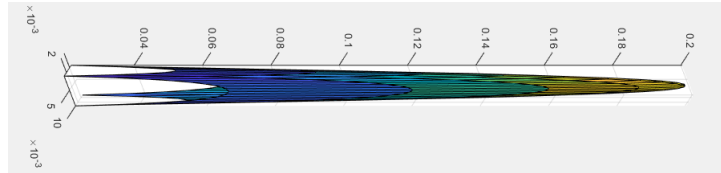
Figure 7.6: Steady state profile inside a $0.01*0.005m$

7.2.2 Construction

Before reaching the final version of the module, several drafts were manufactured and experimented, from which lessons in terms of materials and designs, were learned for the final version of the module.

7.2.2.1 First module drafts

The first module focused on allowing a uniform flow in a temperature isolated module. Several 3-parts (hot channel, air-gap, cold channel) prototypes were 3D-printed using a laser polymerized resin method (fig. 7.7). From these prototypes the lessons learned were to tighten the three parts thanks to screws, and that the module should present outside devices to plug the tubing on to ensure sealing (threads were difficult to print).

Figure 7.7: First trials of 3D printed modules

As the *transparent* resin was actually more translucent than transparent, and thus not suitable for Schlieren measurements, poly-carbonate windows were integrated on the sides of the hot and cold channel, and of the air-gap to allow observation (fig. 7.8).

Figure 7.8: Transparent resin module with enclosed poly-carbonate side-windows

However, leakage occurred at the resin-poly-carbonate junction. Moreover due to the size of the module, the 3-D printing parts presented deformations due to gravity effect during the printing process, impacting the water tightness of the module.

To ensure flat surfaces and improve water tightness, a new module was made of an assembly of poly-carbonate sheets (fig. 7.9).
Due to the fact that the thickness of the material is significantly larger than the laser's focus point, laser cutting does not offer straight cuts; therefore, a cutting method utilizing a drill bit is preferred.
The gluing of the parts still did not provide a sufficient precision to ensure a good water-tightness.
Moreover, an all transparent module is not compatible with an optical method where light reflection should be avoided not to pollute the the optical measurement.

Figure 7.9: Module made of an assembly of poly-carbonate parts

7.2.2.2 Final module

Plastic was chosen for the module material for the first drafts, as high temperatures are at stake in AGMD: an insulating material seemed more relevant.
As the previous attempts with this material did not prove conclusive due to leakages and sometimes breakage, an inox module with transparent windows is considered to palliate the water tightness issues.

As Kroiss et al. [163] from Technical University of Munich had to design a similar module for reverse osmosis compatible with optical measurements (figs. 7.10 and 7.11), inspiration was drawn from their design.

(a) The new membrane test cell. (b) Exploded assembly drawing of the new membrane test cell.
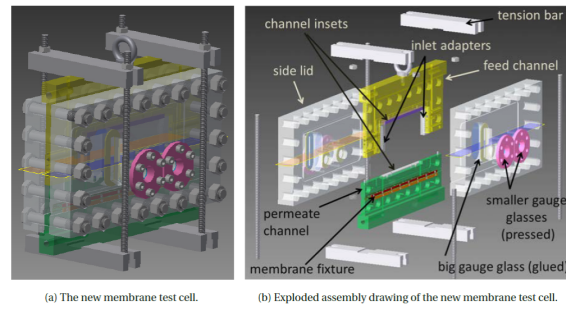
Figure 7.10: General view of the TUM module [163]
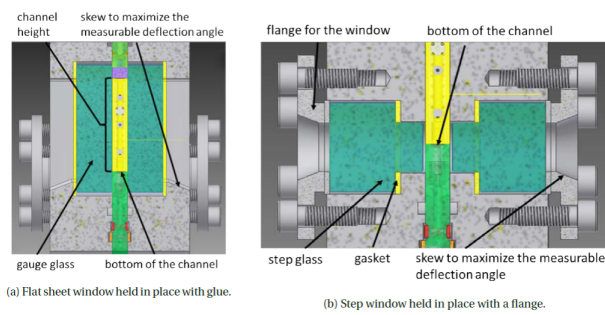
(a)
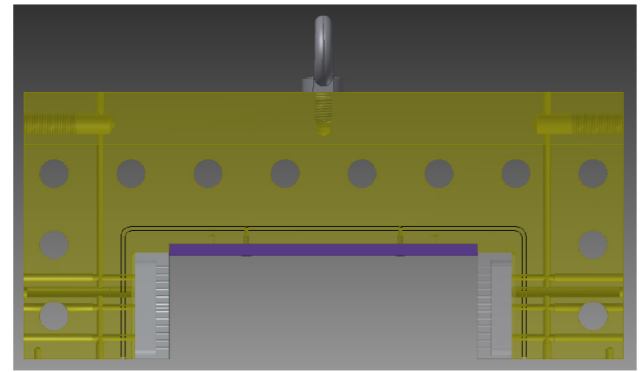
(b)

Figure 7.11: observation windows (a) and hot water feed channel of the TUM module (b) [163]

Here is thus the final AGMD module, inspired from Kroiss design (figs. 7.12) and built in partnership with a local steel manufacturer:
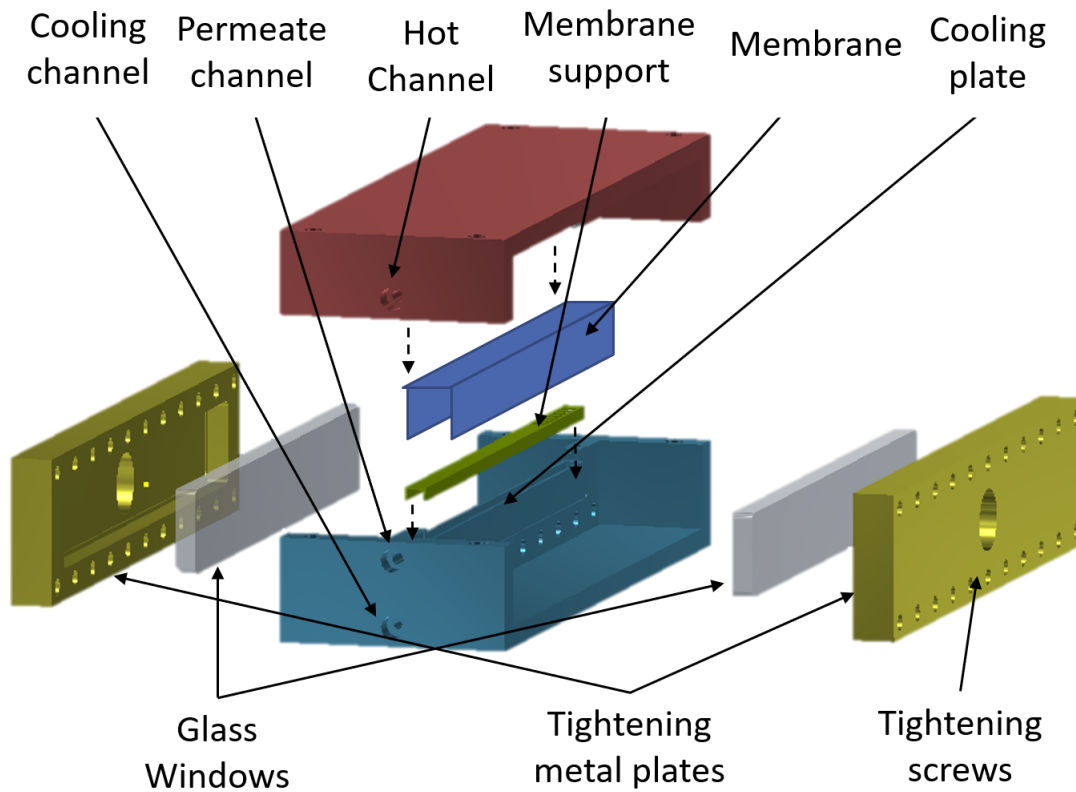
Figure 7.12: Design and components of the module inspired from Kroiss' module

The module is composed as a double sandwich. Vertically are assembled a hot part, a membrane support, and a cold part also encompassing the air-gap in order to reduce the leaks issue (fig. 7.13). The air-gap height can be modified eventually by adding some metal sheets at the cold channel wall.
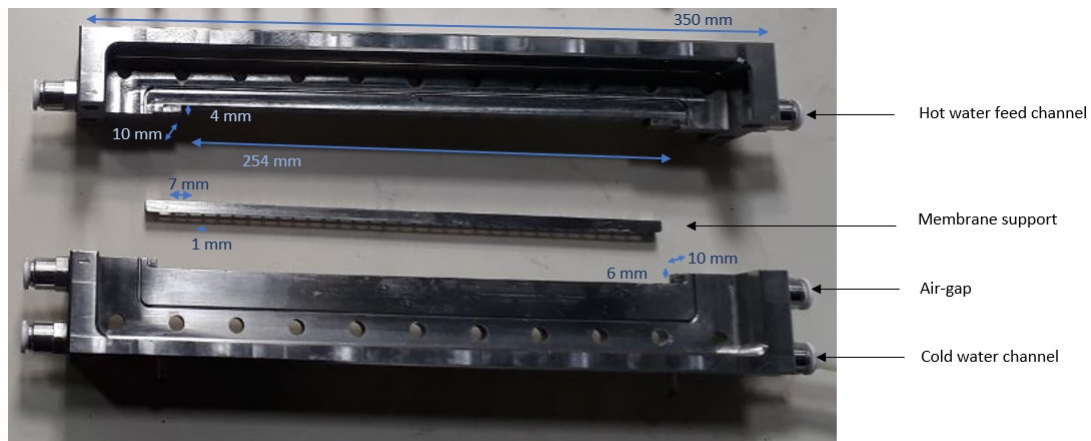
Figure 7.13: Picture of the three vertical elements of the AGMD module: hot water channel, membrane support, cold part, from top to bottom

The hot water feed channel in the hot part has no wall. The cold water channel in the cold part is totally encased in the part, and topped by the air-gap channel devoid of wall. The membrane support forms the walls of the air-gap (fig. 7.14, top).
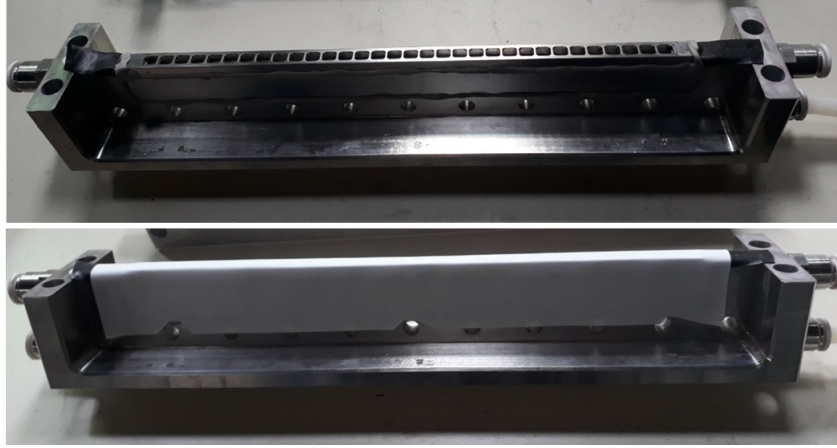
Figure 7.14: Membrane support on top of the air-gap

The membrane is wrapped around the membrane support thanks to plumber's putty (see section 7.2.3 and fig. 7.14, bottom).

The poly-carbonate windows and their inox covers, painted in black to reduce light reflection, are mounted on both sides of the module (fig. 7.15 and 7.16).

Figure 7.15: Module's windows and covers
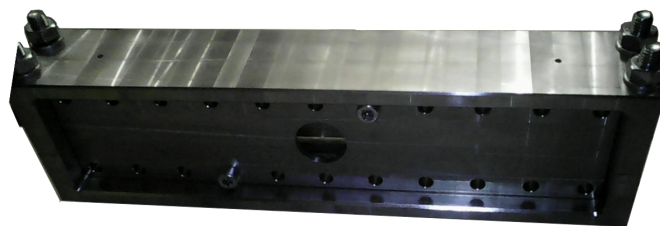
Figure 7.16: Picture of the module inspired from Kroiss' module

7.2.3   Sealing materials

Several sealing materials were tried to ensure the water tightness of the module: silicon destroys the membrane and is not reusable; rubbers of different thicknesses and O-rings are not strong enough to hold the required pressure; plumber's putty is finally the selected solution.

Figure 7.17: Plumber putty applied on the hot and cold parts of the AGMD module

7.2.4   Permeate film

Due to surface tension (see section G.2.3) , the water film building up on the cold plate of the air-gap channel material, in the configuration where the hot channel is at the bottom ,is between 2 and 4mm thick. Due to capillary forces in the outlet pipe, this film can accumulate even thicker inside the air-gap channel.

Consequently, the actual thickness of the air layer in the air-gap is thinner than the actual air-gap size, and might even be nonexistent in case of flooding of the air-gap. This has to be taken into account when comparing experimental results to theoretical results, as the water film is set to 0.5mm in the 3DH&MT model.

In the final module, the air-gap outputs size is on the order of magnitude of the water capillary length, leading to flooding of the air-gap before the permeate flow can exit. Thus the module has to be used vertically so that the gravity forces compensate the capillary forces and the permeate flow can go out before filling up the air-gap.

7.2.5   Input flow

To maintain constant contact between the water and the membrane, the hot water channel must be loaded, thus the inlet and outflow flows must be equalized via valves.

When the module is used vertically, the difference in height between the inlet and outlet of the hot channel generates a natural flow through the hot channel. If the pressure drop from friction against the walls does not compensate for this height variation, then the hot channel is not completely filled with water because the incoming flow is lower than the flow generated by gravity. The only way to get around this problem is to control the outflow of the hot channel.

7.3   Schlieren set-up

The Schlieren method is a versatile observation method whose different parameters can be tuned in order to suit the resolution expectations and the various physical constraints of the experiment.

7.3.1   Schlieren configurations and optical limitations

Schlieren set-ups can take mainly two configurations: aligned with lenses, or in Z with mirrors (fig. 7.18).
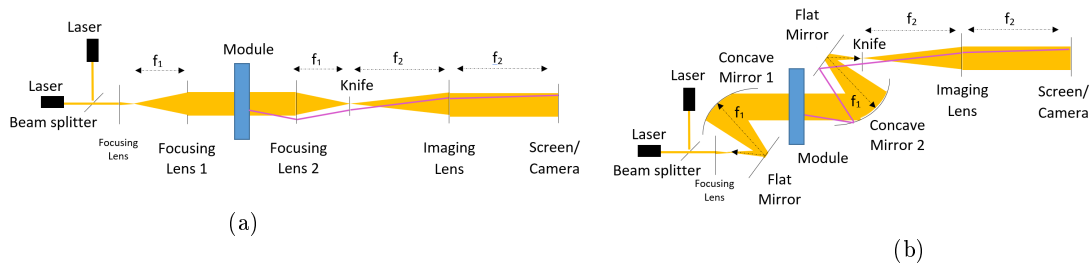
Figure 7.18: Aligned (a) and Z- (b) Schlieren Configurations (in purple a deflected ray)

Both set-ups have their pros and cons: lenses are generally more expensive than mirrors of the same size due to the fact that they require two optical surfaces to be manufactured. Lens systems require more space in length than mirror systems. Lens systems can suffer achromatism, whereas mirror systems are subject to coma and astigmatism [71].

For space reason, and to control the light atmosphere more easily by encasing the whole set-up in a black box, the Z-configuration is chosen.

Hence the set-ups will be the following (fig. 7.19):

(a)

(b)
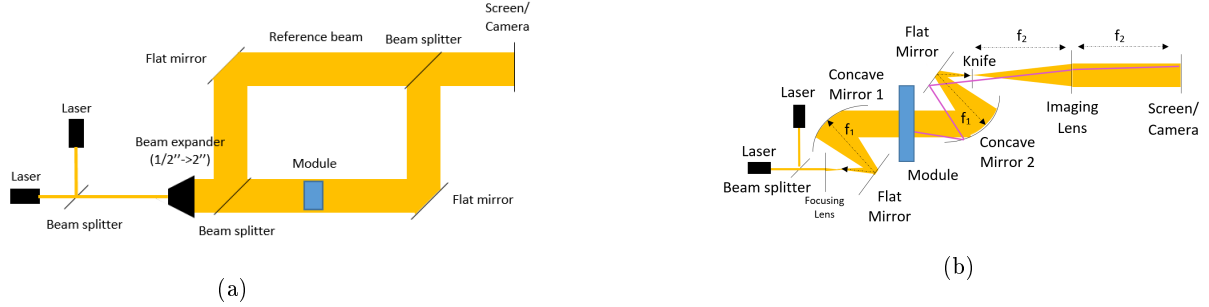
Figure 7.19: Interferometry (a) and Z-Schlieren (b) configurations

7.3.2 Instrumentation and optics

The different equipment (among which the laser wavelengths) of the Z-Schlieren configuration were chosen according to the choice (see section 5.2.1.5) of coupling three polarization measurement methods: two wavelengths Schlieren, two wavelengths Interferometry and dyes.

However, in the course of experiments, the dye and optical methods appeared incompatible as the dye method requires the absorption of the light by the dye, whereas the optical methods need the light to cross the module.

Moreover, the Interferometry set-up could not be experimented. Hence the results presented in this work are only based on Schlieren method.

This paragraph intends to list the optical equipment required for Z-Schlieren method and detail their functioning as well as characteristics. The detailed list can be found in section F.

7.3.2.1 Optics

The lenses are chosen as achromatic doublets, focusing the rays of two specific wavelengths on one point [45].

One of the most significant aberrations that mirrors might suffer is spherical aberration[1]. This occurs primarily at the mirror's borders, thus wider mirrors than necessary are picked. As the channel to observe is 5mm thick, and a magnification factor of the optical set-up bigger than one is foreseen, optics of diameter 50mm are chosen.

The mirrors are chosen silver coated as it is the most reflective and uniform coating across the visible spectrum (95%) with a high reflectance and lasting durability [106].

As the mirrors are used off-axis, both coma and astigmatism arise. Coma[2] is reduced by limiting the angle at which the mirror is used (5° at most, [128]) and maximizing the focal length of the mirror used.

Moreover, thanks to a Z-Schlieren set-up with exactly the same mirrors and the same (but opposite) angle between the two mirrors and the optical axis, this effect is canceled [128].

Astigmatism[3] also arises from the off-axis use of mirrors, but cannot be eliminated. However, it can be partially limited by using a horizontal filter at the sagittal focal point, and using mirrors with large (>6) f/numbers ($=f/D$) [128]. As the selected mirror diameter is 50mm, optics of focal length of minimum

---

[1]spherical aberration: when rays far from the axis are more deflected than the closer ones. It results in a confusion circle at the focal point

[2]coma: when annular regions of the mirror focus as a line at the focal point

[3]astigmatism: when horizontal and vertical lines of waves focus in different planes a few millimeters around the focal plane, as two perpendicular lines, the tangential focal point (vertical) and the sagittal one (hortizontal)

Marie-Alix Dalle

300mm are required. Since the sensitivity of the Schlieren set-up increases with the focal length of the second focusing element (section 5.2.2.2), 500mm focal length concave mirror are selected, $f_1 = 500mm$.

For space reasons, the magnification factor is set to 2. The imaging lens has thus a focal length of $f_2 = 1000mm$. Buying a simple imaging lens is thus much cheaper than buying a camera objective of the same focal length.

Using flat mirrors on both arms of the Z avoids the blocking of the beam by the module.

7.3.2.2 Light source

To avoid the issue of the point-like focus point when using a laser, a LED flashlight with a slit was tried, however even the brightest lamp found on the market did not seem bright enough after crossing two layers of poly-carbonate.

Thus, in this study, laser light sources were preferred. The power of the laser used in this study is limited by the desire not to need a bigger security process. The laser wavelengths were selected at a time where the dye method was still considered. Hence the wavelengths were chosen to be the most distinct from each other while respecting the requirements for use in a dye method with Rhodamine B and Sulfurhodamine: 532 and 635nm, whose beam is elliptical.

7.3.2.3 Schlieren filter

Since a laser is selected as a light source, the beam focuses as a point at the focal point of the optical system, hence the use of a knife is compromised. A filter of gradient transmission is thus used [163]: the NDL-10C-4 from Thorlabs, with the following characteristics:
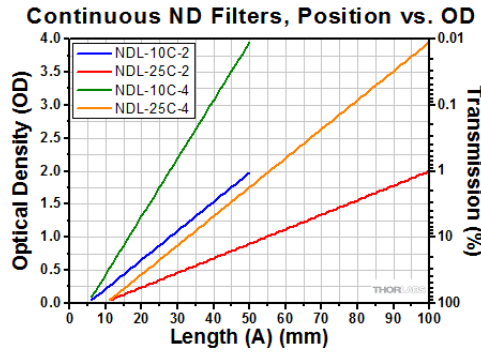
Figure 7.20: Characteristics of the gradient filter (in green)

This graph allows to link the position on the filter x (in mm) to the transmission t of the filter (in %: $t = \frac{I(x)}{I_{ini}}$ with I_{ini} the intensity of the beam before the filter) at that location through the following equation:

$$a = \frac{45}{4} log_{10}\left(\frac{1}{t}\right) \tag{7.1}$$

Thus the variation of landing ordinate on the filter of a deflected ray can be determined through

$$\Delta a = a_\alpha - a_0 = \frac{45}{4}\left(log_{10}\left(\frac{1}{t_\alpha}\right) - log_{10}\left(\frac{1}{t_0}\right)\right) = \frac{45}{4}\left(log_{10}\left(\frac{I_{ini}}{I_\alpha}\right) - log_{10}\left(\frac{I_{ini}}{I_0}\right)\right) = \frac{45}{4}log_{10}\left(\frac{I_0}{I_\alpha}\right) \tag{7.2}$$

where I_0 is the intensity of the non deflected ray crossing the filter, and I_α the one of the deflected ray.

7.3.2.4 Camera

There are two cameras at disposal at University Luxembourg: a Fujifilm XT2 with a X-Trans CMOS III APS-C sensor (23.6 mm x 15.6 mm), and a NIKON D800 with a Bayer CMOS FX sensor. The following chart summarize their specifications (fig. 7.2):

	Fujifilm XT 2	NIKON D800
Sensor	CMOS APS-C	CMOS FX
Filter	X-Trans III	Bayer
Sensor size	23.6 mm x 15.6 mm	24 mm x 36 mm
Effective pixels	24.3 Mpx	36.3 Mpx
Resolution	6.53 Mpx/cm	7360 x 4912
ISO-sensitivity range	200 - 12800 ISO	100 - 6400 ISO
Shutter speed range	$\frac{1}{8000}$s -	$\frac{1}{8000}$s - $30s$
Serial capture	Max. 8 pictures/s	Max. 4 pictures/s

Table 7.2: Comparison of camera characteristics
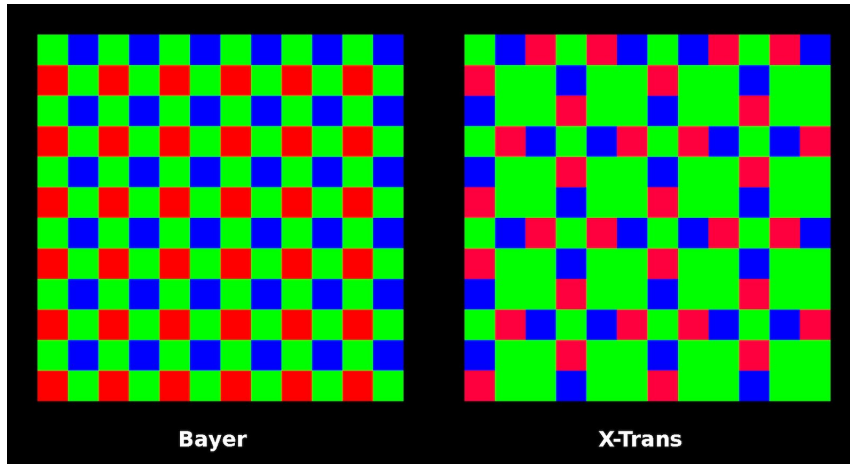
Figure 7.21: Bayer and X-Trans filters

Fig. 7.21[4] depicts the color filters placed just before the camera sensor, allowing the color determination of the light received by each pixel.

For availabilities reasons, the camera used is the Fujifilm XT-2. However when the 2 Wavelengths Schlieren will be implemented, a Bayer filter, with a more balanced apparition of each of the three colors, seems more indicated, as the sensitivity of the camera chip should be equal for both chosen wavelengths.

The camera is used without any lens, as the imaging lens does the work of the camera's lens. Hence a protection for the camera chip is added to the camera (to avoid dust entering the camera), made of polycarbonate.

To reduce the camera noise to the minimum the ISO is set to the minimum value, 100 ISO. Thus to get enough light, the exposure time is increased.

In the work of Kroiss et al. [45], 35 images were taken in the same experimental conditions, and the intensity and standard deviation of a random pixel in the middle of the picture were analyzed in a 8 bits .jpg format and a 14 bits .raw format. It was found that the standard deviation was always higher than one intensity value whatever the chosen format. Thus in their set-up using .raw instead of .jpg storage did not improve the accuracy. In this thesis work .jpg files are also used.

As the camera pixel's size is $3.9\mu m$, and the magnification factor of the Schlieren set-up is 2, the theoretical spatial resolution is $1.95\mu mm$: the closest detectable ray to the membrane is thus the one entering the module at $1.95\mu mm$ from the membrane.

---

[4]https://thepenguin.eu/2018-09-28-fuji-cameras-x-trans-sensors-and-post-processing/

7.3.2.5 Resolution of the Schlieren set-up

As the filter is 50mm large, for an equal determination of the temperature variation in both directions, the maximum observable angle is roughly (to the module channel height, which is significantly small in front of the focal length) $\alpha_{max} = atan\left(\frac{\frac{50}{2}}{f_1}\right) = atan(\frac{25}{500}) = 0.049rad$. The corresponding angle on the water side is thus $\alpha_{w,max} = asin\left(\frac{n_{air}}{n_{water}}sin(\alpha_{max})\right) = 0.037grad$.

Following eq. 5.10, the maximal refractive index gradient observable is thus $\frac{\partial n}{\partial x}|_{max} = \frac{\alpha_{w,max}}{L}$ with L the module length, here 10mm: $\frac{\partial n}{\partial x}|_{max} = 3.75m^{-1}$.

Over the temperature range of this work, the relationship between the refractive index and temperature can be assumed linear (fig. 7.22), with a slope of $0.0002°C^{-1}$:
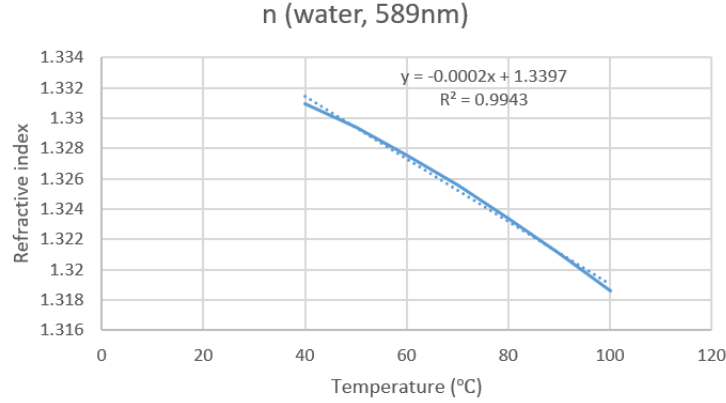
Figure 7.22: Variation of refractive index with temperature

Hence the maximal temperature gradient observable is thus $\frac{\partial T}{\partial x}|_{max} = \frac{\partial n}{\partial x}|_{max}\frac{1}{0.0002} = 18°C/mm$.

The resolution, defined in eq. 5.14 can be calculated with $(\frac{dn}{dz})_{min} = \frac{n_{air}}{L}\frac{t_0}{f_1}\frac{1}{\frac{dt}{dx}}C_{min}$. Here, $\frac{dt}{dx} = -t$, thus the resolution varies along the filter. At the transparent side, the resolution is about $0.0000004mm^{-1}$ (or $0.002°C/mm$) and goes towards $0.004mm^{-1}$ ($20°C/mm$) at dark border of the filter. Thus a use of the filter closer to the transparent side complies with the requirements for a two-wavelength Schlieren method, exposed in section 5.2.2.2.

7.4 Support simulations

Several MATLAB simulations were carried out in parallel of the experiments. The goal of the first package was to support the module design. A second category of simulations aim at understanding better the behavior of light rays in the optical set-up and forecast the resulting intensity profiles, based on [148] and [55].

7.4.1 Module design support

Due to the bending of light rays towards areas of lower temperatures, the rays crossing the desalination module are bending towards the membrane, and depending on the width of the module, a certain amount of rays can be blocked by the membrane. Fig. 7.23 shows an example of the output of such a simulation: the black rectangle represents the module, the red lines represent light rays. The membrane is located at the top of the module, and the flow is perpendicular to the figure. d_{min} is the minimum observable distance from the membrane as a result of this phenomenon.
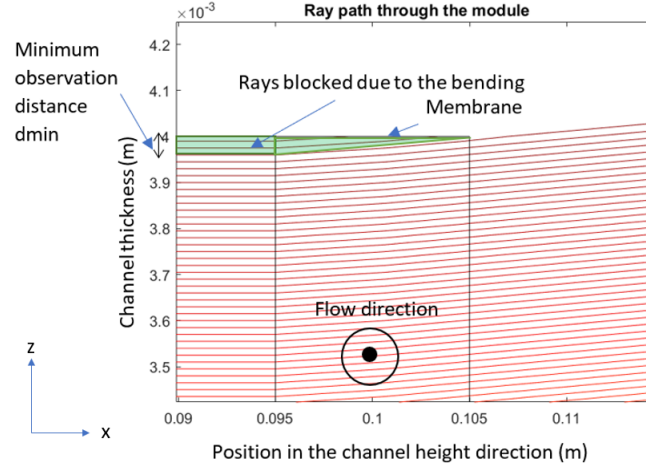
Figure 7.23: Zoom on the light rays path close to the membrane

The temperature gradient close to the membrane is of biggest interest in this study, hence the information carried by the closest detectable ray to the membrane ($1.95\mu m$, dependent on the imaging system, see section 7.3.2.4) is the most valuable. Thus, the width of the module should allow this ray to exit the module without bouncing on the membrane.
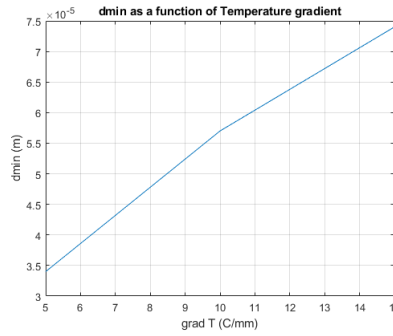
Figure 7.24: dmin as a function of the temperature gradient for a boundary layer of 3mm, a bulk temperature of 313K and a module thickness of 0.01m

For a temperature gradient of 10°C over a boundary layer of 3mm at 313°C in a module of height $L = 0.01m$, the first light ray blocked by the membrane is located at $d_{min} = 5.5.10^{-5}m$ from the membrane (see fig. 7.24). This light ray is called the observable ray closest to the membrane.

The MATLAB code also served to determine the minimal accuracy required for the experimental set-up in order to observe both temperature and concentration profiles, given two wavelengths and a maximum temperature and concentration difference between the bulk phase and the membrane.

The graph below shows the variations of the refractive index as a function of the temperature variation and salinity variation, around a given state of T=20 °C and S=10g/kg, for the two wavelengths selected, 532nm and 635nm (fig. 7.25).
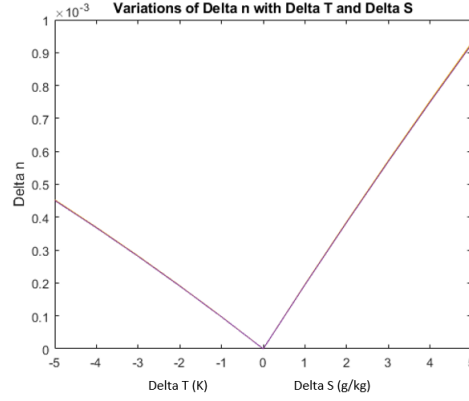
Figure 7.25: Variation of the refractive index as a function of the temperature and salinity profiles for two different wavelengths

Water refractive index variations with temperature and salinity gradients are represented in the same graph to appreciate and compare the sensitivity of the water refractive index to these two variables. Moreover, these dependencies for two different wavelength are superimposed for comparison reasons.

As can be observed through the slopes of the curves in fig. 7.25, the refractive index has a weaker dependence on temperature than on concentration. Therefore, a higher resolution is needed to observe the dependency of the refractive index on temperature than on concentration.

In order to differentiate both profiles in a two-wavelengths Schlieren method using these two wavelengths, the set-up should be able to resolve refractive index variations smaller than the refractive index variation between the two wavelengths for given temperature and concentration differences, divided by the height of the corresponding boundary layer. Hence for a 5K temperature variation over a 2mm boundary layer, this minimum measurable refractive index variation should be smaller than $0.18.10^{-5}.mm^{-1}$.

7.4.2 Ray tracing

To choose the different optical elements, and forecast the resulting observable intensity on the screen under different optical and operating parameters conditions, a MATLAB code is written to reproduce the theoretical path of the light rays.

Several kinds of temperature profiles (linear, polynomial imported from an excel table) can be set as inputs of this algorithm, on one or both sides of the channel (membrane and wall). Other variable inputs of the code are the light beam wavelength, the hot bulk temperature T_b^h, the temperature variation between the bulk phase and the membrane, the hot water channel height. The geometry of the module, as well as the characteristics of the lenses and mirrors and their 2D location in the set-up are configurable via the **Lens** object (see section D for more details).

Then the code calculates the light rays' trajectory in the **Ray** object via two functions (*bendingbeamInGRIN* and *bendingbeamInLenses*, see section D for more details). The first function (*bendingbeamInGRIN*) calculates the beam trajectory in the variable refractive index environment of the module; and the second function (*bendingbeamInLenses*) calculates the beam trajectory through the set of lenses.

The code outputs different graphs. First, a top view of the optical set-up and the rays trajectories (fig. 7.26):
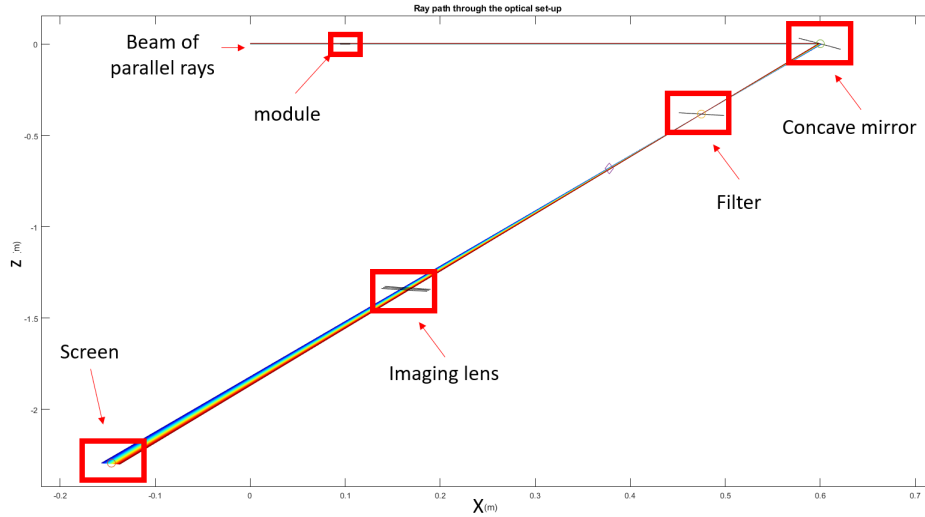
Figure 7.26: Rendering of the MATLAB Ray-tracing simulation: top view of the set-up

In particular, a close-up on the module can be achieved (fig. 7.27):
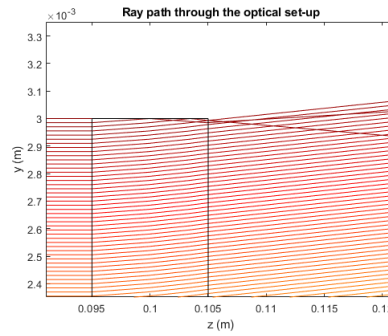
Figure 7.27: Close up of the membrane: the reflection of the rays on the membrane can be taken into account or not

On this graph, some light rays are deflected towards the membrane: a specific feature of the algorithm allows the rays to be reflected on the membrane, or simply blocked.

Finally, the code also displays the resulting intensity on the screen (fig. 7.28). On this plot, the ordinate represents the light intensity while the abscissa represents the spatial extension of the light patch on the screen. In this case, the temperature in the module was constant and homogeneous, thus the intensity on the screen is constant.
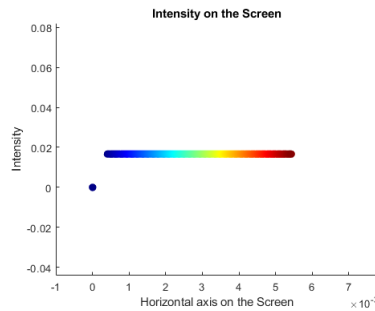
Figure 7.28: Resulting simulated intensity on the screen without temperature variation in the hot water channel

The rainbow color code for the rays helps distinguishing the provenance of the rays (the redder ray coming from the membrane side of the module) (fig. 7.29), and identifying a reversing phenomenon for instance (section G.4.3).
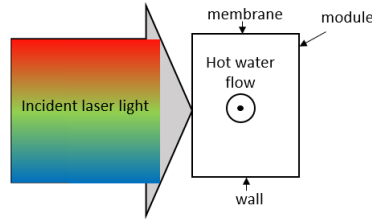
Figure 7.29: Rainbow color code for the light rays localization in the ray-tracing code

Each simulation can be summarized by compiling the temperature profile, the resulting intensity profile on the screen and the rays path as follows (fig. 7.30):
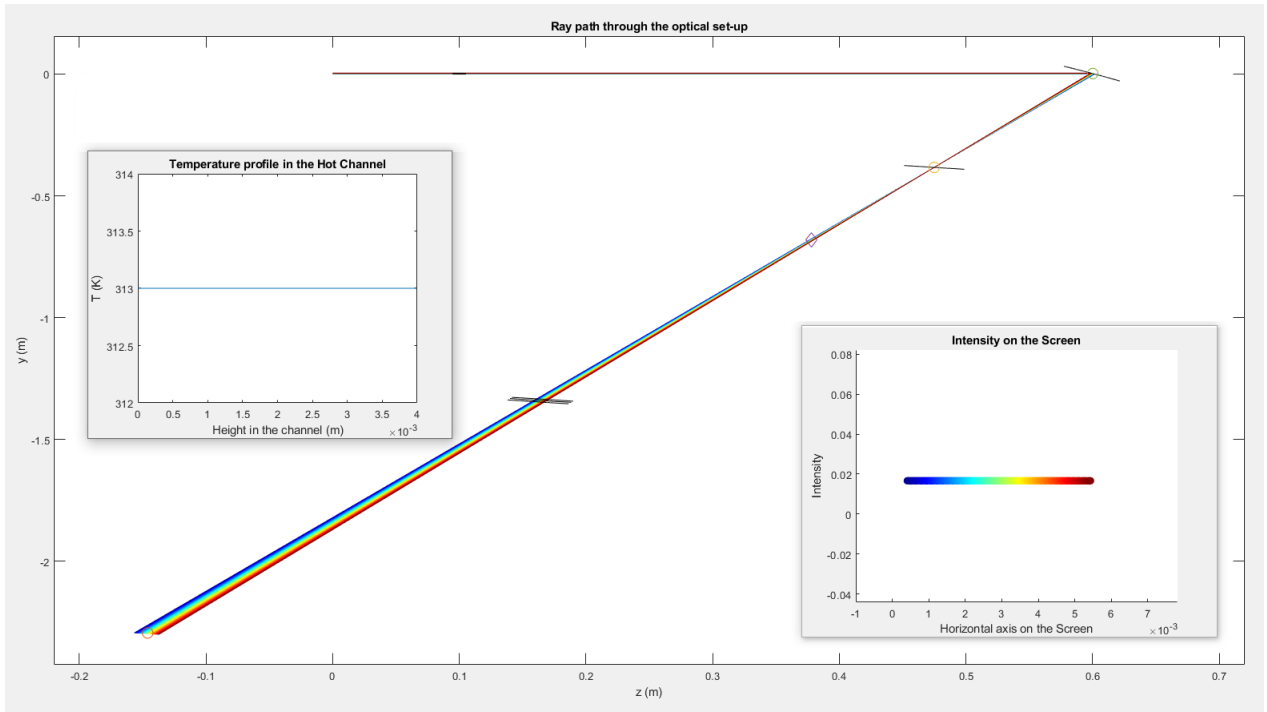
Figure 7.30: Complete ray tracing simulation without temperature variation

In this graph, no temperature variation is imposed in the module (left subpicture), thus the resulting intensity on the screen is constant (right subpicture).

The following picture 7.31 summarizes a ray tracing simulation where a temperature profile is imposed in the module.
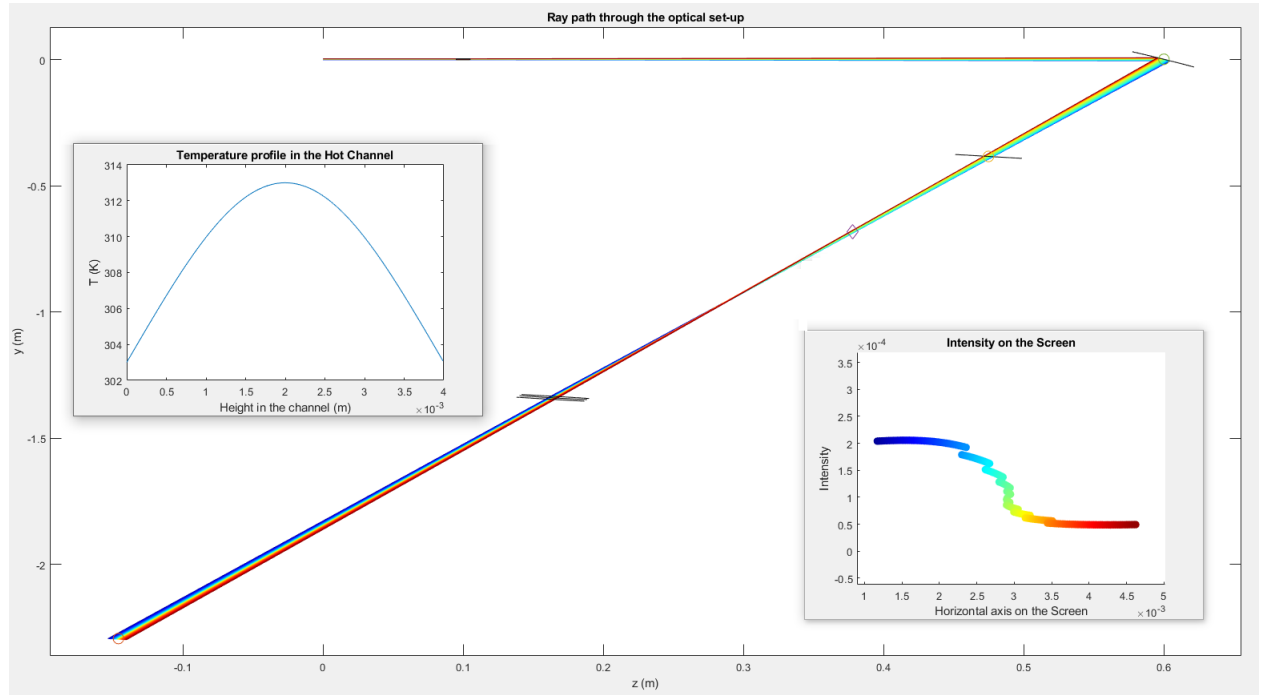
Figure 7.31: Complete ray tracing simulation with temperature variations in the hot water channel

As can be observed, the temperature profile simulated presents two decreasing temperature gradients on both sides (membrane and wall) of the module. As a result, the light rays are deflected towards the external sides of the module, and of the knife. Indeed, it can be observed in fig. 7.31 that the light beam does not focus as a point at the knife extension, it presents a visible extension. Thus, the resulting intensity on the screen shows a lower intensity on the membrane side (red rays) and a higher intensity on the wall side (blue rays), coherent with the impact of the transmission function of the filter located at the focal point of the convergent mirror.

This code can even be used in reverse, by entering the temperature profile obtained with the Schlieren method (left subfigure of fig. 7.32)) as an input of the MATLAB ray-tracing simulation (fig. 7.32).

Marie-Alix Dalle
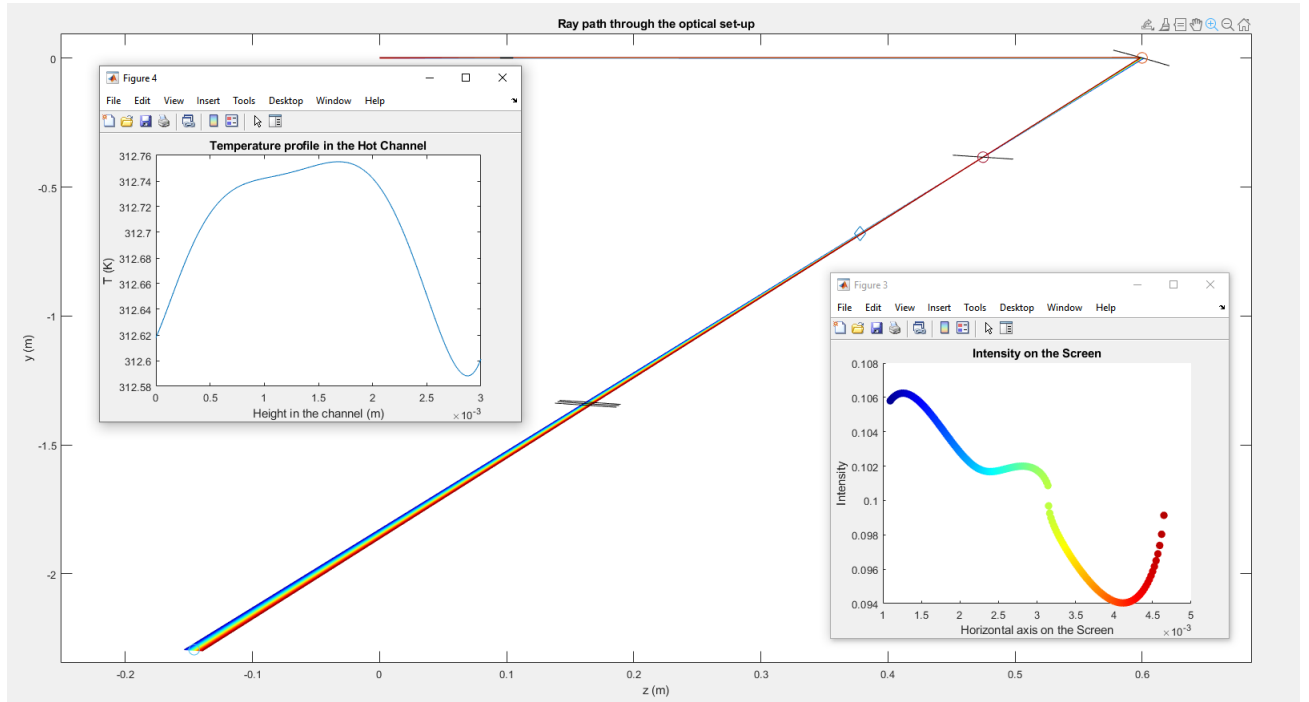
Figure 7.32: Reconstruction of the intensity profile from a temperature profile obtained by Schlieren measurement

It is to be noted that the absolute intensity values are arbitrary and should not be taken as fixed.

7.5 Conclusion on the test-facility

This experimental set-up partially answers the first research question by providing an observation method of the temperature profile inside a hot water channel, with a theoretical spatial resolution of $1.95\mu m$, a maximum observable temperature gradient of $18°C/mm$, and a resolution varying from $0.002°C/mm$ to $20°C/mm$ depending on the localization on the filter.

Inlet hot and cold temperatures can be monitored, as well as the flow to a certain extent.

This set-up could be improved by enhancing the heat insulation, thus broadening the range of accessible hot temperatures.

Adding a second laser would complete the research question by providing a concentration profile measurement.

Through a slight modification of the module (shape of the membrane support), measurement could be carried inside the air-gap.

The AGMD could be easily modified to adjust the air-gap size.

Chapter 8

Dataset from the facility and 3DH&MT code validation

The test facility is used to generate measurements in order to observe the polarization occurring in the AGMD device in correlation with the fresh water output measurement, as well as to validate the 3DH&MT numerical model.

8.1 Experiment protocols

The boundary conditions of the tests conducted in the frame of this dissertation work is the following:

Inlet flux (m/s)	Hot water channel T	Cold water channel T
0.18 - 0.2 m/s	60 - 75 °C	14.5°C

Table 8.1: Experiments matrix

The inlet flux was fixed by the current capacities of the set-up. The corresponding Reynolds number values are comprised between 2524.9 and 3675.8, in the transition between laminar and turbulent flows zone (Reynolds numbers reported in AGMD literature: from 272 to 1634 [165]; 177 [138], ≈ 10 [100]).

The cold water channel temperature was fixed, as literature reported little dependency of the energy efficiency and fresh water outflow on this parameter (section 3.4), and set at a value close to what could be encountered using low-tech cooling method (B.2). The hot water channel temperatures are in the range reported in literature, and limited by the heat losses occurring in the pipes.

8.1.1 Optical set-up alignment

Alignment of the optics was inspired from Eyerer et al. [45].

The horizontality of the laser beam and the height of the optical equipment was verified thanks to a bubble ruler and diaphragms.

The vertical position of the different optics is finely tuned using diaphragms and micrometric tables from Thorlabs, making sure that the beam stays parallel and that the optics are precisely located, as their position can impact the performance of the set-up (see section 8.2.2).

8.1.2 Measurement protocol

The measurement protocol must ensure that the operating conditions (inlet flow, hot and cold water channel temperatures, ambient illumination) remain constant throughout the measurement time.

Several measurements are performed for each operating conditions to ensure the reproducibility of the measure.

The inlet and outlet hot and cold channel temperatures are measured with thermocouples, while the outlet hot water flow and the permeate output are measured using a bucket, a watch and a scale.

The inlet hot water temperature is varied from one measurement session to another.

As heat is lost in the circuit despite the insulation efforts, and as the flow slows down (section 7.2.5), measurements should not last too long to ensure almost constant temperature and flow conditions.

On the other hand, as the permeate flow is quite low, a significant amount of time is required to make sure that the measured permeate mass is well beyond the error margin of the instrument used.

Overall, measurement sessions of about 20min are chosen.

Due to the requirement for a very stable light atmosphere, and despite the presence of a light atmosphere controlling box, photographs are shot at night to ensure a stable ambient illumination.

The extensive measurement protocol is detailed in section E.

8.2   Reconstruction algorithm

This section describes the algorithm used to interpret the pictures taken with the Schlieren experiment and extract the temperature gradients at the membrane interface and boundary layer thicknesses.

8.2.1   Description of the algorithm

By comparing the light intensity reaching a given pixel in images taken with a varying temperature profile and with an homogeneous temperature in the hot channel, the gradient filter's transmission function enables the determination of the displacement x of the ray corresponding to that particular pixel along the gradient filter. This displacement can then be linked to the deflection angle α (fig. 8.1).
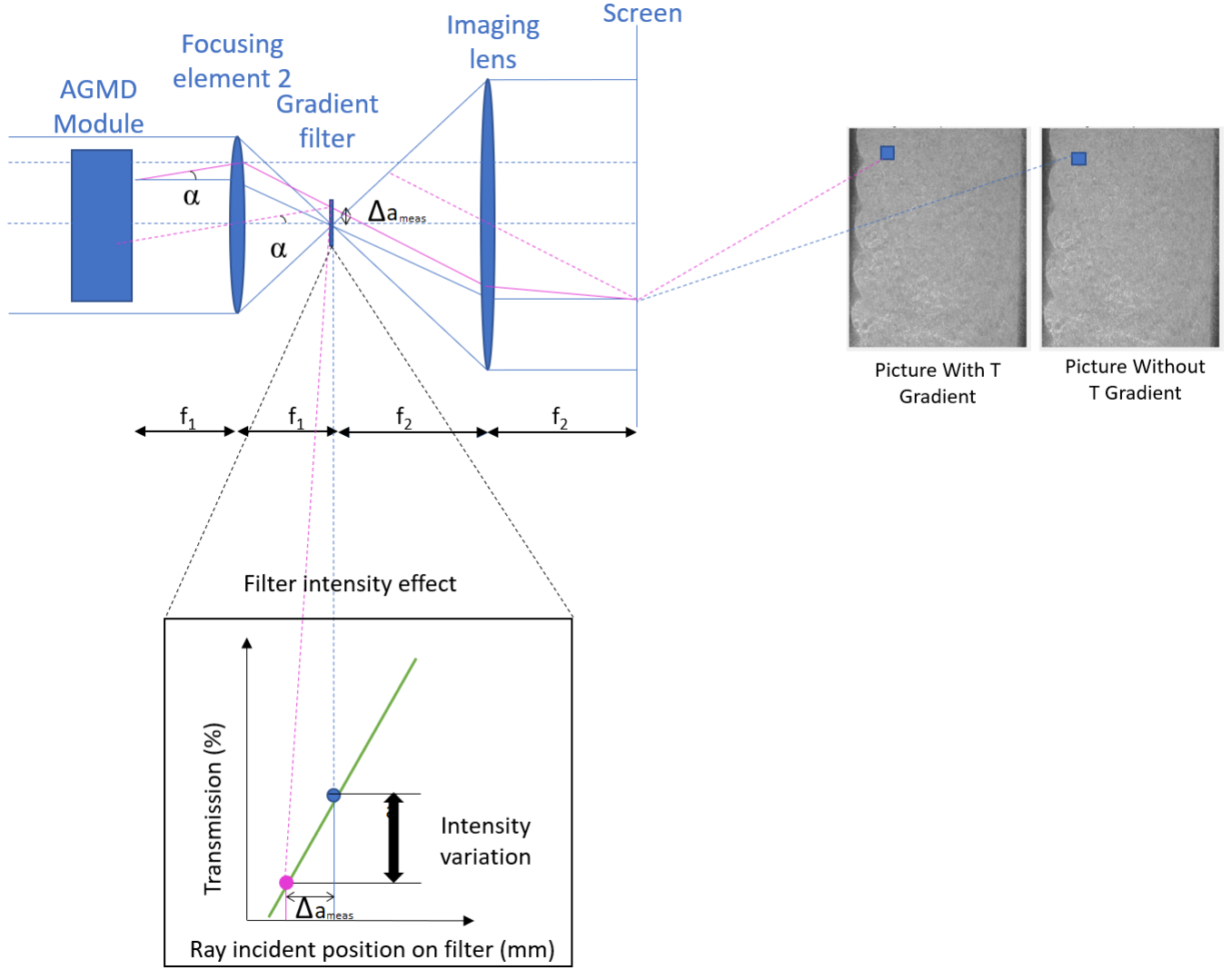
Figure 8.1: Reconstruction algorithm. In blue a non-bent ray, in purple a deflected ray

For each picture taken in the context of experiment, the intensity I of each pixel is compared to the intensity I_0 of this same pixel on the picture taken with homogeneous temperature. Thanks to the relation described in eq. 7.2, this ratio of intensity can be linked to the ray displacement on the filter:

$$\Delta a_{meas} = \frac{45}{4} log_{10} \left(\frac{I_0}{I} \right) \tag{8.1}$$

Knowing the focal length of the second concave mirror f_1 placed before the filter, the apparent angle α_{app} (in green on fig. 8.2) from which the light ray is deflected is calculated as $\alpha_{app} = atan \left(\frac{\Delta a_{meas}}{f1} \right)$.

However, due to the poly-carbonate window impacting the light ray path, the real angle from which the light ray is deflected inside the hot water channel is α_{real} (in blue on fig. 8.2). Fig. 8.2 describes how to take into account the impact of the poly-carbonate window and how to calculate α_{real}:
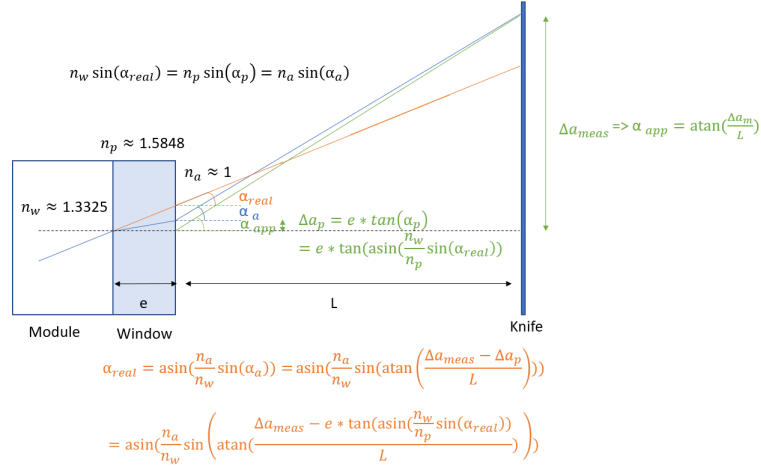
Figure 8.2: Correction of the deflection angle impacted by the poly-carbonate window

Finally, the real angle α_{real} (in orange on fig. 8.2) is the solution of the non linear following equation:

$$\alpha_{real} = asin\left(\frac{n_a}{n_w}sin\left(atan\left(\frac{\Delta a_{meas} - e * tan\left(asin\left(\frac{n_w}{n_p}sin(\alpha_{real})\right)\right)}{L}\right)\right)\right) \tag{8.2}$$

solved using MATLAB function *fzero* with α_{app} as an initial guess.

Then the temperature gradient at the membrane interface is found using eq. 5.10 and the correlation between temperature and refractive index (fig. 7.22):

$$\frac{dT}{dz} = \frac{\alpha_{real}}{L * 0.0002} \tag{8.3}$$

The images are recorded in .jpg format, and read in Matlab via the function *imread* (and then *im2double*), providing 3 tables of doubles corresponding to the red, green and blue components of this picture. The green sensors of the camera chip are saturated by the green laser light. Thus, the blue component of the images is used in the algorithm as the pixel value, as it provides a suitable variation of values correlated to the incident light intensity.

The camera response is not linearly dependent on the incoming intensity. This specific response can be found by taking 6 pictures of the same scene with low dynamic range and different exposure times, and use MATLAB's *cameraresponse* function, providing the correlation between the value recorded on the pixel of the camera chip (*pix*) to the log of the incoming intensity (fig. 8.3).
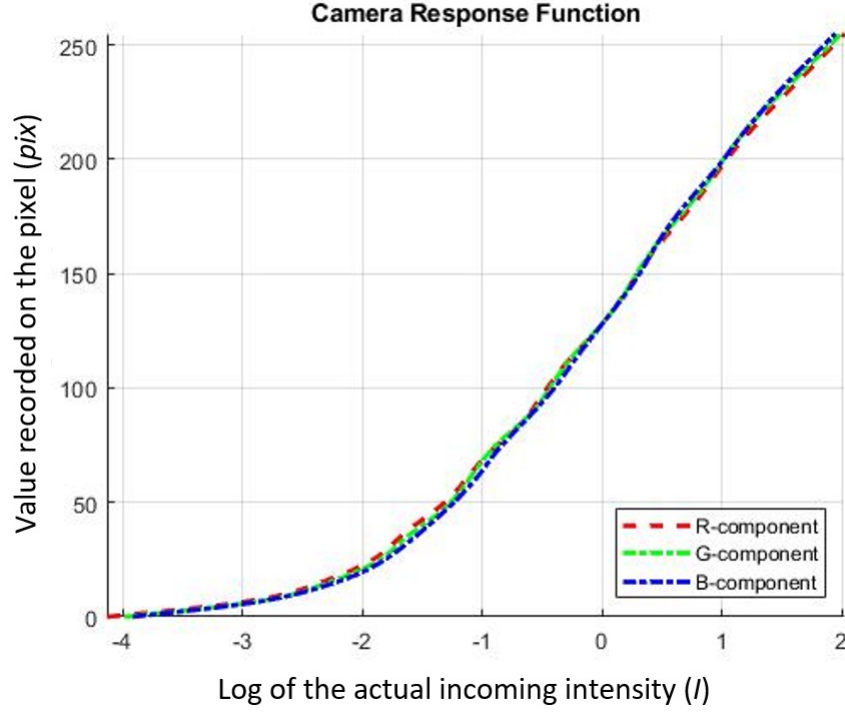
Figure 8.3: Camera Response Function calculated via MATLAB: the pixel value (pix) is represented against the log of the actual incoming intensity (I)

As the actual range of values of the image table after being read by *imread* and *im2double* MATLAB functions is between 0 and 1, the pixel value range of this curve 8.3 is brought down from [0,256] to [0,1]. The inverse curve, providing the log of the incoming intensity as a function of the pixel value (between 0 and 1), is interpolated using a 7th-order polynomial providing the best fit. The resulting polynomial p is used in the main reconstructing algorithm. Indeed, in the algorithm presented in fig. 8.1 and eq. 8.1, it is the actual intensity I of the light beam landing on the camera chip which is at stake, whereas the camera only provides a pixel value pix. Eq. 8.1 becomes:

$$\Delta a_{meas} = \frac{45}{4} log_{10} \left(\frac{p(pix_0)}{p(pix)} \right) \tag{8.4}$$

with pix_0 and pix respectively the value in a given pixel from images taken with a homogeneous and a varying temperature profile.

Moreover, there is a lot of noise and hence the reconstruction pixel per pixel is not very meaningful. Thus a low-pass filter (Butterwoth) is applied:
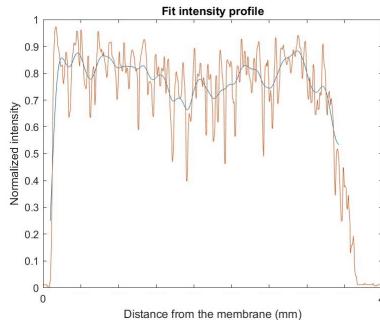
(a) with a temperature profile
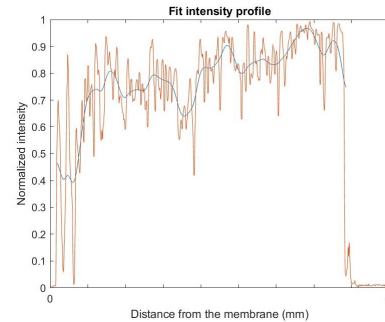
(b) with an homogeneous temperature

Figure 8.4: Intensity profile (in orange) with the filtered data (in blue)

The noise appears to have a wavelength of less than half a millimeter (the minimum observable pattern runs over less than half a millimeter), thus the cut-frequency of the low-pass filter is chosen accordingly.

The following picture shows the mean of 32 pictures taken in the same conditions (with homogeneous temperature and no flow) at a few seconds of interval (fig. 8.5):
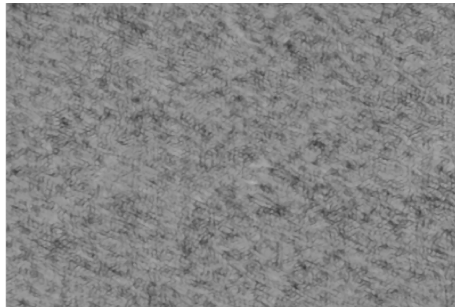
Figure 8.5: Mean of 32 pictures of the module with homogeneous temperature and no flow

The noise appears to be significant as the averaging did not smooth it. The source of the noise is identified as the poly-carbonate windows of the module and the small window protecting the camera chip:
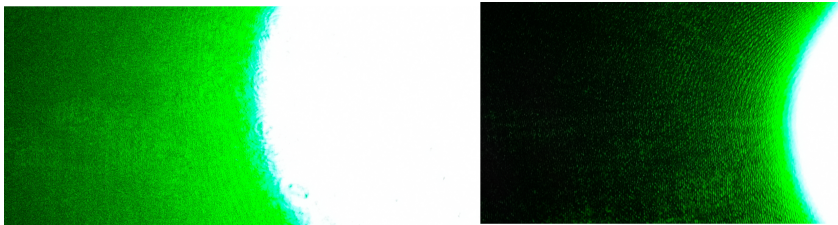
Figure 8.6: On the left, a picture of the laser with the poly-carbonate sheet protection; on the right, a picture of the laser without poly-carbonate sheet

Indeed, as can be seen on this picture, the addition of the poly-carbonate generates diffraction and a granular pattern, very similar to the one presented in fig. 8.5.

The camera is triggered remotely thanks to a phone app (Camera Remote, by Fuji) to reduce the risk of translation between the pictures. As the pump of the cooling system introduces vibrations in the set-up, there is still some minor translation between pictures to determine. Moreover, the membrane interface does not appear flat, due to the membrane support (see left hand side of fig. 8.7 a)).

(a) Original picture

(b) Binarized picture
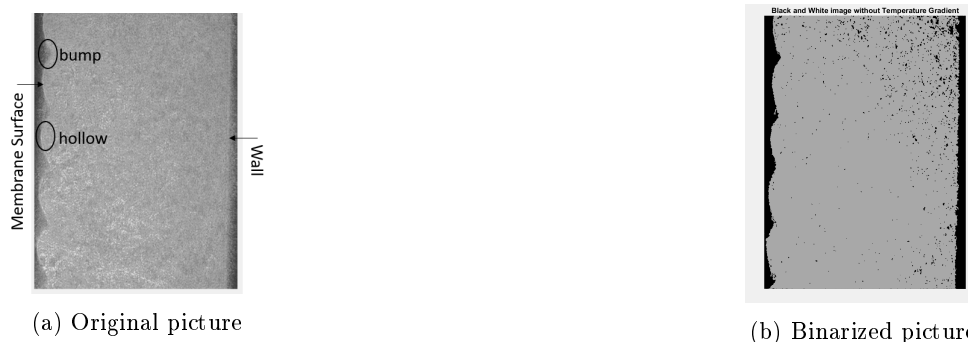
Figure 8.7: Schlieren pictures of the hot channel of the module a) original b) with binarization treatment. Membrane interface on the right border; hot water channel wall on the left. The water flows from bottom to the top.

Hence, an algorithm is constructed to determine the translation between a picture taken with an

homogeneous temperature and a picture taken with a temperature profile. This algorithm calculates a two-dimensional cross-correlation between the pictures.

To identify the membrane interface in the pictures, the picture is first binarized by dividing it into "dark" and "bright" pixels (see fig. 8.7 b)). Then, the position of each row's first "bright" pixel is saved in a table named *border*. Similarly, the opposite wall of the hot water channel is detected as the last pixel with an intensity value greater than a predetermined threshold. Finally, a moving-average filter is applied to this table to smooth the curve and approximate the interface of the membrane (fig. 8.8), and the opposite wall is fitted using a 15th-order polynomial.
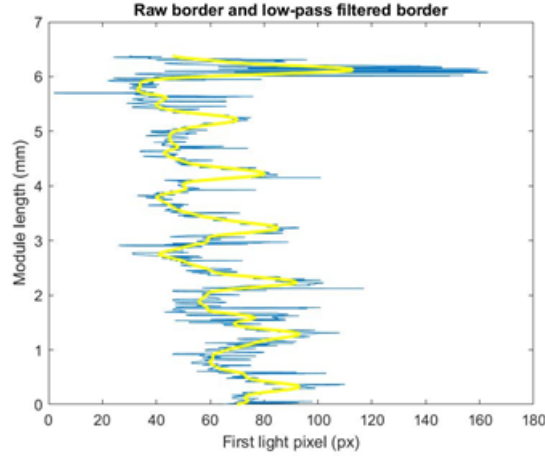
Figure 8.8: Index of the first "light" pixel of each line, representing the membrane interface, raw data in blue, interpolated data in red

Then, for each pixel row of the image starting from the membrane's border (indicated in *border*), a reconstruction of the temperature profile is attempted using the algorithm described in fig. 8.1.

A low-pass filter (Butterworth) is applied to the raw data to smooth out the apparent noise, and converted to a temperature profile.

Temperature profiles vary significantly between pixel lines along the hot water channel, making it difficult to determine a mean gradient at the membrane interface within the hot channel. To improve the data quality and representativeness, all lines located at the membranes' "bumps" are eliminated. Indeed, locating the membrane's border in these locations is quite difficult due to the diffraction, making gradient reconstruction unreliable. Additionally, "bumps" correspond to locations where the membrane is in contact with its support, no evaporation occurs there.

Then, for each hollow of the membrane, a mean of twenty temperature profiles around the "hollow" center is calculated, and the temperature gradient at the membrane interface and boundary layer thickness for the initial conditions (T_{hot} and V_{in}) are determined using these mean temperature profiles at the membrane hollow.

Due to the unknown integration constant (due to a high heat loss at the wall side, there is no guarantee that the maximum temperature in the channel corresponds to the temperature of the inflow), the membrane temperature is arbitrarily set to 0° C, and rather than considering the exact temperatures, which are only indicatives, the slopes of the temperature profiles and the absolute temperature variations should be considered.

8.2.2 Error sources

The error sources in this experiment are of several type: they can be due to the misplacement of the optics; the image captation system; the reconstruction algorithm presented above (section 4.2.4).

All of them are explored in the next sections.

8.2.2.1 Errors from the misplacement of the optics

All the optical equipment are located on a micrometric table (section F), enabling their location at the precision of 0.5mm per tour of the adjustment ring.

Spatial resolution. The positioning of the different optical elements can have an impact on the spatial resolution.

Indeed, the misplacement Δx_{mirror} of the mirror (fig. 8.9) induces an enlargement of the image on the screen by a factor of $e_{mirror} = \frac{f_2}{f_1}\left(\frac{(L-f_1+\Delta x_{mirror})\Delta x_{mirror}}{f_1} + \frac{f_1-\Delta x_{mirror}}{f_1}\right)$, where D is the original beam diameter, L the distance between the two mirrors, and $f1$ and $f2$ the focal lengths of the mirror and the imaging lens respectively. For a 0.5mm misposition ($\Delta x_{mirror} = 0.5mm$), the enlargement factor is $e_{mem} = 1.0005$.
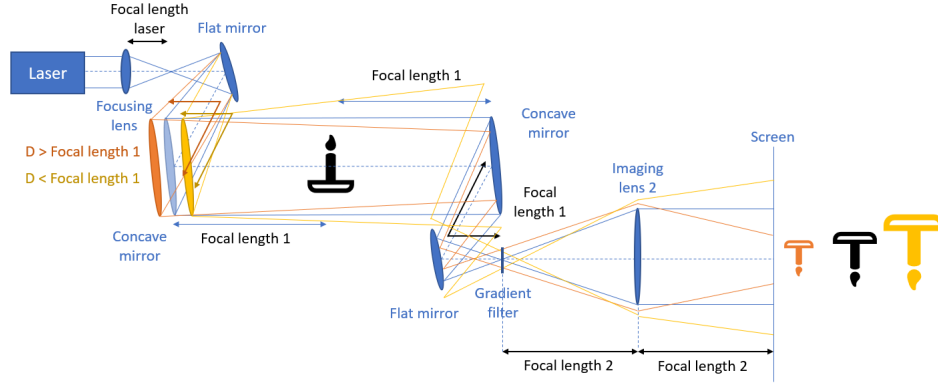
Figure 8.9: Change in beam path when the first mirror is misplaced (in orange the changes if the mirror is too far from the focal point of the first lens; in yellow if the mirror is too close)

As seen in this image, a misalignment of the first mirror is extremely obvious, as the resulting beam is not parallel and changes in diameter with the screen's position. Thus, this misalignment can be easily corrected using diaphragms to control the diameter of the beam, and the mistake caused by this misalignment can be quantified by the difference in the diameter of the beam at each mirror locations.

A misplacement Δx_{screen} in the screen (fig. 8.10) also results in a deformation of the image on the screen. This error is hard to evaluate as it depends on the angle of the deflected rays. Taking a maximum deflection of roughly 5mm at the focal point for the ray coming from the furthest corner of the channel ($tan(\alpha_{max}) = \frac{5mm}{fl}$), an overall maximum deformation of $e_{screen,max} = \Delta x_{screen} tan(\alpha_{max})\frac{f_1}{f_2}$ is obtained. For a misplacement of $\Delta x_{screen} = 0.5mm$, the error is $0.0025mm$.
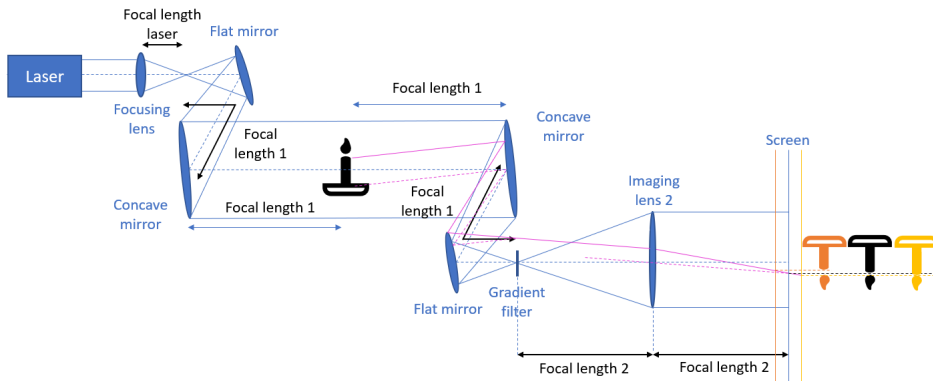
Figure 8.10: Change in beam path when the screen is misplaced (in orange the changes if the screen is too close to the knife; in yellow if it is too far; in purple the path of a ray being deflected by a schliere)

If the screen is misplaced, the image on the screen does not perfectly reflect the object as the deflected rays do not land at their right place but a bit upper or lower, thus deforming the image.

Intensity resolution. If the gradient filter is misplaced by Δx (fig. 8.11), it results in a change in the intensity coefficient of $e_{filter} = 10^{-\frac{4}{45}tan(\alpha)\Delta x}$ for a ray of deflection angle α. For $\Delta x_{filter} = 0.5mm$,

Marie-Alix Dalle

the resulting coefficient in intensity variation is $e_{filter} = 0.9997953467 I_0$.
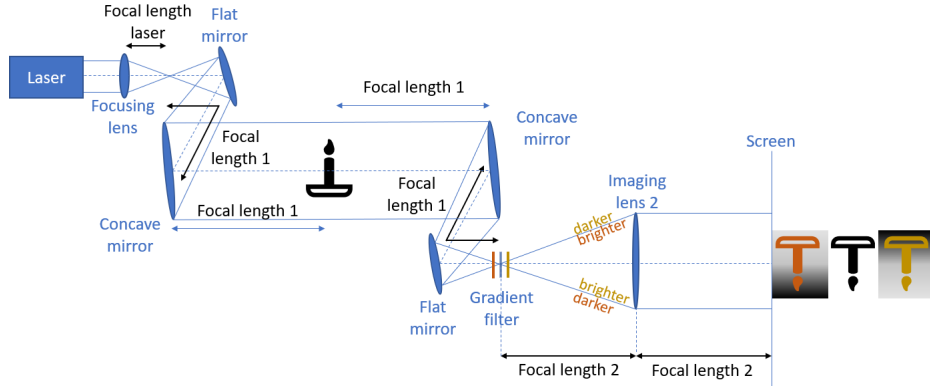
Figure 8.11: Change in beam path when the gradient filter is misplaced (in orange the changes if the filter gradient is before the focal point of the mirror; in yellow if it is after)

If the knife is misplaced, the image on the screen will present an intensity variation even without any schliere.

8.2.2.2 Errors from the image captation

Spatial Resolution. The pixel size of the camera sensor is $3.9\mu m$. Since the optical set-up has a magnification coefficient of 2, 1mm on the camera sensor equates 0.5mm on the module, and hence the theoretical spatial resolution of the described setup is $1.95\mu m$.

Intensity Resolution. The intensity on the camera chip is registered by entire values between 0 and 256, that the *im2double* function brings down to between 0 and 1. That means that the pixel values are discrete values $\pm\frac{1}{256} \approx 0.0039$.

The camera also produces noise (section G.6.2.7), and the Signal to Noise ratio for Fujifilm XT-2 is said to be 40dB up to ISO 400 [1], meaning that under these conditions (verified in the experiments), $40dB = 10log_{10}(S/N)$ (if S and N are considered to be voltage) thus $N = 10^{-4}S$.

8.2.2.3 Errors from the reconstruction algorithm

Spatial Resolution. As the position of the membrane is not identifiable to the nearest pixel, the accuracy range of the membrane determination pixels is in this configuration, $e_{mem} \approx 0.78 pix$ (see fig. 8.12, e_{mem} is the average distance between the orange and purple curves defining the 95% confidence interval).
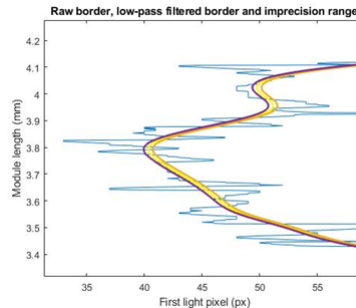
Figure 8.12: Evaluation of the pixel imprecision of the membrane border determination. In blue the original identified border; in orange the moving average; in purple and yellow the moving min and max of the border curve determining the imprecision range of the membrane border identification.

---

[1] https://fotoforum.net/camaras/fuji-xt2/

Intensity Resolution. A 95% confidence interval is calculated for the filtering of the intensity profile for each pixel line of the picture, which is spread all along the calculations.

Overall, the measured temperature gradient at the membrane interface is affected by the intensity measurement uncertainty as follows:

$$\frac{\Delta dT}{\Delta I} = \frac{45}{4f_1} \frac{1}{0.0002 * L} * \frac{p'(I_0) - p'(I)}{1 + (\frac{45}{4f_1}(p(I_0) - p(I)))^2} \frac{n_a}{n_w} \frac{cos(atan(\frac{45}{4f_1}(p(I_0) - p(I))))}{\sqrt{1 - (\frac{n_a}{n_w}sin(atan(\frac{45}{4f_1}(p(I_0) - p(I)))))^2}} \quad (8.5)$$

with:
- p the camera response curve
- L the module length
- I_0 the intensity after the filter with an homogeneous temperature and I with a varying temperature profile

8.2.2.4 Errors' summary

As a conclusion, the method's spatial resolution is on the order of magnitude of $resol_{spatial} = pixsize \pm pixsize\left(1 - \frac{1}{e_{mirror}}\right) = 1.95 \pm 9.7*10^{-4} \mu m$ while the precision is on the order of magnitude of $exact_{spatial} = (1 - e_{mirror}) * e_{screen,max} = (1 - 1.0005) * 0.0025mm = 1.25 * 10^{-6}mm$. The method's intensity resolution is on the order of magnitude of $resol_{spatial} = 0.0039 * p'(p^{(} - 1)(I_0))$ while the precision is on the order of magnitude of $exact_{spatial} = I_0 \pm (1 - 0.99979) * 10^{-4}p^{-1}(I_0)$.

8.2.3 Output from the reconstruction algorithm

This algorithm outputs the temperature profiles at different locations along the flow, with a rainbow color code attributed to the data to represent this evolution along the module channel. The most reddened temperature profile curves are placed upstream of the flow, while the most blued temperature profile curves are located downstream (fig. 8.13).

It also produces the temperature gradient at the membrane interface (slope of the temperature profile at the membrane side), as well as the membrane boundary layer thickness (distance to the membrane at which 90% of the maximum temperature of the profile is reached).
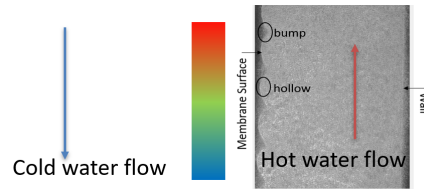
Figure 8.13: Rainbow color code for the rays localization in the reconstruction algorithm

8.3 Results and discussion

The test facility allows to produce two main outputs for different inlet flows and temperatures:
- the permeate flow
- the Schlieren pictures that are interpreted via an algorithm to extract the temperature gradient at the membrane interface and the boundary layer thickness

The matrix of the performed tests is the following (fig. 8.2):

Inlet flux (l/min)	Hot water channel T	Cold water channel T	Reynolds number
0.180	59.67	14.5	2524
0.202	60.25	14.5	2863
0.184	72.82	14.5	3087
0.207	73.48	14.5	3490
0.215	74.45	14.5	3675
0.202	74.68	14.5	3464
0.189	75.79	14.5	3278

Table 8.2: Optical experiments matrix

8.3.1   Permeate flow measurement

The permeate flow is measured directly by weighting the produced permeate over a given period of time.

8.3.1.1   Permeate flow measurement resolution

The permeate flow of a given experiment is collected in a bucket, weighted at the end of the experiment. The mass measure is then divided by the measurement duration to get the corresponding flow. Thus the precision of the permeate flow measurements depends on the precision of the scale (0.01g), and of the time measurements, (<1s).

Regarding temperature and pressure, the precision is that of the sensors, and of the averaging necessary as the temperatures fluctuates of several decimals over the course of a few seconds.

8.3.1.2   Permeate flow measurement results

The permeate flow measurements performed with the final module are plotted in fig. 8.14, as a function of the feed flow temperature T_{hot} (a)) and as a function of the inlet velocity V_{in} (b)).

(a) temperature of the hot water   (b) inlet velocity
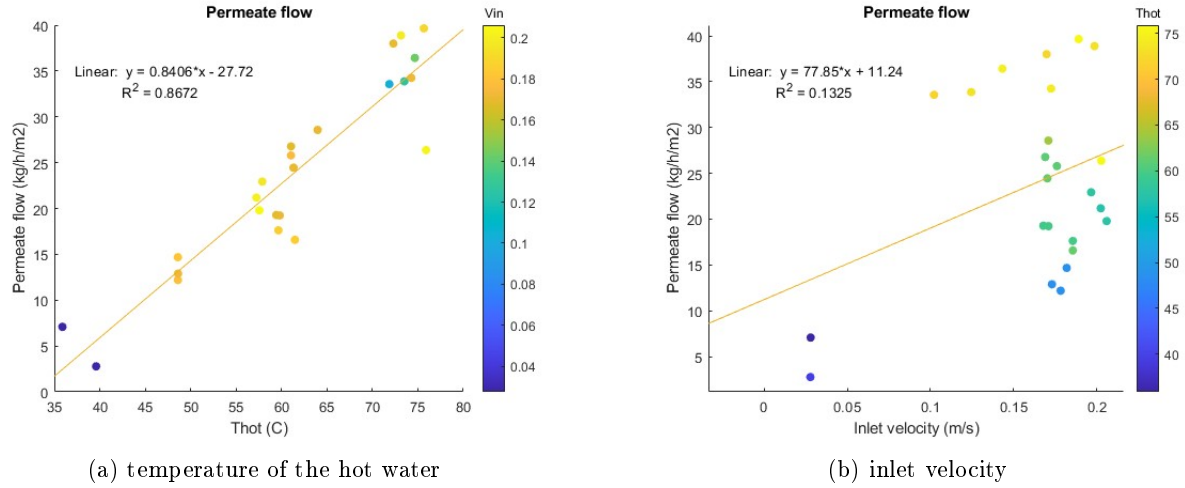
Figure 8.14: Permeate flow of the final module as a function of a) temperature of the hot water and b) inlet velocity

The permeate flow presents a strong dependency on the feed flow temperature T_{hot} (fig. 8.14 left), whereas the dependency to the inlet velocity V_{in} is barely observable (fig. 8.14 right). A linear fit is chosen as equation 5.15 shows a linear relationship between the permeate flow and the bulk temperature.

8.3.1.3   Permeate flow measurement discussion

The high dependency of the permeate flow with inlet temperature is coherent with the fact that with higher inlet temperature, more energy is provided to the surface water molecules which can then evaporate more.

One possible explanation for the low dependency of permeate flow on inlet velocity could be that the limiting phenomenon is the evaporation rate, and not the heat input to the interface molecules. The evaporation rate might be limited by the diffusion rate in the air-gap, as the current AGMD numerical models assume (see section 3.3). Another track of explanation is that despite the conception efforts the fully developed velocity flow is not reached within the current module length, and hence the velocity profile reached in the module might not be correlated to the inlet velocity.

The output temperature of the hot feed is several degree lower than the inlet temperature. Thus the evaporation rate must decrease along the hot feed flow, and the permeate outflow might not be constant along this flow. Consequently, cumulative permeate outflow should not increase linearly with the module length.

The table 8.3 below gathers some experimental permeate flow measurements performed on AGMD.

Air-gap thickness (mm)	Inlet hot temperature (°C)	Coolant temperature (°C)	Membrane pore diameter (μm)	Permeate flow ($kg/m^2/h$)	Source
3	70	20	0.45	40-50	[68]
10	40-80	20	0.2	0-5	[165]
4.352	65-80	20	0.92	10-14	[44]

Table 8.3: Experimental permeate flow measurements in AGMD

These results show a huge discrepancy, depending on membrane material and characteristics, and air-gap dimensions. However, our results appears in agreement with these results.

8.3.2 Temperature profiles measurement

The temperature profiles, inferred indirectly thanks to the algorithm described in section 8.2, allow the determination of a temperature gradient at the membrane interface, and a boundary layer thickness.

8.3.2.1 Temperature profiles measurement resolution

The resolution is discussed in section 8.2.2.

8.3.2.2 Temperature profiles measurement results

The following figures 8.15 represent the reconstruction of several (20) temperature profiles located around one of the hollows of the membrane (fig. 8.13), for the same inlet velocity ($V_{in} \approx 0.2m/s$) and hot water inlet temperature ($T_{hot} \approx 74°C$), reconstructed from pictures taken on different dates. This shows the reproductibility of the method: despite persistent variation between both recordings, the temperature profiles at the membrane side (left) are quite similar for identical conditions at different dates.
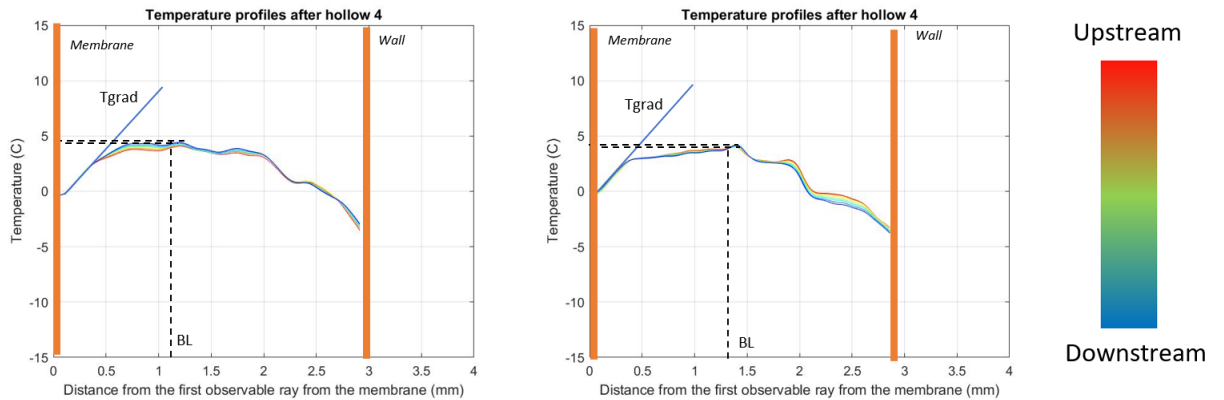
Figure 8.15: Reconstruction of the temperature profile for 20 pixel rows around one of the hollows (5) of the membrane for $V_{in} \approx 0.2m/s$ and $T_{hot} \approx 74°C$. The blue line indicates how the temperature gradient is calculated, while the black dotted line indicates how the boundary layer thickness is determined

Each curve represents the temperature profile reconstructed for a particular row. The color of the curves corresponds to the row's location in the channel according to figure 8.13.

Due to the high heat transfer coefficient of the module material, two temperature gradients may be noticed in all circumstances, one at the membrane (left side) and one at the wall (right side). This last significant temperature drop can be mitigated by improving the module's insulation.

The following plot (fig. 8.16) shows the impact of inlet temperature T_{hot} on the temperature profile, as it represents twenty temperature profiles located around one of the hollows of the membrane at an inlet velocity of about $V_{in} \approx 0.180 m/s$ and for two different hot water temperatures, $T_{hot} = 73°C$ and $T_{hot} = 60°C$.
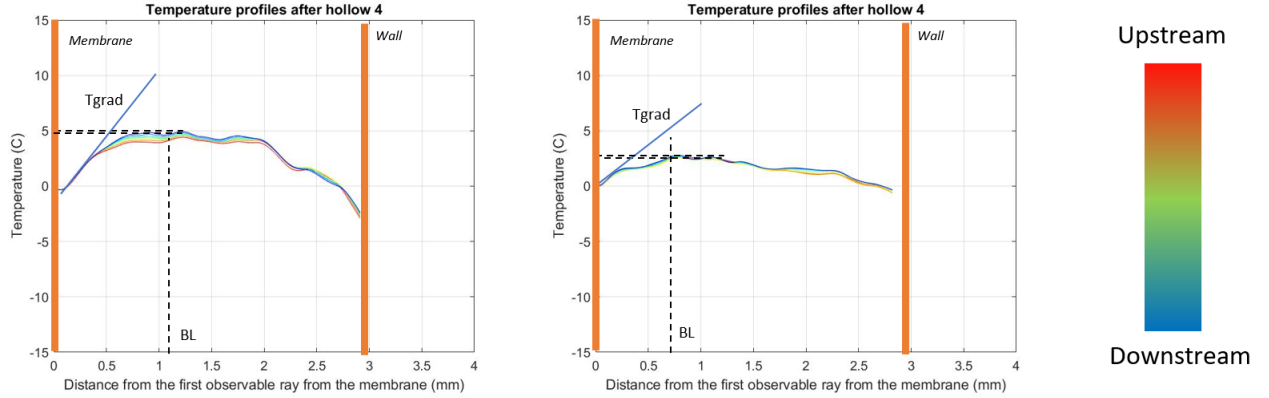
Figure 8.16: Reconstruction of the temperature profile for 20 pixel rows around one of the "hollows" (6) of the membrane for $V_{in} \approx 0.180 m/s$ and $T_{hot} = 73°C$ (a)) and $T_{hot} = 60°C$ (b)). The blue line indicates how the temperature gradient is calculated, while the black dotted line indicates how the boundary layer thickness is determined

As expected, the temperature gradient at the membrane interface for a higher inlet hot water temperature is steeper than for a lower hot water temperature.

The following plot (fig. 8.17) shows the impact of inlet flow on the temperature profile, representing twenty temperature profiles located around one of the hollows of the membrane at a hot water temperature of about $T_{hot} = 74°C$ and for two different inlet velocities $V_{in} \approx 0.180 m/s$ and $V_{in} \approx 0.225 m/s$.
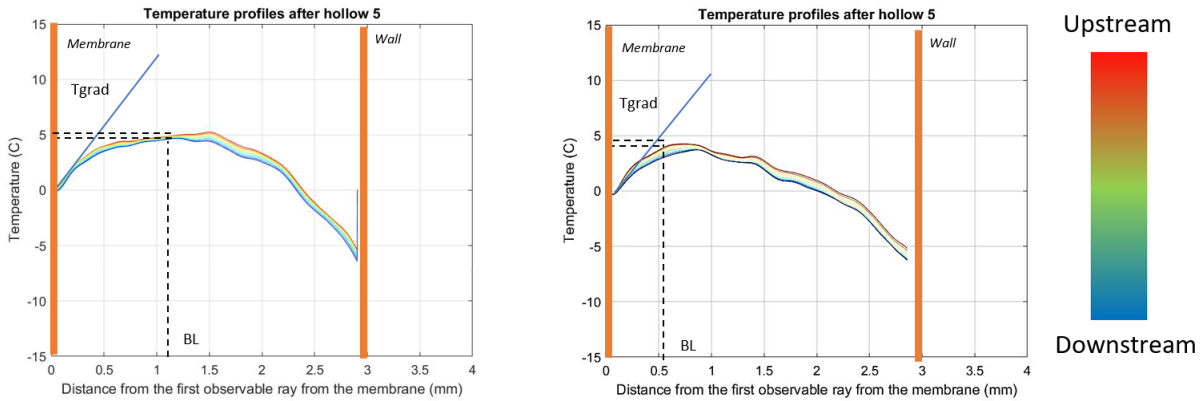
Figure 8.17: Reconstruction of the temperature profile for 20 pixel rows around one of the "hollows" (6) of the membrane for $T_{hot} = 74°$ and $V_{in} \approx 0.180 m/s$ (a)) and $V_{in} \approx 0.225 m/s$ (b)). The blue line indicates how the temperature gradient is calculated, while the black dotted line indicates how the boundary layer thickness is determined

The dependency of the boundary layer thickness and temperature gradient at the membrane interface on the inlet velocity is not clear. However the velocity range of the experiments is maybe not wide enough

to assess the influence of this parameter.

A change in the temperature profile also seems to develop along the membrane as shown in fig. 8.18 representing the temperature profiles at two different hollows of the membrane for the same measurement.
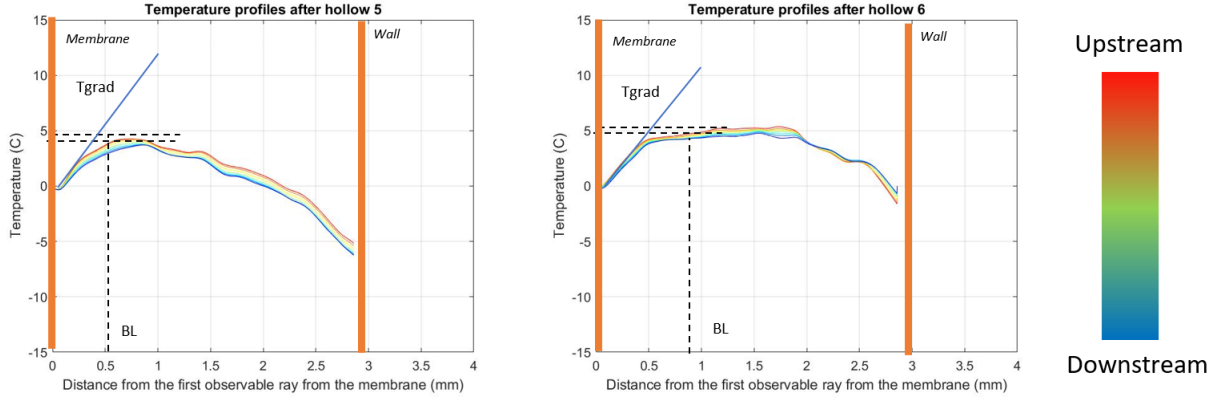
Figure 8.18: Reconstruction of the Temperature Profile for 20 pixel rows around one of the "hollows" (a) 5; b) 6) of the membrane for $T_{hot} = 74°$ and $V_{in} \approx 0.225 m/s$ (b)). The blue line indicates how the temperature gradient is calculated, while the black dotted line indicates how the boundary layer thickness is determined

These results are summarized in the following graph 8.19 representing the boundary layer thickness and the temperature gradient at the membrane interface as a function of the inlet velocity (V_{in}):
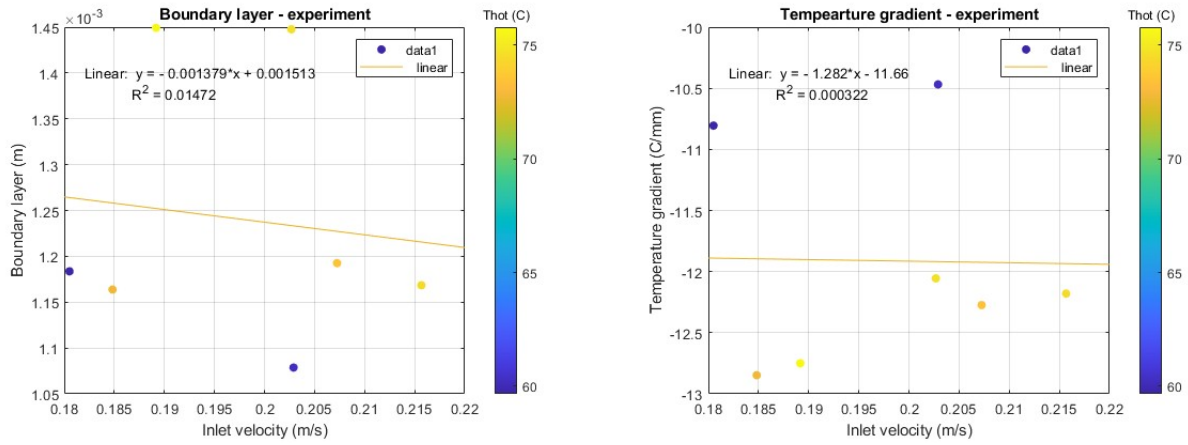
Figure 8.19: Boundary layer thickness and temperature gradient at the membrane interface for different inlet temperatures and flows

There is no clear trend in these graphs: the inlet velocity does not seem to influence clearly neither the temperature gradient at the membrane interface nor the boundary layer thickness.

The following plots 8.20 represent the temperature gradients at the membrane interface and boundary layer thickness as a function of the hot temperature:
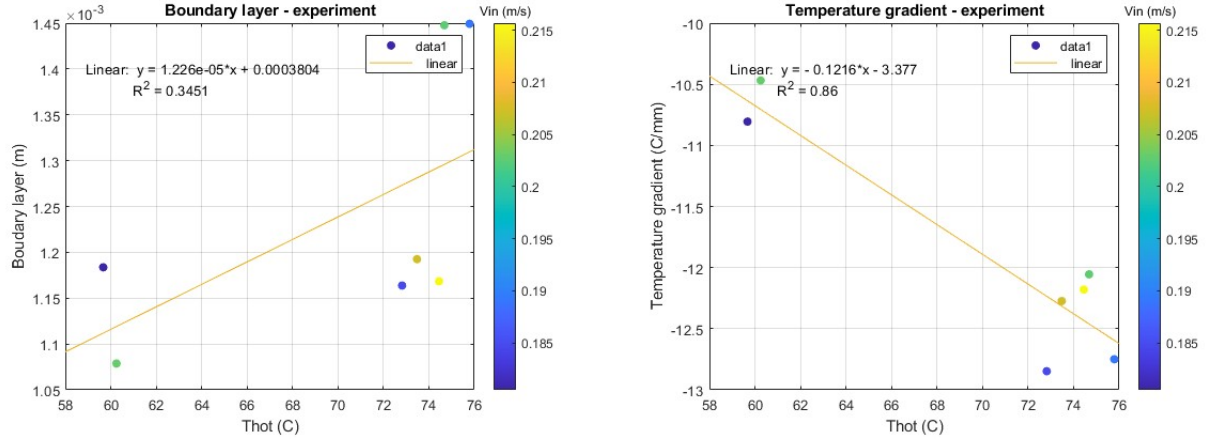
Figure 8.20: Boundary layer thickness and temperature gradient at the membrane interface for different inlet temperatures and flows

It can be observed that a lower inlet temperature results in a smaller temperature gradient at the membrane interface, and a smaller boundary layer. The linear interpolation represented in fig. 8.20 along with the corresponding R^2 shows that temperature gradient at the membrane interface presents a strong dependency on the hot inlet temperature. On the other hand, the linear interpolation for the temperature boundary layer thickness does not show a particular trend.

According to MATLAB ray-tracing simulation (section 7.4.2), for these temperature gradients, the first observable ray from the membrane is located at $6.8.10^{-5}m$ from the membrane, as shown in fig. 8.21, which is already less than the camera's spatial resolution.
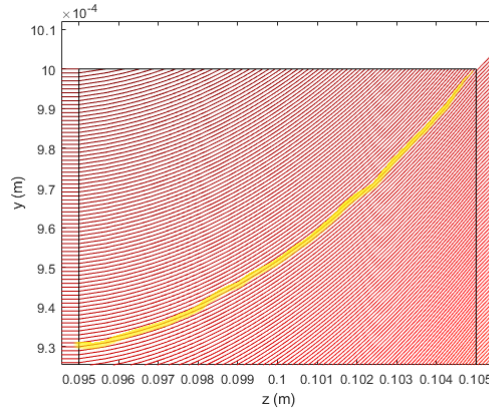
Figure 8.21: First observable ray for a temperature gradient of $13°C/mm$ at the membrane interface

8.3.2.3   Temperature profiles measurement discussion

As no experiment disclosing the inside temperature profile of an AGMD device, these experimental results will be confronted to simulated ones.

Alklaidi et al. [11] investigated numerically the thermal and velocity boundary layer thickness of an air-gap membrane distillation device. The hot channel and air-gap thicknesses are 2mm, the hot inlet temperature is 70°C and the cold inlet temperature is 20°C. The resulting temperature gradient at the membrane interface is about 0.075 times the temperature difference between hot and cold inlets temperatures (50°C), on a distance of about 0.2 times the hot channel thickness:

$$|grad(T)^m| = 0.1875 * (T_b^h - T_b^c) \tag{8.6}$$

or about $9.37°C/mm$ (see fig. 8.22). The thermal boundary layer thickness is about between 0.4 and 0.8 (depending on the location along the channel) times the hot channel thickness, or between 0.0008m and 0.0016m.
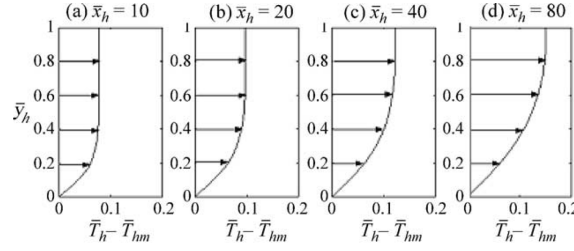
Figure 8.22: Simulated temperature gradient $(\overline{T}_h - \overline{T}_{hm})$ at different locations $(\overline{x}_h)$ of the hot channel as a function of the channel's height $(\overline{y}_h)$ from Alklaibi et al. [11]

The experimental results for temperature gradients and boundary layer thickness presented in this work are in the same order of magnitude as the numerical results from [11], the larger temperature gradient found in this work could be explained by the lower cold inlet temperature (15°C). When applied to our experimental conditions, the formula visually inferred from [11] for the temperature gradient (see eq. 8.6) provides highly correlated results with our measures (see fig. 8.23).
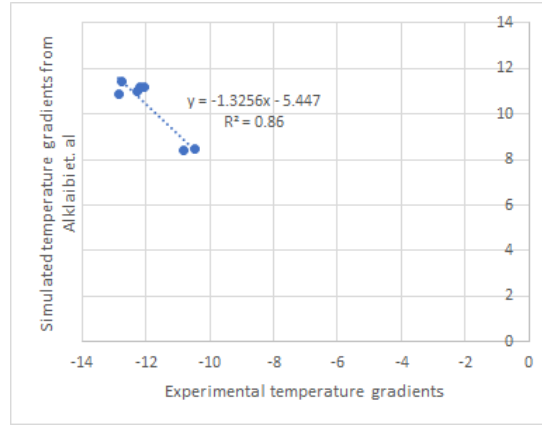
Figure 8.23: Comparison of the experimentally obtained temperature gradients with the theoretical relationship inferred from Alklaibi et al. [11]

Moreover, as can be seen in this study [11], the temperature gradient at the membrane interface appears to be constant along the hot water channel, which supports the averaging of the temperature gradients performed in this study.

The boundary layer thicknesses can be compared to theoretical ones.

For laminar flows the thermal boundary layer thickness is given by the Prandtl boundary layer theory: $BL_{Pr} = 5\sqrt{\frac{\nu x}{U_0}}Pr^{-1/3}$ with U_0 the bulk velocity, x the position along the channel length, ν the kinematic viscosity and Pr the Prandtl number.

For turbulent flows, the thermal boundary layer thickness is equal to the turbulent velocity boundary layer thickness: $BL_{turb} = \frac{0.37x}{Re_x^{1/5}}$ with $Re_x = \frac{U_0 x}{\nu}$.

As the Reynolds numbers of the experiment conditions are comprised in the transition zone, both of these thermal boundary layers thicknesses are calculated (fig. 8.24):
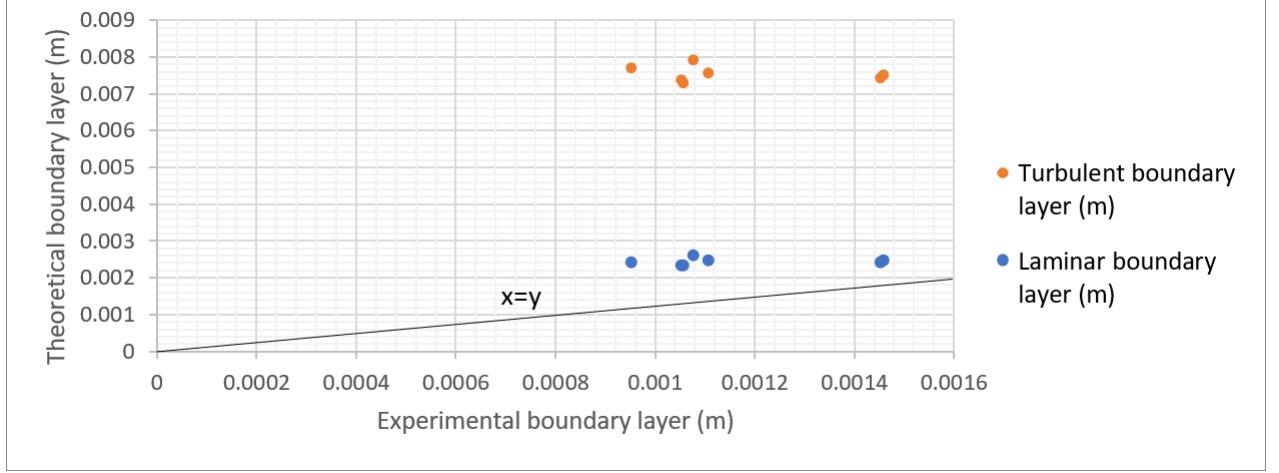
Figure 8.24: Laminar (blue) and turbulent (orange) boundary layer thickness as a function of the experimentally measured boundary layer thicknesses

The measured thermal boundary layers have the same orders of magnitude as these theoretical thermal boundary layers, but no agreement is found, and the experimentally determined thermal boundary layer thicknesses are smaller than any of the theoretically calculated thermal boundary layer thicknesses. The reason for this discrepancy might be attributed to several factors. Being in the flow transition area might render the different theories inapplicable to these experiments. According to Schlichting et al. [125], the transition zone occurs at Reynolds numbers of about 2300 occurs at a length equivalent to thousands pipe diameter downstream. This appears to validate the results: the measured thermal boundary layers are most likely still laminar and not yet fully developed, hence the smaller values obtained experimentally compared to the theoretical ones. Moreover, a calculation using the formulas from Rudi et al. [120] confirms a hydraulical entry length of 0.088m and thermal entry length of 1.15m, showing that the fully developed flow is not reached inside the module.

The similar phenomenon is observed in the Alklaibi paper [11], where the thermal boundary layer thickness increases downstream the hot channel.

Heat losses on the wall side may also affect the thickness of the thermal boundary layer: indeed, the bulk temperature in the absence of this heat loss may be higher than the current observable temperature, implying that the temperature boundary layer could be larger in the absence of this temperature gradient. Another hypothesis is that the roughness of the membrane impacts the turbulence of the flow and renders the Reynolds number not representative.

The discrepancy between the observed thermal boundary layer and the theoretical ones could potentially be explained by the occurrence of evaporation at the membrane interface. Indeed, the thermal boundary layer theory assumes that the plate on which the boundary layer forms is heated and maintained at a constant temperature, and describes mainly diffusion and convection heat transfer phenomenon inside the liquid phase. Whereas in the case of the membrane interface of the hot water channel of air-gap membrane distillation, evaporation occurs, generating a convective heat transfer through the interface. In particular, as developed in Addendum A.1, the liquid temperature at an evaporative interface is slightly lower than the one of the gas phase side of this interface. This consideration may render the theoretical thermal boundary layer thickness calculations obsolete.

Overall, the obtained experimental results show that the constructed experimental setup is capable of high spatial resolution measurements of temperature gradient in AGMD hot water channel. The challenge of acquiring data extremely close to the membrane (<0.2 mm) remains, but the reconstructed temperature profiles has shown that the thermal boundary layer extends beyond this region and could have been accurately captured.

Another important phenomenon to take into account is the fact that the resulting intensity profile is only 3mm thick whereas the hot water channel is 4mm thick. It is not due to the membrane position, as

the water tends to push the membrane and the membrane support towards the outside of the hot water channel. It is not either due to the membrane support, as the temperature profiles are measured at places where the membrane is pushed towards the outside of the hot water channel. The fact that the light beams are impacting the mirror with an angle $\theta \approx 0.13 rad$ decreases the final picture's dimensions on the camera by less than 2%. The fact that the optics might be misplaced can affect the picture dimensions by a few percent (see section 8.2.2). These factors only can not explain the important discrepancy observed (about 25%). One other hypothesis evoked is the fact that the module might be not perfectly perpendicular to the beam, thus resulting in a smaller beam section in the final screen: an angle of 5°between the light beam and the normal to the module's window can explain a reduction of the window width by 25%. Another reason might come from a phenomenon of light beam reversing due to the shape of the temperature gradient and the focal lengths of the optics (see section G.4.3), as can be observed in fig. 8.25.
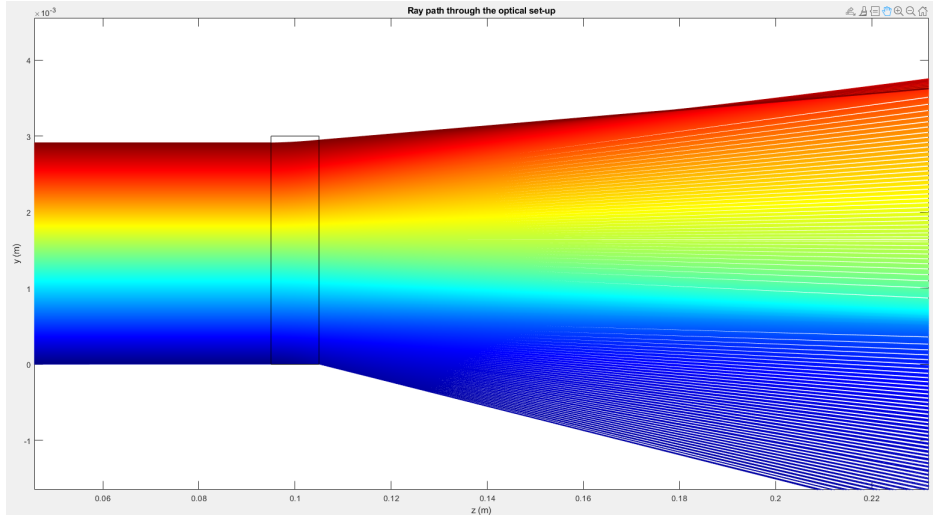
Figure 8.25: Reversing phenomenon when reproducing one of the experimentally reconstructed temperature gradient with the ray-tracing code

8.4 Comparison with numerical results from 3DH&MT model

The experimental temperature and feed flow velocity conditions listed in table 8.2 were simulated using the 3DH&MT model in order to compare both model and experimental results.

8.4.1 Numerical results

The 3DH&MT model is used to simulate the exact same hot and cold water channel inlet temperatures and velocities condition as in the experiment, as listed in table 8.1, in order to compare the resulting temperature gradient at the membrane interface and boundary layer thicknesses, in the aim of appreciating and validating the 3DH&MT model.

Figure 8.26 compares the simulated temperature profiles to the experimental profiles, for identical initial temperature and velocity conditions. The measured temperature profiles are then arbitrarily offset so that the calculated and measured membrane temperatures fit. The absolute measured temperature values are unknown, as described in 8.2 due to the lack of a bulk temperature measurement.
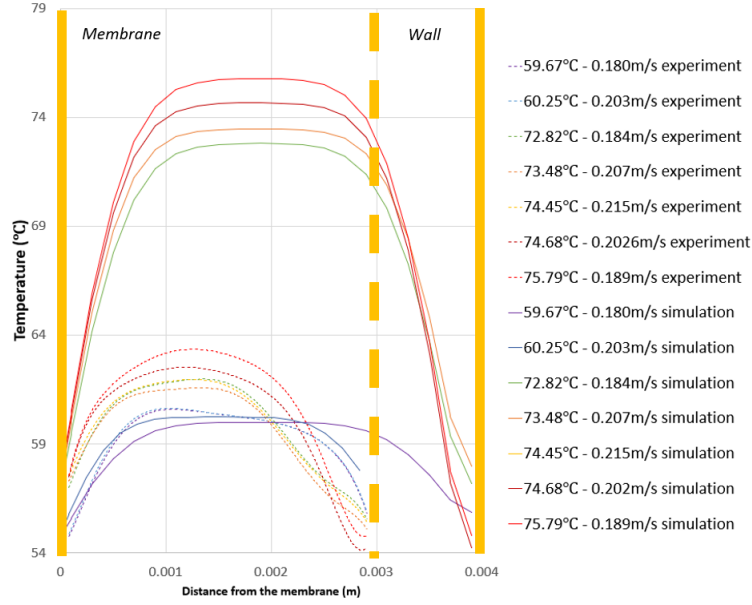
Figure 8.26: Simulated (plain lines) and experimental (dotted lines) temperature profiles at different boundary conditions

Despite the insulation efforts, a significant temperature variation occurs at the wall opposite to the membrane. The simulations attempt to replicate it by introducing a heat flow at the wall side calculated from the temperature profiles obtained during the experiments.

Fig. 8.26 confirms that the temperature gradients at the membrane interface increases with the inlet temperature.

Another important fact to notice in fig. 8.26 is that the reconstructed temperature profile from measurement does not fit the 4mm channel width, as discussed in section 8.3.2.3.

The experimental and simulated temperature gradients at the membrane as a function of the hot inlet temperature T_{hot} or velocity V_{in} are compared in fig. 8.27 and 8.28.

(a)

(b)
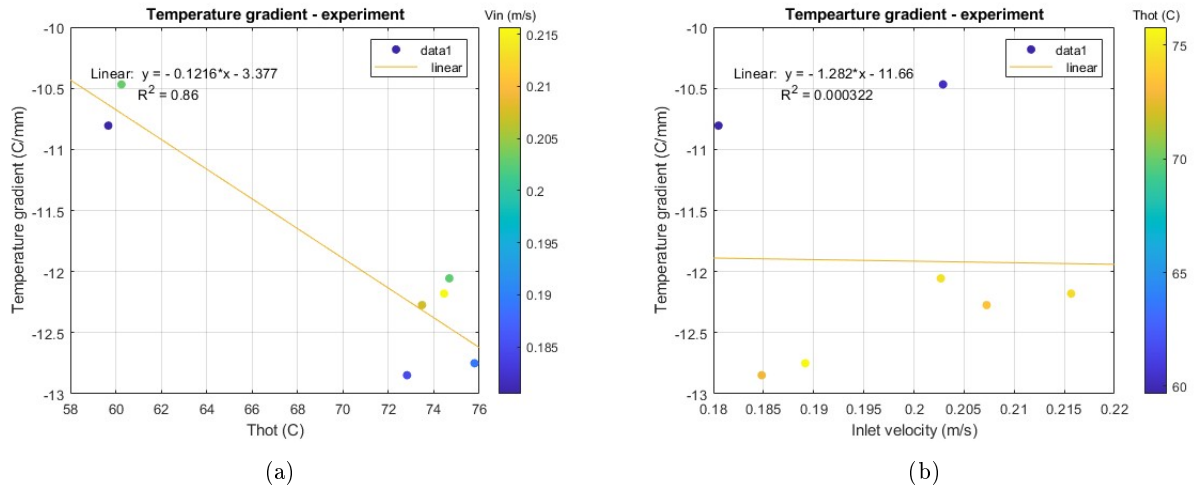
Figure 8.27: Comparison of the experimental temperature gradients at the membrane interface as a function of (a)) the hot inlet temperature (b)) the hot inlet velocity
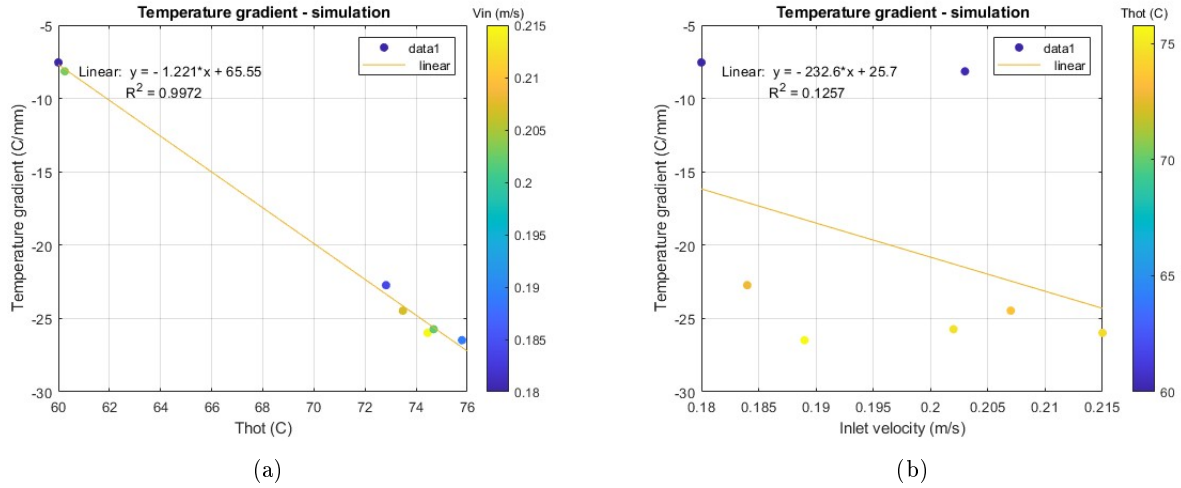
Figure 8.28: Comparison of the simulated temperature gradient at the membrane interface as a function of (a)) the hot inlet temperature (b)) the hot inlet velocity

Experimental and simulated temperature gradients at the membrane interface differ by several degree. Both show a strong correlation with the inlet temperature T_{hot} and a very weak one with inlet velocity V_{in}.

The experimental and simulated boundary layer thicknesses as a function of the hot inlet temperature T_{hot} or velocity V_{in} are compared in fig. 8.29 and 8.30.
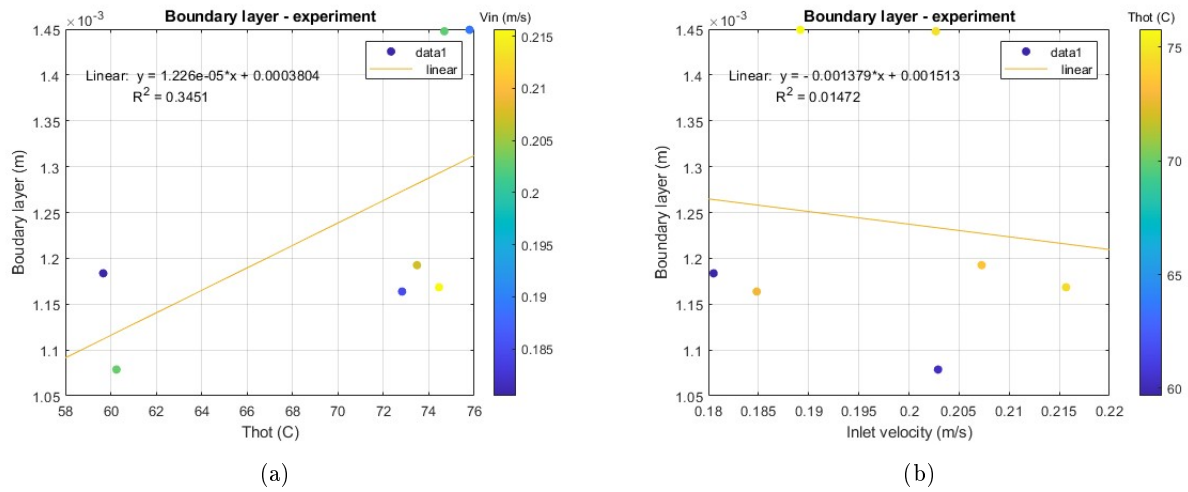
Figure 8.29: Comparison of the experimental boundary layer thickness as a function of (a)) the hot inlet temperature (b)) the hot inlet velocity

(a)   (b)
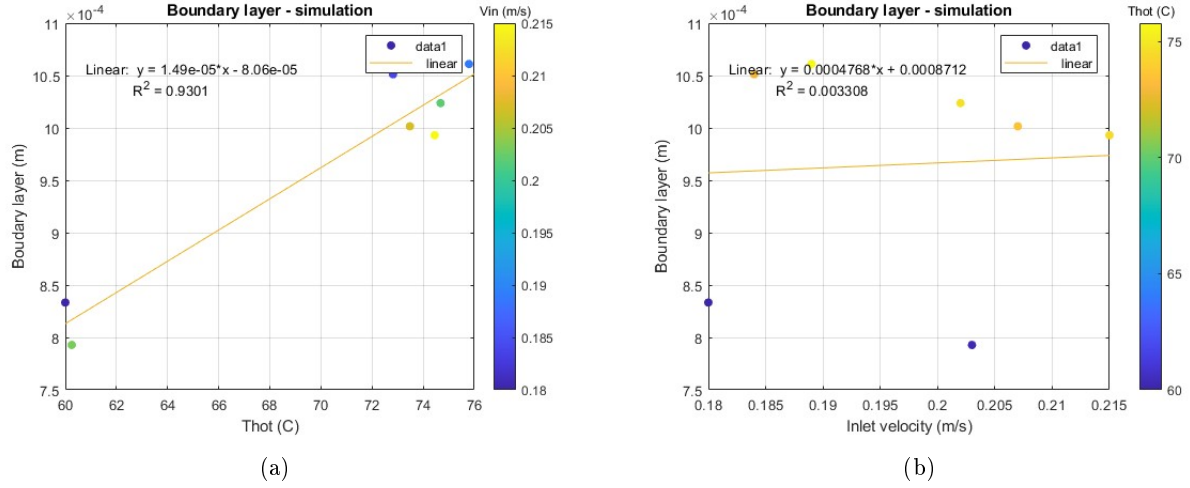
Figure 8.30: Comparison of the simulated boundary layer thickness as a function of (a)) the hot inlet temperature (b)) the hot inlet velocity

Both simulated and experimental boundary layers thicknesses are in a similar range. However, if the simulated boundary layer thicknesses show a strong dependency on inlet temperature T_{hot}, it is not the case of the experimental results.

The permeate flow, represented in fig. 8.31 and 8.32 as a function of the hot inlet temperature T_{hot} or velocity V_{in}, shows a great dependency on the inlet temperature of the hot channel, whereas there seem to be no dependency on the inlet velocity on this small velocity range. Moreover the experimental and simulated datas seem to agree reasonably.

(a)   (b)
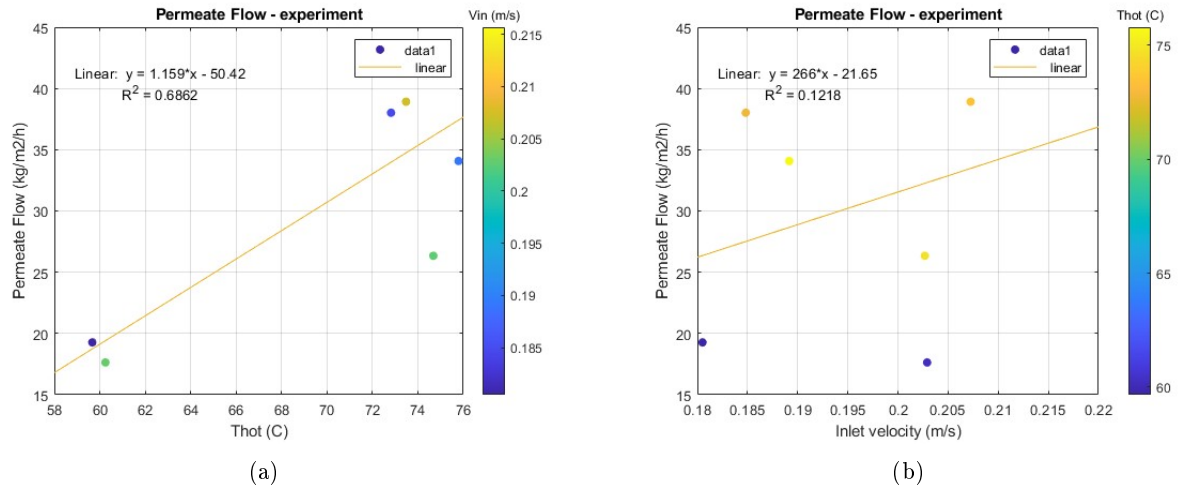
Figure 8.31: Comparison of the experimental permeate flow as a function of (a)) the hot inlet temperature (b)) the hot inlet velocity

(a) (b)
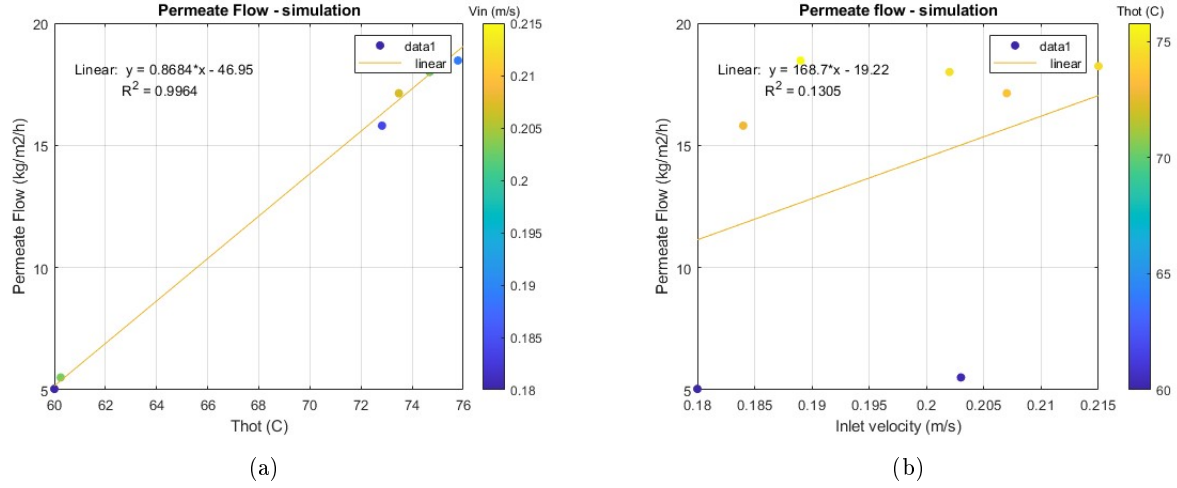
Figure 8.32: Comparison of the simulated permeate flow as a function of (a)) the hot inlet temperature (b)) the hot inlet velocity

In fig. 8.33, the experimental and numerical results are depicted one against the other for boundary layer thickness, temperature gradient at the membrane interface and permeate flow. The line of x=y is depicted too to show how good the experimental and numerical dataset correlate.

In particular, the calculated and experimental permeate flows show a quite good ($R^2 \approx 0.7$) agreement (fig. 8.33), even though there exist a coefficient factor different from one between both dataset.

No correlation ($R^2 < 0.4$) can be found regarding the boundary layer thickness between experimentation and numerical simulation, even though the values are not so far from the y=x axis. The disagreement between experimental and numerical data seem to increase with inlet hot temperature.

Finally, regarding the correlation with the temperature gradient at the membrane interface, datas are surrounding the curve of y=x hinting a good correlation, even though the linear interpolation of the data shows a much stronger coefficient factor between both numerical and experimental values, despite a $R^2 > 0.8$ (8.33).
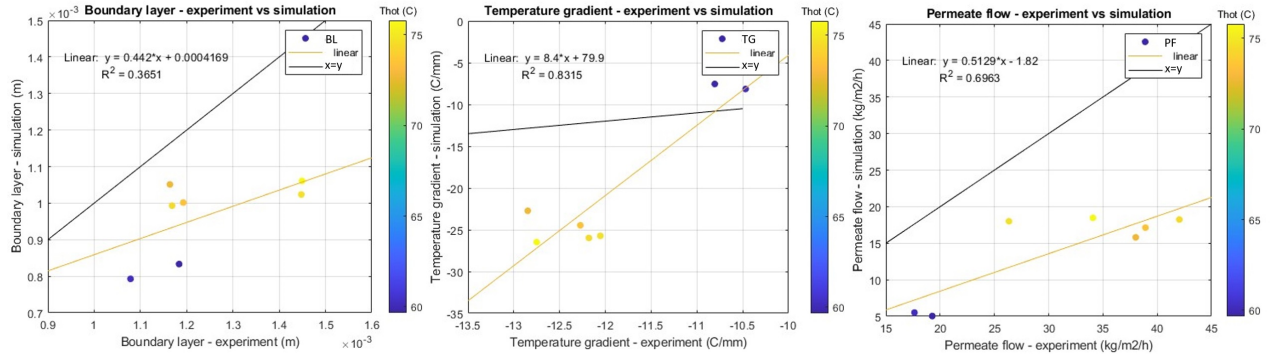
Figure 8.33: Correlation between the experimental and simulated boundary layers thicknesses, temperature gradients at the membrane interface and permeate flow obtained for different initial conditions

These graphs show that the experimentally determined permeate flow and boundary layer thicknesses are overestimated compared to the simulated values. The measured temperature gradients at the membrane interface, however, are smaller than the simulated ones at high inlet temperatures, and higher at low inlet temperatures.

8.4.2 Experimental and numerical results' comparison discussion

The simulated boundary layer thicknesses and the experimental ones do not correlate so well. As both simulation and experiment were conducted with the same boundary conditions and in particular the same module length, this result seems to confirm the assumption made in section 8.3.2.3 that the membrane roughness impacts the Reynolds number. Indeed, one of the limitation of the 3DH&MT code is that it

does not take into account water shear stress at the membrane, which can impact the flow. Additionally, the membrane support might impact the flow: the regular wave patterns presented at the membrane interface due to the water pressure against the membrane support might impact the flow regime just like a spacer would do (see section 3.2.2). Indeed, a study of very similar obstacles in a channel showed that these affect a lot the flow, as well as enhance the heat transfer [92]). Smith et al. [133] determined critical height delimiting range of weak flow response and large-scale separation motion (see fig. 8.34).
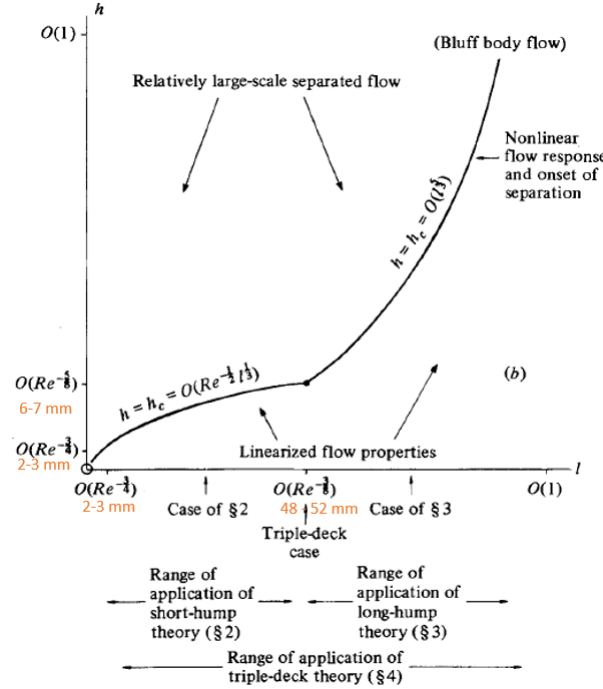
Figure 8.34: Critical height of a hump in a smooth pipe as a function of the hump's length and the Reynolds number. In orange, the values for our experimental conditions ([133])

Based on this graph, and as the membrane support present obstacles of 1mm long (see fig. 7.13), the critical height is $h_c = Re^{-\frac{1}{2}} l^{\frac{1}{3}}$, or about 1.7mm, which is higher than the actual height of the support (1mm). The current situation is thus in the linearized flow properties domain, the obstacle has a limited impact on the flow.

Alternately, the inaccuracy of the simulation may result from heat losses on the wall side affecting the entire measured temperature profile and, consequently, the thickness of the boundary layer. Indeed, the maximum observed temperature in the channel might not be the expected bulk temperature, and the experimental boundary layer thickness being calculated based on the distance from the membrane at which 90% of the bulk temperature is reached might be erroneous.

However, the simulation of very strong heat transfers at the wall side at steady state did not seem to confirm this hypothesis as it resulted in a much lower temperature at the wall side, but with a constant and stable bulk temperature equal to the inlet temperature. This simulations tends to show that the flow is not at steady state in the experiment (not fully developed), and hence the simulation does not represent very well what is happening in the experiment.

These heat losses at the wall deforming the measured temperature profile can also be the reason why the temperature gradients at the membrane side are higher than the calculated ones at low temperatures and lower at high temperatures. Indeed, the heat losses increase with the inlet temperature profile, thus worsening the deformation of the overall temperature profile, and impacting the temperature gradient at the other wall.

An additional explanation to the discrepancy between experiment and calculations regarding the temperature gradient at the membrane is the fact that the coolant is powered at a certain flow, whereas in the code only a constant temperature boundary condition is applied. Depending on the amount of

power the coolant can carry away and the amount of power brought by the hot inlet feed, the measured temperature gradient at the membrane can be increased or decreased compared to calculated ones.

Other possible explanations for this discrepancy between experiment and simulation can arise from the low quality poly-carbonate windows of the module (high quality glass windows were out of budget), generating a lot of diffraction, and hence a great amount of noise. Additionally, the intensity profile filtration method introduces some errors in the experimentally reconstructed temperature profiles.

Moreover, even though the non linearity of the camera response was taken into account, it might be possible that the saturation of the camera chip causes the experimental temperature profiles to be flattened. Introducing a filter before the camera would help reduce the saturation at the camera.

The small efficient surface of the membrane in the experiment might facilitate the rise of boundary layer phenomenon altering the results.

The higher values for measured permeate flux compared to simulated ones could be explained by the fact that the membrane characteristics between the code and reality differ due to a lack of information regarding the membrane used for the experiment.

The fact that the permeate flow shows a quite good agreement between experiments and simulation despite very different temperature gradients at the membrane interface and boundary layers thicknesses seems to confirm that the discrepancy comes from the optical observation method, and not from physical phenomena not taken into account in the 3DH&MT model.

Another element to take into account is the fact that the Schlieren observation method integrates the temperature profile along the whole hot water channel width, whereas the calculation provides the temperature profile at the side of the channel. As can be seen in figure 8.35 presenting the calculated temperature profiles in the middle of the channel and at the side, the temperature gradients decrease towards the side of the module.
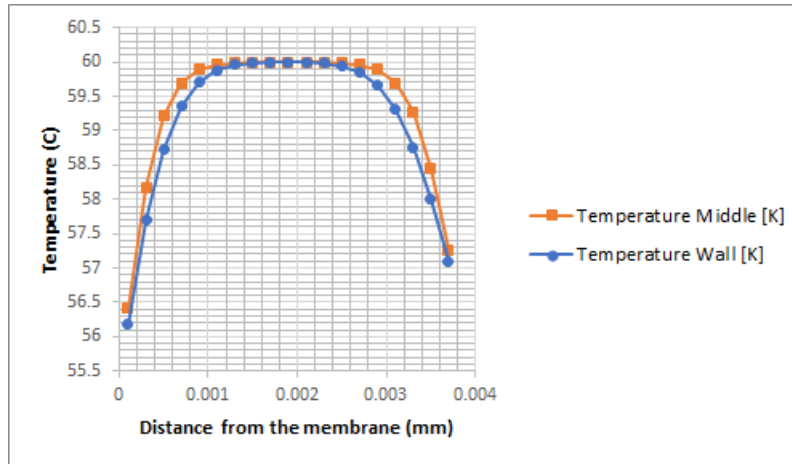
Figure 8.35: Simulated temperature profiles in the middle of the hot water channel (orange) and at the channel side wall (blue)

The downstream processes (diffusion and convection in the air-gap, and condensation on the cold plate) can also impact the temperature gradient inside the hot water channel. Indeed, the permeate thickness is assumed to be 0.5mm in the 3DH&MT code: when used horizontally, the permeate thickness in the module is measured at 2mm; and when used vertically, this thickness disappears. The modeling of the evaporation and condensation phenomena was investigated in the framework of this work (see section A.1). The influence of the position of the module on the diffusion and convection phenomena inside the air-gap, evoked in section 4.1.2.2, would also benefit from further research.

8.5 Conclusion on the dataset

This first dataset provides temperature gradients at the membrane interface, thermal boundary layer thicknesses and permeate flows for different boundary conditions in coherence with the datas reported in the literature. The test facility appears relevant in observing the energy input to the membrane interface and could thus be used directly to assess experimentally the best experimental conditions (boundary conditions, gap filling material, spacers, module geometries...) providing the process' highest energy efficiency and fresh water output.

In parallel, the comparison between the measurement of this test facility and the calculations of the 3DH&MT code for AGMD appears to validate this code, as the values lie within a comparable range with strong correlations, and the discrepancies can be explained by experimental default. The 3DH&MT model could thus maybe save experimental time by simulating several boundary conditions.

Chapter 9

CFD assessment of spacers' performance

In tandem with the setup of the test facility, CFD calculations are performed and analyzed according to the framework presented in section 6.4 on the two novel spacers geometries proposed in section 6.3. In particular, as a reminder, due to reserves on the current evaporation theories, the simulation are adiabatic and the thermal mixing is evaluated through a combination of CoV calculation and average perpendicular velocity at the membrane plane.

9.1   Results of CFD assessment of spacers' performance

Fig. 9.1 represents the flow movements generated by the different spacer geometries inside the control volume. It shows the velocity profiles in the center cross section of each of the four novel spacer geometries investigated. It is to be noted that in this chapter the membrane is presented on top of the hot water channel for visibility reasons. As described in 6.4, the gravity is not taken into account in this simulation as the calculation is adiabatic and both liquids introduced into the domain have the same density.
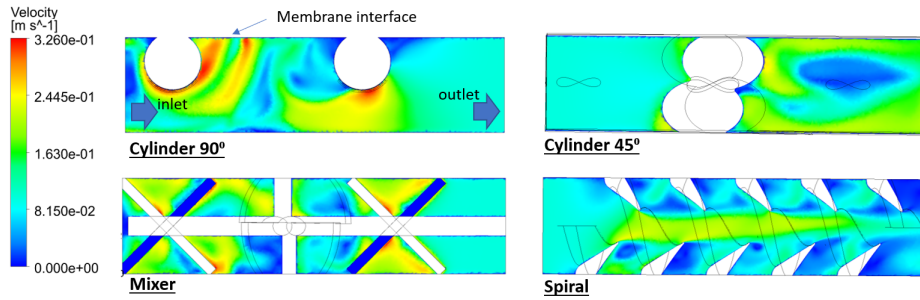
Figure 9.1: Velocity profile inside every spacer geometry

In this specific plane, the *mixer* geometry appears to produce the highest velocities inside the module, even close to the membrane, contrary the *spiral* geometry, inducing a high velocity in its center only. This is confirmed by the representation of the local perpendicular velocities Vz of which Vp is the average over the (x, y) plane located 0.1mm below the membrane (fig. 9.2):
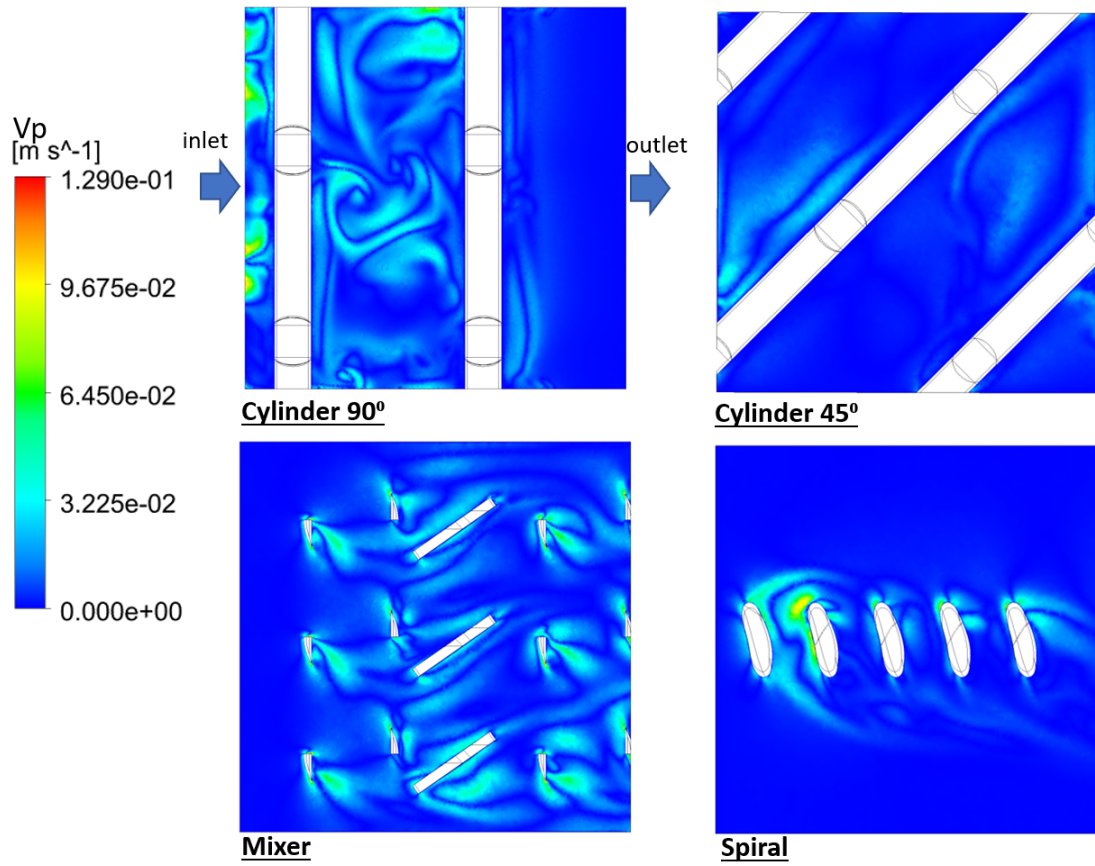
Figure 9.2: Vp profile for every spacer geometry

The *mixer* spacer appears to present the widest range of perpendicular velocities at the membrane, indicating flow reversal in some areas, and hence that there is no laminar boundary layer building up in this area. Indeed, as a reminder from section 6.4, Vp is used as a proxy for the formation of a boundary layer as the simulation is adiabatic.

The next three figures represent respectively the pressure drop (fig. 9.3), the CoV (fig. 9.4) and the Vp (fig. 9.5), for each investigated inlet velocity and each spacer geometry.
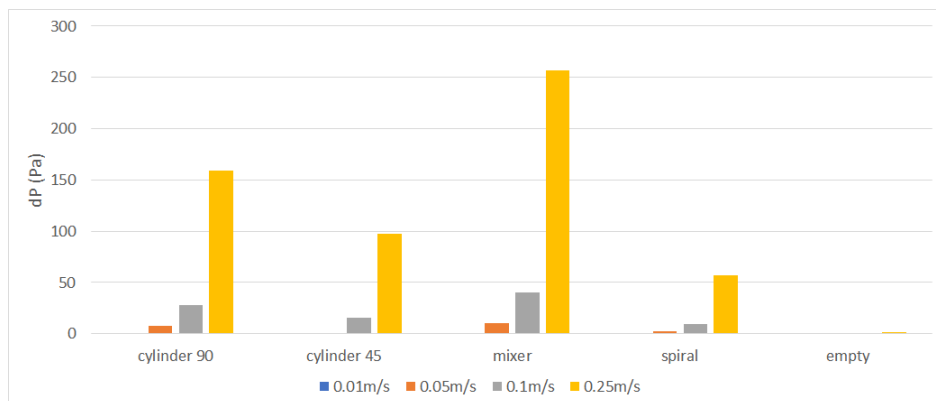
Figure 9.3: Pressure drop for every spacer geometry and all investigated inlet velocities
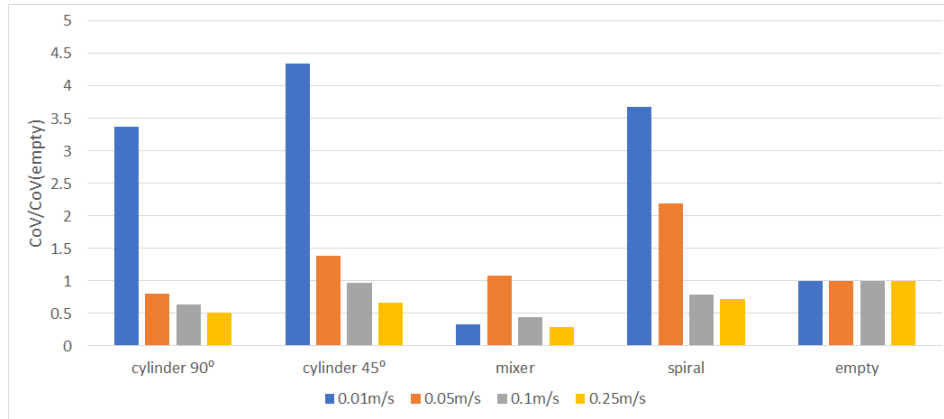
Figure 9.4: CoV for every spacer geometry and all investigated inlet velocities
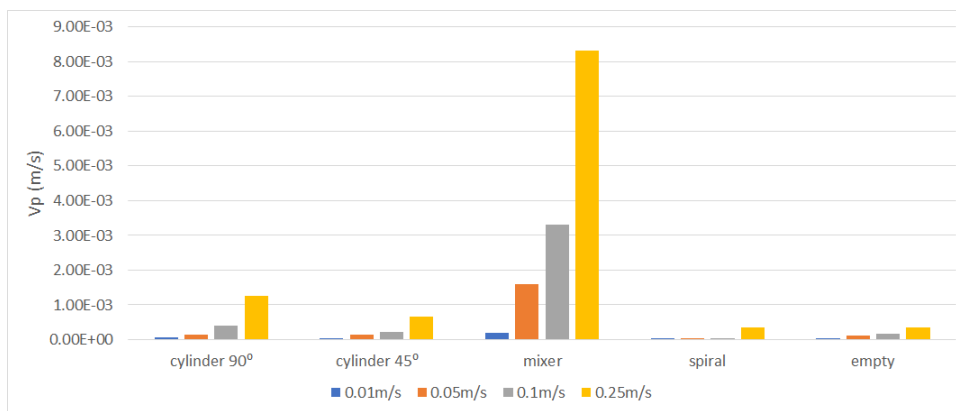
Figure 9.5: Vp for every spacer geometry and all investigated inlet velocities

These figures confirm that the pressure drop is higher in a spacer filled channel than for an empty channel, independently on the spacer geometry selected. The velocity perpendicular to the membrane interface and close to it is also always higher in a spacer filled channel than an empty one, with the exception of the *spiral* geometry.

The pressure drop, CoV and Vp increase with the inlet velocity.

To complete fig. 9.4, the CoV value for each spacer is represented as a function of the inlet velocity.
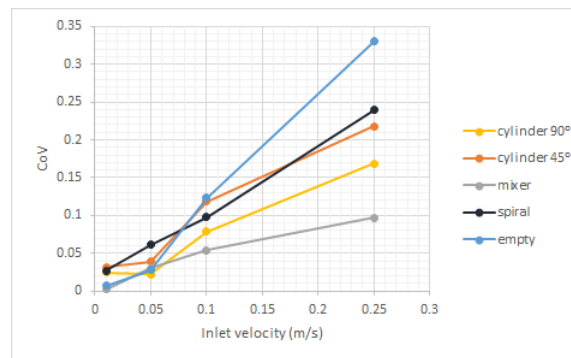
Figure 9.6: CoV of the different spacers for different V_{in}

As a conclusion, the presence of spacers always results in significantly decreased CoV whatever the selected geometry and the inlet velocity, except at very low velocities (below 0.1m/s).

A representation of the perpendicular velocity against the CoV is provided in fig. 9.7:
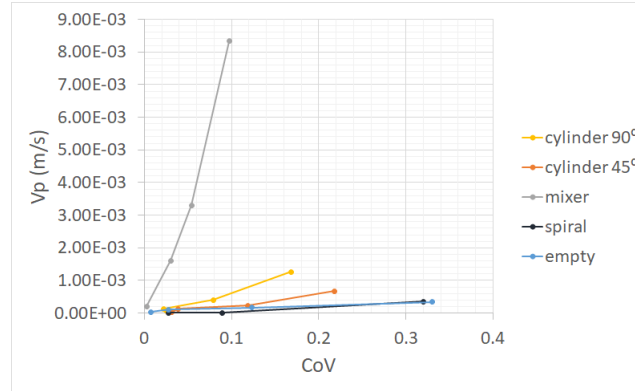
Figure 9.7: Vp against COV for the different spacer geometries

From fig. 9.7 it can be inferred that the *mixer* geometry is the one providing the best mixing performances as it produces the highest perpendicular velocities for the lowest CoV.

In fig. 9.8 the CoV is represented against the pressure drop between inlet and outlet of the test domain, for the different spacer geometries.
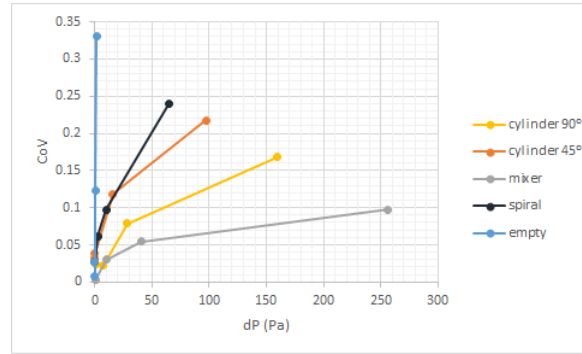
Figure 9.8: CoV of the different spacers against pressure drop

For all spacer geometries, the CoV increases with pressure drop, although the relationship is non linear in all cases. In addition, CoV increase seems to approach a limit as dP continues to increase.

The sensitivity analysis regarding the *spiral* geometry is represented in figs. 9.9, 9.10 and 9.11, depicting the CoV of the different *spiral* variations against the inlet velocity and the pressure drop respectively. These plots show a variation of the mixing performances of the spacers.
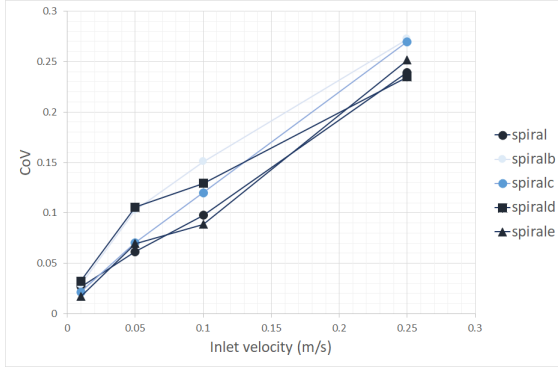
Figure 9.9: CoV as a function of the inlet velocity for the different *spiral* geometries variations
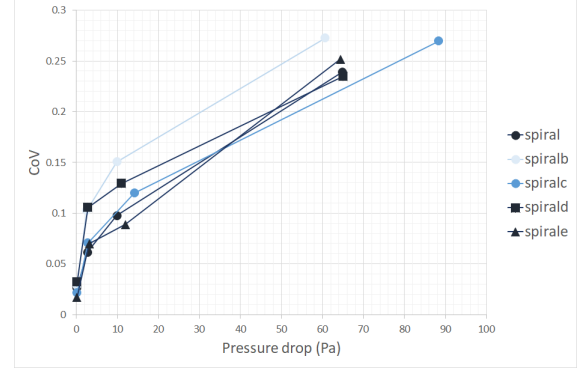
Figure 9.10: CoV against the pressure drop for the different *spiral* geometries variations
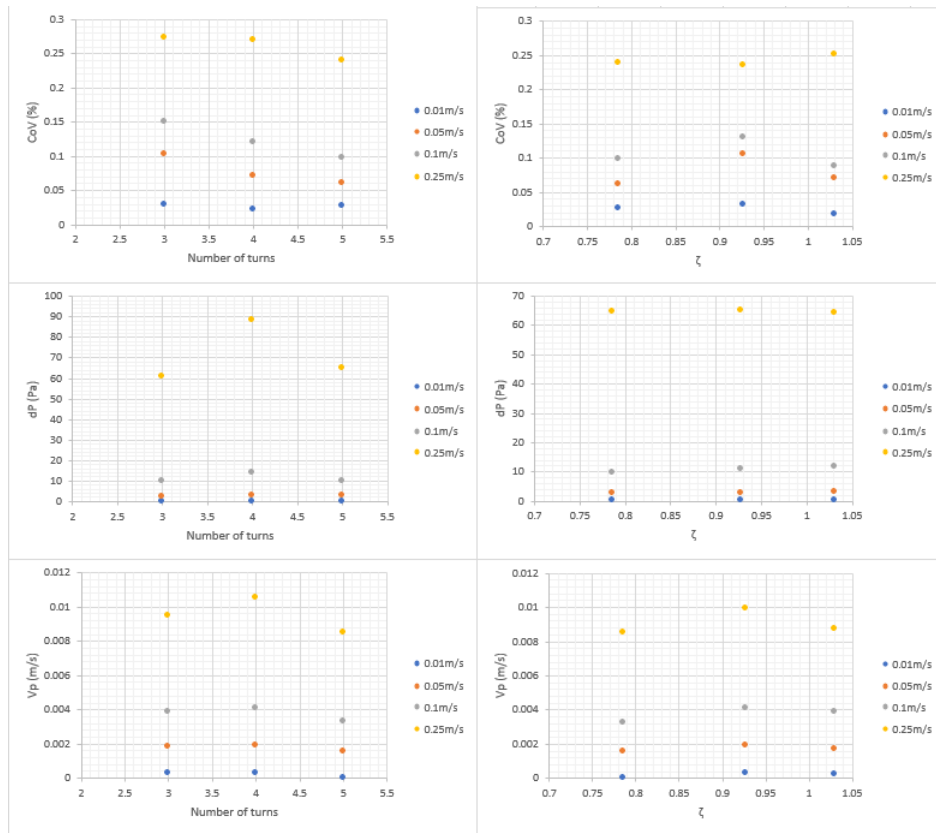
Figure 9.11: Impact of the spiral geometry on the spacer performances

The variation in the spiral pitch (number of turns along the test section length) is depicted in a gradient of blue, lighter blue meaning a smaller number of turns. The variation in the spiral wall steepness is represented with the different markers, triangle having steeper walls than square and than round.

From these graphs can be observed that at a given inlet velocity, both reducing the number of turns and steepening the spiral walls improve the mixing, with an advantage to the steepening of the walls (*spirald* and *spirale*) for $V_{in} > 0.15m/s$.

At a given pressure drop, these geometrical modifications improve the mixing performances as it decreases the CoV without a clear trend regarding the dominant parameter.
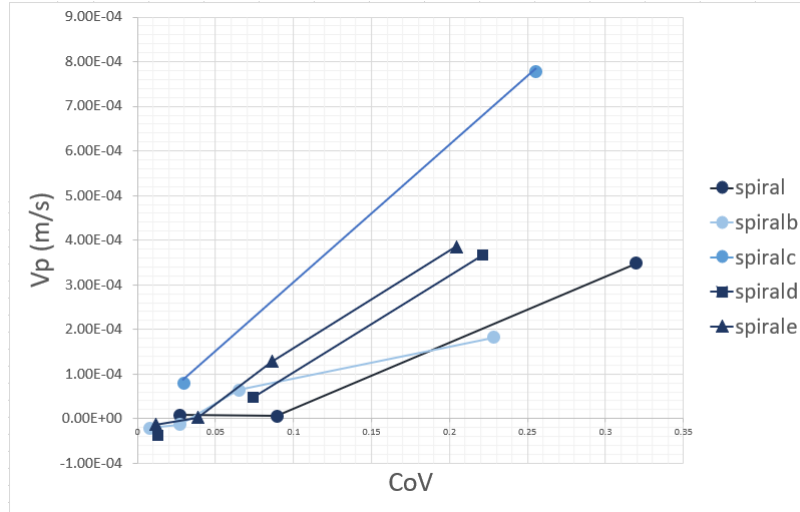
Figure 9.12: Perpendicular velocity against CoV for the different *spiral* geometries variations

Regarding the representation of the perpendicular velocity against CoV (fig. 9.12), the steepening of the spiral walls also leads to improved mixing, while the trend concerning the number of turns is not confirmed.

To put these geometrical considerations in perspective, fig. 9.13 presents the results of fig. 9.10 in fig. 9.8 to compare these modified spiral geometries to the other spacer geometries:
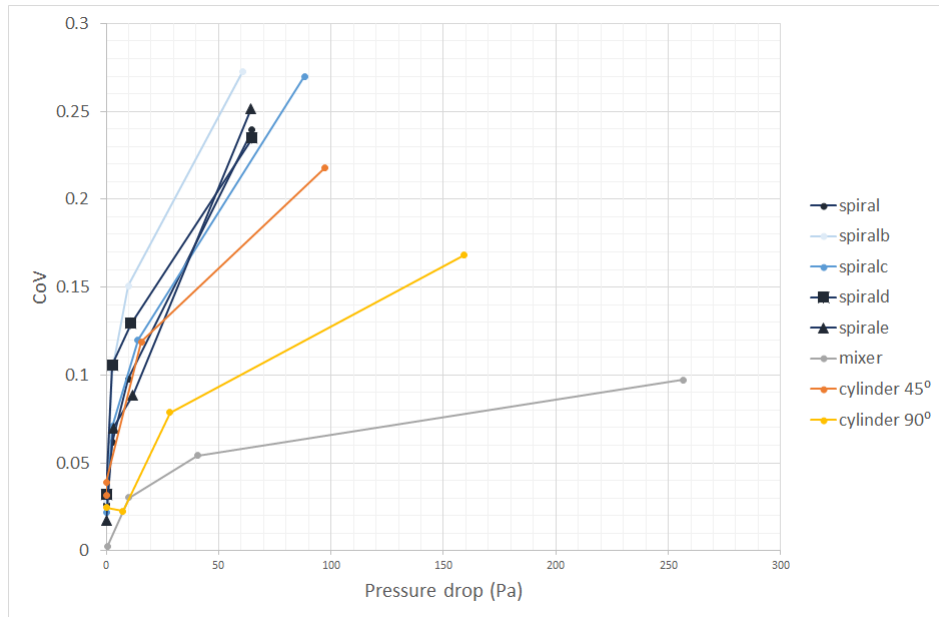
Figure 9.13: CoV against dP for all the spacers geometries and the different *spiral* geometries variations

Most of these geometrical modifications brought to the *spiral* spacer geometry improved its performance in terms of mixing, but not as much as a total change of the geometry.

Fig. 9.14 compares performance of the *mixer* geometry with the conventional *cylinder 90°* one.
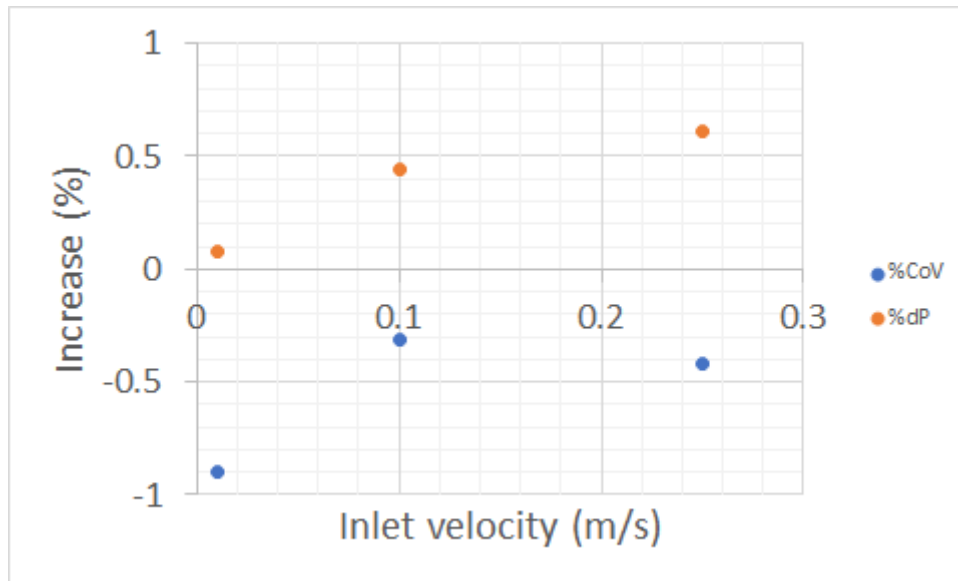
Figure 9.14: Comparison of the performances of *cylinder 90°* versus *mixer*

mixer's values for both CoV and dP are compared to *cylinder 90°*'s values. The *mixer* produces pressure drop about 50% higher than *cylinder 90°* and improves the CoV by about 40%. The mixer geometry CoV improvement is the highest and the dP increase the lowest at low inlet velocities.

Pressure drop and spacers' voidage are not correlated for the tested geometries (fig. 9.15). Therefore, it seems that the observed variance in pressure drop can be attributed to the difference in geometry and not to a variation in space occupation which also could affect the flow velocity and hence the velocity by modifying the channel cross section.
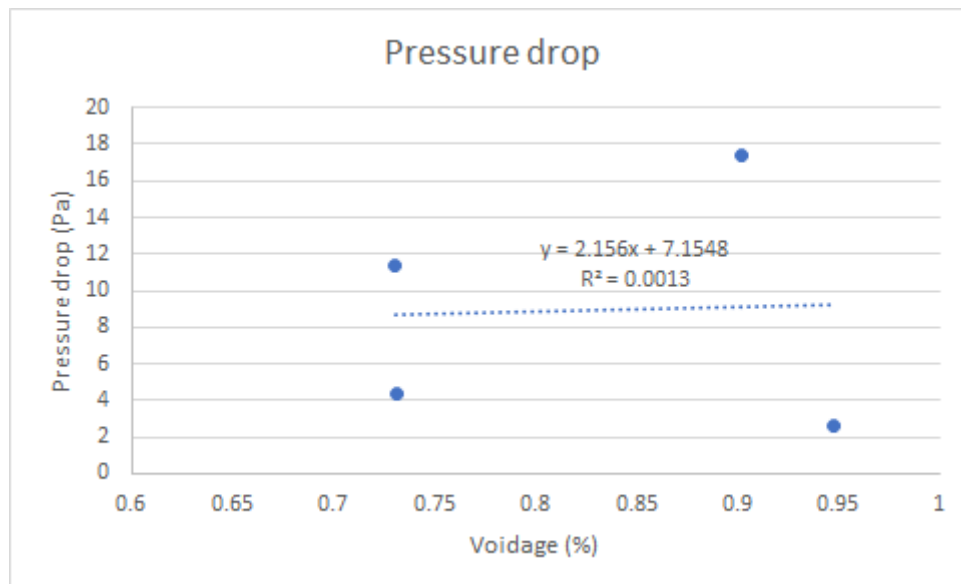
Figure 9.15: Pressure drop versus spacer's voidage

9.2 Discussion of CFD assessment of spacers' performance

The results presented in this study are consistent with observations provided by previous research. Indeed, this simulation confirms that the circular cross-section fibers net-type spacer presents a lower

pressure drop (fig.9.3) when used at 45° from the flow direction rather than perpendicular and parallel to it [38]. However, the mixing performances of *cylinder 90°* appear always better than those of *cylinder 45°*: its perpendicular velocity is always higher (fig. 9.5), and its CoV always lower (fig. 9.6).

These results also confirm that an empty channel always presents the smallest pressure drop (fig. 9.3). As soon as a spacer is introduced in the channel, the pumping power demand increases. However, above an inlet velocity of 0.1m/s, the mixing is always improved by the presence of a spacer, as can be seen by the decrease in the CoV and increase in the velocity perpendicular to the membrane (fig. 9.6).

This threshold can be interpreted as the fact that at very low Reynolds the spacers do not sufficiently impact the flow which is very laminar. Thus diffusion stays the main driver of the mixing and happens more easily when there are no walls inside the test section.

As shown in section 6.1, an appropriate formulation and interpretation of CoV appears as a relevant mixing indicator, correlating well with typically used Sherwood number. It allows to assess the quality of the interlayer mixing by complex 3D spacer geometries, for which adaptation of Lévêque is not feasible.

The parameter Vp provides complimentary information to CoV. Indeed, they are positively correlated (fig. 6.2), meaning that when the velocity is high the mixing performance is low. This suggests CoV indicates the mixing performance in the whole channel cross section, while Vp provides local information regarding the formation of a boundary layer. The fact that the two do not vary simultaneously in the direction of improved mixing (they would be negatively correlated) might be a result of mixing occurring largely through diffusion (for a low CoV with a low Vp) or primarily via convection (for a high Vp with a high CoV). It may also occur as a consequence of the formation of a boundary layer (as a result of spacer geometry) in an otherwise well-mixed channel.

These simulations also confirm that pressure drop and spacer mixing performance are negatively correlated. Thus optimizing both in parallel still requires further investigation of novel designs.

SM geometries based on industrial standards perform well, and merit further research in mixing enhancing devices operating in a laminar flow regime.

Of the two novel proposed geometries, the *spiral* spacer presents the closest behavior to an empty channel: the lowest pressure drop (fig. 9.3) with similar CoV (fig. 9.6). It is thus well suited for situations where a spacer is mandatory for structural reasons, but no additional pumping energy demand desired. Indeed, for a given mixing expectation, it is the spacer producing the smallest pressure drop.

The *mixer* presents the highest perpendicular velocity at the membrane (several orders of magnitude higher than the other geometries) and the smallest CoV than all spacers, albeit with the higher pressure drop of all spacers. It is thus a perfect candidate for applications where the mixing is more important than the energy consumption, as at a given pressure drop it is the spacer geometry presenting the best mixing, both in terms of global concentration homogeneity (low CoV), and in local convection at the membrane interface (high Vp).

As an illustration, a rough calculation based on the experimental results shows that the heat losses in an empty channel are on the order of 40 to 60 J/m^3 (simulated results give values up to 150 J/m^3). Thus, two areas of efficiency of the spacers can be delimited (see fig. 9.16): below 40 J/m^3 the spacer saves energy overall, whereas above 150 J/m^3 only heat is saved but productivity is improved. The first area is mainly dominated by the *spiral* geometry, whereas the second is ruled by the *mixer* geometry.
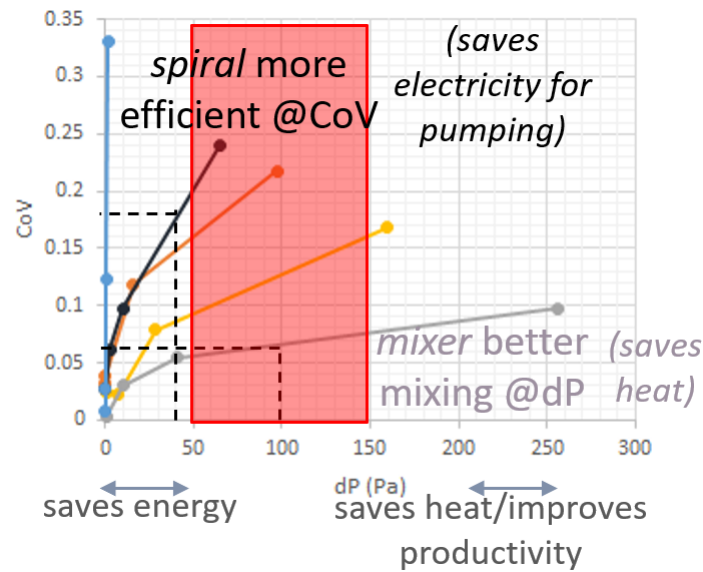
Figure 9.16: Efficiency regimes of the spacers

While the *spiral* spacer is physically similar to the helical spacer described in Shrivstava et al. [131] it does not exhibit the same increase in mass transfer, which is estimated to be four times more than in an empty channel at the same flow rate. This could be because, despite their similarity, the particular characteristics of the design of this spacer type have significant impact on the performance. Indeed, as the sensitivity analysis shows, the angle of the spiral walls has a great impact on the mixing performances of the *spiral* spacer. Moreover, in comparison to the twisted tape, the *spiral* spacer provided in this study presents a hole in the center.

Variations within the spacer's design has a huge impact: one can not state that one particular spacer shape performs the best as it depends on its geometrical parameters.

Conclusion of part III: achievements

The Schlieren method was implemented as part of an experimental test-bench enabling the observation of inside temperature profiles across the hot water channel of a tailor made module, allying relevance for the chosen method with crucial characteristics such as waterproofness.

Three variables are simultaneously measured: measures of the permeate flow, observation of the temperature gradient at the membrane interface and boundary layer thickness.

Overall, the Schlieren method, providing a continuous temperature profile perpendicular to the hot water channel and closest to the membrane, is successful in distinguishing between distinct temperature profiles based on their location in the channel, or the operational conditions, and provides consistent results with the literature, and are the first experimental poof for MD. It allows the determination of both a temperature gradient at the membrane, and a boundary layer thickness in the hot water channel.

The comparison of the first results obtained with the test facility are compared with calculated results using the 3DH&MT model. The temperature gradients at the membrane interface and permeate flows are of the same order of magnitude and show similar trends with strong correlations, partly validating the 3D code. Explanation are provided to explain the discrepancies observed regarding the boundary layer thickness values. Further measurements could reinforce this validation.

Moreover, the two novel spacer geometries presented expand the application range and research possibilities for MD spacers, providing advantages in two very distinct spacer roles. In the first role, the spacer serves primarily as a structural component, and thus the smallest possible pressure drop is desired. The *spiral* geometry is the most adapted in this situation because it minimizes the pressure drop. When improved mixing is the target of the spacer, the best mixers with minimal pressure drops are sought. Here it is the *mixer* geometry that answers this need the best.

Furthermore the different geometrical parameters of a specific geometry can greatly impact its mixing performances.

The CoV coupled to the perpendicular velocity Vp appears as a relevant mixing indicator to assess the performance of mixers of complex 3D geometries.

General conclusion

Among all existing water desalination technologies, the advantage of Membrane Distillation is to rely on low-grade heat, the most degraded form of energy, which can be obtained from the sun or from any industry that emits heat into the environment. Its limitation is its low permeate flow compared to current industrial desalination solutions.

By the introduction of an air-gap between the hot and cold water streams, Air-Gap Membrane Distillation increases the energy efficiency of this process, however at the expense of a slower mass transfer.

To improve AGMD's performance, both theoretical and experimental approaches are proposed in this work.

The first research question (*what does the temperature gradient look like inside the AGMD'hot channel?*), is answered thanks to the development of an experimental facility allowing the observation of the temperature gradient in the hot channel of a tailor-designed AGMD module.

The choice of an optical observation method required the design of a specific AGMD module, built to enable the observation as close to the membrane as possible, both in laminar and turbulent conditions. This module was designed in an attempt to reproduce the expected industrial conditions in terms of geometry and flow.

The experimental facility relies on an optical observation method (Schlieren), allowing the visualization of the continuous hot water channel temperature (and later concentration) profiles, under different operating conditions (inlet hot and cold temperatures, inlet velocity). This test-bench has a spatial resolution of $1.95 \pm 9.7.10^{-4} \mu m$ and allows to observe maximal temperature gradients of $18°C/mm$. Its resolution, varying from $0.002°C/mm$ to $20°C/mm$ depending on the localization on the filter, enables to use it as a two-wavelength Schlieren method in a second time. This optical method, often used for visualization, is used here for quantification of the heat transfer phenomenon thanks to the use of a filter gradient instead of the usual Schlieren knife, and a specific interpretation algorithm. The use of a gradient filter also broadens the observable temperature gradient range compared to a knife.

A reconstruction algorithm is proposed, which gives steps to further interpret the Schlieren pictures, and generates the corresponding continuous temperature profiles. The spatial resolution is impacted by this method and the observable ray closest to the membrane is thus at 0.07mm from it. This algorithm showed that the test-bench is successful in distinguishing between distinct temperature profiles based on their location in the channel, and the operational conditions. It allows the determination of both a temperature gradient at the membrane, and a boundary layer thickness in the hot water channel. In particular, it shows consistent results with the literature, such as an increasing boundary layer thickness along the hot water channel, an increasing temperature gradient with the inlet temperature, and a temperature profile quasi independent on the inlet velocity.

A ray-tracing simulation is constructed to forecast the results of the optical method and confirm the observed temperature profiles.

The current limitations of the set-up mainly relies on the positioning of the module and the temperature and flow conditions which have to be more carefully monitored for the next trials. Improvements can also be performed thanks to better quality windows.

Overall, this achievement allows an unprecedented access to the phenomenon occurring inside the hot water channel and especially close to the membrane. The understanding of the process is thus deepened thanks to the provided experimental results regarding the performance of the AGMD module, both in terms of output flow and temperature profile (temperature gradient at the membrane and boundary layer thickness). The energy transfer efficiency can thus be compared between different operating conditions in order to optimize them and improve AGMD performances.

The second research question (*how accurate are the existing models to describe this temperature gradient?*) is answered thanks to the comparison of the experimental results obtained with the previously discussed experimental facility to the expected results of the 3DH&MT model developed at University of Luxembourg.

Experimental and numerical data show similar trends and orders of magnitude, and interesting correlations. Tracks of improvement are identified to increase the accuracy of the results.

Both experiments and models present shortcomings that, if remedied, might enhance the accuracy of the comparison and thus strengthen the model experimental validation.

The main application of this result is that the experimentally validated 3DH&MT model can thus be used to simulate more complex 3D AGMD geometries in order to optimize its efficiency.

The third research question (*how can spacer geometries influence AGMD performances?*) is answered via the conduction of numerical CFD simulation of two novel spacer geometries, compared to the conventional currently used ones. These alternative spacer geometries are proposed to improve mixing and hence boost AGMD permeate flow without significantly raising pumping energy requirement. Based on a review of industrial mixing strategies, particularly static mixers, two novel spacer geometries are proposed. Their performance are evaluated under various flow conditions, and compared to that of traditional net-type spacers designs. According to the results of the testing, the *spiral* design produces the minimum pressure drop for a given mixing performance, which is useful in situations where spacers are structurally necessary and energy is restricted. The *mixer* geometry, on the other hand, provides the best mixing performance for a given pressure drop, which is of relevance when the primary purpose is to boost mixing regardless of the rise in energy consumption.

The spacer performance analysis could be improved by the introduction of an energy efficiency parameter, as well as the evaporation at the membrane interface.

This work on spacers broadens the range of available spacer geometries and their domain of application, thus contributing to the improvement of AGMD performance by reducing its energy consumption, and increasing its energy efficiency.

Thus, this work contributed to AGMD support by providing a comprehensive experimental and numerical framework of study of the heat transfers of the process. The different obstacles to evaporation can thus be further studied to deepen the understanding of the relevant phenomenon. Moreover, several solutions to overcome these obstacles are proposed: through the optimization of operating conditions via the experimental set-up; through the optimization of the module geometry via the validated 3D H& MT model; or thanks to the introduction of special geometry spacers to enhance the convection inside the channels.

Outlook

To remedy the limitations identified in the current work, several further research tracks are identified.

The module might be upgraded by allowing full optical access to the entire channel length in high-quality glass (SQ1, Schott). A filter dimming the intensity reaching the camera chip could also be a great improvement to reduce the imprecision of the method.

Using aerogels[1] to insulate the wall could be an interesting addition to ensure that the temperature gradient recorded at the membrane is not tainted by the heat losses at the wall.

The membrane support might be adjusted so that the membrane is folded upward on one half and downward on the other, allowing visibility on both sides of the membrane, given that the circumstances in these two compartments (hot water channel and air-gap) are fairly comparable.

Adding a thermocouple to measure the bulk temperature inside the hot water channel would also increase the accuracy of the reconstruction algorithm by providing the integration constant to the algorithm.

Regarding experiments, the initial concept of coupling Schlieren and interferometry data might be implemented to strengthen the validity of these findings.

Experiments with other air-gap filling materials could also be carried out with the set-up in order to assess the impact of these different materials on the temperature profiles.

Experiments with the two lasers and salty water would, of course, be the highlight of this project, in order to validate the concentration profiles provided by the 3DH&MT model.

Other experiments could focus on opaque layers on any membrane type (such as fouling or scaling), or the study of diffraction patterns caused by membranes (since it is unique to flow and membrane characteristics, it can be interesting).

Additionally, the study of the influence of the membrane support pattern on the flow and heat and mass transfers might interestingly complete this work.

Performing experiments by introducing spacers into the hot water channel could also be utilized to confirm the numerical simulation evaluating the impact of spacers on the AGMD's permeate flow and energy efficiency.

On the theoretical side, the efficiency parameter E defined in Chernyshov et al. [30] appears to be more relevant for analyzing the overall energy efficiency of MD processes than just GOR, which does not take into account pumping energy.

Moreover, a life-cycle analysis of membrane production to see if using a membrane vs a standard distillation set-up makes sense would be interesting to choose which type of spacer to use or not. Some reflections were started, using OpenLCA and looking for previous LCA analysis of aspects of AGMD (PTFE for instance [64]), but this task requires a substantial budget to have access to broader LCA databases.

Finally, any boundary layer phenomenon can be observed and quantified using the optical test bench developed in this thesis. As heat is the most degraded form of energy, being able to monitor its losses and optimize its transfer is of great interest.

Furthermore, AGMD could be applied to other types of water than just salty water, as long as the undesirable components are not evaporating at the operating temperatures. In particular, AGMD could be applied to waste water.

Additionally, in the context of depleting fertilizer resources, some nutrients like phosphorous are diluted to the ocean. As discussed in Xie et al. [164], AGMD alone and in combination with other desalination processes, could be one way to recover these nutrients (N, P, K), either from waste water (as shown in Teoh et al. recovering ammonia, phosphate and potassium from aquaculture wastewater [146])) or from the ocean.

Another interesting and promising alternative for drinking water production would be the treatment of wastewater, less energy intense, for which MD could be an asset, by helping in the removal of micropollutants from groundwater [16], or wastewater [132]

---

[1] http://www.buyaerogel.com/product/enova-aerogel-ic3100/ or http://www.buyaerogel.com/product/airloy-x116-thin-films/

Appendix

Appendix A

Evaporation simulation

This part intends to answer the concerns regarding the temperature jump observed at the evaporative interface, that current AGMD models do not take into account due to the liquid-vapor equilibrium assumption (see sections 4.1.3.1 and 4.1.2).

This questioning is also motivated by the will to better understand the relative roles of evaporation and diffusion in the air-gap in order to minimize the mass transfer resistance caused by these two phenomenon.

A.1   Evaporation theories

Two current theories for evaporation are the Classical Kinetic Theory (CKT) and the Statistical Rate Theory (SRT).

A.1.1   Classical Kinetic Theory (CKT)

In this theory, gas molecules are modeled as hard spheres in random motion, with a mean free path l.

The equilibrium collision rate of vapor molecules with a flat liquid vapor surface can be determined by integrating Maxwell-Boltzmann function over the velocity of the molecules striking this surface [2]:

$$j^V = \int_{-\infty}^{+\infty} \int_{-\infty}^{+\infty} \int_{-\infty}^{0} mv_z F(\overrightarrow{v}) dv_x dv_y dv_z = \int_{-\infty}^{+\infty} \int_{-\infty}^{+\infty} \int_{-\infty}^{0} mv_z \left(\frac{m}{2\pi k_B T^V} \right)^{\frac{3}{2}} e^{-\frac{m(v_x^2 + v_y^2 + v_z^2)}{2k_B T^V}} dv_x dv_y dv_z$$

$$= m \left(\frac{m}{2\pi k_B T^V} \right)^{\frac{3}{2}} \left(\frac{2k_B \pi T^V}{m} \right) \frac{k_B T^V}{m} = P^V \left(\frac{m}{2\pi k_B T^V} \right)^{\frac{1}{2}}$$

where j^V_{CKT} is the vapor molecular flux, P^V is the vapor pressure, T^V the vapor temperature, m the mass of a molecule and k_B the Boltzmann constant. This distribution is only strictly correct under equilibrium [104].

Similarly, the equilibrium collision rate of water molecules with a flat liquid vapor surface can be written: $j^L = P^L \left(\frac{m}{2\pi k_B T^L} \right)^{\frac{1}{2}}$, and the resulting evaporation rate (difference between the collision rate of the molecules on both sides of the surface) is:

$$j^{LV}_{CKT} = P^V \left(\frac{m}{2\pi k_B T^V} \right)^{\frac{1}{2}} - P^L \left(\frac{m}{2\pi k_B T^L} \right)^{\frac{1}{2}} \tag{A.1}$$

At equilibrium, $T^V = T^L = T_{eq}$ and $P^V = P^L = P_{eq}$, respectively, implying that the evaporation rate is equal to zero.

Hence, this equation has been assumed to be valid for near-equilibrium conditions, and used with the phase-specific variables T and P, T^V, P^V, T^L and P^L.

This resulting equation for the evaporation flux is in disagreement with the experimental results, two experimental parameters σ_{evap} and σ_{cond} representing the fraction of molecules striking the surface and

actually changing phase are added, yielding the Hertz-Knudsen equation:

$$j_{CKT}^{LV} = \sqrt{\frac{m}{2\pi k_B}} \left(\sigma_{evap} \frac{P_s\left(T^L\right)}{\sqrt{T_I^L}} - \sigma_{cond} \frac{P^V}{\sqrt{T_I^V}} \right) \tag{A.2}$$

In MD, the vapor liquid equilibrium (VLE) equations are applied, as vapor and liquid are assumed to be in equilibrium state at the temperature and pressure within the pores [80]. This equilibrium states that the vapor pressure of a particular specie is proportional to its concentration in the liquid, and the temperature of the liquid. In this situation, the state equations are: $P^L = P^V$, $T^L = T^V$ and $G^L = G^V$, which appears to be consistent with this classical kinetic theory of evaporation.

However, equation A.2 involves the experimental determination of two unknowns, σ_{evap} and σ_{cond}, for which the literature reports a difference in σ values of up to three orders of magnitude across multiple investigations [104].

Additionally, the simplifying assumption that $\sigma_{evap} = \sigma_{cond}$ results in differences between theoretical and experimental results. Indeed, this equation yielded non-physical findings for the interfacial surface temperatures, as multiple studies reported a temperature jump at the interface of several degrees [104] which this theory does not allow.

A.1.2 Statistical Rate Theory (SRT)

Statistical Rate Theory (SRT) is a relatively recent theory (1977) that describes the rate of particle transport across a phase boundary. It is based on the quantum-mechanical concept of state transition probability, and Boltzmann' definition of entropy [2]. Section G.3.3 develops the details of this theory.

The resulting evaporative mass flux is the following:

$$j_{SRT}^{LV} = K_{eq} \left(e^{\frac{\Delta_s^{LV}}{k_B}} - e^{\frac{-\Delta_s^{LV}}{k_B}} \right) \tag{A.3}$$

where Δs depends only on measurable parameters T, P, and the water phonon terms (see section G.3.3.2 for detailed calculations):

$$\frac{\Delta s^{LV}}{k} = 4 \left(1 - \frac{T^V}{T^L} \right) + \left(\frac{1}{T^V} - \frac{1}{T^L} \right) \Sigma_{l=1}^3 \left(\frac{\Theta_l}{2} + \frac{\Theta_l}{exp\left(\Theta_l/T^V\right) - 1} \right)$$
$$+ \frac{v_\infty^L}{k_B T^L} \left(P^V + \frac{2\gamma^{LV}}{R_c} - P_\infty(T^L) \right) + ln \left(\left(\frac{T^V}{T^L} \right)^4 \frac{P_\infty(T^L)}{P^V} \right) + ln \left(\frac{q_{vib}(T^V)}{q_{vib}(T^L)} \right) \tag{A.4}$$

and K_{eq} is defined as the equilibrium evaporation flux, calculated using the classical kinetic theory. This application of classical kinetic theory at equilibrium is explained by the fact that at equilibrium, liquid and vapor are assumed to have the same temperature and the evaporation flux compensates for the condensation flux thus the collisions between the vapor molecules and the liquid can be assumed elastic.

A similar approach, assuming that while crossing the interface a water molecule carries with itself a quantum of heat, provides an expression for the heat flux [2]:

$$q_{SRT}^{LV} = Q_{eq} \left(e^{\frac{\Delta_s^{LV}}{k_B}} - e^{\frac{-\Delta_s^{LV}}{k_B}} \right) \tag{A.5}$$

with $Q_{eq} = P_s(T^L) \left(\frac{2k_B T^L}{m\pi} \right)^{\frac{1}{2}}$ derived from the CKT.

Persad [2] found a good correlation (fig. A.1) between this expression and the measured heat flux difference at the surfaces:

$$q_{cond}^{LV} = -\kappa^L \bigtriangledown T_i^L . \overrightarrow{i}_n - \kappa^V \bigtriangledown T_i^V \overrightarrow{i}_n \tag{A.6}$$
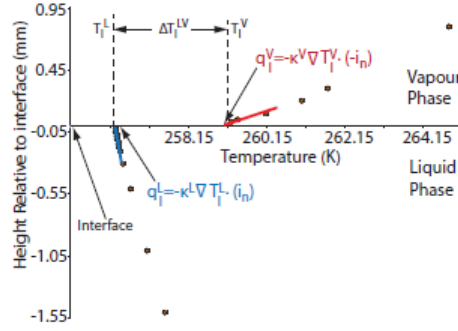
Figure 4.8: Ethanol evaporation temperature profile from the work of Persad and Ward [4]. The heat fluxes to the interface from the liquid and vapour phases, and the interfacial temperature discontinuity are shown.

Figure A.1: Heat fluxes discontinuities at the evaporative interface [2]

At steady-state, all the energy brought to the interface by conduction is assumed to be used for the evaporation: $q_{cond}^{LV} = q^{LV}$ [2].

The advantage of SRT is that there is no fitting parameter.

A.1.3   Role of total pressure

The overall pressure does not appear in the evaporation equations (section A.1): several hypotheses regarding its effect on evaporation are proposed:
- to begin with, pressure has a significant impact on the energy storage capacity of hydrogen bonds. The amount of energy that hydrogen bonds can store is significantly less than the bond strength, and is highly pressure dependent. When the hydrogen bond's energy storage capacity is exceeded, the liquid's chemical potential of the liquid equals that of gas and the liquid boils [40].
- Increased pressure results in more collisions or collisions with higher energy on the surface, providing more opportunities for water molecules to overcome the energy barrier of the hydrogen bonds in principle. However, once a water molecule has escaped from the liquid and turned into vapor, it can encounter more vapor molecules traveling in the opposite direction, increasing its chances of being condensed again.

Perhaps all of these effects cancel each other out, and the only effect of total pressure on evaporation is visible in the diffusion rate of newly evaporated molecules.

A.2   SRT model

The 3DH&MT model's evaporation modeling is comparable to that of CKT. Based on Persad' thesis [2] and the Statistical Rate theory's mass and heat fluxes expressions, a C++ model is written with the intention of later on implementing it in the 3DH&MT model, and with the goal of determining whether evaporation or diffusion is the faster phenomena in this situation (section A.1.2).

SRT' heat flux, q_{SRT}^{LV} corresponds to the energy carried by the water molecules across the interface. It only depends on the temperature difference at the interface $T_{int}^L - T_{int}^V$, as well as the pressure condition just above the interface (section A.1.2).

q_{cond} or the total energy provided to the interface, is the energy brought by conduction in both phases (and convection in the liquid phase in 2D):

$$q_{cond} = -\lambda^L \nabla T^L + \lambda^V \nabla T^V \approx -\lambda^L \frac{T^L int - T_{int-1}^L}{l_{cell}} + \lambda^V \frac{T^V int + 1 - T_{int}^V}{l_{cell}} \tag{A.7}$$

it depends on the temperature of the liquid cell (of length l_{cell}) just before the interface $T^L int - 1$ and of the vapor cell just after the interface T_{int+1}^V.

In Persad' experiments, evaporation takes place in an atmosphere of pure vapor (no air), and it is assumed that all the energy brought to the interface by conduction by both phases (liquid and vapor),

q_{cond} is used for evaporation, which means that $q_{SRT}^{LV} = q_{cond}$ all the time, and no convection can occur. The balance thus reads:

$$Q_{eq}(e^{\frac{\Delta_s LV}{k_B}} - e^{\frac{-\Delta_s LV}{k_B}}) = \epsilon \left(-\lambda^L \frac{T^L int - T_{int-1}^L}{l_{cell}} + \lambda^V \frac{T^{int+1} - T^V int}{l_{cell}} \right) \tag{A.8}$$

The unknowns are $T^L int$ and T_{int}^V, and there is only one equation. Thus a second one is required:

$$q_{SRT}^{LV} = j_{SRT}^{LV} \left(h(T_i^V, P^V) - h(T_i^L, P^L) \right) \tag{A.9}$$

where the enthalpies h should be known.

There are two main parameters constraining evaporation: the quantity and the speed at which energy is brought to the interface; and the energy that can be released from the interface by mass diffusion. If not enough energy is brought to the interface by conduction (or convection), the water molecules do not get enough energy to break their hydrogen bonds. If the mass diffusion rate is too slow, then the saturation pressure is reached and water molecules can not evaporate. Here, q_{cond} is a function of the temperature gradients determining the velocity at which the energy is brought to the interface $q_{cond} = f(T_{i-1}^L, T_i^L, T_{i+1}^V, T_{i+2}^V)$; whereas q_{SRT}^{LV} mainly depends on the interfacial temperatures, $q_{SRT}^{LV} = f(T_i^L, T_{i+1}^V, P^V(T^V i + 1, \rho_{i+1}), P_s(T_i^L))$.

However, it was observed that the resulting evaporation mass fluxes were extremely dependent on the difference between P_v and P_{sat}: a variation of a few pascals may result in a shift of many orders of magnitude in the evaporation flux. Persad confirmed that a precision of at least up to four decimals was required. In particular, the saturation pressure curve at the experiment conditions is not well defined conditions, and the experimentation required to obtain it was beyond capabilities of this research project.

At first, this was considered a significant obstacle to the implementation of SRT in the 3DH&MT model. After more consideration, this rapid rise in mass flux as soon as P_v goes away from P_{sat} may be evidence that the evaporation phenomena is several orders of magnitude quicker than diffusion, and therefore that the equilibrium assumption for the evaporation phenomenon is not nonsensical.

Thus a more pertinent research track could be to go deeper into the diffusion equation in order to have a better understanding of the parameters that affect it. Moreoever, before implementing SRT in the 3DH&MT model, it would be necessary to extend the application of this balance (eq. A.8) to convection and not pure steam air atmosphere.

Appendix B

Improving the sustainability of AGMD

The overall objective of this work is to improve the energy efficiency and the attractiveness of AGMD.

Just like Nature already found solutions for water desalination, it also already found solution for each of the subfunctions composing an AGMD process: heating, evaporating, diffusing, condensating, cooling, pumping. As all of these processes require energy to work, finding ways to power those functions through natural energy flows would improve the energy efficiency of AGMD.

Indeed, for every transformation, an energy flow is needed. And for energy to flow, a gradient is necessary: whether a height difference for a body to fall down; a temperature difference for the environment to cool down a cup of coffee; a difference of potential for electrons to flow. Some of these gradients can be found naturally, allowing for an apparently free use of energy, meaning that no energy is required from the operator for the action to occur. But energy is hidden behind every transformation.

Taking advantage of natural gradients can be a good way to reduce the use of non renewable natural resources.

B.1 Heating

Heating is necessary in AGMD to create a temperature difference between the hot and cold water stream, and power the evaporation/condensation system at the core of the technology.

The most obvious nature based solution for the heating function of AGMD is the sun.

B.1.1 Solar radiancy based heating

Solar ovens are based on three phenomenon:
- reflection of the solar radiation on the side reflectors, concentrating the energy to the center of the process (where is the pan)
- absorption of the concentrated solar radiation thanks to a black pan
- green-house effect thanks to the glass covering the pan: the radiation of the black body due to its temperature are contained inside the oven for a better efficiency

The bigger the surface of the reflectors the more energy is concentrated. And given Descartes' law of reflection of light rays on reflectors an optimum shape and geometry for these reflectors can be defined.

The Sun radiancy presents a peak for the wavelength $500nm$. From Wien' law, its temperature as a black body can be deduced: $\lambda_{max}T_S = 2900\mu m.K$ hence $T_S = 5800K$. Stefan' law helps to calculate the total energy provided by the Sun: $E_S = \sigma T_S^4$ with σ Stefan-Boltzmann constant, equal to $5.67.10^{-8}J.K^{-4}.m^{-2}.s^{-1}$. Thus, $E_S = 64.10^6 W.m^{-2}$. Since solar radiancy is electromagnetic, it does not dissipate in space. Thus by energy conservancy, the total power emitted by the whole solar surface, is the power received by the supersphere with a rayo equal to Earth-Sun distance D_{T-S}. The areal power received on the surface of this supersphere is called Earth Solar Constant (CST).

$$P_{tot} = E_S S_S = E_S 4\pi R_S^2 = 3.9.10^{26}W \tag{B.1}$$

$$CST = \frac{P_{tot}}{S_{megasphere}} = \frac{P_{tot}}{4\pi D_{T-S}} = 1387.64W.m^{-2} \tag{B.2}$$

The areal power received by Earth surface at different latitudes and at different periods of the year gives a broad idea of the surface needed to heat a certain amount of water to 60 or 80°C.

As a minimum of $90kWh_t/m^3$ is required for AGMD [41], and given that the luxembourguish solar energy is comprised between 0.7 and $6.6kWh/m^2$[1], between 128 and $13m^2$ of mirror surface are necessary to produce $1m^3/day$.

B.1.2 Heating Pump

A heat pump is a heat exchanger working in reverse: extracting the calories from a cold source to provide them to a hot source, via a refrigerant fluid. Due to the fluid's extremely low boiling temperature, it becomes a gas in the evaporator, in contact with the external source (water/air) at a very low temperature. This gas being still quite cold is compressed in a compressor to reach a higher (preferred) temperature, which is released in the required area through a condenser. In the condenser the refrigerant is liquefied and expanded to be cooled.

Such a device could be used to refresh the water of the cold channel after it went through the module, and heat the flux of the hot channel exiting the module.

The refrigerant fluids are CFC, HCFC and HFC. Only the latest are considered less harming for the environment.

B.2 Cooling

Several technologies exist for a natural or at least non electricity consuming cooling.

B.2.1 Latent heat based cooling

Zeer pot or Desert cooler is inspired from desert cooling based on the latent energy needed by the water to turn into vapor. Traces of the use of such a process date back from 3000 years before Christ.

Constituted of two concentric clay pots filled with moist sand in between them, the temperature variation between the outside and the inside can reach 5 to 20°C.

The energy balance can be written as:

$$\frac{\Delta E_\Sigma}{\Delta t} = \Psi_{in} - \Psi_{out} \tag{B.3}$$

where Ψ_{out} is the heat flux due to the liquid evaporation and Ψ_{in} is the heat flux due to the higher ambient air temperature. Of course, if the Zeer pot is directly in the sun, the heat flux due to direct radiance, accounted in Φ_{in}, will be much larger than the heat flux of evaporation and hence the system will heat.

E_Σ depends on the heat capacity C_Σ of the system Σ, which is the quantity of heat required to increase its temperature by 1 °C, $E_\Sigma = C_\Sigma T$.

Ψ_{in} is a convective heat flux between the air and the pot, $\Psi_{in} = C_{interface}(T^{air} - T^{pot})$ with $C_{interface}$ the conductance of the interface.

Ψ_{out} is due to the liquid evaporation at the pot's surface: when a liquid is at a lower temperature than its ebullition temperature at the given pressure, it means that in mean, the molecules don't have enough energy to turn to gas. But this energy varies with time and between molecules. In the end, some molecules get enough energy to turn to gas, and the molecules staying have a lower energy. Hence, $\Psi_{out} = L_v \dot{m}$ with L_v the latent heat and $\dot{m}$ the mass flux of water evaporated. $\dot{m}$ can be evaluated by $\dot{m} \approx S P_{eq}(1 - H)$, with S the evaporation surface, P_{eq} the saturation vapor pressure and H the relative humidity. But in theory, this flux depends also on the climatic conditions (wind uniforms the pressure, which tends to be higher at the interface due to the evaporation process, and hence accelerates it) and the pot characteristics (thickness and porosity).

Hence the balance becomes:

$$C_\Sigma \frac{dT}{dt} = L_v \dot{m} + C_{interface}(T^{air} - T^{pot}) \tag{B.4}$$

---

[1]https://fr.weatherspark.com/y/53907/Météo-moyenne-à-Luxembourg-tout-au-long-de-l'année

This equation, approximated in the first order, is independent on the geometry of the system, but in practice the bigger the device the slower the process.

B.2.1.1   Solution for a constant mass flux

In the case of a constant mass flux of evaporation (if the sand is always moisted), then $\dot{m} = constant$ and the solution can be written as:

$$T_{pot} = (T_0 - \frac{L_v}{C_{int}}\dot{m} - T_{air})e^{-\frac{C_{int}}{C_\Sigma}t} + \frac{L_v}{C_{int}}\dot{m} + T_{air} \tag{B.5}$$

B.2.1.2   Solution for a variable mass flux

In the case of a variable mass flux of evaporation (if the sand is only watered once), then $\dot{m}$ will proportional to the evaporation surface, $\frac{dm}{dt} = -\alpha\frac{m}{\rho H}$ hence, $m = m_0 e^{-\frac{t}{\tau}}$ with $\tau = \frac{\rho H}{\alpha}$, H the height of the pot, and α the proportional factor.

Hence the solution for the temperature is the following:

$$T_{pot} = T_0 - \frac{L_v m_0}{C_\Sigma}\frac{\tau}{\tau - \frac{C_\Sigma}{C_{int}}}(e^{-\frac{t}{\frac{C_\Sigma}{C_{int}}}} - e^{-\frac{t}{\tau}}) \tag{B.6}$$

B.2.1.3   Application

In this situation, a constant mass flux of evaporation is assumed, thanks to a constant water feed of the sand.

An experiment should be implemented, with a thermometer to evaluate the rate at which the water evaporates, and the time needed to reach the desired temperature inside the Zeer pot. After defining the heat transfer provided by the hot channel, one could define the flux for the cooling system.

B.2.2   Radiancy-based passive cooling

The night radiancy process is long known and has been used in Bengale to make ice since immemorial times. At that time, clay pots on corn straw were used by clear and cool nights (above 10°). Now the technique is a bit more evolved due to the discovery of new materials, and this process can also be used in sunlight.

A tangible experience of this phenomenon is morning dew: air and ground do not cool at the same speed, air might be cooler than ground during the day but this trend reverses during the night, and the radiancy emitted by ground at night in the infrared cools it.

B.2.2.1   Theory

The theory behind this process is based on a few laws:

- **Heat transfer by conduction/convection between two bodies**: in this case, $\Psi_{air} = kC(T^{air} - T)$ where $(T^{air} - T)$ is the temperature difference between the body and air and C is a proportionality coefficient called conductance.
- **Heat transfer by radiance**: a black body radiates as much energy as it received: $\Psi_{Stefan} = \sigma T^4$ with σ the Stefan constant ($\sigma = 5.67.10^{-8}W.m^{-2}.K^{-4}$) and T its absolute surface temperature. The wavelength peak of this radiance is given by Wien' law: $T\lambda_{max} = b$ with b the Wien displacement constant, equal to $2.8977729(17).10^{-3}mK$. While radiating, this black body is losing energy, and if no energy is brought aside, the body will cool down.
- **First Thermodynamic law**: considering constant mass and pressure, the internal energy variations of a body are given by $dU = Se\rho C_p dT$ where S is the exchange surface of the body, e its thickness, ρ its density and C_p its heat capacity at constant pressure.
- **Descartes' law**: a light ray arriving on a surface with an angle i with the normal to the surface is reflected with this same angle in a symmetrical direction regarding this normal. This law helps designing the fridge (height and tilting angle of the sides), since the radiation emitted by the black body has to leave the fridge as soon as possible (in one bounce at most).

The variation of internal energy U is equal to the sum of inlet and outlet heat fluxes across the body during dt (incident solar radiation heat flux; convection heat flux with ambient air; and the emitted Stefan' radiation). Combining all these equations gives:

$$dU = Se\rho C_p dT = \Psi^{sun} S dt + \Psi^{air} S dt - \Psi_{Stefan} S dt = \Psi^{sun} S dt + kC(T^{air} - T) S dt - \sigma T^4 S dt \quad \text{(B.7)}$$

with S the exchange surface between the two bodies and hence:

$$e\rho C_p \frac{dT}{dt} + \sigma T^4 + kCT = \Psi^{sun} + kCT^{air} \quad \text{(B.8)}$$

This equation tells two things: if there is no solar radiation (at night or with a material perfectly reflective to solar radiation), and if the heat transfer by convection with the air is small enough, the black body can cool down. Moreover, this cooling process is independent on the size of the black body (but not its thickness).

B.2.2.2   Black Body

This phenomenon relies on the black body theory. A black body is a hypothetical body which absorbs perfectly all the electromagnetic wavelengths reaching its surface without reflecting or transmitting it. This absorbed energy creates a thermal agitation in the black body, which radiates the same amount of energy it received, but the spectra of this emission depends on the body temperature (Wien' law).

Since it absorbs all wavelengths even in the visible, it is called black body. But if heated enough, it might radiate in the visible spectrum.

In Nature no such body exists. But any insulated enclosure, closed except for a very small opening, plays the role of a black body.

B.2.2.3   Nesting fridge

To transform a black body into a cooler, it first has to reflect solar radiations, in order not to heat. Moreover, in order to cool down, its emission spectra has to fit in the wavelengths range passing through the atmosphere (8-13.5 μm), so that these radiance can be lost in space, which is cold. A white paint with titanium oxides, which are "black" for the infra-red, meet these requirements. In Latil et al. [36], a plate covered with this paint is placed at the bottom of a cavity whose walls are covered with an infra-red reflector, and tilted at a small angle (about 15°) in order to dissipate most of the radiation. This cavity is then surrounded by an insulating material such as polystyrene, and covered by a polyethylene sheet acting like a cover, transparent to infrared.

Such a set-up was reported to provide a 20 to 25°C temperature difference with external air at night time. Nesting several like-chamber allows to reach up to a 35°C temperature difference at night time [36].

In Raman et al. [113], instead of white titanium paint, seven layers of HfO2 and SiO2 are employed, which reflect 97% of incident sunlight while radiating brightly and selectively in the atmospheric transparency window. Such a cooler can cool up to 4.9°C below ambient temperature when exposed to direct sunlight at $850 W.m^{-2}$.

The performance of such fridges depends on the air humidity [136].Clouds (or buildings, trees...) are also a limitation to this process, as the infrared radiancy emitted by the black body risk to be re-emitted towards the black body.

B.2.3   Absorption Fridge

The absorption fridge (or Einstein Fridge) is based on the evaporation of a liquid with a very low boiling point at a low temperature, which absorbs the heat from the cool environment. It requires a coolant fluid (ex: ammonia, water) and one absorbing fluid which acts as a little compressor at molecular scale (resp. water, lithium bromide)[115]. Indeed, instead of compressing the vapor, the coolant is dissolved in the absorbing fluid which is then compressed, as it is more efficient. The pressurized liquid is thus heated, and the coolant becomes vapor, while the absorbing liquid goes back to the absorber. In the condensator, the coolant rejects heat while condensating, before evaporating again due to expansion in the evaporator [20].

The Platen-Mutens design uses a third fluid in order to operate without a pump and solely rely on heat instead of work, making the use of electricity useless.
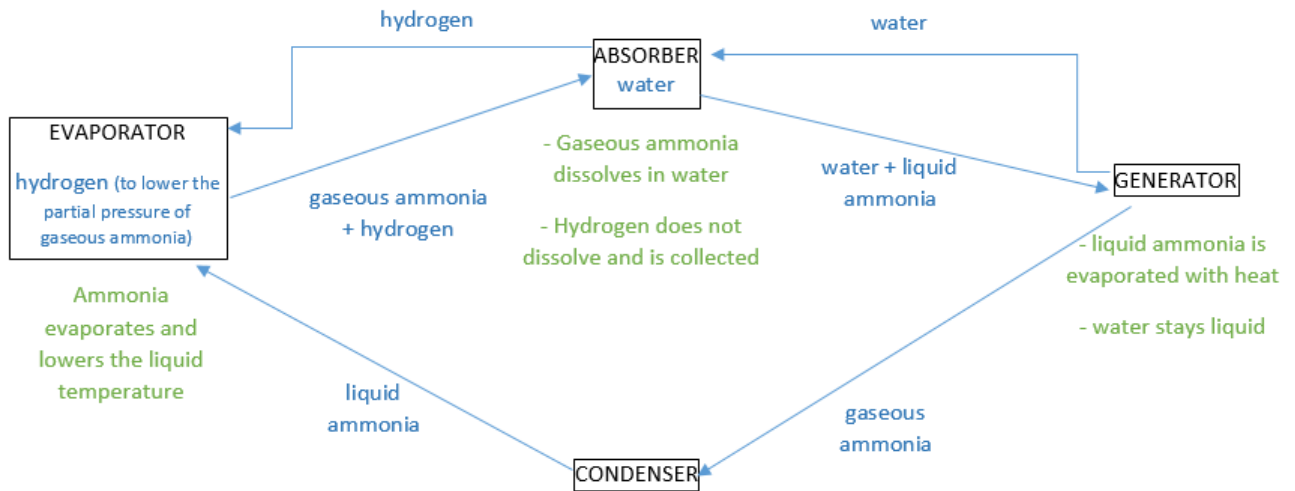
Figure B.1: Sketch of the absorption Fridge process

B.3 Condensation

As the condensation rate impacts the vapor pressure in the air-gap, and thus the evaporation rate, enhancing condensation can improve the permeate outflow.

B.3.1 Dark beetle

The dark beetle lives in the desert and collects water from the fog thanks to a combination of hydrophilic and hydrophobic surfaces, and little bumps on his back, catalyzing condensation [142].

Figure B.2: Black Beetle collecting water from the fog [142]

Several water harvesting technologies are inspired by this little animal.

B.3.2 Thorny lizard

The thorny lizard uses capillarity to pump water from the soil moisture thanks to very small and convoluted channels on his back.

Figure B.3: Thorny lizard and its convoluted capillarity channels on his back, to collect water [143]

B.3.3 Spider webs

The spider webs are making the most of water surface tension to improve water collection. Thanks to a succession of tangles and threads, the water condensed on the threads slowly migrates towards the tangles, where it has a larger surface to adhere to, leaving the threads dry and ready to condensate more water.

The driving force of this phenomenon is the wind.

Figure B.4: Structure of a spider web enhancing the water collection [145]

B.4   Diffusion and convection

As evaporation can occur only as long as the saturation pressure is not reached immediately above the water surface, ensuring that diffusion rapidly transports the vapor molecules away from this surface is an effective technique to sustain the evaporation flow and hence increase the AGMD's fresh water permeate output.

B.4.1   Air flow cooling

An air flow can be beneficial for cooling a body via convection, but it can also be used to accelerate diffusion, or the removal of evaporated water molecules from the water surface, in order to sustain the evaporation process.

The prairie dogs create natural circulation in their burrows using the Venturi effect, thanks to openings of various heights and diameters [141].

Termites use a similar approach to naturally ventilate their nest: as the sun warms the air at the upper openings, it becomes lighter and rises, creating suction for the colder air at the bottom, and leading in the aspiration of external air via the nest's bottom apertures (fig. B.5, [144]).

Figure B.5: Termite mound

B.4.2   Convection

The shape can also be a natural convection heat exchange enhancer, and accelerate the cooling. The cactus shape, while presenting the smallest surface perpendicular to the solar radiation, to reduce the heating, also maximizes the surface parallel to the sun rays, to increase the cooling surface and maximize the convection heat exchange with the wind.
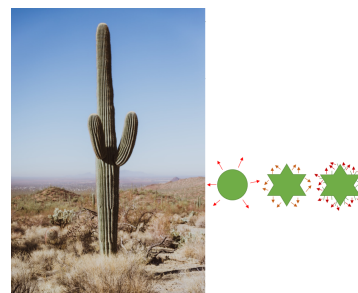
Figure B.6: Cactus

B.5 Capillary Pumping

Capillary suction, the pumping mechanism of trees and mangroves, could be used to pump water.

B.6 Membranes in nature

The PTFE membranes currently used in AGMD are actually the main part of the AGMD module which is not low-tech as it requires highly technical processes to be produced. Finding alternatives could improve AGMD accessibility.

B.6.1 Eggshells

Eggshell is a porous membrane letting gas pass but not the liquids. It is mostly made of calcium carbonate, crystallized as calcite on a protein membrane. One can easily precipitate carbonate calcium under calcite form with limewater and Perrier, but if the nucleation sites are missing, the cristallisation will not occur [56].
Experimentation did not prove conclusive.

B.6.2 Clay

Clay is also being studied as an eco-friendly alternative for membrane [77], with important thermal, chemical and mechanical properties in tangential microfiltration.

Conclusion

To maximize AGMD's energy efficiency, only those processes and technologies that directly rely on a naturally occurring energy flow source (mostly heat from the solar radiation) or a shape that utilizes a naturally occurring energy flow (shape for convection or condensation) are kept.
To summarize, AGMD process needs energy to reach the surface water molecules so that they can evaporate, and a mean of rapidly removing these water vapor molecules from the surface t allow for the evaporation of additional vapor molecules. Another source of energy flow is required to make the water flow. And one last source of energy flow is necessary to cool down the condensation plate.

In order to supply the energy directly to the surface, to avoid loss of heat via diffusion in the hot water channel, a combination of mirrors condensing the solar radiation towards the surface of the hot water channel can be used.

To remove the water vapor molecules from the surface, two methods can be combined: increasing the diffusion rate, via a sweeping flow of air just above the water surface thanks to a Venturi effect, carrying the vapor molecules away from the surface to condense; and increasing the condensation rate via a condensation plate that replicates the patterns of the dark beetle's skin.

With regards to fluid circulation, the pump might be eliminated by heating capillary tubes from the top, resulting in capillary pumping via evaporation.

About the cooling part of AGMD, the radiancy based cooling coupled to a cactus-like shape could maximize the cooling of the cool plate while contributing to heating the hot water channel by reflection of sun rays and radiation.

Fig. B.7 shows a sketch view of what an AGMD module encompassing all these alternatives would look like. No membrane anymore is required in this set-up.
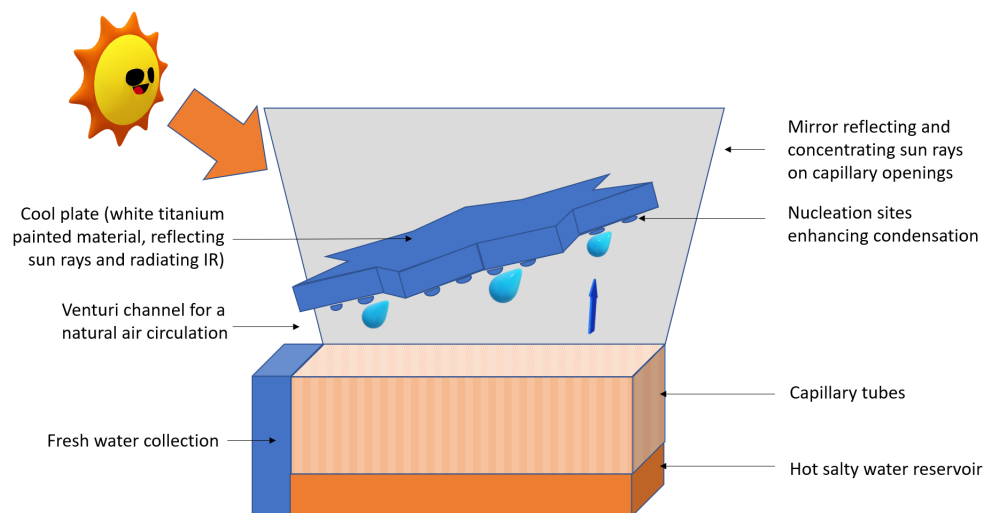
Figure B.7: Improved AGMD module using biomimetism

A subsequent step in this area of research would be to construct such a prototype and evaluate its performances.

Annex

Appendix C

Papers

Three papers were written and submitted to different journal in the course of this work.

- Experimental Characterization of the Temperature Gradient inside a Membrane Distillation Module - published in Energy Reports, impact factor 4.9
- Novel spacer geometries for AGMD mixing enhancement - submitted to Desalination
- Experimental Validation of a 3D code for AGMD - in progress

Appendix D

Conventions of the ray tracing code

The objects used in the ray-tracing code are the following:
- **Lens**=[xpositionLens, R1, R2, e, Diam, index, intensity, thetaLens, zpositionLens] with:
  - (1) xpositionLens: position of the Lens on the optical axis;
  - (2) R1: radius of the left face of the lens (<0 if center on the left of x);
  - (3) R2: radius of the right face of the lens (<0 if center on the left of x);
  - (4) e: thickness of the lens;
  - (5) Diam: diameter of the lens;
  - (6) index: refractive index of the lens material (-1 for mirrors);
  - (7) intensity: parameter changing the ray intensity (for the temperature gradient)
  - (8) thetaLens: inclination of the Lens compared to the optical axis, or the angle between the optical axis of the lens to the horizontal;
  - (9) zpositionLens: position of the lens perpendicular to the optical axis.
- **Ray**=[z, x, theta, iin, iout, index, Boolean, beta, path, intensity] with:
  - (1) z: position perpendicular to the optical axis;
  - (2) x: position along the optical axis;
  - (3) theta: angle between the ray and the horizontal;
  - (4) iin: angle between the incident ray and the surface normal;
  - (5) iout: angle between the exiting ray and the surface normal;
  - (6) index: refractive index of the medium at this position;
  - (7) Boolean: 1 if the ray can continue/0 if it is blocked by a wall;
  - (8) beta: angle of the optical axis with the horizontal of a reference;
  - (9) path: optical path traveled by the ray;
  - (10) intensity: intensity of the light ray.

The geometrical relations used in this code are the following:

Definition of the angle between the incident ray and the surface normal of the optical equipment When projecting the directing vector of the ray on the directing vector of the surface normal of the optical equipment the cosine of the angle between those two vectors is obtained: $\frac{\overrightarrow{ray}}{|ray|} \cdot \frac{\overrightarrow{normal}}{|normal|} = cos(iin)$. To attribute a direction to this angle, one has to consider the difference between the angle of this ray and the horizontal, and the angle between the surface normal and the horizontal.

Similarly, the angle between the surface normal and the horizontal is equal to the tangent of the ratio of z and x coordinates of the segment between the center point of the lens and the point on the surface considered, and the direction of this angle is determined by the direction of the radius of the mirror.
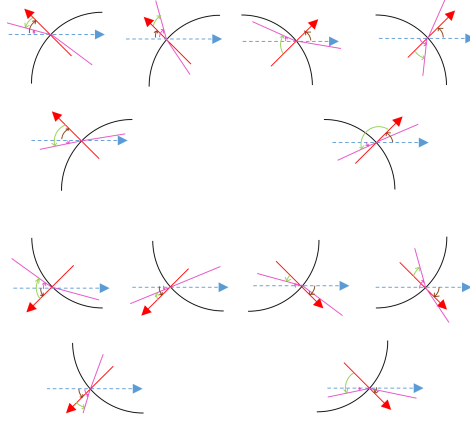
Figure D.1: Angles definition (in pink: the ray; in black the optic equipment surface; in red the optical equipment surface normal; in blue the horizontal / Angles: in pink: theta, in green, iin, in brown, alphan)

To determine the position of the point where all the parallel rays focus after the convex mirror, the following relationships are used:
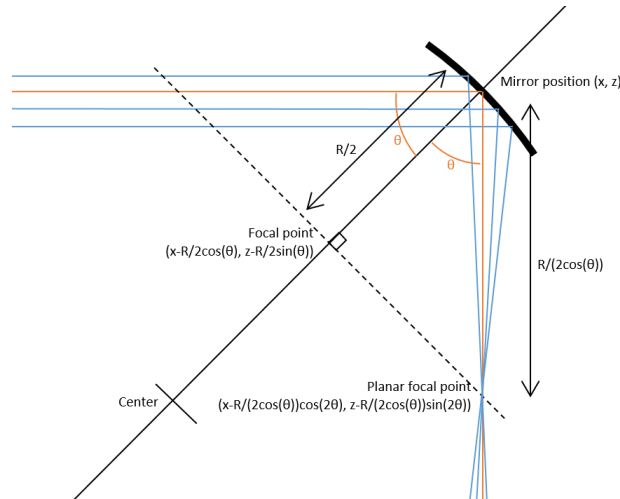
Figure D.2: Position of the planar focus point for a convex mirror

The conventions used are the following: the angle theta between the horizontal or the normal and the ray is determined in the direction from the horizontal or the normal towards the ray. alphanormal is the angle between the normal of the medium and the horizontal, it is positive.

The lens or mirror radius is positive if the lens or mirror surface is concave towards the optical axis
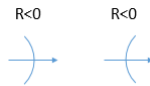
Figure D.3: Convention for the lenses radiuses

Appendix E

Detailed measurement protocol

The measurement protocol is the following:
- launch the heater
- take a new camera battery for the day or plug it
- take 20 pictures with an homogeneous temperature
- wait for the temperatures to stabilize in the module (using Flexlogger)
- measure the flow by filling the big graduated cylinder for 1mn exactly (precision $\pm 1s$) and weighting it on the scale (precision $10^{-2}g$), then empty the graduated cylinder in the intermediate tank, and weight it empty (precision $10^{-2}g$)
    - if it is too low (smaller that 400ml for the valve fully opened), close the big quarter-turn valve, open the small quarter-turn valve just above the module to remove the air bubbles
- place the collecting bucket at the end of the permeate pipe, note the starting hour (precision $\pm 1s$)
- note the starting temperatures (from the Flexlogger, precision 10^{-2} °C)
- note the end time, remove the collecting bucket, weight it, then empty it and weight it empty (precision $10^{-2}g$)
- measure again the flow
- note the final temperature

It was noticed that despite the efforts to control the light atmosphere in a box, the ambient light still impacts the intensity on the pictures. Thus they are all taken at night to ensure uniformity.

Appendix F

List of Material used in the set-up

The following table (table F.1) present the list of material used in this project:

Name	Quantity	Brand	Description
beam splitter 1/2"	1	Thorlabs	https://www.thorlabs.com/thorproduct.cfm?partnumber=BSW
Laser 532	1	Thorlabs	https://www.thorlabs.com/thorproduct.cfm?partnumber=CPS
Laser 635	1	Thorlabs	https://www.thorlabs.com/thorproduct.cfm?partnumber=CPS
Gradient filter	1	Thorlabs	https://www.thorlabs.com/thorproduct.cfm?partnumber=NDL-1
Concave mirrors	2	Thorlabs	https://www.thorlabs.com/thorProduct.cfm?partNumber=CM750-5
Flat mirrors	2	Thorlabs	
Imaging lens	1	Thorlabs	https://www.thorlabs.com/thorproduct.cfm?partnumber=ACT508-
Filter holder	1	Thorlabs	https://www.thorlabs.us/thorproduct.cfm?partnumber=XF50/M#ad
Micrometric table	4	Thorlabs	https://www.thorlabs.com/thorproduct.cfm?partnumber=PT1B/M#ad
Heater	1	Julabo	SL with H20S circulating fluid
Cooler	1	Julabo	F32

Table F.1: List of Material used in the Schlieren Set-up

The membranes at disposition are the following (fig. F.2):

Reference	Brand	Material	Pore $\varnothing$	Thickness	Porosity	Entry Pressure	Dimensions
FGLP14250	Merck	PTFE	$0.2\mu m$	$150\mu m$	85%	1bar	142mm
FHLP14250	Merck	PTFE	$0.45\mu m$	$150\mu m$	85%	0.63bar	142mm
FALP14250	Merck	PTFE	$1\mu m$	$150\mu m$	85%	0.5bar	142mm
FSLW14200	Merck	PTFE	$3\mu m$	$150\mu m$	85%	0.7bar	142mm
LSWP14250	Merck	PTFE	$5\mu m$	$150\mu m$	60%	0.05bar	142mm
LCWP14250	Merck	PTFE	$10\mu m$	$130\mu m$	60%	0.03 bar	142mm
PM5015	Porex	PTFE	$30-60\mu m$	$1.5mm$	$50-60\%$	30 -120 mbar	rectangle
PM3010	Porex	PTFE	$25-35\mu m$	$1mm$	$55-60\%$	40-140mbar	rectangle
PM5020	Porex	PTFE	$45-60\mu m$	$2mm$	$55-65\%$	15mbar	rectangle

Table F.2: Characteristics of the different available membranes

Appendix G

Vulgarization

All along this dissertation, the intention to understand every physical phenomenon at its roots and to vulgarize it, up to a camera functioning, was present. However as it is not the goal of this exercise, some of this vulgarization is collected here for the curious reader.

G.1 Energy and models

Energy is what allows transformations. These transformations can happen through the work of forces, or through a heat input.

G.1.1 Energy

Energy is neither consumed nor produced, according to the First Law of Thermodynamics; it is transformed from one form to another. The majority of Earth' energy sources originate from nuclear energy, whether from on-board sources or energy fluxes reaching Earth. Indeed, nuclear energy is generated in nuclear power plants using Earth components (uranium), and deep radioactive rocks heating neighboring rocks generate geothermy. The energy fluxes that reach Earth, such as solar light and radiations, are the result of the sun and nearby stars' internal nuclear reactions (fusion). They are also the source of the majority of other energy sources on Earth. Indeed, the sun generates wind by heating air masses and powers the water cycle, which generates hydroelectricity by heating and evaporating water. The sun also provides food for plants via photosynthesis. These plants can be used as an energy source directly as biomass, or as muscle energy via digestion, or as fossil fuels following a million-year concentration process at extreme temperatures and pressures underground.

Only wave energy comes from gravitational energy provided by the neighboring stars.

Not all energy sources are equivalent (fig. G.1): some are fluxes, while others are storages. The sun's (and nearby stars') radiations are a flow of energy, propelling the wind energy flow, whereas photosynthesis is a storage process, storing this solar energy flow in plants and fossil fuels. Fissile materials are also a storage. Energy flows can be used only at the available power level, when and where it is available, whereas stored energies can be used at the desired power level whenever and wherever it is desired. Certain storage forms (uranium) are denser than others (wood), requiring less material to convert the source to the same amount of usable energy, while others (fossil fuels) require more time to reconstitute than others (wood).

None of these energy sources, with the exception of food, are the final forms of energy required for human life: electricity, work and heat.

To convert energy from one form to another, a converter is required (fig. G.2). This converter has a fixed efficiency that is never 100%. For instance, photosynthesis has an energy efficiency of approximately 3-10%, and each trophic level has an efficiency of 10%. Thus, the further an animal is from a plant-based diet, the less energy efficient it is at collecting solar energy. And the same holds true for any type of energy source: the more conversions, the greater the energy losses.

Similarly, not all forms of energy are equivalent. Certain forms of energy, such as potential or kinetic energy, are easily transformed into another, but once energy reaches the form of low grade heat, it becomes difficult to convert it to another form of energy, as the molecules are agitated in all directions without any

preferential direction: the energy is diluted. According to the Second Law of Thermodynamics, the use of any form of energy ends up in the production of low grade heat (entropy), that cannot be recovered: the potential energy of a skier is converted to kinetic energy as he descends the slope, and then to heat melting the snow as he brakes to come to a stop at the bottom. Thus, all of the initial energy used to bring the skier on the top of the slope has been eventually converted to melted snow, which is extremely difficult to convert to another form of energy.

Source	Storage or Power	Density	Renewability time	Form
Fossil Fuels	Storage	Very dense	$\approx 10000y$	Chemical
Biomass	Storage	Dense	$\approx 10y$	Chemical
Solar energy	Power	Diluted	instantaneous/intermittent	Radiation
Wind	Power	Diluted	instantaneous/intermittent	Kinetic
Lake	Storage	Dense	$\approx 1y$	Potential
Uranium	Storage	Very very dense	No	Chemical
Geothermy	Power	Dense	Constant	Heat
Wave	Power	Diluted	instantaneous/intermittent	Kinetic

Table G.1: Energy sources

Convertor	Energy Source	Energy form conversion chain	Efficiency
Power plant	Fossil fuel/Biomass	Chemical→Thermal→Kinetic→Mechanical→Electricity	$\approx 30\%$ / $\approx 70\%$ with cogeneration
Power plant	Uranium	Radiative→Thermal→Kinetic→Mechanical→Electricity	$\approx 30\%$ / $\approx 70\%$ with cogeneration
Wind turbine	Wind	Kinetic→Mechanical→Electricity	
Solar panels	Solar radiation	Electromagnetic→Electricity	$\approx 20\%$
Solar thermal	Solar radiation	Electromagnetic→Thermal→Kinetic→Mechanical→Electricity	
Hydroelectricity	Lake	Potential→Kinetic→Mechanical→Electricity	
Tide & Wave plants	Tide & Waves	Kinetic→Mechanical→Electricity	
Thermal Motor	Fossil Fuels	Chemical→Mechanical→Kinetic	$\approx 60\%$
Electrical motor	Electricity	Electricity→Movement	$\approx 99\%$
Electrical heating	Electricity	Electricity→Heat	$\approx 99\%$
Heater	Fossil Fuels	Chemical→Heat	
(human) Body	Plants	Chemical→Heat and Movement	$\approx 5\%$

Table G.2: Energy Converters

G.1.2 Exergy

Exergy is the maximal useful work a system could provide if it rejected the unused thermal energy in a thermal energy reservoir of reference at temperature T_0 and pressure P_0 until the system is in perfect equilibrium with this reservoir. The useful work one can collect is $W_{useful} = H - Q$, with H the enthalpy and Q the heat exchanged with the outside. This work is maximal for an isentropic transformation, for which $\Delta S_{universe} = \Delta S_{syst} + \Delta S_{ext} = 0$. Thus $\Delta S_{syst} = -\Delta S_{ext} = -\frac{Q_{ext}}{T_{ext}}$ and hence $Q_{syst} = -Q_{ext} = T_{ext}\Delta S_{syst}$.

Thus, an exergetic study of a system provides an accurate estimate of the energy that has been degraded.

Exergy is only conserved if the process is reversible [162].

G.1.3   Earth' energy budget

The main energy fluxes upbring on Earth is solar energy. Gravitational energy and thermal energy coming from Earth' nucleus only represent a small fraction of the overall energy flux upbring to Earth. The total solar power received by Earth is 173PW, which corresponds to a mean solar power on the ground of $340W.m^2$. This represent a total amount of energy received by the Earth surface of $5.47.10^{24}J$.

Of this total amount of incident solar energy of $340W.m^2$, $77W.m^{-2}$ are reflected by the atmosphere towards space, and $30W.m^{-2}$ by Earth surface towards space. Both these reflected energies correspond to 30% of the incoming flux, and are called albedo, dependent on the ground cover (plants, ice...).

Of the residual 70%, $67W.m^{-2}$ are absorbed by the atmosphere (O_3 absorbs UV, water vapor absorbs IR, clouds partly absorb visible wavelength), $24W.m^{-2}$ are converted into convection (source of winds) and $78W.m^{-2}$ contribute to evaporation of ocean water and thus to the water cycle. Earth surface also absorbs $168W.m^{-2}$ of direct solar energy.

The heated atmosphere reemits $324W.m^{-2}$ of IR radiation towards the Earth Surface, and the heated Earth reemits $350W.m^{-2}$ of IR radiation towards the atmosphere.

Both Earth and atmosphere also emits IR radiation towards space, respectively $40W.m^{-2}$ and $195W.m^{-2}$. This radiation is called "outgoing long wave radiation" and is the main way Earth system looses energy.

Hence the total Earth Energy Budget is quite balanced (the loss of energy through high wavelength radiation is compensated by the absorption of small wavelength radiation from the Sun).

Greenhouse gases, emitted by the combustion of fossil fuel through humans activities [90], impact this energy budget by absorbing some wavelengths of the IR flux and reemitting it towards the Earth, hence increasing its temperature.

G.1.4   Distinction between steady-state and equilibrium

Steady state describes a system where the properties do not change with respect to time. It is constant but dynamic. It describes an open system entropy driven (entropy increases).

Thermodynamic equilibrium describes a system where nothing changes at all. It is static, there is no macroscopic flow of matter or energy. It describes a closed system where Entropy is constant. In particular, at thermal equilibrium, there is no heat transfer, and temperatures are equal. Thermodynamic equilibrium is a particular case of steady state situations.

Local thermodynamic equilibrium describe a state where the system can be spatially divided into cells or micro-phases of infinitesimal size in which classical thermodynamic equilibrium conditions can be assumed. The idea is that energy and matter can freely flow from one cell to another slowly enough for the local thermodynamic equilibrium in each cell to be still a valid approximation. For this assumption to be valid, the order of magnitude of the relaxation time for the cell to reach local thermodynamic equilibrium has to be much shorter than the order of magnitude of the relaxation time for the macroscopic system to change.

Classical Thermodynamic is the study of these exchanges at near thermodynamic equilibrium, based on the laws of Thermodynamic.

Statistical mechanics relates thermodynamic behavior to microscopic parameters (interactions between individual particles), helped developing statistical thermodynamic, and describe out- of the equilibrium systems.

Non-equilibrium thermodynamic is a new branch of thermodynamic tackling with non-equilibrium systems. The condition of validity of this new branch is "local thermodynamic equilibrium".

Ordinary mechanics consider the behavior of a single state whereas statistical mechanics consider a statistical ensemble, a probability distribution over all possible states of the system with a collection of virtual and independent copies of the system in various state

G.2   Matter, Pressure and Temperature

Matter is composed of little bricks, the atoms, linked together thanks to one of the Four Fundamentals Interactions, Electromagnetism (along with Gravity created by mass, Strong Interaction at the nuclear level, and Weak Interaction responsible for Beta radiation).

Atoms are described thanks to the atomic orbitals model (Lewis model is older and less complete), which forecasts the probability of presence of an electron around the nucleus.

Heat is kinetic energy of the particles. Temperature of a body is related to the amount of kinetic energy the atoms of this body have: $\overline{E}_{kinetic} = \frac{3}{2}k_B T$ (average kinetic energy of a 3D-molecule). This kinetic energy makes the atoms vibrate and move, explaining the different states of matter: solid, liquid, gas. Liquid molecules are more agitated than solid molecules, and they can move relative to each other. Gas molecules are even more agitated and are completely free. The limit between a gas and a liquids lays in the relative strength between thermal agitation and attraction between molecules [48].

The collisions between molecules and a surface create the pressure. The more molecule there is the more collisions occur; and higher the temperature, higher the agitation of the molecules and hence the more collisions occur too.

G.2.1 Mass transfers

Mass transfer can occur through advection or diffusion.

Convection encompasses both diffusion and advection:
- diffusion occurs at the microscopic level, and is due to Brownian movements driven by a concentration gradient (or a chemical potential gradient)

$$\frac{\partial \Phi}{\partial t} = \bigtriangledown . (D \bigtriangledown \Phi) = 0 \tag{G.1}$$

  with D the diffusion coefficient. There is also self-diffusion of one specie into itself.
- advection occurs at a macroscopic level, driven by a macroscopic movement of the bulk fluid

$$\frac{\partial \Phi}{\partial t} + \bigtriangledown . (\overrightarrow{u} \Phi) = 0 \tag{G.2}$$

with $\overrightarrow{u}$ the fluid velocity.

G.2.2 Heat transfers

Heat transfers can occur through radiation, convection and conduction. Radiation can occur without material, whole convection and conduction only can occur when matter is present.

Heat conduction is equal to heat diffusion: heat is diffused through a material without any mass transfer, only via the vibrations of the molecules spreading from one molecule to another.

Heat convection occurs with a mass transfer: either mass diffusion (free convection) or mass convection (forced convection).

Latent heat (heat needed for a phase change) and sensible heat (the heat one can feel) must not be mistaken.

In this situation, part of the heat transferred to the interface from the vapor and liquid phases via convection and conduction is used to evaporate water. At steady state no heat is accumulated at the interface, all the heat received by the interface is used for evaporation.

G.2.3 Surface tension and capillarity

The attraction force between molecules in a liquid is greater than thermal agitation. A molecule inside a liquid is subjected to attraction forces of its neighbors (Van Der Waals or cohesive forces). Due to the symmetry of the environment, these forces are compensated: the mean resultant is null. On the surface with a gas, solid or another liquid, the situation is asymmetrical because the attraction forces (cohesive forces) of like molecules from the liquid are different than the attraction forces (adhesive force) of unlike molecules from the gas, solid or other liquid. As a result, the attraction force's mean resultant is not null.

In a water-air interface, the adhesive forces of air molecules on water molecules of the interface are significantly weaker (less numerous and farther away) than the cohesive forces exerted by water molecules on the water molecules of the interface. As a result of the attraction forces, the surface water molecules are drawn towards the liquid's interior. This phenomena is called surface tension. Because half of the cohesive force from liquid molecules is lacking, the molecules on the surface have less interaction with their counterparts, and a liquid tends to present the smallest surface area [48].

In a water-glass interface, the adhesive forces of glass molecules on the water molecules of the interface are greater than the cohesive forces exerted by water molecules on the water molecules of the interface. Hence, the resultant of the attraction forces tends to attract the surface water molecules to the glass surface, causing them to spread. This phenomena is called wetting.

To increase a liquid's surface area by dA, one must provide energy dW equal to that required to bring additional molecules to the surface: $dW = \gamma dA$, with γ the liquid surface tension. As a result, surface tension is defined as the energy necessary to increase the surface of a liquid by one unit. In the case of a droplet of water on a solid surface, there are 3 interfaces: solid-liquid, liquid-gas and solid-gas, each of which has its own surface tension (γ_{SL}, γ_{LG}, γ_{SG}). The energy differential between the dry and wet surfaces can be defined as the spreading parameter: $S = E_{dry} - E_{wet} = \gamma_{SG} - (\gamma_{SL} + \gamma_{LG})$. If $S > 0$, the liquid spreads because the wet surface's energy is lower than that of the dry surface.

Because of this surface tension, it is possible to compute the minimum thickness of the water film over a particular surface, which minimizes the system's free energy at a given volume Ω:

$$F_{film,e} = -S\Sigma + P(e)\Sigma \tag{G.3}$$

with $\Sigma = \frac{\Omega}{e}$, the surface of liquid in contact with the solid.

Adding some molecules to the liquid can impact the surface tension.

Water has a higher affinity for glass than for air (and even than from water), thus the spreading parameter is positive and the water tends to spread on the glass. On a capillary tube, ie a tube of very small diameter, the water tends to spread on the inside walls the glass tube as long as the weight of the water column ($mg = \rho V g = \rho g(\pi r^2 H)$) is smaller than the surface tension forces ($2\pi r\gamma cos(\theta)$).

Hence the maximum height H at which the liquid rises in the capillary tube is then:

$$H = \frac{2\gamma cos(\theta)}{r\rho g} \tag{G.4}$$

with r the radius of the tube, ρ the density of the liquid in $g.cm^{-3}$, also known as Jurin' law.

To determine the static profile h(r) of a non-wetting macroscopic drop of water laid on a surface, the interface must be described introducing the local curvatures and the different physical parameters.

The system being at equilibrium,the pressure difference between any point just below the interface at a distance r to the axis can be written, corresponding to a thickness h(r) and a point on the contact line (where r=R and h=0). $\Delta p_{r,h(r)} = \Delta p_{R,0} - \rho g h(r)$.

If a sphere is considered with P_i the internal pressure and P_e the external pressure, the volume variation is $dV = \frac{d}{dR}\left(\frac{4}{3}\pi R^3\right) = 4\pi R^2 dR$ and the surface variation is $dA = \frac{d}{dR}\left(4\pi R^2\right) = 8\pi R dR$. Hence the work of the pressure forces is: $\partial W = -P_e(4\pi R^2)dR + P_i(4\pi R^2)dR = (P_i - P_e)4\pi R^2 dR$. This work compensates the work of the superficial tension, $\partial W = \gamma dA = \gamma 8\pi R dR$. Hence, by equalizing those two terms, the pressure difference across the spherical surface is $\Delta P = P_i - P_e = \frac{2\gamma}{R}$. This relation is generalized by Laplace as the Laplace Pressure: $p_\alpha - p_\beta = \gamma(\frac{1}{R_1} + \frac{1}{R_2}) \Leftrightarrow \Delta p = \gamma C$ with C the interface curvature, $C(R) = \frac{2\theta}{R}$ for a spherical profile.

It can thus be written: $\gamma C(r) = \gamma C(R) - \rho g h(r)$. Hence, with the expression of $C(r)$ under its general form in radial symmetry:

$$\frac{\gamma}{\sqrt{1 + (\frac{dh(r)}{dr})^2}}(\frac{1}{1 + (\frac{dh(r)}{dr})^2}\frac{d^2}{dr^2}h(r) + \frac{1}{r}\frac{d}{dr}h(r)) = \gamma C(R) - \rho g h(r) \tag{G.5}$$

Marie-Alix Dalle

The first simplification occurs for the case of droplets with a low contact angles ($\approx 0.01rad$), ie in the lubrication approximation, $(\frac{dh(r)}{dr})^2 \ll 1$.

$$-(\frac{d^2}{dr^2}h(r) + \frac{1}{r}\frac{d}{dr}h(r))) = \gamma C(R) - \frac{h(r)}{\kappa^{-2}} \tag{G.6}$$

with κ^{-1} the capillary length, $0\sqrt{\frac{\gamma}{\rho g}}$.

This equation allow one analytic solution:$h(r) = C(R)\kappa^{-2}(1 - \frac{I_0(\frac{r}{\kappa^{-1}})}{I_0(\frac{R}{\kappa^{-1}})})$ with $I_\nu(a)$ the Bessel function of order ν at the point a.

Another model is the one of gravitar crepes, for radius very big compared to the capillary length ($\approx 2.7mm$ for water). It predict a constant thickness of the droplet (except close to the triple line), given by:

$$e = 2\kappa^{-1}sin(\frac{\theta}{2}) \approx \kappa^{-1}\theta \tag{G.7}$$

G.3 Fluid mechanics

There are several ways to describe a fluid: at microscopic level (atomistic approach, thanks to Boltzmann equation), at macroscopic level (continuum approach thanks to Navier-Stokes equations; density, velocity and pressure vary smoothly in space and time), and at a mesoscopic level (the kinetic theory, solving a discrete version of the Boltzmann equation).

G.3.1 Kinetic theory of Gases

In this model, a gas is described as a large number of identical submicroscopic particles all in constant rapid and random motion. The major assumption of this model is that the size of the particles is very small compared to the average distance between the particles. Moreover the particles are assumed to have no interaction between themselves apart from elastic collisions, hence it describes ideal gases (no Van der Waals forces, no relativistic speeds, no quantum exchange interactions...). A sufficiently high number of particles, of the exact same mass, is also required, for the statistical treatment to be applicable.

Temperature is a measure of the agitation of particles (kinetic energy), and pressure is the result of the collisions of these particles on a wall.

Intuitive explanation of why the particles are agitated in all directions as a steady state. Let's assume that in a recipient all particles go in the same direction at the same speed: then this is an unstable system because the slightest change in speed or direction of one molecule will create a collision with another molecule and eventually all molecules will be impacted.

G.3.2 Maxwell-Boltzmann Statistic

Maxwell-Boltzmann Statistic is a probability distribution used to determine the distribution of particles between several energy levels at equilibrium. It is the basis of gas kinetic. The assumptions are that the particles do not interact between each other, so it works for perfect gases (but not for liquids), at thermal equilibrium.

The distribution maximizes entropy of the system.

The Boltzmann equation is a statistic modeling of a fluid particles dynamic, which describes its statistical behavior out of equilibrium, based on the probability distribution for the position and momentum of a typical particle:

$$\frac{\partial f}{\partial t} = \left(\frac{\partial f}{\partial t}\right)_{forces} + \left(\frac{\partial f}{\partial t}\right)_{diffusion} + \left(\frac{\partial f}{\partial t}\right)_{collision} \tag{G.8}$$

with f the statistical distribution function for the velocity v at time t and position x.

Boltzmann equation governs the evolution of a system towards its equilibrium. Maxwell-Boltzmann distribution is a solution to the Boltzmann equation at equilibrium.

$$f(v)d^3v = \left(\frac{m}{2\pi kT}\right)^{\frac{3}{2}} e^{-\frac{mv^2}{2kT}} d^3v \tag{G.9}$$

this represents the fraction of particles within d^3v centered on a velocity vector of magnitude v, with k the Boltzmann constant.

G.3.3   SRT

G.3.3.1   Statistical mechanics

A macroscopic system is composed of a very large number of microscopic subsystems (atoms, molecules...). A macrostate is defined as the specific combination of large-scale observable macroscopic properties defined entirely by thermodynamic properties; whereas a microstate is defined as the precise arrangement (positions, velocities etc...) for all microscopic particles, that could give those properties. To a given macrostate can correspond a large number of microstates, each with a specific probability. According to statistical mechanics, all microstates consistent with its thermodynamic properties are equally likely.

Statistical mechanics is based on the concept of counting the ways in which energy (macrostate) can be distributed (statistical ensemble of microstates) and establishes a link between the macroscopic properties and the microscopic states, whereas ordinary mechanics focuses on the behavior of a single macrostate.

Then, if a system is left alone long enough, its particles and energy will find their way into all possible microstates given the laws of physics, and the vast majority of possible energy distributions will bring the system very close to a single macro state that's the state of thermal equilibrium in which energy is spread out maximally and temperature, pressure and other variables have the values predicted by classical thermodynamics.

The macroscopic state of a system is characterized by the distribution of its microstates, whose entropy, according to Boltzmann definition of Entropy, is:

$$S = k_B log(\Omega) = -k_B \Sigma_i p_i ln(p_i) \tag{G.10}$$

with Ω the number of microstates consistent with the macrostate, p_i the probability that the i's microstate occurs during the system's fluctuations.

The key concepts of Statistical rate theory are [2] a phase boundary (separation between two phases of a system), a single particle or energy quantum transport in a time interval, and the system configuration.

SRT considers volumes large enough to allow for a thermodynamic description of the phase (well defined thermodynamic variables), in the vicinity of (and including) the boundary; and small enough to allow for the local equilibrium assumption: no gradient exists within the cell. While the small volumes are assumed to be in local equilibrium, the phases are not assumed to be in equilibrium, in particular the bulk phase is not assumed to have a uniform temperature.

Using energy reservoirs, SRT assumes that the system is isolated. For instance in the evaporation process, the small volumes are not isolated because with each particle changing phase, latent heat is exchanged. Hence the little volumes are surrounded by "energy reservoirs", with the reservoir surrounding the small liquid volume being significantly larger than the reservoir surrounding the small vapor volume.

Thanks to the local equilibrium assumption, each phase of the small volume can be considered as a canonical ensemble, with a defined temperature and thus a finite range of quantum mechanical energies.

Let λ_f be the molecular distribution with N^V molecules in the vapor phase, and N^σ molecules in the liquid surface. $\Omega(\lambda_f)$ is the number of microstates corresponding to this molecular distribution. Similarly, let λ_k be the molecular distribution with $N^V + 1$ molecules in the vapor phase, and $N^\sigma - 1$ molecules in the liquid surface, and $\Omega(\lambda_k)$ the number of microstates corresponding to this molecular distribution.

The probability of a transition from a state corresponding to the molecular distribution λ_f to a state corresponding to the molecular distribution λ_k can be calculated thanks to Schrödinger equation, and it is assumed that this probability is constant for all the quantum mechanical states of the possible molecular distributions that are within the energy range of the small volume, and called k_{LV}.

Thus the probability of a transition from a molecular distribution λ_f to a molecular distribution λ_k at any instant during δt across the area δA is the product of the probability of finding the system in

a quantum mechanical state of molecular distribution λ_f at the instant t, with the probability of the transition to any quantum mechanical state of the distribution λ_k (k^{LV}) times the number of states corresponding to the distribution λ_k, ($\Omega(\lambda_k)$) [156]:

$$\tau(\lambda_f, \lambda_k) = \frac{k^{LV} \Omega(\lambda_k) \delta A}{\Omega(\lambda_f) \delta t} \tag{G.11}$$

According to Boltzmann definition of entropy (eq. G.10), $\Omega(\lambda_k) = e^{\frac{S(\lambda_k)}{k_B}}$, hence in G.11:

$$\tau(\lambda_f, \lambda_k) = \frac{k^{LV} e^{\frac{S(\lambda_k)}{k_B}} \delta A}{e^{\frac{S(\lambda_f)}{k_B}} \delta t} = \frac{k^{LV} \delta A}{\delta t} e^{\frac{S(\lambda_k) - S(\lambda_f)}{k_B}} \tag{G.12}$$

Similarly, the converse phenomenon (one vapor molecule converting to a water molecule) is explained as follows:

$$\tau(\lambda_f, \lambda_i) = \frac{k^{LV} \delta A}{\delta t} e^{\frac{S(\lambda_i) - S(\lambda_f)}{k_B}} \tag{G.13}$$

G.3.3.2 Derivation of the Entropy variation for SRT

Following [156] and [155], the entropy is calculated using Euler relation: for the vapor phase $S^V = N^V \left(\frac{h^V - \mu^V}{T^V} \right)$ and for the surface $S^\sigma = N^\sigma \left(\frac{u^\sigma - \mu^\sigma}{T^\sigma} \right) - \frac{\gamma A}{T^\sigma}$. Hence the entropy of the isolated system can be calculated as $S(N^V, N^\sigma) = N^\sigma \left(\frac{u^\sigma - \mu^\sigma}{T^\sigma} \right) - \frac{\gamma A}{T^\sigma} + N^V \left(\frac{h^V - \mu^V}{T^V} \right) + S^L(N^V, N^\sigma)$.

According to the conservation of Energy, $N^V h^V + N^\sigma u^\sigma + U^L(N^V, N^\sigma) = (N^V + 1)h^V + (N^\sigma - 1)u^\sigma + U^L(N^V + 1, N^\sigma - 1)$. Hence $U^L(N^V + 1, N^\sigma - 1) - U^L(N^V, N^\sigma) = u^\sigma - h^V$.

The change in entropy of the system is $\Delta S_{\sigma V} = \left(\frac{h^V - \mu^V}{T^V} \right) - \left(\frac{u^\sigma - \mu^\sigma}{T^\sigma} \right) + S^L(N^V + 1, N^\sigma - 1) - S^L(N^V, N^\sigma) = \left(\frac{h^V - \mu^V}{T^V} \right) - \left(\frac{u^\sigma - \mu^\sigma}{T^\sigma} \right) + \left(\frac{u^\sigma - h^V}{T^L} \right)$.

Assuming $T^\sigma = T^L$ and that $\mu^\sigma = \mu^L$, the previous equation becomes:

$$\Delta S_{\sigma V} = h^V \left(\frac{1}{T^V} - \frac{1}{T^L} \right) + \left(\frac{\mu^L}{T^L} - \frac{\mu^V}{T^V} \right) \tag{G.14}$$

At equilibrium, the chemical potential of the molecule in the liquid phase must equal that of the molecule in the vapor, hence the liquid phase may be approximated as slightly compressible and the chemical potential may be written in terms of a reference state. If the reference state is chose as the saturation condition, then:

$$\mu^L(T^L, P_e^L) = \mu(T^L, P_\infty(T^L)) + v_\infty^L(P_e^L - P_\infty(T^L)) \tag{G.15}$$

with v_∞^L the specific volume of the saturated liquid phase.

By assimilating the vapor phase to an ideal gas, the chemical potential of the vapor phase can be rewritten:

$$\mu^V(T^L, P_e^V) = \mu(T^L, P_\infty(T^L)) + k_B T^L ln \left(\frac{P_e^V}{P_\infty} \right) \tag{G.16}$$

with P_∞ the saturation vapor pressure.

Moreover the conditions at equilibrium must be $\frac{\mu_e^L}{T_e^L} = \frac{\mu_e^V}{T_e^V}$ and $T_e^L = T_e^V = T^L$. Inserting G.15 and G.16 in this relation gives:

$$\frac{\mu(T_e^L, P_\infty(T_e^L))}{T_e^L} + v_\infty^L \frac{(P_e^L - P_\infty(T_e^L))}{T_e^L} = \frac{\mu(T_e^L, P_\infty(T_e^L))}{T_e^V} + k_B ln \left(\frac{P_e^V}{P_\infty} \right) \tag{G.17}$$

$$v_\infty^L \frac{(P_e^L - P_\infty(T_e^L))}{T_e^L} = k_B ln \left(\frac{P_e^V}{P_\infty} \right) \tag{G.18}$$

Hence

$$P_e^V = P_\infty e^{\frac{v_\infty^L (P_e^L - P_\infty(T_e^L))}{k_B T_e^L}} \tag{G.19}$$

And thus, at equilibrium, it is assumed that CKT can be applied and that $K_e = P_s(T_e)\left(\frac{m}{2\pi k_B T_e}\right)^{\frac{1}{2}} = P_\infty e^{\frac{v_\infty^L(P_e^L - P_\infty(T_e^L))}{k_B T_e^L}}\left(\frac{m}{2\pi k_B T_e}\right)^{\frac{1}{2}}$.

If surface tension at the water surface needs to be accounted for, $P^L = P^V + \frac{2\gamma^{LV}}{R_c}$ can be expressed with R_c the radius of curvature of the water surface and γ^{LV} the surface tension.

Thus G.15 becomes:

$$\mu^L(T^L, P_e^L) = \mu(T^L, P_\infty(T^L)) + v_\infty^L\left(P_e^V + \frac{2\gamma^{LV}}{R_c} - P_\infty(T^L)\right) \tag{G.20}$$

An expression for the chemical potential of the vapor phase assumed to behave as an ideal gas can be calculated using Boltzmann statistics and the Oppenheimer approximation:

$$\frac{\mu^V(T^V, P^V)}{T^V} = -k_B ln\left(\left(\frac{m}{2\pi h^2}\right)^{\frac{3}{2}} \frac{(k_B T^V)^{\frac{5}{2}}}{P^V}\right) - k_B ln(q_{vib} q_{rot} q_{elec}) \tag{G.21}$$

with q_{vib}, q_{rot}, q_{elec} respectively the vibrational, rotational and electronic partition function.

The partition function can also provide an expression for the enthalpy of the vapor phase:

$$h^V = 4k_B T^V - D_e + k_B \Sigma_{l=1}^3 \frac{\Theta_l}{2} + k\Sigma_{l=1}^3 \frac{\Theta_l}{exp\left(\Theta_l/T^V\right) - 1} \tag{G.22}$$

G.14 can finally be rewritten as a function of known parameters:

$$\frac{\Delta S_{\sigma,V}}{k} = 4\left(1 - \frac{T^V}{T^L}\right) + \left(\frac{1}{T^V} - \frac{1}{T^L}\right)\Sigma_{l=1}^3\left(\frac{\Theta_l}{2} + \frac{\Theta_l}{exp\left(\Theta_l/T^V\right) - 1}\right)$$
$$+ \frac{v_\infty^L}{k_B T^L}\left(P^V + \frac{2\gamma^{LV}}{R_c} - P_\infty(T^L)\right) + ln\left(\left(\frac{T^V}{T^L}\right)^4 \frac{P_\infty(T^L)}{P^V}\right) + ln\left(\frac{q_{vib}(T^V)}{q_{vib}(T^L)}\right) \tag{G.23}$$

Since $\mu^L = h^L - T^L s^L$ and $\mu^V = h^V - T^V s^V$, thus $\frac{\mu^L}{T^L} = \frac{h^L}{T^L} - s^L$ and $\frac{\mu^V}{T^V} = \frac{h^V}{T^V} - s^V$ and in the previous equation: $\Delta S_{\sigma V} = h^V\left(\frac{1}{T^V} - \frac{1}{T^L}\right) + \left(\frac{h^L}{T^L} - s^L - \frac{h^V}{T^V} + s^V\right) = s^V - s^L + \frac{1}{T^L}(h^L - h^V)$.

A phonon is an internal molecular vibration frequency. Indeed, in order for a molecule to evaporate, it needs to overcome the attraction energy with its surrounding molecules. Larger values of phonons would be then expected to require more energy to excite them to escape the liquid.

G.4 Light theory

Light can be described as either a wave with a specific wavelength and intensity (wave optics), or as particles that behave like discrete wave packets (geometric optics). Indeed, Newton's initial description of light as particles demonstrated its limitations when confronted to light interferences (light+light=shadow). Thus, Einstein proposed the wave-particle duality: each photon carries an energy proportional to its frequency, $E = h\nu$ with h the Planck constant and ν the frequency.

As discussed in section 5.2.1.4, among the three optical solutions described below (Interferometry, Schlieren and Shadowgraphy), only Interferometry is based on a wave property of light necessitating the use of wave optics (phase); geometric optics should suffice to model Schlieren and Shadowgraphy. However, the use of a laser (perfectly coherent light) precludes the assumption that the different light rays emitted by this light source are independent from each other and act "individually", thus wave optics is required [98].

G.4.1 Geometric optics

The geometric optics rules are the following: a lens is made up of an axis and a focal point, at which the rays parallel to the axis focus. A light ray parallel to the axis exits the lens through the focal point. A ray going through the focal point exits parallel to the axis. A light ray passing through the center of the lens is not deflected. A beam of parallel light rays focuses after the lens on a point where the parallel ray passing through the lens's center crosses the focal plane.

G.4.2 Fourier optic

Fourier Optic is based on the principles of wave optics, which states that light propagates as an electromagnetic wave, and thus obeys Maxwell's laws, which are fundamental premises of electromagnetism.
Indeed, electromagnetic waves are emitted by electrically charged particles undergoing acceleration.
Electromagnetic waves can be defined as follows:

$$E = A \sin(\frac{2\pi}{\lambda}(ct - x) + \Phi) \tag{G.24}$$

where x is the geometric path length and Φ is the phase, which can also be re-written in terms of length as the optical path length $OPL = \frac{\lambda}{2\pi}\Phi$.

According to Huygens-Fresnel principle, valid in the paraxial approximation, each location reached by a wave behaves exactly like a secondary source of this wave.
According to Fraunhofer Diffraction, the lens generates in its image focal plane the Fourier transform of the object, decomposing it into simpler exponential functions. The Fourier Transform of a function is the extension of the Fourier series development to non periodical functions. It represents a function by the spectral density from which it originates: $F(f).\xi \rightarrow \hat{f}(\xi) = \int_{-\infty}^{+\infty} f(x)e^{-i\xi x}dx$ with f an integrable function on $\Re$.
Let Σ be an opening surface in plane $z = 0$, P a point on this surface, $E(P)$ the amplitude of the incident wave on P, K a constant (fig. G.1). A wave arriving at M(x,y) in the plane z=r has the following amplitude:

$$dE(M) = \frac{1}{PM}KE(P)d\Sigma e^{i\Phi_{PM}} = \frac{1}{PM}KE(P)d\Sigma e^{i\frac{2\pi PM}{\lambda}} \tag{G.25}$$

the term $\frac{1}{PM}$ traduces the fact that the intensity decreases on the sphere surface (conservation of energy through the surface of the sphere) and Φ_{PM} the phase delay between P and M. Hence the total intensity reaching M is given by the sum of these contributions from every point of the surface Σ:

$$E(M) = K \int \int_{\Sigma} \frac{E(P)}{PM}e^{i\frac{2\pi PM}{\lambda}}d\Sigma \tag{G.26}$$

As $\overrightarrow{PM} = \overrightarrow{PP'} + \overrightarrow{P'M} = r\overrightarrow{e}_z + (X - x)\overrightarrow{e}_x + (Y - y)\overrightarrow{e}_y$ then $| PM |= \sqrt{r^2 + (X - x)^2 + (Y - y)^2} = \frac{1}{r}\sqrt{1 + \frac{(X-x)^2}{r^2} + \frac{(Y-y)^2}{r^2}}$. Thus for M really close the optic axis, $X - x << r$ and $Y - y << r$, and with a limited development of the previous equation: $| PM |$ becomes $| PM |= r\left(1 + \frac{1}{2}\left(\frac{X-x}{r}\right)^2 + \frac{1}{2}\left(\frac{Y-y}{r}\right)^2\right)$, plugged in G.26 gives:

$$E(M) = \frac{Ke^{i\frac{2\pi r}{\lambda}}}{PM} \int \int_{\Sigma} E(P)e^{\frac{i\pi}{\lambda r}\left((X-x)^2 + (Y-y)^2\right)}dXdY \tag{G.27}$$

For $\frac{X^2}{\lambda r} << 1$ (corresponding to an observation at infinity), also known as the Fresnel number, this can be rewritten: $e^{\frac{i\pi}{\lambda r}(X-x)^2} \approx e^{\frac{i\pi}{\lambda r}x^2}e^{-\frac{2i\pi}{\lambda r}Xx}$, and hence in G.27

$$E(M) = \frac{Ke^{i\frac{2\pi r}{\lambda}}}{PM} \int \int_{\Sigma} E(P)e^{\frac{i\pi r}{\lambda}}e^{-\frac{2i\pi}{\lambda r}(Xx+Yy)}dXdY \tag{G.28}$$

Let's define $t(P) = t(X, Y)$ the transmission function, such that $E(P) = E_0(P)t(X, Y)$. Thus in G.28:

$$E(M) = \frac{Ke^{i\frac{3\pi r}{\lambda}}E_0(P)}{PM} \int \int_{\Sigma} t(X, Y)e^{-\frac{2i\pi}{\lambda r}(Xx+Yy)}dXdY \tag{G.29}$$

This last equation represents the Fourier transform of the transmission function t.
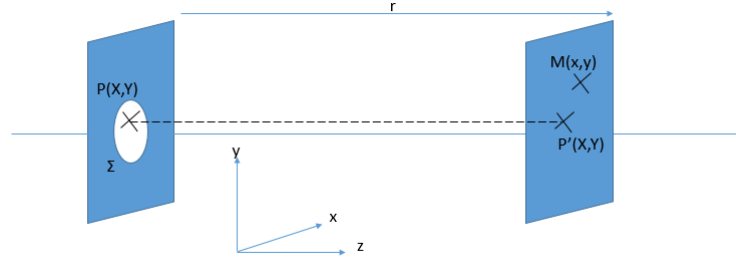
Figure G.1: Schema for the Fraunhofer optics

When a lens is crossed for the second time, the operation is equivalent to a reversed Fourier transform, and in the end, the imaging plane and the initial object plane are said to be conjugated planes: whatever appears in the object plane also appears in the imaging plane.

G.4.3   The "reversing" phenomenon

The second big challenge was that the image on the screen seemed to "reverse" (right becoming left) when hot water was poured in.

When filling the module with hot water, the image on the screen was "changing direction", the left side appearing on the right and vice-versa. This phenomenon would appear whether water was flowing or not, just as long as the water inside the module was hot.
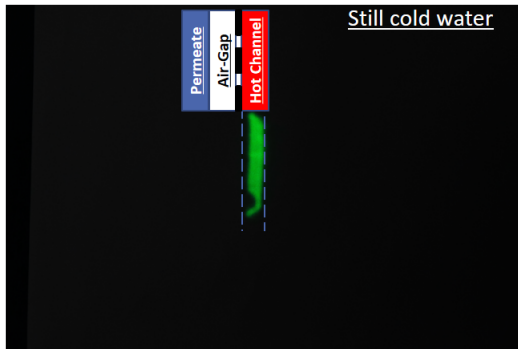
Figure G.2: Schlieren Picture of the screen when cold water is still in the module. The black mark indicates the membrane side.
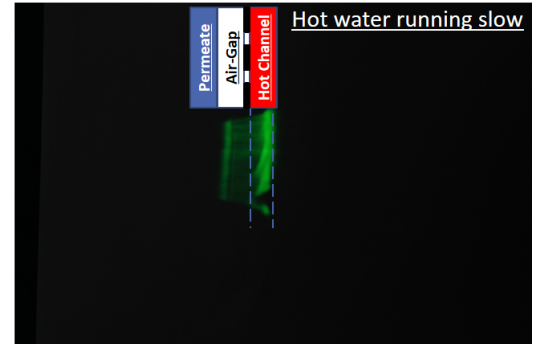
Figure G.3: Schlieren Picture of the screen when hot water is running slow in the module. The black mark indicates the membrane side.

A first interpretation was that the temperature gradient was so strong that it would bend all the rays towards the membrane (and maybe there would be also a very strong temperature gradient at the wall side), where they would be reflected, hence "reversing" the image on the screen.

However, the little ray tracing code applied to very various temperature gradients never led me to observe such change on the screen.

A discussion with Alexander Kroiss led me to read the article [54]. The "reversing phenomenon" is actually due indeed to the fact that under high refractive index gradients, the medium can behave as a lens. New temperature profiles were tried with the ray tracing simulation, that could finally produce a reversion.

The following lines, based on [54] will intend to explain that phenomenon.

The wave equation, driving the behavior of light, is:

$$\frac{\partial^2 u}{\partial t^2} = c^2 \left(\frac{\partial^2 u}{\partial x_1^2} + \frac{\partial^2 u}{\partial x_2^2} + \frac{\partial^2 u}{\partial x_3^2} + ... \right) \tag{G.30}$$

When looking for an harmonic solution of the wave equation, it is looked under the form: $p'(x,y,z,t) = p(x,y,z)e^{j\xi t}$. Plugging this in G.30 the following equation is obtained, also known as the Helmholtz equation:

$$\Delta p' + \left(\frac{\xi}{c}\right)^2 p' = 0 \tag{G.31}$$

and if $k = \frac{\xi}{c} = \frac{2\pi}{\lambda}$ is the wave number ,with p the wave disturbance , $\overline{k} = \frac{\sqrt{\iota\mu}}{\Omega} = \frac{2\pi}{\lambda}$ the wave number, with ι the dielectric constant , μ the permeability , $\Omega = 2\pi\gamma$ the angular frequency , γ the frequency of the light oscillation , λ the wavelength.

Thus $\frac{\partial p'}{\partial x} = \frac{\partial p}{\partial x}e^{j\Omega t}p(x,y,z)\frac{1}{p(x,y,z)} + p(x,y,z)\frac{\partial j\Omega t}{\partial x}e^{j\Omega t} = p'(x,y,z)\frac{\partial ln(p(x,y,z))}{\partial x} + p'(x,y,z)\frac{\partial j\Omega t}{\partial x}$

and $\frac{\partial^2 u}{\partial x^2} = \frac{\partial p'(x,y,z)}{\partial x}\frac{\partial ln(p(x,y,z))}{\partial x}+p'(x,y,z)\frac{\partial^2 j\Omega t}{\partial x^2}+p'(x,y,z)\frac{\partial^2 ln(p(x,y,z))}{\partial x^2}+\frac{\partial p'(x,y,z)}{\partial x}\frac{\partial j\Omega t}{\partial x} = (p'(x,y,z)\frac{\partial ln(p(x,y,z))}{\partial x}+$
$p'(x,y,z)\frac{\partial j\Omega t}{\partial x})\frac{\partial ln(p(x,y,z))}{\partial x}+p'(x,y,z)\frac{\partial^2 j\Omega t}{\partial x^2}+p'(x,y,z)\frac{\partial^2 ln(p(x,y,z))}{\partial x^2}+(p'(x,y,z)\frac{\partial ln(p(x,y,z))}{\partial x}+p'(x,y,z)\frac{\partial j\Omega t}{\partial x})\frac{\partial j\Omega t}{\partial x} =$
$p'(x,y,z)\left(\frac{\partial ln(p(x,y,z))}{\partial x}\right)^2+p'(x,y,z)\frac{\partial^2 j\Omega t}{\partial x^2}+p'(x,y,z)\frac{\partial^2 ln(p(x,y,z))}{\partial x^2}+2p'(x,y,z)\frac{\partial ln(p(x,y,z))}{\partial x}\frac{\partial j\Omega t}{\partial x}+p'(x,y,z)\left(\frac{\partial j\Omega t}{\partial x}\right)^2 =$
$p'(x,y,z)\left(\left(\frac{\partial ln(p(x,y,z))}{\partial x}\right)^2 + \frac{\partial^2 ln(p(x,y,z))}{\partial x^2}\right)+2p'(x,y,z)\left(\frac{1}{2}\frac{\partial^2 j\Omega t}{\partial x^2} + \frac{\partial ln(p(x,y,z))}{\partial x}\frac{\partial j\Omega t}{\partial x}\right)+p'(x,y,z)\left(\frac{\partial j\Omega t}{\partial x}\right)^2$.

In the y and z direction the expression are similar hence, in G.31:

$$p'\left(\left(\frac{\partial ln(p)}{\partial x}\right)^2 + \left(\frac{\partial ln(p)}{\partial y}\right)^2 + \left(\frac{\partial ln(p)}{\partial z}\right)^2 + \frac{\partial^2 ln(p)}{\partial x^2} + \frac{\partial^2 ln(p)}{\partial y^2} + \frac{\partial^2 ln(p)}{\partial z^2}\right)$$
$$+2p'\left(\frac{1}{2}\frac{\partial^2 j\Omega t}{\partial x^2} + \frac{1}{2}\frac{\partial^2 j\Omega t}{\partial y^2} + \frac{1}{2}\frac{\partial^2 j\Omega t}{\partial z^2} + \frac{\partial ln(p)}{\partial x}\frac{\partial j\Omega t}{\partial x} + \frac{\partial ln(p)}{\partial y}\frac{\partial j\omega t}{\partial y} + \frac{\partial ln(p)}{\partial z}\frac{\partial j\Omega t}{\partial z}\right) \tag{G.32}$$
$$-p'\left(\left(\frac{\partial \Omega t}{\partial x}\right)^2 + \left(\frac{\partial \Omega t}{\partial y}\right)^2 + \left(\frac{\partial \Omega t}{\partial z}\right)^2 - \left(\frac{\omega}{c}\right)^2\right) = 0$$

If $D = \left(\frac{\partial}{\partial x}\right)^2 + \left(\frac{\partial}{\partial y}\right)^2 + \left(\frac{\partial}{\partial z}\right)^2$ in G.32:

$$p'\left(D(ln(p)) + \Delta(ln(p))\right)$$
$$+2p'\left(\frac{1}{2}\Delta(j\Omega t) + grad(ln(p)).grad(j\Omega t)\right) \tag{G.33}$$
$$-p'\left(D(\Omega t) - \left(\frac{\Omega}{c}\right)^2\right) = 0$$

This equation is verified if every term is equal to zero:

$$D(\frac{\Omega t}{k_0}) = \left(\frac{k}{k_0}\right)^2 = \left(\frac{n}{n_0}\right)^2$$

$$D(ln(p)) + \Delta(ln(p)) = 0$$

$$grad(ln(p)).grad(j\Omega t) = -\frac{1}{2}\Delta(j\omega t)$$

The first equation can be rewritten:

$$D(\frac{\Omega t}{k_0}) = grad(\frac{\Omega t}{k_0}).grad(\frac{\Omega t}{k_0}) = \left(\frac{k}{k_0}\right)^2 = n^2$$

If s is the unity vector such that $s = \frac{grad(\frac{\Omega t}{k_0})}{\sqrt{D(\frac{\Omega t}{k_0})}} = \frac{grad(\frac{\Omega t}{k_0})}{n}$: hence $ns = grad(\frac{\Omega t}{k_0})$ and $rot(ns) = rot.grad(\frac{\Omega t}{k_0}) = 0$.

In geometrical optics, $\lambda \to 0$ or $\overline{k} \to \infty$, the previous equation diverges, and Debye proposed an approximate solution as: $u = Ae^{i\overline{k}_0 E}$ with A the amplitude factor and $E = E(x,y,z)$ the wave front.

Marie-Alix Dalle

Let's consider a cartesian orthonormal referential (x,y,z) in which a light ray traverses along the z axis an inhomogeneous refractive index media. The light ray is thus bent by this variation of refractive index, and one can define a referential $\left(\overrightarrow{T}, \overrightarrow{N}\right)$ with $\overrightarrow{T}$ the tangent vector to the ray, and $\overrightarrow{N}$ its perpendicular vector resulting in a direct and orthonormal referential. Thus these vectors can be rewritten $\overrightarrow{T} = \frac{1}{\sqrt{y'^2+z'^2}}\binom{z'}{y'}$ and $\overrightarrow{N} = \frac{1}{\sqrt{y'^2+z'^2}}\binom{-y'}{z'}$.
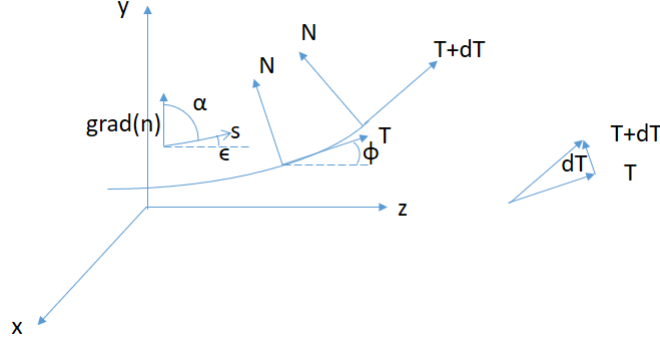

Figure G.4: Conventions used in the optical calculation for the reversing of the image on the screen observed when hot water is in the module

Let's note s the curvilinear abscissa. Since it is known that $\overrightarrow{T}.\overrightarrow{T} = 1$, then $2\overrightarrow{T}.\frac{d\overrightarrow{T}}{ds} = 0$ thus $\frac{d\overrightarrow{T}}{ds} \perp \overrightarrow{T}$ and hence $\frac{d\overrightarrow{T}}{ds} \propto \overrightarrow{N}$. The proportional coefficient between $\frac{d\overrightarrow{T}}{ds}$ and $\overrightarrow{N}$ is the curvature: $\frac{d\overrightarrow{T}}{ds} = \gamma\overrightarrow{N} = \frac{1}{R}\overrightarrow{N}$ with R the radius of the osculation circle to the curve in this specific point.

Let's note ϕ the angle between $\overrightarrow{T}$ and the horizontal axis. Thus $\overrightarrow{T}$ can be rewritten $\overrightarrow{T} = \binom{\cos(\phi)}{\sin(\phi)}$, and $\overrightarrow{N} = \binom{-\sin(\phi)}{\cos(\phi)}$. Besides, $\gamma\overrightarrow{N} = \frac{d\overrightarrow{T}}{ds} = \binom{-\sin(\phi)\frac{d\phi}{ds}}{\cos(\phi)\frac{d\phi}{ds}}$: hence, $\gamma = \frac{d\phi}{ds}$.

Moreover, $\tan(\phi) = \frac{y'}{z'}$ thus by derivating, $(1+\tan^2(\phi))\frac{d\phi}{dt} = \left(\frac{y'}{z'}\right)' = \frac{y''z'-z''y'}{z'^2}$. Since $R = \frac{1}{\gamma} = \frac{ds}{d\phi} = \frac{ds}{dt}\frac{dt}{d\phi} = \frac{\sqrt{z'^2+y'^2}}{\frac{y''z'-z''y'}{z'^2}} = \frac{\sqrt{z'^2+y'^2}}{\frac{y''z'-z''y'}{z'^2}} = \frac{\sqrt{z'^2+y'^2}}{\frac{y''z'-z''y'}{z'^2+y'^2}} = \frac{(z'^2+y'^2)^{\frac{3}{2}}}{y''z'-z''y'}$. For $t = z$ (or: instead of having $(y(t), z(t))$ by considering $y = f(z)$), it is obtained $z' = \frac{dz}{dt} = 1$, $z'' = 0$ and $y' = \frac{dy}{dt} = \frac{dy}{dz}$. Thus:

$$R = \frac{\left(1 + \left(\frac{dy}{dz}\right)^2\right)^{\frac{3}{2}}}{\frac{d^2y}{dz^2}} \tag{G.34}$$

The curvature can also be calculated another way: $\overrightarrow{\gamma} = \frac{d\overrightarrow{s}}{ds} = \frac{\partial s}{\partial x}\frac{dx}{ds} + \frac{\partial s}{\partial y}\frac{dy}{ds} + \frac{\partial s}{\partial z}\frac{dz}{ds} = \frac{\partial s}{\partial x}s_x + \frac{\partial s}{\partial y}s_y + \frac{\partial s}{\partial z}s_z$ (*). Moreover, since $\mid s\mid^2 = 1$, then $grad(\mid s \mid^2) = 0 = 2(s_x grad(s_x) + s_y grad(s_y) + s_z grad(s_z))$ (**). By sustracting (*) and (**) it is obtained: $\overrightarrow{\gamma} = s_x\left(\frac{\partial\overrightarrow{s}}{\partial x} - grad(s_x)\right) + s_y\left(\frac{\partial\overrightarrow{s}}{\partial y} - grad(s_y)\right) + s_z\left(\frac{\partial\overrightarrow{s}}{\partial z} - grad(s_z)\right) = s_x\left(\frac{\partial s_x}{\partial x}\overrightarrow{e_x} + \frac{\partial s_y}{\partial x}\overrightarrow{e_y} + \frac{\partial s_z}{\partial x}\overrightarrow{e_z} - \frac{\partial s_x}{\partial x}\overrightarrow{e_x} - \frac{\partial s_x}{\partial y}\overrightarrow{e_y} - \frac{\partial s_x}{\partial z}\overrightarrow{e_z}\right) + s_y\left(\frac{\partial s_x}{\partial y}\overrightarrow{e_x} + \frac{\partial s_y}{\partial y}\overrightarrow{e_y} + \frac{\partial s_z}{\partial y}\overrightarrow{e_z} - \frac{\partial s_y}{\partial x}\overrightarrow{e_x} - \frac{\partial s_y}{\partial y}\right.$ $s_z\left(\frac{\partial s_x}{\partial z}\overrightarrow{e_x} + \frac{\partial s_y}{\partial z}\overrightarrow{e_y} + \frac{\partial s_z}{\partial z}\overrightarrow{e_z} - \frac{\partial s_z}{\partial x}\overrightarrow{e_x} - \frac{\partial s_z}{\partial y}\overrightarrow{e_y} - \frac{\partial s_z}{\partial z}\overrightarrow{e_z}\right) = \left(s_y\left(\frac{\partial s_x}{\partial y} - \frac{\partial s_y}{\partial x}\right) + s_z\left(\frac{\partial s_x}{\partial z} - \frac{\partial s_z}{\partial x}\right)\right)\overrightarrow{e_x} + \left(s_x\left(\frac{\partial s_y}{\partial x} - \frac{\partial s_x}{\partial y}\right) + s_z\left(\frac{\partial}{}\right.\right.$ $\left(s_z\left(\frac{\partial s_z}{\partial x} - \frac{\partial s_x}{\partial z}\right) + s_y\left(\frac{\partial s_z}{\partial y} - \frac{\partial s_y}{\partial y}\right)\right)\overrightarrow{e_z}$. As a conclusion,

$$\overrightarrow{\gamma} = -s \times rot(s) \tag{G.35}$$

Moreover, $rot(ns) = 0$, hence $nrot(\overrightarrow{s}) - \overrightarrow{s} \times grand(n) = 0$ so $rot(\overrightarrow{s}) = \frac{1}{n}(\overrightarrow{s} \times grad(n))$ and thus:

$$\mid rot(\overrightarrow{s})) \mid = \frac{1}{n}\mid s \mid \mid grad(n) \mid sin(\alpha) \tag{G.36}$$

where α is the angle between $\overrightarrow{s}$ and $\overrightarrow{grad}(n)$

Marie-Alix Dalle

Since $\overrightarrow{s}$ and $\overrightarrow{rot}(s)$ are perpendicular, thanks to G.35 and G.36, $\mid \overrightarrow{\gamma} \mid = \mid s \mid \frac{1}{n} \mid s \mid \mid grad(n) \mid sin(\alpha) = \mid s \mid^2 \frac{1}{n} \mid grad(n) \mid sin(\alpha)$ or:

$$\mid \overrightarrow{\gamma} \mid = \frac{\mid grad(n) \mid}{n} \sin(\alpha) = \frac{1}{R} \tag{G.37}$$

If $\phi = \frac{\pi}{2} - \alpha$ and $grad(n) = \frac{dn}{dy}$, using G.37 and G.34:

$$\mid \overrightarrow{\gamma} \mid = \frac{1}{R} = \frac{\frac{d^2 y}{dz^2}}{\left(1 + \left(\frac{dy}{dz}\right)^2\right)^{\frac{3}{2}}} = \frac{dn}{dy} \frac{cos(\phi)}{n} \tag{G.38}$$

By noticing that $\cos^2(\phi) = 1 - \sin^2(\phi) = 1 - \tan^2(\phi)\cos^2(\phi)$ and hence $\cos(\phi) = \frac{1}{\sqrt{1 + \tan^2(\phi)}}$, G.38 can be rewritten:

$$\mid \overrightarrow{\gamma} \mid = \frac{1}{n} \frac{dn}{dy} \frac{1}{\sqrt{1 + \tan(\phi)^2}} = \frac{1}{n} \frac{dn}{dy} \frac{1}{\sqrt{1 + \frac{y'^2}{z'^2}}} = \frac{1}{n} \frac{dn}{dy} \frac{1}{\sqrt{1 + y'^2}} \tag{G.39}$$

Combining G.38 and G.39, $\frac{\frac{d^2 y}{dz^2}}{\left(1 + \left(\frac{dy}{dz}\right)^2\right)^{\frac{3}{2}}} = \frac{1}{n} \frac{dn}{dy} \frac{1}{\sqrt{1 + y'^2}}$ or

$$\frac{\frac{d^2 y}{dz^2}}{1 + \left(\frac{dy}{dz}\right)^2} = \frac{1}{n} \frac{dn}{dy} = \frac{dln(n)}{dy} \tag{G.40}$$

, hence $\frac{y'' dy}{1 + \left(\frac{dy}{dz}\right)^2} = dln(n)$. Noting that $y'' dy = \frac{dy'}{dz} dy = dy' \frac{dy}{dz} = y' dy'$, then $\frac{y' dy'}{1 + \left(\frac{dy}{dz}\right)^2} = dln(n)$, and when integrating: $[\frac{1}{2} ln(y'^2 + 1)]_{y_0}^{y} = [ln(n)]_{n_0}^{n}$ thus $\frac{1 + y'^2}{1 + y_0'^2} = \left(\frac{n}{n_0}\right)^2 = \frac{\cos^2(\phi_0)}{\cos^2(\phi)} = \frac{\sin^2(\phi_0)}{\sin^2(\phi)}$ (***).

If it is assumed that $\frac{dy}{dz} \ll 1$ hence $\left(\frac{dy}{dz}\right) \ll 1$ and in G.40: $\frac{d^2 y}{dz^2} = \frac{1}{n} \frac{dn}{dy} = \frac{dln(n)}{dy}$ hence $\left(\frac{dy}{dz}\right)_l = \int_{z=0}^{z=l} \frac{1}{n} \frac{dn}{dy} dz = tan(\phi_l)$ (the integration can be conducted along z instead of s for small refractive index gradients or for very short module in the z direction: in those cases, the integral over z is very similar to the integral over s). Going further and assuming $\frac{dn}{dy} = cst$, and $\phi \ll 1$, the previous equation becomes: $\phi_l = \frac{1}{n} \left(\frac{dn}{dy}\right)_0 l$. To go further in the approximation, instead of $\frac{dn}{dy} = cst$ the approximation can be prolongated: $\frac{dn}{dy} = \left(\frac{dn}{dy}\right)_0 + \left(\frac{d^2 n}{dy^2}\right)_0 (y - y_0)$ and hence the integral becomes: $\phi_l = \frac{1}{n} \left(\frac{dn}{dy}\right)_0 \left(l + \left(\frac{d^2 n}{dy^2}\right)_0 \frac{l^3}{6}\right)$

Assuming that $n' = \frac{dn}{dy} = const$, (meaning that one single light ray is submitted to a constant refractive index gradient, not that the gradient is constant in the entire module), $n = n_0 + n'(y - y_0)$ can be written with $\frac{n'(y - y_0)}{n_0} \ll 1$, thus $\left(\frac{n}{n_0}\right)^2 \approx 1 + \left(2 \frac{n'}{n_0}\right)(y - y_0)$ (limited development). By assuming that $y_0' = 0$ in (***), $y'^2 = \left(\frac{n}{n_0}\right)^2 (1 + y_0'^2) - 1 = \left(\frac{n}{n_0}\right)^2 - 1 \approx \left(2 \frac{n'}{n_0}\right)(y - y_0)$. Hence $z = \int_{z_0}^z dz = \int_{z_0}^z \frac{dz}{dy} dy = \int_{z_0}^z \frac{1}{y'} dy = \int_{z_0}^z \frac{1}{\sqrt{2 \frac{n'}{n_0}(y - y_0)}} dy = \frac{2}{\sqrt{2 \frac{n'}{n_0}}} \int_{z_0}^z \frac{dy}{2\sqrt{y - y_0}} = \sqrt{\frac{2 n_0}{n'}} [\sqrt{y - y_0}]_{z_0}^z = \sqrt{\frac{2 n_0}{n'}} (\sqrt{y - y_0})$. Thus for $z = l$, $l = \sqrt{\frac{2 n_0}{n'}(y_l - y_0)}$, or $\frac{l^2 n'}{2 n_0} = y_l - y_0$. Moreover, the slope of the ray at $z = l$ is $y_l' = \frac{y_l - y_0}{l - l/2}$ hence combining this last equation with the previous, it is obtained: $y_l' = \frac{l n'}{n_0}$.
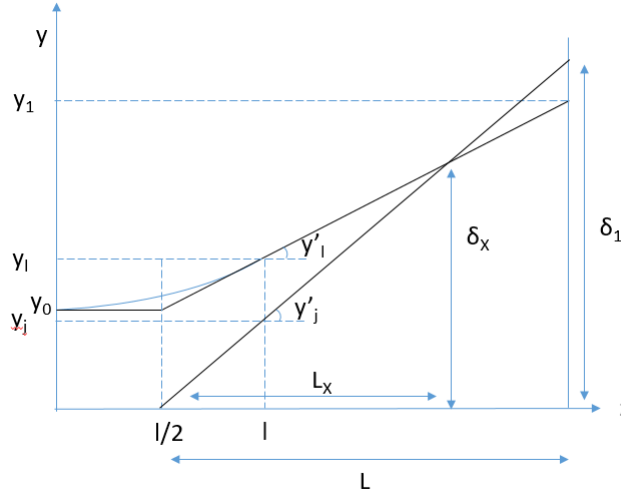
Figure G.5: Conventions used to approximate the bending of a ray (blue) by straight lines (black)

To take into consideration the distance to a screen L, the following variable can be created $y'_l = \frac{y_1 - y_0}{L}$ and since $y'_l = \frac{ln'}{n_0}$, then $y_1 - y_0 = \frac{Lln'}{n_0}$.

Introducing $\delta_1 = \frac{Lln'_w}{n_w}$ with x_w the variable at the (bottom) wall; δ the boundary layer thickness; and $\eta_0 = \frac{y_0}{\delta}$ and $\eta_1 = \frac{y_1}{\delta_1}$ respectively the boundary layer coordinate and the screen coordinate.

Then $\eta_1 = \frac{y_1}{\delta_1} = \frac{y_0 + \frac{Lln'}{n_0}}{\frac{Lln'_w}{n_w}} = \frac{n_w y_0}{lLn'_w} + \frac{n'n_w}{n_0 n'_w} = \frac{y_0}{\delta} + \frac{n'n_w}{n_0 n'_w} = \frac{\delta}{\delta_1}\eta_0 + \frac{n'n_w}{n_0 n'_w}$.

If L^* is the incoming intensity of the light ray and E^* the resulting intensity on the screen, then: $L^* dy_0 = E^* dy_1$, or $\frac{E^*}{L^*} = \frac{dy_0}{dy_1} = \frac{\delta}{\delta_1}\frac{d\eta_0}{d\eta_1} = \frac{\delta}{\delta_1}\frac{d\eta_0}{dy}\frac{dy}{d\eta_1} = \frac{\delta}{\delta_1}\frac{\frac{1}{\delta}}{\frac{\delta}{\delta_1}\frac{d\eta_0}{dy} + \frac{n_w}{n'_w}\frac{d}{dy}\left(\frac{n'}{n_0}\right)} = \frac{1}{1 + \delta_1\frac{n_w}{n'_w}\frac{n_0 n'' - n'^2}{n_0^2}} = \frac{1}{1 + Ll\frac{n_0 n'' - n'^2}{n_0^2}}$.

E^* becomes infinite when $\frac{d\eta_1}{d\eta_0} = 0$, which means that a focal line (a line corresponding to a high gradient of amplitude) develops in these specific conditions.

Based on G.5, $\tan(y'_l) = \frac{\delta_X - y_0}{L_X}$ and $\tan(y'_j) = \frac{\delta_X}{L_X}$ thus $L_X = \frac{y_0}{\tan(y'_j) - \tan(y'_l)}$: the two most extreme exiting rays are crossing if L (the distance between the device and the screen) is bigger than L_X.

When using a 100mm (instead of 1000mm) focal length mirror, the reversing phenomenon disappears as the crossing happens after the mirror.

This reversing phenomenon was reproducible with the ray-tracing simulation code. Thus it appears that both the distance between the module and the mirror, and the temperature gradient (mostly ΔT) have an impact on the existence or not and the eventual position of the focal point after the mirror:
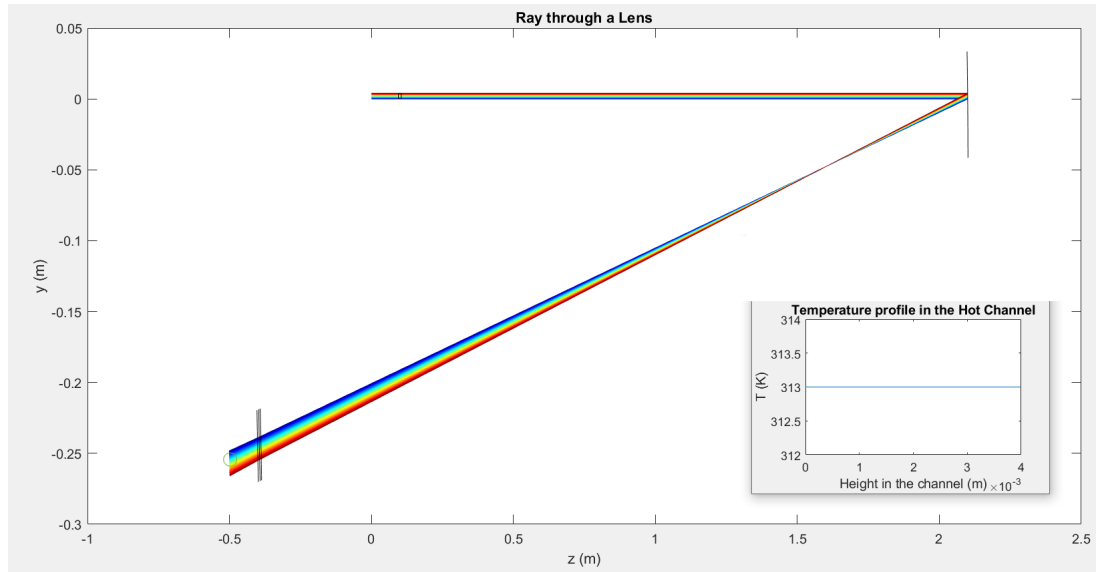
Figure G.6: Simulation of the optical path without any temperature gradient in the module, with a mirror of 500mm focal length and 750mm diameter.

Actually, this "reversing" phenomenon is not an issue in itself, if the Schlieren Set-up is well set.

G.5   Reminder on the measures

A measure can not be interpreted without an error magnitude. The error can come from the operation process of the sensors, the translation of the initial value into a value interpretable by the computer, the way the computer stores this value.

Here is a reminder of different notions that will be of importance in the choice of the materials:
- **Exactness**: It can be divided into *Accuracy* (the amount of uncertainty in a measurement with respect to an absolute standard; sum of the errors due to gain (error rate x measure), offset (fixed value), and linearity (error rate x range of measurement)) and *Fidelity* (which measures the dispersion of the results, equal to $\pm \frac{V_{max}-V_{min}}{2}$).
- **Resolution**: smallest absolute change that can be detected ($\frac{VoltageSpan}{2^{nbbitresolution}}$, knowing that the number of bit of resolution can be affected by the counts of noise: x counts of noise diminishes the number of bit resolution by $\sqrt{x}$)
- **Sensitivity**: variation between the output signal as a function of the variation of the input signal
There are also the following concepts:
- **Repeatability**: dispersion of successive results obtained with the same method on an identical matter under the same conditions (same operator, same measurement tool, same location, repetition on a short term)
- **Reproducibility**: dispersion between individual results obtained with the same method on an identical matter under different conditions (different operators, or different location).

Thus the more accurate and sensitive sensors will be chosen, and converter and connector devices with at least the same accuracy and precision selected.

For calculations, measures with a normal distribution are needed, and homoscedastic (which means that the dispersion is homogeneous, the stochastic error variance of the regression is the same for every observation). Thus once a set of datas is obtained, it must be verified that there is no variance too high (Cochrane test), nor outlier average values (Grubbs test).

The repeatability limit, r, is the maximal acceptable gap between two measures taken in the same location with the same method: $r = 2.83\sigma_r$.

The reproducibility limit, R, is the maximal acceptable gap between two measures taken in different locations $R = 2.83\sigma_R$.

G.6 Material

The functioning of the different elements used in the experimental set-up is described in this section.

G.6.1 Laser

A laser is the acronym for "light amplification by stimulated emission of radiation". It is spatially and temporally coherent. A laser is composed of a resonator, an optic cavity composed of two mirrors among which one at least is partially reflective (some of the beam is reflected inside the cavity and some is transmitted through the mirror surface). The phenomenon is based on the fact that the electrons of the atoms have different energy levels, the lowest one characterizing the thermodynamic equilibrium, being n=1; and the higher energy levels can be reached if the electrons absorbs one electromagnetic wave/photon of a similar energy as the energy difference between this level and the next one; and vice-versa, from the highest levels the electrons can go down the lower energy levels by emitting photons carrying an energy similar to the difference of energy between the two levels. To have a phenomenon of amplification, all the electrons have to be in the higher state (otherwise some of the rays could be absorbed by the atoms so that some electrons can reach a higher level and the resulting intensity would be lower). An external energy source is thus required to bring back the electrons to a higher excitation state.

Several technologies exist. In a diode laser, the pumping is ensured by an electrical current. They are very compact, cheap, even if the light is less pure and less directional than the Gaz lasers.

G.6.2 Camera

G.6.2.1 Filter

A color filter is placed just before the camera sensor, to allow the color determination of the light received by the sensor. These filters combine pixels of 3 opposed colors in a specific pattern: each pixel only lets the photons with the same wavelength through. Hence a specific wavelength can be attributed to the light intensity detected by the sensor, and the color of the pixel can be reconstructed thanks to algorithms based on the interpolation of the intensity values and wavelengths of the neighboring pixels.

Several types of filters (patterns, colors...) exist in cameras, the most well spread being the Bayer filter. Fujifilm developed a new X-Trans filter with the objective to reduce the optical aberrations, and prevent the use of a low-pass filter, allowing a better image resolution (fig. 7.21).

In his 1976's patent, Bryce Bayer describes the green photosensors as "luminance-sensitive elements" and the blue and red ones as "chrominance-sensitive elements", and he uses in his filter twice as many green photosensors as blue and red ones in a 2x2 pattern, to replicate the human physiology, more sensitive to green light [25].

Hence the 6x6 X-Trans pattern with more green pixels than in the Bayer increases the luminance resolution while decreasing the chrominance resolution. In the X-Trans filter the distance between two red or two blue pixels can be as high as 6 pixels in a raw or column, hence the interpolation work needed to reconstruct the colors behind the green squares is more difficult and more like a guess. Moreover the big squares of 4 green pixels can impact pictures with a lot of green (Iridient X-Transformer gives a better output).

G.6.2.2 Format storage

The images can be stored in 8 bits files .jpg or 14 bits files .raw. The raw format is a non-destructive compressed file: no data is lost. JPEG format is a compressed format were some datas are lost: for instance some color gradient can be converted in a uniform color patch, or overexposed areas can not be "repaired".

G.6.2.3 Sensor

Both charge-coupled devices (CCDs) and Complementary Metal Oxide Semiconductor (CMOS) were invented around the same time, but at the beginning CCDs were more performant (resolution and sensitivity) than CMOS. Nowadays, these CMOS are beginning to replace the CCDs thanks to their lower energy consumption and price, however they still have some progress to make on the noise and sensitivity part [87]. Both of them rely on the photoelectric effect to detect light: when a photon interacts

with a crystallized silicon to promote electrons from the valence band to the conduction band. The number of electrons released by the silicon semiconductor material when stroke by a photon depends on the wavelength of the light ray and its intensity: it is called the Quantum efficiency. The limit of light frequency above which the material can release electrons is called "threshold frequency" and depends on the material and is linked to the linking energy of the electrons that can be emitted. Thus, the speed of the emitted electrons is independent of the intensity of the light source, but the kinetic energy of the electrons emitted depends linearly on the frequency of the incident light. This phenomenon is quasi instantaneous ($10^{-9}s$).

A semi conductor is a material with insulator properties but for which the probability that an electron can contribute to an electrical current, even small, is high enough. Hence, its conductivity is between that of an insulator and that of a conductor. It is described in physics thanks to the electronic band theory: an electron in the solid belongs to an atom and can only have some specific ranges of energy called bands, and some levels are not reachable by the electron, called gaps. These bands are due to the discrete energy level an electron in an atomic orbital can have. When several (N) atoms are bonded together to form a solid, their atomic orbitals overlap, and according to Pauli exclusion principle (no two electrons in the same solid can have the same quantum number), each atomic orbital has to split into N molecular orbitals each of a different energy. When the number of atoms is high enough, these molecular orbitals are almost continuous and form a band. The electrons located in the most external orbitals of the atoms can bond with others and take part in electrical conductivity. They are called valence electrons. The band gaps have different width depending on the energy level: they are thinner at higher energy levels. The most important bands are the ones close to the Fermi level E_F, which is the thermodynamic work required to add one electron to the body. In metals and conductors, the last full band (valence band) and the half-full one just above (conduction band) are overlapping, and enclosing the Fermi level. In semi-conductors and insulators, the Fermi level is located in a gap, surrounded by the valence band just below (the last full band), and the conduction band just above (empty). Thus a semi-conductor is an insulator for which the energy difference between the conduction and the valence bands is small enough to allow conduction if this energy difference is provided to the electrons (heat, electromagnetic field, light...). Indeed it is the conduction band that allows electrons to circulate in the solid. To increase the permeability of the gap, one can add some atoms to break the purity of the solid: adding electrons-rich atoms increases the electron density (N-dopage), since the supplementary electrons in the valence band of these electrons-rich atoms will not be able to bond with any other electrons of the valence band of the regular solid's atoms, they will be free and easily excited towards the conduction band; and adding electrons-poor atoms increases the holes-density (P-dopage).

A P-N junction is the contact between a semiconductor doped P and a semiconductor dope N. If a positive tension is applied to the P region, the positive majority carriers (holes) are rejected towards the junction, while negative majority carriers (electrons) of the N-doped region are attracted to the junction. There, at the junction, either the electrons fall into holes and emit a photon, or they continue their road through the other semiconductor until the other electrode (current circulating). If a negative tension is applied to the P region, the carriers are getting away from the junction on both side and block the current. Hence a P-N junction is the basis of the diode.

Bipolar transistors are formed by double junction N-P-N and P-N-P: the semiconductor in the middle is about 1 μm thick being the "base" and the extreme semiconductor being the emitter and the collector. When submitting the emitter side to a positive tension, the emitter-base junction is passing, while the base-collector junction is blocked. However the base is thin enough to allow the emitter carriers to cross it without being able to recombine: hence they arrive in the collector, producing a current controlled by the initial current.

The MOS sensors are composed of three different thin layers: one metal, one insulator and one semi-conductor P-doped, with 2 N-doped inclusions. When a photon of a energy superior to he gap is received by the semiconductor, an electron is promoted from the valence band to the conduction band, leaving a hole (positive) behind. Driven by the field applied to the metal, the electron will migrate t the interface between the semiconductor and the insulator and stay stuck in a Potential sink, while the hole will migrate towards the ground electrode. The number of electrons that can be collected depends on the sink capacity, function of the surface and tension applied to the grid as well as the insulator thickness.

Sensitivity represents the efficiency of the conversion of electromagnetic radiation into electrical signals.

The CMOS sensors were less sensitive at the beginning because their efficient light-sensitive surface was smaller due to the electrical tracks that wire the circuits, and which are now buried into the chip. CMOS consist in an array of transistors, working on voltage instead of current (hence requiring less power). Each photodiode has its own amplifier, and is able to process locally. Due to these functionalities on the pixel area, the light-capture surface of the pixel is smaller.

CCD transfers each electron emitted from pixel to pixel of the same vertical stripe to a global amplifier for the whole chip. [107]

G.6.2.4   Resolution

It is not the number of pixel of the sensor that matters the most, but the number of pixel compared to the size of the chip.

Different sizes of sensors exist: the full frame and the cropped frame (ASP-C). If two sensors have the same number of pixels, the full frame sensor will have less noise than the cropped frame sensor because the pixels will be bigger.

G.6.2.5   Settings

A camera has three main settings:
- the ISO: ISO means International Standardization Organization. It is originally a measure of the film sensitivity to light, or its "speed": the less sensitive to light is the film, the more exposure to light it requires to produce the same image density as a more sensitive film (slow film). At microscopic scale, this is explained by the composition of the film: if the film is composed of thin particles, they will be more numerous and the chemical reaction will spread more slowly. As a result, the faster films where also the ones with highest grain, and lower precision. Now with numerical camera, these norms have been kept because the customer is used to it, but the sensitivity of the camera sensor is now fixed. Indeed, the sensitivity of the sensor is its ability to detect accurately the number of photon reaching it. The more accurate the sensor, the more exact the number of photon it measures. And this property is fixed and dependent only on the sensor fabrication. Arbitrarily, this sensitivity is fixed to 100 ISO. Nowadays, the ISO value is an indication to the camera for image transformation: increasing the ISO on a numerical camera increases the output signal of the light sensor.
- the shutter-speed or exposure time: it represents the time during which the sensor is exposed to the incident light and hence the quantity of energy reaching the sensor when taking the picture. The ideal speed is inversely related to the focal length ($\frac{1}{f}$, around 125 to 250) but for a moving object a higher speed is required (500-1000) while for a low lighten object a lower speed will be necessary (30-50)
- the aperture size or f-number: the aperture determines the depth of field of the picture. The f-number is calculated as the ratio of the focal length over the diameter of the opening, $N = \frac{f}{D}$, and is noted f/N. With a wide-opening (f/2, f/2.8), the background will be blur but the object will be very sharp; it is also advisable in low light. A medium opening (f/5.6, f/8) will still provide a sharp subject and the background will be recognizable. A small opening is ideal for landscape pictures.

The camera has three main modes:
- Mode P: in this mode the camera sets the shutter speed and the aperture for us
- Mode A: "aperture priority mode": in this mode, the user sets the aperture or f-stops (f/aperture), and the camera chooses the shutter speed
- Mode S: "shutter priority mode": in this mode, the user sets the shutter speed, and the camera chooses the aperture

ISO and exposure time are thus closely related: with a higher ISO, the amount of light required is lower thus the exposure time can be shorter, and vice versa.

G.6.2.6 Sensitivity

The sensitivity of the sensor can be measured in lux, which is the light flux through a unit surface, lm/m^2, where lumen are based on human perception, which means that it depends on the wavelengths as the human eye does not perceive all wavelengths so intensively, or in PPF (photosynthetic photon flux density, $mole.m^{-2}.s^{-1}$).

For each photon received, the camera will produce a certain amount of electrons, this is called the Quantum efficiency. The Full Well capacity describes the maximum amount of electrons one pixel can handle.

G.6.2.7 Noise

Let's define the RSN, ratio signal over noise, as the fraction of the mean value expected to the variation around this mean.

The noise in photography is mainly due to the photonic noise, or the sensor sensitivity to light due to the irregular arrival of photons on the camera sensor, which provides a constant RSN (dependent on the sensor only); and electronic noise, which provides a growing RSN as the exposition of the picture is increasing:

Due to the duality wave/corps of the photons, the amount of light reaching every little cell of the sensor is discrete and not continue. The number of photons received by the cell follows a Poisson-law. If the expected amount of photons is small, then even one photon more, or less, will have a bigger impact on the precision of the result than if the expected number of photons received per cell was higher. Indeed, the ratio signal(mean number of photons expected) over noise (variation around this mean) (RSN) is bigger for a higher signal, because the dispersion in Poisson law is proportional to the square root of the mean.

Note: Since the ISO on a numerical camera are only increasing the output signal of the sensor cells, the RSN stays the same because both the mean and the noise will be amplified equally.

The electronic elements of the camera are also producing a noise (dependent on temperature for instance): and this noise can be assumed constant compared to the photonic noise. Hence the lower the signal, the lower is the RSN since the noise is constant.

The dark current is the electric current that flows through photosensitive devices such as a photomultiplier tube, photodiode or CCD even when no photons are entering the device. It is due to the aleatory movement of electrons

As a conclusion, it is to be noted that to avoid the noise, a good light exposition of the picture is the most important parameter.

Different noises exists:
- Gaussian Noise: it is an electronic noise caused by the Johnson-Nyquist noise, inherent to the sensor and dependent on the illumination level and the temperature of the sensor
- Salt and Pepper Noise: this noise is caused by analog to digital converter errors or photodiode leakage currents at slower shutter speed
- Shot Noise: these noises follow the Poisson distribution
    - Photon Shot Noise (PSN): it is the dominant noise in dark areas or at higher exposure, caused by statistical quantum fluctuations, ie variations in the number of photons sensed at a given exposure level. The root mean square value of this noise is proportional to square root of image intensity; this noise at different pixels are independent of one another and follows a Poisson Distribution
    - Dark current shot noise (DCSN): dark current due to thermally generated electrons
- Periodic Noise: this noise is caused by electrical/electromechanical interferences during the image capturing process. This noise can be reduced by applying notch filter in the frequency domain.
- Pattern noise:
    - Fixed Pattern Noise (FPN): this noise refers to the spatial pattern constant from frame to frame, and due to dark current variations from pixel to pixel

– Photoresponse Non-Uniformity (PRNU): it is the variation in pixel responsivity
- Read Noise: this noise is caused by the transistors and amplifier. In color camera, more amplification is used in the blue color channel than in the red or green, thus there can be more noise in the blue channel. It reprensents the lowest signal the sensor can read because it is the noise level when the sensor is not exposed to light [70]
    – Reset Noise: this noise is due to thermal noise, which causes voltage fluctuations in the reset level of a pixel.
    – On-chip Amplifier Noise:
    – Off-chip Amplifier Noise:
    – Quantization Noise: this noise is introduced when the output is digitised and is caused by quantizing the pixels of a sensed image to a number of discrete levels. It follows a uniform distribution and is signal independent if other noise sources are big enough to cause dithering.

The total noise can be expressed through:

$$\sigma_{N_{TOT}}^2 = \sigma_R^2 + \sigma_{N_{PE}}^2 + \sigma_{N_{DARK}}^2 + C_{NL} \tag{G.41}$$

with:

$$\sigma_{N_{PE}}^2 = \sigma_{PSN}^2 + \sigma_{PRNU}^2 \tag{G.42}$$

and:

$$\sigma_{N_{DARK}}^2 = \sigma_{DSN}^2 + \sigma_{FPN}^2 \tag{G.43}$$

In Reibel et al. [116], a methodology is proposed to estimate the noises of a camera, by using a monochromatic light, and increasing the input illumination. The protocol is the following:
- acquire a high number of images (Num) in succession and calculate the mean image intensity $I_{mean} = \frac{\Sigma_{L=1}^{Num} M_L(j)}{Num}$, $\forall j \in CMOS$.
- repeat this step for various illumination from dark to saturation
- calculate the random-noise-free response $N_{TOT}(j)$ for each pixel of the matrix $N_{TOT}(j) = S(j)I + N_{OBS}(j)$, $\forall j \in CMOS$, with I the uniform illumination applied to the CMOS and $N_{OBS}(j)$ the radiometric dark value
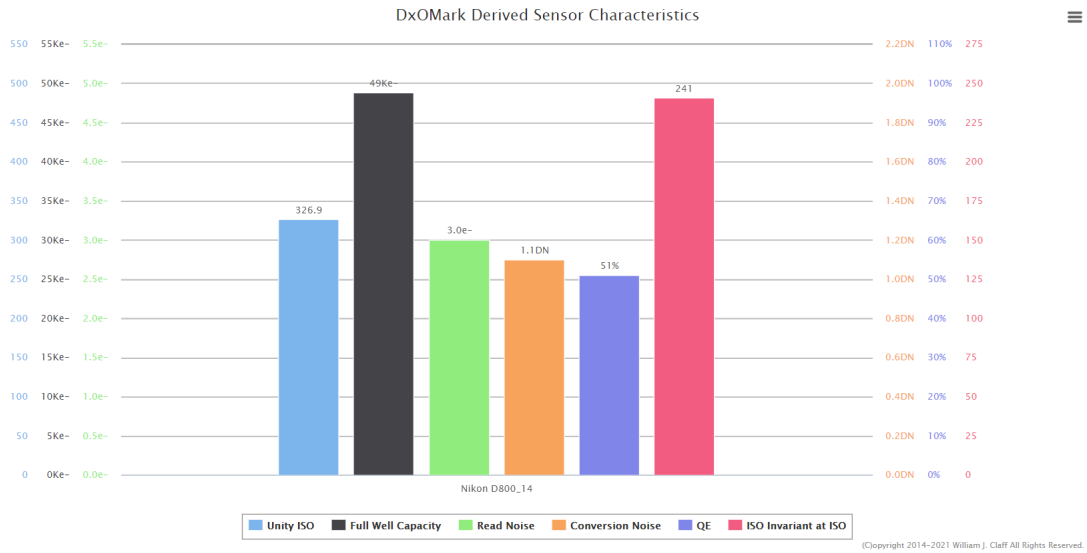
Figure G.7: Characteristics of the CMOS sensor of the Nikon D800 [31]

G.6.3   Membrane conception

The most commonly used techniques for preparation of polymeric membranes include [78]:
- phase inversion: a demixing process to turn a solution into a solid (porosity and pore size can be controlled by the polymer concentration)
- interfacial polymerization,

- stretching: a solvent free technique where the polymer is heated above melting point and extruded into thin sheets stretched to make it porous (for highly cristalline polymers)
- track-etching: the irradiation of a nonporous polymeric film with energetic heavy ions leading to the formation of linear damage. A precise control of the pore size (cylindrical pores parallel to the membrane) is possible with this method.
- electrospinning: the application of a high potential between the polymer solution droplet and the grounded collector: when the electrostatic potential becomes sufficiently high and overcomes the surface tension of the droplet a charged liquid jet is formed (for fibrous membranes, with precise control on the fiber size)

The mass transfer resistance of the membrane can be decreased thanks to the presence of macrovoids below the surface layer [78].

G.6.4 Sea water

Sea water is mainly composed of Cl^-, Na^+, SO_4^{2-}, Mg^{2+}, Ca^{2+}, K^+, Br^-, Sr^{2+}.

The concentration of these elements differs depending on the sea water type.

The salt rate admitted for potability is 0.5g/l, to be compared with the 35g/l found in mean in the seas.

Sea Water is a very complex medium. There are microorganisms, and a lot of different components, not always constant.

Index

Bibliography

[1] Water desalination report 2014, 2014.

[2] P. Aaron H. Statistical Rate Theory Expression for Energy Transported during Evaporation. PhD thesis, University of Toronto, 2014.

[3] M. A. Abdelkareema, M. El Haj Assada, E. Taha Sayedc, and B. Soudand. Recent progress in the use of renewable energy sources to power water desalination plants. Desalination, -.

[4] M. A. E.-R. Abu-Zeid, X. Lu, and S. Zhang. Enhancement of the air gap membrane distillation system performance by using the water gap module. Water Supply, 20(7):2884–2902, Nov. 2020.

[5] L. Acevedo, J. Uche, and A. Del-Amo. Improving the Distillate Prediction of a Membrane Distillation Unit in a Trigeneration Scheme by Using Artificial Neural Networks. Water, 10(3):310, Mar. 2018.

[6] I. E. Agency. World energy outlook 2018. Technical report, International Energy Agency, 2018.

[7] S. Al-Sharif, M. Albeirutty, A. Cipollina, and G. Micale. Modelling flow and heat transfer in spacer-filled membrane distillation channels using open source CFD code. Desalination, 311:103–112, Feb. 2013.

[8] A. Ali, F. Macedonio, E. Drioli, S. Aljlil, and O. Alharbi. Experimental and theoretical evaluation of temperature polarization phenomenon in direct contact membrane distillation. Chemical Engineering Research and Design, 91(10):1966–1977, Oct. 2013.

[9] A. Alkhudhiri, N. Darwish, and N. Hilal. Membrane distillation: A comprehensive review. Desalination, 287:2–18, Feb. 2012.

[10] A. Alkhudhiri and N. Hilal. Membrane distillation—principles, applications, configurations, design, and implementation. Emerging Technologies for Sustainable Desalination Handbook, 55–106., 2016.

[11] A. Alklaibi and N. Lior. Transport analysis of air-gap membrane distillation. Journal of membrane science, 2005.

[12] A. Alsaadi, N. Ghaffour, J.-D. Li, S. Gray, L. Francis, H. Maab, and G. Amy. Modeling of air-gap membrane distillation process: A theoretical and experimental study. Journal of Membrane Science, 445:53–65, Oct. 2013.

[13] A. Anvari, A. A. Yancheshme, K. M. Kekre, and A. Ronen. State-of-the-art methods for overcoming temperature polarization in membrane distillation process: A review. Journal of Membrane Science, 2020.

[14] S. Armbruster, O. Cheong, J. Lölsberg, S. Popovic, S. Yüce, and M. Wessling. Fouling mitigation in tubular membranes by 3d-printed turbulence promoters. Journal of Membrane Science, 2019.

[15] A. Asadi Tashvigh and B. Nasernejad. Soft computing method for modeling and optimization of air and water gap membrane distillation - a genetic programming approach. DESALINATION AND WATER TREATMENT, 76:30–39, 2017.

[16] M. B. Asif, W. E. Price, Z. Fida, A. Tufail, T. Ren, and F. I. Hai. Acid mine drainage and sewage impacted groundwater treatment bz membrae distillation: Organic micropollutant and metal removal and membrane fouling. 2021.

[17] I. E. Association. World balance. https://www.iea.org/sankey/#?c=World&s=Balance. Accessed: 2021-12-19.

[18] H. Attia, M. S. Osman, D. J. Johnson, C. Wright, and N. Hilal. Modelling of air gap membrane distillation and its application in heavy metals removal. Desalination, 424:27–36, Dec. 2017.

[19] S. Augustin. Watercone. http://www.watercone.com/product.html. Accessed: 2021-12-19.

[20] R. T. Balmer. Vapor and Gas Refrigeration Cycles. Modern Engineering Thermodynamics. Elsevier, 2011.

[21] F. A. Banat and J. Simandl. Theoretical and experimental study in membrane distillation. Desalination, 95(1):39–52, Mar. 1994.

[22] F. A. Banat and J. Simandl. Desalination by Membrane Distillation: A Parametric Study. Separation Science and Technology, 33(2):201–226, Jan. 1998.

[23] P. Bandelier. Le dessalement d'eau de mer et des eaux saumâtres. https://www.encyclopedie-energie.org/le-dessalement-deau-de-mer-et-des-eaux-saumatres/. Accessed: 2021-12-19.

[24] S. Bandini, A. Saavedra, and G. C. Sarti. Vacuum membrane distillation: Experiments and modeling. AIChE Journal, 43(2):398–408, Feb. 1997.

[25] B. E. Bayer. Color imaging array, 1976.

[26] J. C. Berg, M. Boudart, and A. Acrivos. Natural convection in pools of evaporating liquids. Journal of Fluid Mechanics, 24(04):721, Apr. 1966.

[27] M. Borgnia, S. Nielsen, A. Engel, and P. Agre. Cellular and molecular biology of the aquaporin water channels. Annual Review of Biochemistry, 68:425–458, 1999.

[28] E. H. Cabrera Castillo, N. Thomas, O. Al-Ketan, R. Rowshan, R. K. Abu Al-Rub, L. D. Nghiem, S. Vigneswaran, H. A. Arafat, and G. Naidu. 3d printed spacers for organic fouling mitigation in membrane distillation. Journal of Membrane Science, 2019.

[29] L. Camacho, L. Dumée, J. Zhang, J.-d. Li, M. Duke, J. Gomez, and S. Gray. Advances in Membrane Distillation for Water Desalination and Purification Applications. Water, 5(1):94–196, Jan. 2013.

[30] M. Chernyshov, G. Meindersma, and A. de Haan. Comparison of spacers for temperature polarization reduction in air gap membrane distillation. Desalination, 183(1-3):363–374, Nov. 2005.

[31] B. Claff. Dxomark derived characteristics. https://www.photonstophotos.net/Charts/Sensor_Characteristics.htm. Accessed: 2021-12-19.

[32] CNRS. Découvrir l'eau. http://www.cnrs.fr/cw/dossiers/doseau/decouv/cycle/stocksEau.html, -. Accessed: 2021-12-19.

[33] K. Cramer. Numerical modeling of Air-Gap Membrane Distillation. PhD thesis, University of Luxembourg, 2019.

[34] A. Criscuoli. Improvement of the membrane distillation performance through the integration of different configurations. Chemical Engeineering Research and Design, 2016.

[35] A. Da Costa, A. Fane, and D. Wiley. Spacer characterization and pressure drop modelling in spacer-filled channels for ultrafiltration. Journal of Membrane Science, 87(1-2):79–98, Feb. 1994.

[36] P. de Latil. Froid gratuit pour les pays chauds. Science et vie, 548:116–120, 1962.

[37] U. Dehesa-Carrasco, C. Pérez-Rábago, and C. Arancibia-Bulnes. Experimental evaluation and modeling of internal temperatures in an air gap membrane distillation unit. Desalination, 326:47–54, Oct. 2013.

[38] D. Dendukuri, S. K. Karode, and A. Kumar. Flow visualization through spacer filled channels by computational fluid dynamics-II: improved feed spacer designs. Journal of Membrane Science, 249(1-2):41–49, Mar. 2005.

Marie-Alix Dalle

[39] G. Diamanti. Eliodomestico. http://gabrielediamanti.com/projects/eliodomestico/. Accessed: 2021-12-19.

[40] R. C. Dougherty. Temperature and pressure dependence of hydrogen bond strength: A perturbation molecular orbital approach. The Journal of Chemical Physics, 1998.

[41] H. C. Duong, P. Cooper, B. Nelemans, T. Y. Cath, and L. D. Nghiem. Evaluating energy consumption of air gap membrane distillation for seawater desalination at pilot scale level. Separation and Purification Technology, 166:55–62, June 2016.

[42] R. Einav, K. Harussi, and D. Perry. The footprint of the desalination processes on the environment. Desalination, 152(1-3):141–154, Feb. 2003.

[43] B. C. Encyclopedia. Flow classification. https://chempedia.info/page/167225059107082235188041130188209015246219235035/. Accessed: 2021-12-19.

[44] M. Essalhi and M. Khayet. Application of a porous composite hydrophobic/hydrophilic membrane in desalination by air gap and liquid gap membrane distillation: A comparative study. Separation and Purification technology, 2014.

[45] S. Eyerer. Experimental Investigation of Boundary Layers in Membrane Desalination using Quantitative Two-Wavelengths Schlieren. PhD thesis, Technical University Munich, 2014.

[46] Forbes. Eroi, a tool to predict the best energy mix. https://www.forbes.com/sites/jamesconca/2015/02/11/eroi-a-tool-to-predict-the-best-energy-mix/#4f3b2636a027. Accessed: 2021-12-19.

[47] C. français de l'eau. L'eau pour l'énegie l'énergie pour l'eau. In Synthèse du colloque préparatoire au 6éme forum mondial de l'eau, 2012.

[48] P.-G. d. Gennes, F. Brochard-Wyart, and D. Quéré. Capillarity and wetting phenomena: drops, bubbles, pearls, waves. Springer, New York, NY, 2010. OCLC: 837651448.

[49] P. Gramann, B. Davis, T. Osswals, and C. Rauwendaal. A new dispersive and distributive static mixer for the compounding of highly viscous materials, 1999.

[50] E. Guillén-Burrieza, J. Blanco, G. Zaragoza, D.-C. Alarcón, P. Palenzuela, M. Ibarra, and W. Gernjak. Experimental analysis of an air gap membrane distillation solar desalination pilot system. Journal of Membrane Science, 379(1-2):386–396, Sept. 2011.

[51] M. Haddadi, S. Hosseini, D. Rashtchian, and M. Olazar. Comparative analysis of different static mixers performance by cfd technique: An innovative mixer. Chinese Journal of Chemical Engineeering, 2020.

[52] A. Hagedorn, G. Fieg, D. Winter, J. Koschikowski, A. Grabowski, and T. Mann. Membrane and spacer evaluation with respect to future module design in membrane distillation. Desalination, 413:154–167, July 2017.

[53] A. Hagedorn, G. Fieg, D. Winter, J. Koschikowski, and T. Mann. Methodical design and operation of membrane distillation plants for desalination. Chemical Engineering Research and Design, 2017.

[54] W. Hauf and U. Grigull. Optical Methods in Heat Transfer. In Advances in Heat Transfer, volume 6, pages 133–366. Elsevier, 1970.

[55] B. Heithorst. Combined CFD and Optical Raytracing Simulation for a Reverse Osmosis Membrane Test Setup. PhD thesis, Technical University Munich, 2015.

[56] M. Hincke, T. The eggshell: structure, composition and mineralization. Frontiers in Bioscience, 17(1):1266, 2012.

[57] I. Hitsov, K. De Sitter, C. Dotremont, P. Cauwenberg, and I. Nopens. Full-scale validated Air Gap Membrane Distillation (AGMD) model without calibration parameters. Journal of Membrane Science, 533:309–320, July 2017.

Marie-Alix Dalle

[58] C.-D. Ho, L. Chen, K.-Y. Wu, C.-H. Ni, and T. L. Chew. Permeate flux enhancement with a helical wired concentric tube in air gap membrane distillation systems. Desalination and water treatment, 201:150–168, 2020.

[59] L. Hofbauer. Desert cloud, 1972-2004. https://www.frac-centre.fr/_en/art-and-architecture-collection/stevens-graham/. Accessed: 2021-12-19.

[60] IDA. Water Security Handbook. •, 2019.

[61] S. J. Jaime, V. Jose M., and S. Carmelo. Case studies on environmental impact of seawater desalination. Desalination, 2005.

[62] I. Janajreh, D. Suwwan, and R. Hashaikeh. Assessment of direct contact membrane distillation under different configurations, velocities and membrane properties. Applied Energy, 185:2058–2073, Jan. 2017.

[63] K. Jijakli, H. Arafat, S. Kennedy, P. Mande, and V. V. Theeyattuparampil. How green solar desalination really is? environmental assessment using life-cycle analysis (lca) approach. Desalination, 2012.

[64] Z. Jingyi, Y. Heyang, D. Yelin, Z. Yuanchun, A.-R. Ibrahim M., H. Zhen, and Y. Chris. Life cycle assessment of a microbial desalination cell for sustainable wastewater treatment and saline water desalination. Journal of Cleaner Production, 2018.

[65] L. Jiuqing, I. Ashkan, L. Yuecun, and L. Glenn. Static mixing spacers for spiral wound modules. Journal of Membrane Science 442 140-148., 2013.

[66] E. Jones, M. Qadir, M. T. van Vliet, V. Smakhtin, and S.-m. Kang. The state of desalination and brine production: A global outlook. Science of The Total Environment, 657:1343–1356, Mar. 2019.

[67] E. Karbasi, J. Karimi-Sabet, J. Mohammadi-Rovshandeh, M. Ali Moosavian, H. Ahadi, and Y. Amini. Experimental and numerical study of air-gap membrane distillation (AGMD): Novel AGMD module for Oxygen-18 stable isotope enrichment. Chemical Engineering Journal, 322:667–678, Aug. 2017.

[68] A. Khalifa, D. Lawal, M. Antar, and M. Khayet. Experimental and theoretical investigation on water desalination using air gap membrane distillation. Desalination, 376:94–108, Nov. 2015.

[69] M. Khayet and C. Cojocaru. Air gap membrane distillation: Desalination, modeling and optimization. Desalination, 287:138–145, Feb. 2012.

[70] A. C. Konstantinidis, A. Olivo, P. R. Munro, S. E. Bohndiek, and R. D. Speller. Optical characterisation of a CMOS active pixel sensor using periodic noise reduction techniques. Nuclear Instruments and Methods in Physics Research Section A: Accelerators, Spectrometers, Detectors and Associated Equipment, 620(2-3):549–556, Aug. 2010.

[71] S. Kook, M. K. Le, S. Padala, and E. R. Hawkes. Z-type Schlieren Setup and its Application to High-Speed Imaging of Gasoline Sprays. SAE International Powertrains, Fuels and Lubricants Meeting, pages 2011–01–1981, Aug. 2011.

[72] C. Koutsou, S. Yiantsios, and A. Karabelas. Direct numerical simulation of flow in spacer-filled channels: Effect of spacer geometrical characteristics. Journal of Membrane Science, 291(1-2):53–69, Mar. 2007.

[73] S. Körber. Experimental Investigation and Optimization of a Schlieren Test Rig for Quantitative Boundary Layer Evaluations on Reverse Osmosis Membranes. PhD thesis, Technical University Munich, 2016.

[74] A. Kroiß, S. Eyerer, J. Kuczaty, C. Ties, S. Wolf, A. Präbst, M. Spinnler, and T. Sattelmayer. Optical Methods for Simultaneous Measurement of Temperature and Concentration Polarization. The International Desalination Association World Congress on Desalination and Water Reuse, page 25, 2015.

[75] A. Kroiss. On the Determination of Local Reverse OsmosisMembrane Properties from Optical Boundary LayerMeasurements. PhD thesis, Technischen UniversitätMünchen, 2019.

Marie-Alix Dalle

[76] H. Kurokawa, O. Kuroda, S. Takahashi, and K. Ebara. Vapor Permeate Characteristics of Membrane Distillation. Separation Science and Technology, 25(13-15):1349–1359, Oct. 1990.

[77] A. Lahsini, J. Bentama, A. Addaou, and M. Rafiq. Caractérisation physico-chimique et étude du frittage d'une argile destinée à l'élaboration de membranes de filtration tangentielle. Journal de Chimie Physique et de Physico-Chimie Biologique, 95(5):1001–1019, May 1998.

[78] B. S. Lalia, V. Kochkodan, R. Hashaikeh, and N. Hilal. A review on membrane fabrication: Structure, properties and performance relationship. Desalination, 326:77–95, Oct. 2013.

[79] D. U. Lawal and A. E. Khalifa. Experimental investigation of an air gap membrane distillation unit with double-sided cooling channel. Desalination and Water Treatment, 57(24):11066–11080, May 2016.

[80] K. W. Lawson and D. R. Lyold. Review membrane destillation. Journal of Membrane Science, 124, 1997.

[81] B. Li and K. K. Sirkar. Novel Membrane and Device for Direct Contact Membrane Distillation-Based Desalination Process. Industrial & Engineering Chemistry Research, 43(17):5300–5309, Aug. 2004.

[82] F. Li, G. Meindersma, A. de Haan, and T. Reith. Optimization of non-woven spacers by CFD and validation by experiments. Desalination, 146(1-3):209–212, Sept. 2002.

[83] F. Li, W. Meindersma, A. de Haan, and T. Reith. Novel spacers for mass transfer enhancement in membrane separations. Journal of Membrane Science, 253(1-2):1–12, May 2005.

[84] G. L. Liu, C. Zhu, C. S. Cheung, and C. W. Leung. Theoretical and experimental studies on air gap membrane distillation. Heat and Mass Transfer, 34(4):329–335, Nov. 1998.

[85] Z. Liu, Q. Gao, X. Lu, L. Zhao, S. Wu, Z. Ma, and H. Zhang. Study on the performance of double-pipe air gap membrane distillation module. Desalination, 396:48–56, Oct. 2016.

[86] O. R. Lokare, P. Ji, S. Wadekar, G. Dutt, and R. D. Vidic. Concentration polarization in membrane distillation: I. Development of a laser-based spectrophotometric method for in-situ characterization. Journal of Membrane Science, 581:462–471, July 2019.

[87] T. Lule, S. Benthien, H. Keller, F. Mutze, P. Rieve, K. Seibel, M. Sommer, and M. Bohm. Sensitivity of CMOS based imagers and scaling perspectives. IEEE Transactions on Electron Devices, 47(11):2110–2122, Nov. 2000.

[88] M. Lévêque. Les lois de la transmission de chaleur par convection. Annales des Mines, Memoires, Series 12,, 1928.

[89] L. Martinez-Diez, M. I. Vazquez-Gonzalez, and F. J. Florido-Diaz. Study of membrane distillation using channel spacers. Journal of Membrane Science, page 12, 1998.

[90] V. Masson-Delmotte, P. Zhai, A. Pirani, S. Connors, C. Péan, S. Berger, N. Caud, Y. Chen, L. Goldfarb, M. Gomis, M. Huang, K. Leitzell, E. Lonnoy, J. Matthews, T. Maycock, T. Waterfield, O. Yelekçi, R. Yu, and B. e. Zhou. Climate Change 2021: The Physical Science Basis. Contribution of Working Group I to the Sixth Assessment Report of the Intergovernmental Panel on Climate Change. Cambridge University Press, 2021.

[91] M. A. Mousavi, H. Reza Mortaheb, and M. Baghban Salehi. Hydrophobizing polyether sulfone membrane by sol-gel for water desalination using air gap membrane distillation. Polymer-Plastics Technology and Materials, 60(1):47–59, Jan. 2021.

[92] K. S. Mushatet, Q. A. Rishak, and M. H. Fagr. Numerical study of laminar flow in a sudden expansion obstacled channel. 2015.

[93] Nanoseen. Mounds facilitates gas exchange. https://nanoseen.com/en/. Accessed: 2021-12-19.

[94] V. K. Natrajan and K. T. Christensen. Development of Fluorescent Thermometry Methods for Microfluidic Systems. 14th Int Symp on Applications of Laser Techniques to Fluid Mechanics, page 13, 2008.

Marie-Alix Dalle

[95] B. J. Nelemans, J. Franciscus, and E. Lahaije. Device suitable for the treatment of a fluid, as well as a method and machine suitable for the manufacture of such a device, 2012.

[96] B. Niceno. An unstructured parallel algorithm for large eddy and conjugate heat transfer simulations. PhD thesis, Technische Universiteit Delft (Teh Nederlands), 2001.

[97] D. of Energy USA. Quadrennial Technology Review - An Assessment of Energy Technologies and Research Opportunities. •, 2015.

[98] A. K. Oppenheim, P. A. Urtiew, and F. J. Weinberg. On the use of laser light sources in schlieren-interferometer systems. Proceedings of the Royal Society of London. Series A, Mathematical and Physical Sciences, 1966.

[99] K. Pak. Dew bank. https://dewbankbeetle.weebly.com/dew-bank.html. Accessed: 2021-12-19.

[100] B. L. Pangarkar and M. G. Sane. Performance of Air Gap Membrane Distillation for Desalination of Ground Water and Seawater. World Academy of Science, Engineering and Technology, 5(3):5, 2011.

[101] P. K. Panigrahi and K. Muralidhar. Schlieren and Shadowgraph Methods in Heat and Mass Transfer. SpringerBriefs in Applied Sciences and Technology. Springer New York, New York, NY, 2012.

[102] R. Pawlowicz. Thermodynamic equation of seawater - 2010. http://www.teos-10.org. Accessed: 2021-12-19.

[103] A. H. Persad and C. A. Ward. Statistical Rate Theory Examination of Ethanol Evaporation. The Journal of Physical Chemistry B, 114(18):6107–6116, May 2010.

[104] A. H. Persad and C. A. Ward. Expressions for the Evaporation and Condensation Coefficients in the Hertz-Knudsen Relation. Chemical Reviews, 116(14):7727–7767, July 2016.

[105] R. Pinol, C. D. Brites, N. J. Silva, L. D. Carlos, and A. Millan. Chapter 6 - nanoscale thermometry for hyperthermia applications. 2019.

[106] S. Plating. Silver aluminium mirror coating. https://www.sharrettsplating.com/blog/silver-aluminum-mirror-coating/. Accessed: 2021-12-19.

[107] N. Postec and P. Picart. Quantification du bruit. http://optique-ingenieur.org/fr/cours/OPI_fr_M05_C06/co/Contenu_19.html. Accessed: 2021-12-19.

[108] H. M. Prasser. Wire-mesh sensors for two-phase flow investigations, Sep 1999.

[109] H.-M. Prasser, D. Scholz, and C. Zippe. Bubble size measurement using wire-mesh sensors. Flow Measurement and Instrumentation, 12(4):299–312, Aug. 2001.

[110] U. W. W. A. Programme and U. Director-General. United nations world water development report 4: managing water under uncertainty and risk, 2012.

[111] M. Rabie, M. S. Salem, A. Y. Ali, A. El-Shazly, M. Elkady, and S. Ookawara. Modeling of an integrated air gap membrane distillation unit utilizing a flat plate solar collector. Energy Reports, 6:1591–1596, Dec. 2020.

[112] G. Raluy, L. Serra, and J. Uche. Life-cycle assessment of msf, med and ro desalination technologies. Energy, 2006.

[113] A. P. Raman, M. Abou Anoma, L. Zhu, E. Rephaeli, and S. Fan. Passive radiative cooling below ambient air temperature under direct sunlight. Nature, 515:540–544, 2014.

[114] M. Ranaweera, V. Venkatesan, E. Guk, and J.-S. Kim. High spatial resolution monitoring of the temperature distribution from an operating SOFC. Conference: 12th European SOFC and SOE Forum, page 9, 2016.

[115] A. Redko, O. Redko, and R. DiPippo. Principles and operation of refrigeration and heat pump systems. Low-Temperature Energy Systems with Applications of Renewable Energy. Elsevier, 2020.

[116] Y. Reibel, M. Jung, M. Bouhifd, B. Cunin, and C. Draman. CCD or CMOS camera noise characterisation. The European Physical Journal Applied Physics, 21(1):75–80, Jan. 2003.

[117] H. Ritchie and M. Roser. Electricity mix, 2020.

[118] S. Rizaldy P. and Q. Susan E. The cell biology of renal filtration. Journal of Cell Biology, 2015.

[119] D. Ross, M. Gaitan, and L. E. Locascio. Temperature Measurement in Microfluidic Systems Using a Temperature-Dependent Fluorescent Dye. Analytical Chemistry, 73(17):4117–4123, Sept. 2001.

[120] M. Rudi and N. Klaus. Praxis der Wärmeübertragung. Hanser, 2015.

[121] A. Ruiz-Aguirre, D.-C. Alarcon-Padilla, and G. Zaragoza. Productivity analysis of two spiral-wound membrane distillation prototypes coupled with solar energy. Desalination and Water Treatment, 2014.

[122] R. B. Saffarini, E. K. Summers, H. A. Arafat, and J. H. Lienhard V. Technical evaluation of stand-alone solar powered membrane distillation systems. Desalination, 286:332–341, Feb. 2012.

[123] J. Sakakibara and R. J. Adrian. Whole field measurement of temperature in water using two-color laser induced fluorescence. Experiments in Fluids, 26(1-2):7–15, Jan. 1999.

[124] P. Schiebener, J. Straub, J. M. H. Levelt Sengers, and J. S. Gallagher. Refractive index of water and steam as function of wavelength, temperature and density. Journal of Physical and Chemical Reference Data, 19(3):677–717, May 1990.

[125] H. Schlichting and K. Gersten. Boundary-Layer theory Ninth edition. 2017.

[126] R. W. Schofield, A. G. Fane, and C. J. D. Fell. Heat and mass transfer in membrane distillation. Journal of Membrane Science, page 15, 1987.

[127] P. F. Scholander. How Mangroves Desalinate Seawater. Physiologia Plantarum, 21(1):251–261, Jan. 1968.

[128] G. S. Settles. Schlieren and Shadowgraph Techniques. Springer Berlin Heidelberg, Berlin, Heidelberg, 2001.

[129] V. T. Shahu and S. B. Thombre. Experimental analysis of a novel helical air gap membrane distillation system. Water Supply, page ws2021002, Jan. 2021.

[130] M. Shakaib, S. Hasani, I. Ahmed, and R. M. Yunus. A CFD study on the effect of spacer orientation on temperature polarization in membrane distillation modules. Desalination, 284:332–340, Jan. 2012.

[131] A. Shrivastava, S. Kumar, and E. Cussler. Predicting the effect of membrane spacers on mass transfer. Journal of Membrane Science, 2008.

[132] T. L. Silva, S. Morales-Torres, C. M. Esteves, A. R. Ribeiro, O. C. Nunes, J. L. Figueiredo, and A. M. Silva. Desalination and removal of organic micropollutants and microorganisms by membrane distillation. 2018.

[133] F. T. Smith, P. W. M. Brighton, P. S. Jackson, and J. C. Hunt. On boundary-layer flow past two-dimensional obstacles. 1981.

[134] P. Sosa-Fernandez, T. Loc, M. Andrés-Torres, M. Tedesco, J. Post, H. Bruning, and H. Rijnaarts. Energy consumption of an electrodialyzer desalinating aqueous polymer solutions. Desalination, 2021.

[135] S. Sudhanshu S. and M. Chandra Mouli R. Effects of internal geometry modifications on the dispersive and distributive mixing in static mixers. Chemical Engineering and Processing: Process Intensification, 2017.

[136] T. Suichi, A. Ishikawa, Y. Hayashi, and K. Tsuruta. Performance limit of daytime radiative cooling in warm humid environment. AIP Advances, 8(5):055124, May 2018.

[137] E. K. Summers, H. A. Arafat, and J. H. Lienhard. Energy efficiency comparison of single-stage membrane distillation (MD) desalination cycles in different configurations. Desalination, 290:54–66, Mar. 2012.

[138] E. K. Summers and J. H. Lienhard. Experimental study of thermal performance in air gap membrane distillation systems, including the direct solar heating of membranes. Desalination, 330:100–111, Dec. 2013.

[139] J. Swaminathan, H. W. Chung, D. M. Warsinger, F. Al-Arzooqi, H. A. Arafat, and J. H. Lienhard V. Energy efficiency of permeate gap and novel conductive gap membrane distillation. Journal of Membrane Science, 2015.

[140] A. Tamburini, A. Cipollina, S. Al-Sharif, M. Albeirutty, L. Gurreri, G. Micale, and M. Ciofalo. Assessment of temperature polarization in membrane distillation channels by liquid crystal thermography. Desalination and Water Treatment, 55(10):2747–2765, Sept. 2015.

[141] A. N. Team. Asymmetric burrow openings create passive ventilation. https://asknature.org/strategy/asymmetric-burrow-openings-create-passive-ventilation/. Accessed: 2021-12-19.

[142] A. N. Team. The beetles that drink water from air. https://asknature.org/strategy/water-vapor-harvesting/. Accessed: 2021-12-19.

[143] A. N. Team. Grooves gather water. https://asknature.org/strategy/grooves-gather-water/. Accessed: 2021-12-19.

[144] A. N. Team. Mounds facilitates gas exchange. https://asknature.org/strategy/mound-facilitates-gas-exchange/. Accessed: 2021-12-19.

[145] A. N. Team. Web continuously collects water from air. https://asknature.org/strategy/water-vapor-harvesting/. Accessed: 2021-12-19.

[146] G. H. Teoh, Z. A. Jawad, B. S. Ooi, and S. C. Low. Simultaneous water reclamation and nutrient recovery of aquaculture wastewater using membrane distillation. 2022.

[147] R. K. Thakur, C. Vial, K. D. P. Nigam, E. B. Nauman, and G. Djelveri. Static mixers in the process industry: a review. Institution of Chemical Engineers, 2003.

[148] C. Thies. Numeric and Experimental Investigation of Concentration Polarization in Membrane Desalination. PhD thesis, Technical University Munich, 2014.

[149] N. Thomas, N. Sreedhar, O. Al-Ketan, R. Rowshan, R. K. Abu Al-Rub, and H. Arafat. 3d printed triply periodic minimal surfaces as spacers for enhanced heat and mass transfer in membrane distillation. Desalination, 2018.

[150] H. Tribusch. How Life Learned to Live: Adaptation in Nature. MIT Press, 1983.

[151] R. Wagensonner. Experimentelle Bestimmung des Transportkoeffizienten in der thermischen Membrandestillation. PhD thesis, Technische Hochschule Deggendorf, 2017.

[152] J. Wang, Y. Liu, U. Rao, M. Dudley, N. D. Ebrahimi, J. Lou, F. Han, E. M. Hoek, N. Tilton, T. Y. Cath, C. S. Turchi, M. B. Heeley, Y. S. Ju, and D. Jassby. Conducting thermal energy to the membrane/water interface for the enhanced desalination of hypersaline brines using membrane distillation. Journal of Membrane Science, 626:119188, May 2021.

[153] P. Wang. Evaluation of MR thermometry with proton resonance frequency method at 7T. Quantitative Imaging in Medicine and Surgery, 7(2):259–266, Apr. 2017.

[154] K. Wangnick. Consulting. Technical report, Wangnick consulting, 2010.

[155] C. A. Ward. Liquid-Vapour Phase Change Rates and Interfacial Entropy Production. Journal of Non-Equilibrium Thermodynamics, 27(3), Jan. 2002.

[156] C. A. Ward and G. Fang. Expression for predicting liquid evaporation flux: Statistical rate theory approach. Physical Review E, 59(1):429–440, Jan. 1999.

Marie-Alix Dalle

[157] D. E. Warsinger, J. Swaminathan, L. A. Maswadeh, and J. H. Lienhard V. Superhydrophobic condenser surfaces for air gap membrane distillation. Journal of Membrane Science, 492:578–587, Oct. 2015.

[158] D. M. Warsinger, J. Swaminathan, L. L. Morales, and M. Bertoni. Visualization of droplet condensation in membrane distillation desalination with surface modification: hydrophilicity, hydrophobicity, and wicking spacers. Proceedings of the 2nd Thermal and Fluid Engineering Conference (TFEC2017), page 8, 2017.

[159] WHO. 10 facts on climate change and health. http://www.who.int/features/factfiles/climate_change/facts/en/index5.html. Accessed: 2021-12-19.

[160] WHO. Progress on drinking water, sanitation and hygiene. http://www.who.int/water_sanitation_health/publications/JMP-2017-report-final-highlights.pdf. Accessed: 2021-12-19.

[161] D. Winter, J. Koschikowski, and M. Wieghaus. Desalination using membrane distillation: Experimental studies on full scale spiral wound modules. Journal of Membrane Science, 375(1-2):104–112, June 2011.

[162] D. Woldemariam, A. Martin, and M. Santarelli. Exergy Analysis of Air-Gap Membrane Distillation Systems for Water Purification Applications. Applied Sciences, 7(3):301, Mar. 2017.

[163] S. Wolf. Implementation of an optical Measuring system for Investigation of Concentration Boundary Layers in Membrane Desalination. PhD thesis, Technical University Muich, 2014.

[164] M. Xie, H. K. Shon, S. R. Gray, and M. Elimelech. Membrane based processes for wastewater nutrient recovery: Technology, challenges, and future direction. 2016.

[165] J. Xu, Y. B. Singh, G. L. Amy, and N. Ghaffour. Effect of operating parameters and membrane characteristics on air gap membrane distillation performance for the treatment of highly saline water. Journal of Membrane Science, 512:73–82, Aug. 2016.